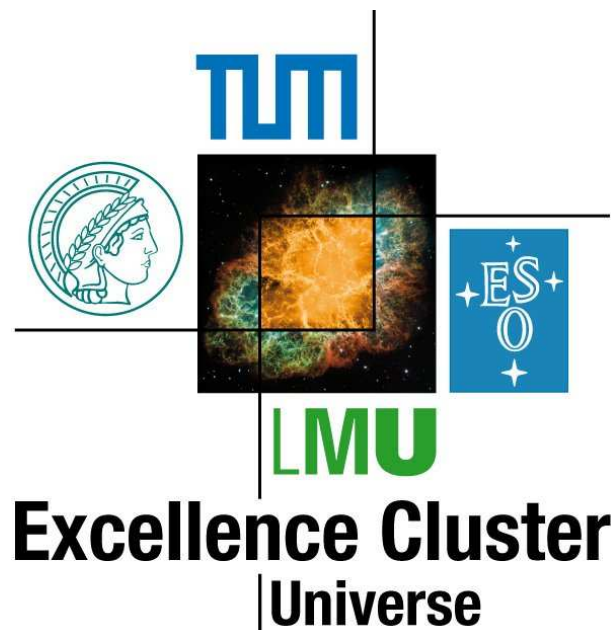


TECHNISCHE UNIVERSITÄT MÜNCHEN  
Physik Department Experimentalphysik E18

Characterization of solid  $D_2$  as source material for  
ultra cold neutrons and development of a detector  
concept for the detection of protons from the  
neutron decay





**TECHNISCHE UNIVERSITÄT MÜNCHEN**  
**Physik Department Experimentalphysik E18**

**Characterization of solid  $D_2$  as source material for  
ultra cold neutrons and development of a detector  
concept for the detection of protons from the  
neutron decay**

Axel Reimer Müller

Vollständiger Abdruck der von der Fakultät für Physik  
der Technischen Universität München  
zur Erlangung des akademischen Grades eines  
Doktors der Naturwissenschaften (Dr. rer. nat.)  
genehmigten Dissertation.

Vorsitzender: Univ.-Prof. Dr. W. Weise

Prüfer der Dissertation: 1. Univ.-Prof. Dr. St. Paul

2. Univ.-Prof. Dr. W. Petry

Die Dissertation wurde am 09.09.2008 bei der Technischen Universität München  
eingereicht und durch die Fakultät für Physik am 09.12.2008 angenommen.



# Contents

<b>1</b>	<b>Introduction</b>	<b>23</b>
1.1	Fundamental research with neutrons . . . . .	23
1.2	Ultra-cold neutrons . . . . .	24
1.3	Neutron decay in Standard Model . . . . .	26
1.4	Conclusion . . . . .	28
<b>2</b>	<b>Towards a strong UCN source</b>	<b>29</b>
2.1	UCN production . . . . .	29
2.1.1	”Conventional” UCN production . . . . .	29
2.1.2	”Superthermal” UCN production . . . . .	30
2.1.3	Superthermal production based on deuterium . . . . .	31
2.2	Deuterium characterization . . . . .	35
2.2.1	Setup of the <i>cubeD<sub>2</sub></i> experiment . . . . .	35
2.2.2	Visible light inspection . . . . .	39
2.2.3	Raman spectroscopy . . . . .	40
2.2.4	Neutron scattering . . . . .	41
2.3	<i>cubeD<sub>2</sub></i> , a test UCN source at the FRMII . . . . .	44
2.3.1	Setup at the FRMII . . . . .	44
2.3.2	UCNs, VCNs and CNs . . . . .	46
2.4	Experimental Results . . . . .	46
2.4.1	Visible light . . . . .	46
2.4.2	Raman spectroscopy . . . . .	52
2.4.3	Neutron scattering data . . . . .	56
2.4.4	The dynamics of solid deuterium . . . . .	60
2.4.5	Influence on the design of UCN sources . . . . .	61
2.4.6	Phonon and multiphonon contribution . . . . .	63
2.4.7	Estimation of the UCN production from $S(q,\omega)$ . . . . .	65
2.4.8	UCN up-scattering losses in deuterium . . . . .	70
2.4.9	Interpretation . . . . .	73
2.5	UCN production results . . . . .	73
2.5.1	UCN versus VCN . . . . .	74
2.5.2	UCN production in gaseous, liquid and solid D <sub>2</sub> . . . . .	75
2.5.3	Effects of freezing and annealing . . . . .	77
2.5.4	UCN production as function of ortho/para concentration . . . . .	79
2.5.5	Cell thickness . . . . .	81
2.6	miniD <sub>2</sub> converter . . . . .	81
2.7	Conclusion . . . . .	82

<b>3</b>	<b>UCN guides</b>	<b>85</b>
3.1	Methods to evaluate the transmission probability of UCN guides . . . .	86
3.1.1	The storage method . . . . .	86
3.1.2	The two hole method . . . . .	88
3.2	Sample tubes . . . . .	88
3.2.1	Samples for UCN valve characterization . . . . .	88
3.2.2	Possible UCN guide materials . . . . .	88
3.2.3	Electro polishing and discharge cleaning . . . . .	89
3.3	Beam measurements . . . . .	89
3.3.1	"UCN valve" and "storage method results" . . . . .	89
3.3.2	Surface roughness, machined versus electro polished . . . . .	91
3.3.3	Efficiency of discharge cleaning . . . . .	91
3.3.4	Different wall coatings on aluminum tubes . . . . .	93
3.3.5	Temperature dependence . . . . .	93
3.4	UCN transport simulation . . . . .	93
3.4.1	The U shaped baffle . . . . .	94
3.4.2	Calibration of the simulation . . . . .	95
3.4.3	<i>cubeD<sub>2</sub></i> data to extract <i>f</i> . . . . .	96
3.5	<i>Storage method</i> and <i>two hole method</i> results . . . . .	98
3.6	Conclusion on the characterization of UCN guides . . . . .	99
<b>4</b>	<b>UCN storage for n-lifetime measurement</b>	<b>101</b>
4.1	UCN trapping using material bottles . . . . .	101
4.2	UCN trapping in magnetic bottles . . . . .	102
4.2.1	Basic theory . . . . .	102
4.2.2	Previous magnetic storage experiments . . . . .	103
4.3	<i>The PENeLOPE</i> project . . . . .	103
4.3.1	<i>PENeLOPE</i> storage container . . . . .	103
4.3.2	<i>PENeLOPE</i> neutron detection . . . . .	105
4.3.3	<i>PENeLOPE</i> proton detection . . . . .	105
<b>5</b>	<b>Proton detection</b>	<b>109</b>
5.1	Requirements . . . . .	109
5.2	Basic detector idea . . . . .	109
5.3	Simulation . . . . .	110
5.3.1	Active area . . . . .	110
5.3.2	Proton interaction . . . . .	111
5.3.3	Light guiding structures . . . . .	113
5.3.4	Stress calculations . . . . .	117
5.3.5	Temperature mapping . . . . .	120
5.4	Material requirements . . . . .	120
5.4.1	Scintillator . . . . .	120
5.4.2	Light guides . . . . .	121
5.4.3	Photon counting units . . . . .	121
5.5	Experimental data . . . . .	121
5.5.1	Low energy proton detection with scintillators . . . . .	121
5.5.2	Low-temperature characterization . . . . .	122

5.5.3	The photon counting unit . . . . .	127
5.5.4	Thin film CsI scintillation counter . . . . .	128
5.6	Main detector concept . . . . .	134
5.7	Evaluation . . . . .	135
<b>6</b>	<b>Large area avalanche photodiodes (<i>LAAPDs</i>)</b>	<b>137</b>
6.1	Basic information . . . . .	137
6.1.1	PiN diode . . . . .	137
6.1.2	APD diode . . . . .	139
6.2	Theoretical description . . . . .	140
6.2.1	Internal gain . . . . .	140
6.2.2	Noise . . . . .	141
6.3	LAAPD structures . . . . .	143
6.3.1	Beveled edge type . . . . .	143
6.3.2	Reach through type . . . . .	143
6.4	Characterization . . . . .	144
6.4.1	Measurement of the working parameters as function of temperature	144
6.4.2	Gain and noise as function of $T$ . . . . .	146
6.4.3	Spectral response . . . . .	150
6.5	Interpretation . . . . .	151
6.5.1	LAAPD performance at low temperature . . . . .	151
6.5.2	Beveled edge type versus reach through type . . . . .	152
<b>7</b>	<b><i>pa</i>ff accelerator</b>	<b>155</b>
7.1	Setup . . . . .	157
7.1.1	Source part . . . . .	157
7.1.2	Diagnostic and monitoring part . . . . .	159
7.1.3	Diagnostic and beam-reduction part . . . . .	161
7.1.4	e-beam part . . . . .	163
7.1.5	Target part . . . . .	164
7.2	Simulations . . . . .	164
7.2.1	The effect of the potential distribution in the source . . . . .	164
7.2.2	The Einzel lens . . . . .	165
7.2.3	Beam transport properties . . . . .	166
7.3	Characterization . . . . .	166
7.3.1	Beam composition . . . . .	167
7.3.2	Beam intensity variations . . . . .	168
7.3.3	Beam energy . . . . .	171
7.3.4	Beam profile . . . . .	172
7.3.5	Beam monitoring system . . . . .	173
7.3.6	Beam visualization . . . . .	174
7.3.7	Electron beam . . . . .	176
7.4	Experimental application of <i>pa</i> ff . . . . .	177
7.4.1	<i>aSPECT</i> . . . . .	177
7.4.2	<i>PENeLOPE</i> . . . . .	177
<b>8</b>	<b>Summary</b>	<b>179</b>

<b>9 Outlook</b>	<b>181</b>
<b>10 Appendix</b>	<b>183</b>
10.1 Oxisorb as converter material . . . . .	183
10.2 Inelastic neutron scattering . . . . .	184
10.3 Two hole method . . . . .	187
10.4 electropolishing and discharge cleaning . . . . .	189
10.4.1 Electropolishing . . . . .	189
10.4.2 DC-discharge cleaning . . . . .	191
10.5 Mechanical and electropolishing . . . . .	191
10.6 <i>FRED</i> versus an analytical calculation . . . . .	192
10.7 Pree preparation of Hamamatsu LAAPDs for cooling tests . . . . .	194
10.8 Simulation results for the proton detector . . . . .	195

# List of Tables

1.1	Energy, velocity and wavelength for different neutron energy regions[1].	23
1.2	Characteristic values for different material corresponding to UCN. . . . .	25
1.3	Parametrization of the free neutron decay. . . . .	27
2.1	Raman shifts in $\text{cm}^{-1}$ for rotational states of $\text{H}_2$ , HD and $D_2$ . . . . .	41
2.2	Miller indices for hcp Bragg peaks of solid deuterium. . . . .	57
2.3	Comparison between different experimental predictions on $\sigma_x$ . . . . .	80
3.1	Different samples used at the <i>two hole method</i> to measure the $\mu$ and $f$ values . . . . .	89
3.2	Comparison between the <i>cubeD2</i> transmission data and the <i>FRED</i> simulation of the <i>cubeD2</i> setup. . . . .	97
3.3	Comparing the results from the <i>storage method</i> and the <i>two hole method</i> for the 2 m Nokado tube. . . . .	98
5.1	Scintillator materials and its properties. . . . .	111
5.2	Calculated stress due to cool down of the CsI layer on various light-guide materials. . . . .	119
5.3	Calculated peak position in ADC channels for the different energy spectra from the listed radioactive sources compared with the measured ones.	127
6.1	List of specified operation parameter from the data sheets of the used two LAAPD types. . . . .	144
7.1	Experiments for fundamental particle research dealing with proton detection from the free neutron decay. . . . .	155
7.2	Requirements on the <i>paff</i> facility. . . . .	156
7.3	Influence of the lens voltage $U_{\text{lens}}$ on the beam focus position. . . . .	162
7.4	Relative correction factor for the intensity loss due to the divergent beam.	166
7.5	Possible reactions of the ion beam atoms $I$ with rest gas atoms $X$ . . . . .	169
10.1	Size distribution of the Oxisorb particles. . . . .	184
10.2	Differences between Polished and Buffed Milled Finishes, Abrasive Grit Numbers and Surface Roughness. . . . .	193
10.3	Trapeze coverage with a thickness of $t=10\text{mm}$ . . . . .	195
10.4	Trapetze coverage with thickness $t=3\text{mm}$ . . . . .	196
10.5	Coverage with circle segments thickness $t=10\text{mm}$ . . . . .	196
10.6	Circle coverage with segments thickness $t=3\text{mm}$ . . . . .	196
10.7	coverage with triangle and cuboids thickness $t=10\text{mm}$ . . . . .	196
10.8	Coverage with triangle and cuboids thickness $t=3\text{mm}$ . . . . .	196



# List of Figures

1.1	Neutron decay on the quark level. . . . .	26
1.2	Left: the development of measured neutron lifetime values over the last 20 years is shown. Right: $g_A$ is plotted versus $g_V$ . The various bands indicate the allowed regions defined by experiments. The value from nuclear experiments and the assumption of CKM unitarity (both vertical), two values for $A$ from the PERKEO collaboration and the two $\tau_n$ values from the world average and Serebrov are shown . . . . .	28
2.1	Scheme of the downscattering process used for superthermal UCN production. The converter is shown in blue, the neutron in red and the excitation in green. The neutron velocity is indicated in the length of the velocity vectors. . . . .	30
2.2	Scheme of the two absorption UCN loss mechanisms. . . . .	33
2.3	Scheme of the two up scattering UCN loss mechanisms. . . . .	34
2.4	Idea of the <i>cubeD<sub>2</sub></i> setup and the realization of the target cell . . . . .	36
2.5	Three of the four deuterium target cells with 30, 20, 10 mm thickness, respectively for the neutron beam. The 5 mm target cell is not shown. The cold neutron entrance window can be seen in the front, the hole for the UCN extraction foil in the back. . . . .	36
2.6	<i>cubeD<sub>2</sub></i> scheme with the target cell on top of a two-stage Gifford McMahon cold head. The first stage is used to cool the radiation shield down to 35 K. The gas supply from the top and the CF 100 cross for thermal isolation are also shown. Cell temperature between 8 K - 300 K could be achieved by the use of a the heater. The beam direction is from left to right. . . . .	37
2.7	Flow diagram of the deuterium gas system for the <i>cubeD<sub>2</sub></i> experiments. The red tubes contain deuterium during nominal operation, the blue ones are vacuum connections. Depending on the valve setting, the deuterium may be transfered between the dump, the Oxisorb converter and the target cell. . . . .	38
2.8	Scheme of the ortho to para converter using the surface contact of liquid deuterium on Oxisorb grains shown on the left. The Raman sampling cell used to measure the ortho deuterium concentrations in the Raman setup of the Walter Meißner Institut and the used Oxisorb grain is shown on the right. . . . .	39
2.9	Left: excitation -emission scheme for photon scattering. Right: Raman setup at the Walter Meißner Institut. . . . .	40

2.10	Scheme of a neutron time-of-flight instrument to measure the scattering function $S(q, \omega)$ . The inlet on the upper left shows the working principle like explained in the text [49]. . . . .	41
2.11	<i>cubeD<sub>2</sub></i> setup used at the FRMII. . . . .	45
2.12	Methods to distinguish between UCN and VCN. . . . .	46
2.13	Deuterium phase diagram. . . . .	47
2.14	Left: solid neon at 20 K frozen in a snow like structure with a gas stream and air impurities. Right: convection zones in liquid neon visible through solid black impurities. The movement along the convection zone is shown by the arrows.. . . .	47
2.15	Stranski and Nake model for crystallization. . . . .	48
2.16	Liquefaction of deuterium. . . . .	49
2.17	Solidification of deuterium slow. . . . .	49
2.18	Deuterium re-sublimation with low saturation. . . . .	49
2.19	Transparent crystal prepared from the liquid and from the gas. . . . .	50
2.20	Deuterium re-sublimation with high saturation. . . . .	51
2.21	Deuterium solidification fast. . . . .	51
2.22	Undercooled deuterium sample. . . . .	52
2.23	Raman plots with hydrogen impurities and with high and low ortho concentration. . . . .	53
2.24	Natural ortho para conversion and measured conversion with our catalyst cell. . . . .	55
2.25	Lattice constant and scheme of a hcp deuterium basic structure. . . . .	56
2.26	Simulated and measured deuterium diffraction pattern for a calculated hcp and measured D <sub>2</sub> structure. . . . .	57
2.27	Preferential crystal direction and a scheme of the ortho crystal disturbed by a para impurity. . . . .	57
2.28	Solid deuterium structure $S(q, \omega = 0)$ as function of the momentum transfer $q$ and different freezing procedures. The region of interest is marked by a color square. . . . .	58
2.29	Possible annealing effect on the structure. . . . .	59
2.30	GDOS from solid deuterium as function of ortho concentration and the deuterium dispersion relation. . . . .	60
2.31	GDOS as function of temperature and a Lenard Jones potential. . . . .	62
2.32	Difference between the GDOS at 4 K, 8 K, 12 K compared to GDOS at 16 K . . . . .	62
2.33	Gdos for different freezing processes and annealing form IN4 . . . . .	62
2.34	Relative down scattering cross section from GDOS compared with Maxwell spectra for cold sources. . . . .	63
2.35	GDOS/ $\omega^2$ to get the single excitations for low and high ortho concentrations. . . . .	64
2.36	Separation of the different multiphonon contributions. . . . .	64
2.37	Dynamic structure factor $S(q, \omega)$ . . . . .	65
2.38	$S(q, \omega)$ as function of ortho para concentration and different freezing. . . . .	67
2.39	$S(q, \omega)$ slow freezing and sublimated sample. . . . .	68
2.40	Scheme of the phase space correction and the UCN production cross section. . . . .	70

2.41	TOFTOF time of flight data on the energy gain side as function of ortho concentration. . . . .	71
2.42	IN4 time of flight data on the energy gain side of the neutron. . . . .	71
2.43	Additional excitation together with Gauss fits. . . . .	72
2.44	UCN-VCN count rate from the <i>cubeD<sub>2</sub></i> test source. . . . .	74
2.45	Variation of the filling time and storing time at the <i>cubeD<sub>2</sub></i> source. . . . .	75
2.46	UCN count rate from deuterium gas and as function of the deuterium density. . . . .	76
2.47	UCN count rate during the phase transition gas liquid solid. . . . .	77
2.48	UCN count rate as function of freezing and annealing. . . . .	78
2.49	Time resolved annealing from the UCN and the CN count rate. . . . .	78
2.50	UCN count rate as function of ortho concentration and the extracted $\sigma_x$ additional loss cross section. . . . .	80
2.51	UCN count rate as function of sample thickness. . . . .	81
2.52	Scheme of the FRMII reactor building showing the location of the planned UCN source <i>miniD<sub>2</sub></i> and the UCN extraction direction. . . . .	82
2.53	Scheme of a new concept for the <i>miniD<sub>2</sub></i> UCN source. . . . .	83
3.1	Top scheme of a) the storage method and b)below two hole method b) to characterize UCN guides by estimating $\mu$ in the first case, $\mu$ and $f$ in the second case. . . . .	86
3.2	Scheme of our UCN valve. . . . .	87
3.3	Raw data from the storage method. . . . .	90
3.4	Calculated $\tau_{\text{loss}}$ as function of sample length together with the fit to get the $\mu$ value. . . . .	90
3.5	Experimental values $\mu$ and $f$ for the stainless steel and coated aluminum tubes from the <i>two hole method</i> . . . . .	92
3.6	Using the <i>FRED</i> software for UCN transport . . . . .	94
3.7	U shaped baffle for UCN transport simulation corresponding to the <i>cubeD<sub>2</sub></i> geometry. . . . .	94
3.8	Parameter studies on a model baffle system. . . . .	95
3.9	Comparison of experimental values with simulations from <i>FRED</i> . . . . .	96
3.10	Comparison between the ratio of the <i>cubeD<sub>2</sub></i> data and the <i>FRED</i> simulation with variation of the diffuse scattering probability $f$ . . . . .	97
3.11	Comparison between the setups from the second beam time. . . . .	97
3.12	Comparison of the $\mu$ value for the Nocado tube from the two different methods and two different UCN sources. . . . .	99
4.1	Scheme of the magnetic storage container for the planed lifetime experiment. . . . .	104
4.2	Energy spectrum of protons and electrons from the free neutron decay. . . . .	105
4.3	Proton trajectories starting inside the storage container with the extraction E- and B field. . . . .	106
4.4	Energy and angular distribution of protons hitting the detector area. . . . .	106
5.1	Basic idea for the proton detector for the PENeLOPE lifetime experiment. . . . .	110
5.2	Spatial radial distribution of the proton hits on the detector and integrated count rate as function of detector radius. . . . .	111

5.3	Proton trajectories and the beam spread inside a CsI layer. . . . .	112
5.4	Left: penetration depth in a CsI scintillator as a function of proton energy. Right: maximum penetration depth as function of incident angle for a 40-keV proton beam. . . . .	112
5.5	Proton energy and proton loss fraction due to a water surface layer thickness. . . . .	113
5.6	The <i>FRED</i> software used for light transport simulations. . . . .	114
5.7	Photon count rate as function of radius of the light guide and trapezoidal angle. . . . .	115
5.8	Twisted light guide. . . . .	116
5.9	Calculated number of LAAAPD detectors needed as function of geometry constrains. . . . .	117
5.10	Left: one of the 36 detector panels for the RMD solution. The LAAPD homogeneity is shown in the inlay. The point like response on the active area of the LAAPD is shown here in false color code. Right: Number of photons reaching the detector as function of the point of origin. 5000 photons were emitted under random directions for each point. . . . .	118
5.11	Study of the necessary support structure of the thin detector panels. . . . .	119
5.12	Setup to measure the risk of scintillator peal of. . . . .	119
5.13	Simulation of the expected temperature gradients of the proton detector. . . . .	120
5.14	Left: Pulse height spectra for different proton beam energies from the <i>pafl</i> accelerator. Right: channel number of the peak maximum as function of the beam. Also shown are the peak maxima from $\gamma$ ray and x-ray lines (green crosses) which have been used for the channel to energy calibration. . . . .	122
5.15	Setup for the first temperature dependence measurements . . . . .	123
5.16	$^{241}\text{Am}$ spectra with CsI(Tl) and a CsI(Tl) scintillator and a photomultiplier as function of wrapping material. . . . .	123
5.17	Temperature dependence of CsI and CsI(Tl). . . . .	124
5.18	Excitation spectra of CsI as function of temperature and the correction factor due to the photomultiplier quantum efficiency. . . . .	125
5.19	Fit of the excitation spectrum and the quantum efficiency of the photomultiplier. . . . .	126
5.20	Spectrum of 30 keV and 40 keV protons with the photomultiplier . . . . .	128
5.21	Scheme of the used setup to measure the efficiency of the thin film CsI layer detector at 50 K. . . . .	128
5.22	Surface of the evaporated CsI measured by raster electron microscopy. . . . .	130
5.23	The average crystal diameter $d_{\text{grain}}$ as estimated from the SEM pictures as a function of the exposition time $t_{\text{exp}}$ to air with relative humidity of 50%. . . . .	130
5.24	Atomic force microscopy pictures of evaporated CsI crystal. . . . .	130
5.25	30 keV proton spectrum of an evaporated CsI crystal at 50 K with an RMD LAAPD. . . . .	131
5.26	40 keV proton spectrum at 50 K with an evaporated CsI crystal as function of exposition time to humid air and change of peak position as a function of heating time afterwards. . . . .	131

5.27	Column structure of the evaporated CsI crystal measured with raster electron microscopy. . . . .	132
5.28	Spectra of 40 keV protons, 15 keV electrons and the background. . . .	133
5.29	Scheme of the planed proton detector . . . . .	134
6.1	Structure of a PiN diode (left-hand side) with the p-doping profile (middle) and the resulting potential profile (right-hand side). The motion of the charge carrier electrons $e$ and holes $h$ are shown inside the electric field $E$ . . . . .	138
6.2	The five different zones of a typical LAAPD structure together with the most important noise currents [150] . . . . .	138
6.3	Scheme of the avalanche multiplication process. . . . .	141
6.4	Electron multiplication for a PiN diode. . . . .	142
6.5	Structure and performance of two different types of LAAPD's beveled edge and reach through. . . . .	143
6.6	U-I working function (characteristic line) for the used LAAPD's as function of temperature. . . . .	145
6.7	Calculated break through voltage as function of temperature. . . . .	145
6.8	Peak position of 5.8 keV as function of temperature and bias voltage. .	146
6.9	LED spectrum normalized to the Fe spectrum as function of bias voltage.	147
6.10	Room temperature data gain compared with published values. . . . .	147
6.11	Gain $M$ as function of bias voltage and temperature. . . . .	147
6.12	Gain as a function of temperature for fixed bias voltages. . . . .	149
6.13	Temperature dependence of the dark current $I_D$ components superficial $I_{DS}$ and volume $I_{DV}$ . . . . .	149
6.14	Left: diode dark current as a function of $M$ for three different temperatures. The different symbols indicate different pressures. Right: a spectrum of 40 keV protons with both LAAPDs at identical conditions and maximal possible $U_{bias}$ . . . . .	150
6.15	Mobility for holes and electrons as a function of doping concentration and temperature. The ratio $\mu_n/\mu_h$ for the low and high doping case is shown on the right hand side [155]. . . . .	152
7.1	Scheme of the paff accelerator. . . . .	157
7.2	Scheme of the extractor type ion source. . . . .	158
7.3	Potentials and distances from the paff accelerator. . . . .	159
7.4	The four sector baffle. . . . .	160
7.5	Faraday cup detector. . . . .	160
7.6	The micro channel plate detector. . . . .	161
7.7	Einzel lens scheme. . . . .	162
7.8	One of the iris collimator. . . . .	163
7.9	Scheme of the electron gun. . . . .	164
7.10	Steerer with two correction coil used for the alignment of the electron beam. . . . .	165
7.11	Ion trajectories inside the source part. . . . .	165
7.12	Simulated 30 keV proton trajectories through the Einzel lens and the distance of the focal point behind the lens as function of the applied voltage. . . . .	166

7.13	Ion mass spectrum to visualize the extracted ions from the source. . . . .	167
7.14	Proton count rate at the MCP detector as function of extraction current. . . . .	169
7.15	Ion count rate at the MCP as function of accelerator voltage and necessary $B$ field and lens setting to get a maximum in count rate. . . . .	170
7.16	Beam intensity variation as function of lens voltage. . . . .	171
7.17	Measured beam profile. . . . .	172
7.18	Faraday cup current with suppression electrode. . . . .	173
7.19	Characterization of the beam monitor system and estimation of the measured count rate and the expected count rate. . . . .	174
7.20	Beam splitting visualized with the phosphor screen. . . . .	175
7.21	Astigmatism of the lens visualized with the phosphor screen. . . . .	175
7.22	x-y scan of the electron beam measured by the Faraday ring . . . . .	176
7.23	Proton spectrum measured with the aSPECT detector. . . . .	177
10.1	Calibration measurements necessary for the two hole method. . . . .	188
10.2	Principle of electropolishing and influence on the work piece surface . . . . .	189
10.3	Shift of chemical composition of a stainless steel surface and the influence of mechanical treatments on the surface composition. . . . .	190
10.4	Working principle of discharge cleaning. . . . .	191
10.5	Problem of scintillator read out from the side addressed by the diploma thesis of Niederberger. . . . .	193
10.6	Etching of the LAAPD to remove the epoxy layers. . . . .	194
10.7	LAAPD damages due to long edging or to strong acids. . . . .	194

# Abstract

Ultra-cold neutrons (UCN) are a well suited tool to address physics beyond the Standard Model of particle physics. Two of the most prominent experiments in this field are the measurement of the lifetime and the electric dipole moment of the free neutron. Both experiments are currently limited by statistics, which shall be improved by a new generation of UCN sources.

In the first part of this thesis, properties of the UCN-converter material solid deuterium (sD<sub>2</sub>) are studied. A series of investigations of various sD<sub>2</sub> crystals by means of optical spectroscopy and neutron scattering resulted in:

- (i) a freezing technique suitable for UCN sources
- (ii) an efficient method to achieve a high ortho concentration,
- (iii) a direct way to calculate the UCN production cross-section from the dynamic structure factor  $S(q, \omega)$ ,
- (iv) the identification of six excitations responsible for UCN production
- (v) the interpretation of one excitation at  $E=12$  meV as a multi-phonon process
- (vi) the discovery of an additional spin-dependent UCN loss mechanism at  $q = 2.1 \text{ \AA}^{-1}$  and  $E = 1.8$  meV.

A complementary series of experiments was performed at the FRMII, testing the production of UCN with the studied sample preparation after different the characterization mentioned above. Besides establishing a technique for annealing sD<sub>2</sub> crystals to improve the UCN production rate, an additional loss cross section ( $\sigma_x = 8$  barn at 4.5 K indirect proportional to the ortho concentration) was found. Based on these findings, a new conceptual layout of the miniD<sub>2</sub> source was developed.

In the second part, the diffuse scattering probability  $f$  and the loss probability per wall collision  $\mu$  were measured for differently prepared UCN guides using the *storage*- and the so called *two - hole* method. Electropolished, rough stainless steel and Al tubes with different coatings at temperature variation and surface conditions were measured. The results were also compared with optical ray-tracing simulations based on the software FRED.

The third part deals with the development of a proton detector for the neutron lifetime experiment PENeLOPE, which is based on gravitational and magnetic UCN storage and counting of the protons from the decay. A concept for a large-area proton detector based on thin scintillation counters operating in cryogenic environment was developed based on simulations and experimental studies. In addition to the characterization of CsI(Tl) and CsI scintillators, a small scale detector with a 1.5  $\mu\text{m}$  thick CsI layer was built. The detector was irradiated with 40 keV protons and 18 keV electrons. The light detection was done using large area photo diodes (LAAPD) at 50 K. The two LAAPD types (high voltage and low voltage ones) used for these tests were characterized down to 20 K. It was found that the noise is highly reduced by cooling down to 200 K or below. For both types cooling increased the usable amplification which reached a plateau at 60 K.

In the context of these tests the tunable proton accelerator *paff* was built, which provides us with tunable proton intensities in the range of  $10 \text{ s}^{-1}$  to  $10^{12} \text{ s}^{-1}$  and energies of 1 - 45 keV.



# Zusammenfassung

Ultrakalte Neutronen (UCN) werden dazu verwendet um Fragen des Standardmodells und weiterführende Theorien der Teilchenphysik zu beantworten. Die zwei prominentesten Experimente in diesem Feld sind die Messung der Neutronenlebensdauer  $\tau_n$  und die Bestimmung des elektrischen Dipolmoments. Da beide Experimente zur Zeit durch die erreichbare Statistik limitiert sind, werden momentan UCN Quellen mit weit höheren UCN Dichten entwickelt.

Im ersten Teil dieser Arbeit wird festes Deuterium, ein wohlbekanntes UCN-Quellen-Material, untersucht. Aus einer Vielzahl an verschiedenen preparierten sD<sub>2</sub> Kristallen konnten wir ein

(i) passendes Ausfrierverfahren für die geplante FRMII-UCN-Quelle mittels optischer- und Neutronenstreuexperimenten erarbeiten.

(ii) Ein Apparat zur Generierung von hohen ortho Konzentrationen wurde entwickelt. Aus dem gemessenen dynamischen Strukturfaktor  $S(q, \omega)$  konnte

(iii) erstmals der Produktionsquerschnitt direkt berechnet werden

(iv) sowie 6 Anregungen, die für die UCN Produktion verantwortlich sind, wurden identifiziert.

(v) Die Anregung bei 12 meV konnte dabei auf einen Multiphononenprozess zurück geführt werden.

(vi) Ebenfalls wurde ein zusätzlicher Verlustprozess durch eine Anregungsmode bei  $q=2.1 \text{ \AA}^{-1}$  mit einer Energie von 1.8 meV (Aufstreuung von UCN) gefunden. Eine Abhängigkeit von der para Konzentration wurde festgestellt.

Zusätzlich wurden die Methoden der Kristallherstellung an einem kalten Neutronenstrahl (FRMII) verwendet um die Auswirkungen auf die UCN Produktion zu untersuchen. Einerseits konnte gezeigt werden, dass das Tempern des sD<sub>2</sub> Festkörpers sich positiv auf die UCN Zählrate auswirkt, andererseits war es nötig einen zusätzlichen Verlustprozess von  $\sigma_x = 8 \text{ barn}$  bei 4.5 K und einer Abhängigkeit von der para Konzentration einzuführen um die experimentellen Ergebnisse mit bis dahin etablierter Theorie zu beschreiben. Auf dieser Grundlage wurde dann ein neues Konzept für die miniD<sub>2</sub> Quelle des FRMII entwickelt.

Um verschiedene UCN Leiter zu qualifizieren wurde im zweiten Teil der Arbeit eine Speichermethode entwickelt und mit der *two hole methode* verglichen. Der Verlustkoeffizient pro Wandstoß und die Wahrscheinlichkeit für diffuse Streuung wurden an einem unbehandelten und einem elektropolierten Edelstahlrohr sowie an Aluminiumrohren mit verschiedenen Innenbeschichtungen als Funktion der Temperatur und Oberflächenreinigung gemessen. Das Optikprogramm FRED wurde für Simulationen des UCN Transports angewendet.

Im dritten Teil wird der Aufbau des geplanten PENELOPE Experiments zur Bestimmung von  $\tau_n$  mittels magneto-gravitativ gespeicherter UCNs und der Messung der Zerfallsprotonen beschrieben. Ein Konzept für den kryogenen großflächigen Protonendetektor basierend auf der Detektion des Lichtes von einer dünnen aufgedampften Scintillatorschicht wird mittels Simulationen und Experimenten entwickelt. Neben der Tieftemperaturcharakterisierung von CsI und CsI(Tl) wurde ein kleiner Testdetektor mit 1.5  $\mu\text{m}$  Schichtdicke gebaut und die Spektren von 40 keV Protonen und 18 keV

Elektronen gemessen. Der Arbeitsbereich der verwendeten LAAPD Halbleiterdetektoren konnte von bisher 200 K erfolgreich bis auf 20 K erweitert werden. Neben dem Verschwinden des thermischen Rauschens konnte gezeigt werden, dass die nutzbare Verstärkung für (Arbeitsbereich hohe Betriebsspannung) sowie (Arbeitsbereich niedrige Betriebsspannung) LAAPDs bei 60 K ein Plateau erreicht.

Im Rahmen dieser Messungen wurde der Protonenbeschleuniger *pa.f.f* aufgebaut, welcher Protonenintensitäten im Bereich von  $10 \text{ s}^{-1}$  bis  $10^{12} \text{ s}^{-1}$  und Energien von 1 keV bis 45 keV liefert.

# Acknowledgment

I would like to express my thanks to Prof. S. Paul who not only gave me the opportunity to do my PhD work at his chair but was also always receptive to new experiments and new questions concerning UCNs during the last 4 years, even if these questions were not always directly correlated with the planned title of my PhD work. Therefore it was possible to achieve contributions to the UCN source, the UCN guides and the detection of the protons from the decay. It was my pleasure and extremely helpful to also get the chance to present and discuss new results at international conferences, workshops and meetings.

As mentioned above the final work as well as the acknowledgment is split into three parts with three different supervisors.

The results from the source part were mainly achieved together with E. Gutschiedl who joined my *cubeD<sub>2</sub>* experiment from the early beginning. He also enthusiastically joined the laboratory tests even on days like Dec.23 or Dec.31. He was, is and will be extremely important for the data analysis and discussions. The same goes for D. Tortorella and his PhD work which played an important role in the presented results. A special thanks is addressed to Ch. Hesse who extremely reliably took care of the electronics and the detector part of the *cubeD<sub>2</sub>* setup, no matter at which time. Most of the time he was also the first to deal with new results, and crazy ideas with criticism and always further motivations.

I. Altarev played the major role in the chapter concerning the UCN guides. The informative discussions during the day and night shifts at the ILL as well as the fact that his office was always open for physical and non-physical discussions were gratefully contributed to the development of the UCN guide chapter as well as the new miniD<sub>2</sub> concept.

J. F. Hartmann as the main supervisor of the PhD work was the leader of the paff accelerator construction, the proton detector development and the systematic studies of the low temperature behavior of the scintillators and semiconductor detectors. At the end a concept of the proton detector was developed out of these previous works. His knowledge and experience together with the help of Ch. Hesse helped me tremendously to adjust the detector electronics for the measurements. I also would like to mention the help of G. Petzold and the interesting discussions I had with him.

I also would like to express to R. Picker for his feedback on the requirements on the proton detector for the lifetime experiment.

My special thanks are addressed to the two mechanics T. Deuschle and H. Ruhland for the quick and 100 percent reliability of their work as well as early discussions of my ideas. H. Angerer helped me a lot to solve electronic and detector problems with his advice and help.

# Collaborations

It was my great pleasure to start a collaboration with the Raman group of the Walter Meißner Institut. They were of great help for the deuterium characterization. L. Tassini and R. Hackel supported us with their apparatus to measure the ortho/para concentration and helped with the data treatment. It is amazing that such great physical achievement has its root in an Oktoberfest visit with the right people. I give my thanks to O. Spieler from the Ludwig Maximilian University Munich who offered me his geology laboratory to make the characterization of the Oxisorb grains.

I also would like to mention the chair of Prof. K. Kinder where we used the electron raster microscope to look at the evaporated CsI crystal surface, which was prepared by M. H. Nacke from the chair of Prof. W. Krücken.

D. Rich, H.F. Wirth and M. Simson helped me to get the *cubeD<sub>2</sub>* experiment running at the FRMII. Even running always under constant time pressure, radiation protection and all the other work, we managed to full-fill all our desired program within one cycle and reached about 90% from our wish list.

Also I would like to say thank you to W. Carli from the Maier Leibnitz accelerator laboratory for being my contact person in accelerator questions and equipment. The installed electron gun was sponsored by A. Ulrich.

T. Unruh from the TOFTOF instrument helped us during our beam times and did not lose his interest in our results later on. He was of great help with the data analyzing as expert in solid state physics.

The other part was H. Schober at the ILL. Even though he is always extremely busy he found a week to join us at measuring our deuterium. The fact that he was sitting next to us during the beam time as well as his visits and data cross checks were essentially for our success.

# Readers

A special thanks to the people who read, corrected and discussed some of the following thesis. E. Gutmiedl, R. Stoepler, F. J. Hartmann, I. Altarev and P. Schricker

A special thanks is addressed to S. Materne and Ch. Hesse, P. Fierlinger, H. Schober, R. Picker and F. J. Hartmann who read and worked through all following 8 chapters of my thesis leading to discussions and step by step development of this final version.

A special thanks to my wife Cathrin Mugaj and my son Lukas Emanuel Mugaj who are the sunshine in my life.

# Chapter 1

## Introduction

### 1.1 Fundamental research with neutrons

Experiments with neutrons can help to arrive at a deeper understanding of nuclear and particle physics, fundamental symmetries, astrophysics and cosmology, fundamental constants, gravitation and the interpretation of quantum mechanics. The properties of free neutrons are used in various experiments as a probe or as object of interest by themselves. They are electrically neutral but strongly interacting, relatively long-lived but decay via the weak interaction.

Neutrons are ideal samples as all known four forces (strong, weak, electro magnetic and gravitation) may be assessed. The available dynamic range of neutron energies , velocities and corresponding wavelength from various neutron facilities is remarkable (cf. table 1.1). At least nine orders of magnitude in energy are covered between ultra-cold and fast neutrons.

	Energy E [eV]	Velocity v [m/s]	Wavelength $\lambda$ [nm]
UCN	$< 0.2 \cdot 10^{-6}$	$< 6$	$> 64$
VCN	$0.2 \cdot 10^{-6} \dots 50 \cdot 10^{-3}$	$6 \dots 100$	$4 \dots 64$
CN	$0.05 \cdot 10^{-3} \dots 25 \cdot 10^{-3}$	$100 \dots 2000$	$0.18 \dots 4$
thermal	$\dots 25 \cdot 10^{-3}$	$\dots 2200$	$\dots 0.18$
epithermal	$25 \cdot 10^{-3} \dots 500 \cdot 10^3$	$2200 \dots 1 \cdot 10^7$	$\dots 0.08$
fast	$> 500 \cdot 10^3$	$> 1 \cdot 10^7$	

Table 1.1: Energy, velocity and wavelength for different neutron energy regions[1].

Neutrons in thermal equilibrium with a moderator at  $T=300$  K (thermal neutrons) have kinetic energies around 25 meV. With a de Broglie wavelength in the order of 0.18 nm comparable to inter atomic distances a whole series of neutron diffraction and scattering experiments are possible for structure analysis in solid state physics. Cold neutrons at lower energies cover the dynamics of solids for systematic studies of phonons and excitations in condensed matter research.

Experiments using cold, very cold and ultra cold neutrons are addressing scientific issues associated with the Standard Model of particle physics and their connection to astrophysics and cosmology. Free neutrons decay with a lifetime of approximately 15

minutes. The first element of the Cabbibo Kobayashi Maskawa matrix may be determined via experiments from the free neutron decay [2] (through precise measurements of the free neutron lifetime  $\tau_n$  and decay correlation coefficients). Hence, neutrons help to test the unitarity of the matrix and with this the three-generation Standard Model. A non vanishing electric dipole moment [3] of the neutron  $d_n$  induces a violation of time-reversal symmetry  $T$  and, if conservation of CPT symmetry holds, also a violation of CP symmetry [4]. The use of ultra-cold neutrons with the possibility to store, manipulate and study them for several minutes in suitable containers leads to steady improvements of  $\tau_n$  and  $d_n$  experiments and also triggered new kind of experiments for example gravitational bound states [5], gravitational phase shift [6], neutron-anti-neutron oscillations [7] and others. A short motivation for the measurement of the free neutron lifetime is given on the following pages.

## 1.2 Ultra-cold neutrons

The interaction of neutrons with matter (in the UCN energy regime) may be simplified by an averaged optical potential called Fermi potential  $V_F$ [8]. The latter fluctuates dramatically across the different nuclides but can be calculated from the measured bound coherent scattering length  $b_c$  [9], the atomic particle density  $N$  and the neutron mass  $M_n = (939 \text{ MeV}/c^2)$

$$V_F = \frac{2\pi\hbar^2 N b_c}{M_n}.$$

If  $E_{\text{kin}} < V_F$  the neutrons undergo mostly total reflection. Typical  $V_F$  values are 252 neV for Be, 335 neV for  $^{58}\text{Ni}$  or 185 neV for stainless steel as can be seen in table 1.2. Ultra cold neutrons are defined as neutrons with sufficient low energy  $E_{\text{UCN}} < V_F$  that they can be stored inside confinements made of high  $V_F$  materials. But due to the fact that the wavefunction of the UCN undergoing total reflection penetrates a small distance into the reflecting surface and may be absorbed there the storage is not loss less. The material coefficient  $\mu$  is introduced to consider the loss probability per wall collision. Some values are also listed at table 1.2. The fact that one can store UCN for long periods makes them an excellent tool to study their fundamental properties with high precision.

### Strong interaction

Neutrons and protons are tightly bound in nuclei via the strong interaction. In contrast to being scattered from the surface, a UCN can also be captured by the wall nuclei. This absorption usually results in the emission of a  $\gamma$ -ray ( $n,\gamma$ ) or charged particle ( $(n,p)$  or  $(n,\alpha)$ ). Up to now the flux of existing UCN sources is not high enough to think of possible UCN surface spectrometer.

### Gravitational interaction

Gravitation plays a very important role for UCN as heights of 2 m in the earth gravitational field  $g$  approximately correspond, to a kinetic energy of 200 neV for neutrons

Element	$\rho$ [g/cc]	$a_{\text{coh}}^{\text{bound}}$ $10^{-13}\text{cm}$	$\sigma_{\text{tot}}$ [barn]	$\mu$ [ $10^{-5}$ 1/bounce]	$V$ [neV]
$Ni^{58}$	8,8	14,4	44	8,6	335
BeO	3,0	13,6	6,6	1,35	261
Ni	8,8	10,6	48	12,5	252
Be	1,83	7,75	1,4	0,5	252
C	2,0	6,6	1,4	0,6	180
Cu	8,5	7,6	43,5	15,5	168
Fe	7,9	9,7	28	8,5	210
Al	2,7	3,45	2,8	2,25	54
V	6,11	-0,382	50		-7,2
Polyethylen	0,92	-0,84			-8,7
$H_2O$	1,0	-1,68			-14,7
Ti	4,54	-3,34	58		-48

Table 1.2: Characteristic values to describe material for their use in UCN physics.  $\sigma_{\text{tot}} = \sigma_{\text{coh}} + \sigma_{\text{incoh}} + \sigma_{\text{abs}}$  corresponding to  $\lambda = 18 \text{ \AA}$  wavelength. The bound coherent scattering length  $a_{\text{coh}}^{\text{bound}}$ , the Fermi potential  $V_F$  and the loss coefficient per wall collision  $\mu$  are shown. A negative Fermi potential, caused by a negative scattering length  $b_c$  as shown in the last four examples leads to an attractive potential for the neutron. All values were measured at room temperature. Data are taken from [8]

with a mass of  $M_n = 1.67 \cdot 10^{-27} \text{ kg}$ .

$$E_{\text{pot}} = M_n g \cdot h = E_{\text{kin}} \quad \rightarrow \quad h_{\text{UCN}} = \frac{M_n g}{E_{\text{kin}}} \quad \xrightarrow{E_{\text{kin}}(\text{UCN})=200 \text{ neV}} \quad h_{\text{UCN}} \approx 2 \text{ m}$$

This can be used for example to study the quantum level structure of the gravitational potential [10], search for phase shifts [6] or violation of the equivalence principle [11]. A more practical benefit is that a UCN storage container of sufficient height may stay open to the top.

## Electromagnetic interaction

Even though the neutron is electrically neutral, due to its spin it has a magnetic moment  $\mu_n$ <sup>1</sup> and therefore a Stern-Gerlach force is exerted on the neutron in an inhomogeneous magnetic field. The direction of the force depends on the orientation of the neutron spin towards the field vector. The low field seekers are repelled ( $V_B < 0$ ), the high field seekers attracted ( $V_B > 0$ ) by the electromagnetic potential  $V_B$  in the gradient field  $\vec{B}$ .

$$V_B = -\mu_n \cdot |\vec{B}| = \underbrace{\pm 60.3 \frac{\text{neV}}{\text{T}}}_{\text{low/high field seekers} \cdot |\vec{B}|} \cdot |\vec{B}|$$

<sup>1</sup>In the following pages  $\mu$  is used to describe the loss probability per wall collision.

UCNs of 120 neV may be stored in magnetic fields of  $\approx 2$  T which are in reach of superconducting magnets. However, 50% with the wrong spin component  $s_z$  are accelerated towards the coils generating the strong field and are eventually lost. Avoiding any wall collisions the other half is stored magnetically. The proof of magnetic storage was shown with a magnetic cup trap [12], the superconducting storage ring Nestor [13], and with a permanent magnet configuration [14]. A more detailed description of a new magnetic storage concept for a neutron lifetime measurement will be given in sec. 4.

### Weak interaction

The neutron is composed of two down and one up quark decaying via the weak interaction into a proton (one down two up) and a  $W$  boson. The latter then decays into an electron and an electron-anti-neutrino. The released energy is distributed over the decay products.

$$n \rightarrow p + e^- + \bar{\nu}_e + 0.783 \text{ MeV}$$

It should be noted that there are two other interesting exotic channels available for the neutron. The radiative decay with an additional photon in the final state [15] and the bound decay into a hydrogen atom and the anti neutrino [16].

The decay is theoretically described by the Standard Model of particle physics. High precision measurements on beta decays can be used to proof assumptions from this model or extended new theories beyond the Standard Model.

## 1.3 Neutron decay in Standard Model

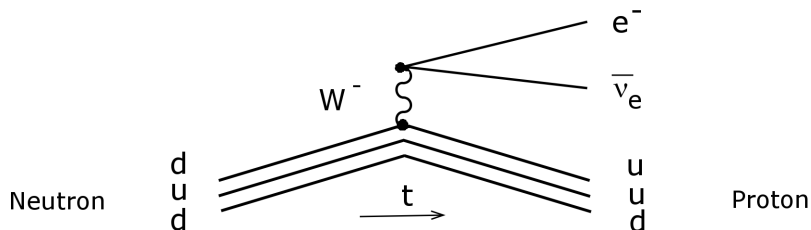


Figure 1.1: Neutron decay on the quark level.

In the Standard Model the free neutron decay on the quark level (see fig. 1.1) is described by a mixed vector  $V_\mu$  and axial vector  $A_\mu$  current. The interaction strength is described by the coupling constants  $g_V$  and  $g_A$  ( $\lambda := g_V$ ). Since the momentum transfers are very small compared to the mass of the exchange boson  $W$ , the theoretical decay can be simplified into a four-fermion, point-like interaction with an effective Lagrangian

$$\mathcal{L}_{\text{int}} = \frac{G_F V_{ud}}{2\sqrt{2}} (V_\mu - \lambda A_\mu) \cdot (v^\mu - a^\mu).$$

Applying the Feynman rules in fig. 1.1 defines the  $V_\mu = \bar{\psi}_u \gamma_\mu \psi_d$ ,  $A_\mu = \bar{\psi}_u \gamma_\mu \psi_d$  for the hadronic part and  $v_\mu = \bar{\psi}_e \gamma_\mu \psi_\nu$ ,  $a_\mu = \bar{\psi}_e \gamma_\mu \psi_\nu$  at the leptonic sector.  $G_F$  is the Fermi coupling constant and  $V_{ud}$  the first element of the Cabibbo Kobayashi Maskawa quark mixing matrix. This matrix connects the electro weak eigenstates  $d', s', b'$  with the mass eigenstates  $d, s, b$ .

$$\begin{pmatrix} d' \\ s' \\ b' \end{pmatrix} = \begin{pmatrix} V_{ud} & V_{us} & V_{ub} \\ V_{cd} & V_{cs} & V_{cb} \\ V_{td} & V_{ts} & V_{tb} \end{pmatrix} \cdot \begin{pmatrix} d \\ s \\ b \end{pmatrix}$$

The unitarity of this matrix as a key point of the Standard Model is a consequence of the universality of the weak interaction gauge theory. Unitarity of the CKM matrix is fulfilled if :

$$|V_{ud}|^2 + |V_{us}|^2 + |V_{ub}|^2 = 1$$

The matrix elements  $V_{us}$  and  $V_{ud}$  are obtained from high energy accelerator experiments. High precision measurements of the neutron decay lead to the missing part  $|V_{ud}|$  to solve the question of unitarity [17]:

$$|V_{ud}|^2(\lambda, \tau_n) = \frac{4903.7(38)}{1 + 3\lambda^2} \cdot \frac{1}{\tau_n}$$

Beside the neutron lifetime also the ratio of the couplings has to be known with high precision. This value can be extracted from the probability distribution of the beta decay parameterized in terms of the neutron spin, the energy and momentum of the decay products [18]

$$dW \propto (g_V^2 + g_A^2)F(E_e) \left[ 1 + a \frac{\vec{p}_e \cdot \vec{p}_\nu}{E_e E_\nu} + b \frac{m_e}{E_e} + \vec{\sigma}_n \cdot \left( A \frac{\vec{p}_e}{E_e} + B \frac{\vec{p}_\nu}{E_\nu} + D \frac{\vec{p}_e \times \vec{p}_\nu}{E_e E_\nu} \right) + \dots \right]$$

In this equation  $F(E_e)$  is the electron energy spectrum and the coefficients  $a, b, A, B, D$  are derived from experiments measuring correlations between the neutron spin and its decay products:

a	=	$\frac{1- \lambda ^2}{1+3 \lambda ^2}$	=	$-0.103 \pm 0.0029$	electron-anti neutrino asymmetry
b	=	0	=	0	Fierz interference
A	=	$-2 \frac{ \lambda ^2 +  \lambda  \cos \Phi}{1+3 \lambda ^2}$	=	$-0.1173 \pm 0.0013$	spin-electron asymmetry
B	=	$2 \frac{ \lambda ^2 -  \lambda  \cos \Phi}{1+3 \lambda ^2}$	=	$0.981 \pm 0.004$	spin-anti neutrino asymmetry
D	=	$2 \frac{ \lambda  \sin \Phi}{1+3 \lambda ^2}$	=	$-4 \pm 6 \cdot 10^{-4}$	T-odd triple-product

Table 1.3: Parametrization of the free neutron decay.  $\Phi$  is the angle between the couplings  $g_A$  and  $g_V$  Equations and values are taken from [1].

Figure 1.2 (left) shows the development of neutron lifetime values over the last 20 years. The agreement among the different measurements was good despite the most recent experiment from Serebrov et.al. [19] with a deviation of six sigma from the DPG average value. This is already a strong motivation to measure  $\tau_n$  with a new storage concept, as described in section 4.

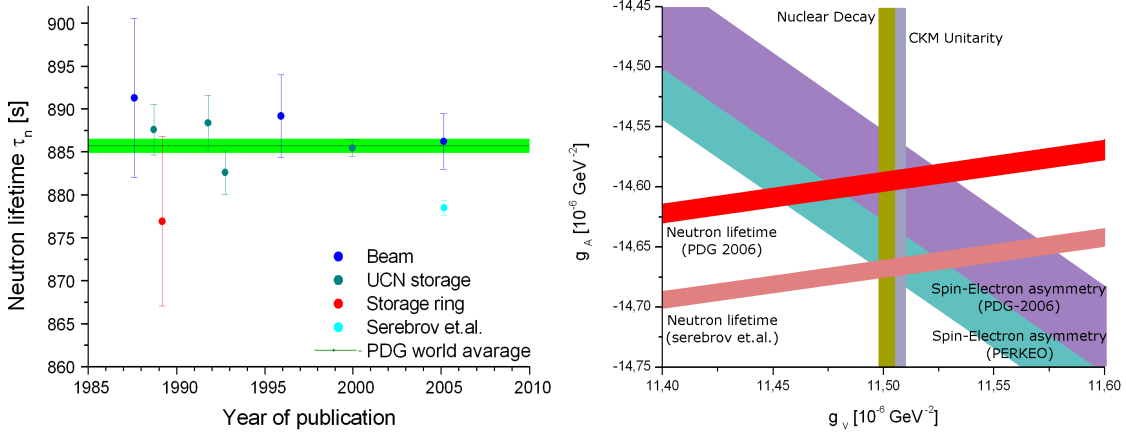


Figure 1.2: Left: the development of measured neutron lifetime values over the last 20 years is shown. Right:  $g_A$  is plotted versus  $g_V$ . The various bands indicate the allowed regions defined by experiments. The value from nuclear experiments and the assumption of CKM unitarity (both vertical), two values for  $A$  from the PERKEO collaboration and the two  $\tau_n$  values from the world average and Serebrov are shown.

On the right side of fig. 1.2, the influence of the two lifetime values (the new one and the PDG value) as well as a new value for  $A$  from the *PERKEO* collaboration on the unitarity problem is shown. Currently it just depends which combination of these values is used to confirm or rule out the Standard Model. Hence, this puzzle has to be resolved.

## 1.4 Conclusion

The experiments described in section 1.2 and in particular, the key experiment to measure  $\tau_n$  are limited at the moment more by statistical than systematic errors because of the comparably low UCN densities available at the operating sources. Together with the limitation of available beam time extensive systematic studies are hardly possible. The still open fundamental physical questions reported above would benefit from improvements on the following subjects:

- ◇ A strong UCN source with high UCN density → chapter 2
- ◇ An efficient guiding system from the source to the experiment → chapter 3
- ◇ A lossless UCN confinement → chapter 4
- ◇ A suitable detector for the decay products → chapter 5

# Chapter 2

## Towards a strong UCN source

### 2.1 UCN production

The highest thermal neutron flux of the order (of  $\Phi > 10^{14} \text{ s}^{-1}\text{cm}^{-2}$ ) is achieved at spallation sources or in nuclear fission reactors. Fast neutrons (MeV) are slowed down inside a heavy water moderator to thermal neutron energies (25 meV). In a second stage they are moderated in a cold source (for example liquid deuterium at 25 K) into the 0.05 - 25 meV energy band (cold neutrons). The most promising methods for further energy reduction (into the neV region) are:

- The extraction from the source of UCN with velocities in the tail of the Maxwell distribution. Conventional UCN production.
- UCN energy loss by excitation of atoms or molecules of a converter material: superthermal source.

After a short introduction to the conventional method, principle and theory of superthermal production are described. The loss mechanisms in a deuterium converter are listed. In the following different techniques and experiments used to characterize  $D_2$  as converter are outlined, before the experimental results are presented. The *cubeD<sub>2</sub>* UCN test source for the FRMII<sup>1</sup>, which was built as part of this work, is explained. In conclusion, the results are discussed and a new concept for the *miniD<sub>2</sub>* UCN source for the FRMII neutron source is presented.

#### 2.1.1 "Conventional" UCN production

The neutron energy spectrum  $d\Phi/dE$  of a thermal (cold) source is described by a Maxwellian velocity distribution with the (cold) moderator temperature  $T_0$ , the Boltzmann constant  $k_B$ , the neutron energy  $E$  and incident flux  $\Phi_0$ .

$$\frac{d\Phi}{dE} = \Phi_0 \cdot \frac{E}{(k_B T_0)^2} \cdot e^{-\frac{E}{k_B T_0}} \quad (2.1)$$

Integrating eq. 2.1 from zero to the Fermi potential  $V_{\text{Fermi}}$  of the wall material provides us with the maximum extractable UCN flux  $\Phi_{\text{UCN}}$  from such a neutron source. If we neglect losses for a moment this leads to a  $T^{-2}$  dependence of the achievable UCN

---

<sup>1</sup>Forschungsneutronenquelle Heinz Maier-Leibnitz FRM II in Munich, Germany.

density  $\rho_{\text{UCN}}$ , which can be approximated by eq. 2.4. Instead of the Fermi potential of the wall we calculated a cut off velocity  $v_g$ .

$$\Phi_{\text{UCN}} = \int_0^{V_{\text{Fermi}}} \frac{d\Phi}{dE} dE \quad (2.2)$$

$$\approx \frac{1}{2} \Phi_0 \left( \frac{V_{\text{Fermi}}}{k_B T} \right)^2 \quad (2.3)$$

$$\rho_{\text{UCN}} \approx \frac{2}{3} \Phi_0 \left( \frac{V_{\text{Fermi}}}{k_B T} \right)^2 \cdot \frac{1}{v_g} \quad (2.4)$$

In the thermal moderator of a typical research reactor the calculated UCN density at  $T = 300$  K is  $40 \text{ UCN cm}^{-3}$ . It increases by two orders of magnitude at thermal equilibrium in a cold source at  $T = 30$  K, but due to their still very high velocity of  $\approx 700$  m/s a long flight path inside the moderator medium is necessary. Because at the same time the amount of UCN is reduced by the internal losses UCN can just be extracted from a few cm from the surface. In total, the usable UCN density is reduced close to the density of  $40 \text{ UCN cm}^{-3}$ . The UCN source at the ILL reactor [8] claims a measured density of this value.

### 2.1.2 "Superthermal" UCN production

We consider a converter material (shown blue in fig. 2.1) with two energy levels. The ground state  $E_g$  and the excited state  $E_{\text{ex}}$  are separated by the energy gap  $\Delta$ .

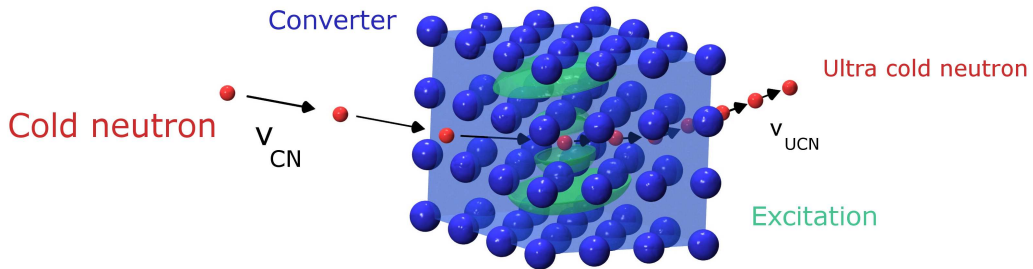


Figure 2.1: Scheme of the downscattering process used for superthermal UCN production. The converter is shown in blue, the neutron in red and the excitation in green. The neutron velocity is indicated in the length of the velocity vectors.

During passage of the neutron (red) through the converter material (blue) the neutron creates an excitation (green) and the required energy  $\Delta$  is taken from the neutron kinetic energy. The neutron is slowed down shown schematically via the length of the velocity vectors. Cold neutrons within the neutron spectrum  $\frac{d\Phi}{dE_i}$  matching the energy level  $\Delta$  lose almost all their kinetic energy, leading to a neutron with very small energy

of around 100 neV (UCN creation). The probability of creating an excitation is given by the cross section  $\frac{d\sigma}{dE}(E_g \rightarrow E_{ex})$ . From the principle of detailed balance (eq. 2.11), the same cross section multiplied with the occupation number (temperature) is used to describe the reverse process when an excitation is destroyed and the neutron gains the energy  $\Delta^2$ . This up-scattering process is a UCN loss channel which is reduced by running at low temperatures, low occupation number of the excitation levels. If the converter has sufficiently large dimensions both reactions lead to a thermal equilibrium between the neutrons and the converter. A Maxwell spectrum corresponding to the converter temperature peaking far above the required UCN energies ( $T_{UCN}(E_{UCN} = 200 \text{ neV}) = 2.3 \cdot 10^{-3} \text{ K}$ ) is produced. Smaller sources<sup>3</sup> avoid this and lead to a net gain in the UCN rate. Instead of a thermal equilibrium an equilibrium between UCN gain and UCN is reached at stable conditions. This kind of source is called superthermal source [12, 8]. Eq. 2.5 can be used to calculate the production rate per converter atom  $P_{\text{atom}}$  as the product of the spectral cold-neutron flux  $d\Phi/dE$  times the down-scattering cross section (transition probability of the neutron initial energy  $E_i$  to the final energy  $E_f$ ).

$$P_{\text{atom}} = \int_0^{E_{UCN}} \int_0^\infty \frac{d\Phi}{dE_i}(E_i) \frac{d\sigma}{dE_i}(E_i, E_f) dE_i dE_f \quad (2.5)$$

To calculate the production rate  $P$  one has to multiply eq. 2.5 by the number density of particles  $N_D$  seen by the cold neutrons.

$$P = N_D \cdot P_{\text{atom}} \quad (2.6)$$

To extract the maximum number of UCN from the source one has to consider the various loss mechanisms; their effect may be described by a lifetime  $\tau_{\text{loss}}$ . Assuming the low-density UCN as a gas, the density  $\rho_{UCN}$  is the key parameter to compare different converter materials, qualify different UCN source concepts or use it as input parameter for predictions of densities in future experiments.

$$\rho_{UCN} = P \cdot \tau_{\text{loss}} \quad (2.7)$$

### 2.1.3 Superthermal production based on deuterium

Converters based on solid deuterium are currently developed at PSI [20], at Los Alamos [21] and at Munich [22]. The production of UCN from solid deuterium has first been studied at PNPI Gatchina [23] and at Los Alamos, where a prototype solid  $D_2$  source is operating. A smaller model of the planned mini $D_2$  UCN source for the FRMII research reactor in Munich was successfully built by the Technische Universität München [24] and tested at the TRIGA reactor in Mainz.

Liquid He is another promising candidate for UCN production. However, it has the disadvantage of necessary lower temperatures to achieve high performance (reduce the up scattering losses). A prototype source was built by [25]. The required temperature is typically below 1 K. In a reactor environment, as it is planned for the Munich source in the vicinity of the reactor core (20 MW thermal power), a liquid He source is not

---

<sup>2</sup>In spectroscopy research these two processes are known as Stokes and Anti-Stokes lines.

<sup>3</sup>Due to the small cross sections for excitations and thus for the UCN production just a small fraction of the cold neutron beam is used to increase the UCN density. Therefore the cold neutrons are not moderated (complete flux affected) they are converted by a converter into UCN.

feasible due to the enormous necessary cooling power. The following efforts are focused on deuterium and the development of a deuterium based solution for the FRMII. Alternative converter materials, under investigation at groups in the US, like CD<sub>4</sub> [26] or O<sub>2</sub> [27, 28] are mentioned for completeness.

## Production cross section

Following eq. 2.5, we need an expression for the down scattering cross section  $\frac{d\sigma}{dE}$  to describe the process of UCN production. This quantity can be extracted from the scattering function  $S(q, \omega)$  as shown in eq. 2.8. The following equations are taken from [29, 30].

$$\frac{d^2\sigma}{dE_i d\Omega}(E_i, E_f, k_i \rightarrow k_f) = \sigma_B \frac{k_f}{k_i} \cdot S(q, \omega) \quad (2.8)$$

The cross section  $\sigma_B$  describes the scattering by a bound nucleus with  $k_i$  and  $k_f$  the initial and final wave vectors of the neutron respectively. The scattering function  $S(q, \omega)$ , also called dynamic structure factor, describes the intensity as a function of  $q$  eq 2.9 momentum transfer and energy transfer  $\omega$  eq. 2.10 and (incident and final energy  $E_{i/f}$  and the scattering angle  $\vartheta$ )

$$q^2 = k_i^2 + k_f^2 - k_i k_f \cos(2\vartheta) \quad (2.9)$$

$$\hbar\omega = E_f - E_i = \frac{\hbar^2}{2m}(k_f^2 - k_i^2) \quad (2.10)$$

In our case we just integrate above the  $d\Omega$  because the angular dependence is of minor interest when the UCN are described as a gas.

It is possible to calculate the one phonon density of states  $Z(\omega)$  from the scattering function  $S(q, \omega)$  (section 10.2). This quantity describes the number of possible excitations as function of their energy. In case of a one-component incoherently scattering<sup>4</sup> system  $Z(\omega)$  can be calculated correctly. In case of an coherently scattering system one can use the incoherent approximation<sup>5</sup>, to calculate  $Z(\omega)$  from the  $q$  integrated  $S(q, \omega)$  [31]. The validity of the incoherent approximation can be tested for example by calculating  $Z(\omega)$  with different constraints on the  $q$  range [32]. In case of particles with mixed contributions from coherent and incoherent scattering, for example  $D_2$  ( $\sigma_{\text{coh}} = 5.592$  barn,  $\sigma_{\text{inc}} = 2.053$  barn [38]) things become more complicated. It even gets worse for multi component systems[31, 33]. Considering a mixture of ortho and para  $D_2$  with their different  $\sigma_{\text{coh}}$  and  $\sigma_{\text{inc}}$  [34] we finally are faced the last mentioned case.

---

<sup>4</sup>Neutron scattering can be described by two parts: incoherent scattering  $\sigma_{\text{inc}}$  at single atoms and coherent scattering  $\sigma_{\text{coh}}$  including interference of neighboring atoms.

<sup>5</sup>In the incoherent approximation one assumes that the scattering length  $b_{\text{inc}}$  and  $b_{\text{coh}}$  are equal. This means that after integration over  $q$  the incoherent part (necessary to determine  $Z(\omega)$ ) can be approximated by averaging over the interference terms from coherent scattering. This approximation is valid if the neutron wave length is small compared to the particle distance or the  $q$  range is sufficiently large. It is trivial full-filled for dominant incoherent scatterer.

Up to now it was the standard technique, within the UCN community [27], [29], [35], [36] to get  $Z(\omega)$  in the incoherent approximation and calculate the cross section with the following equation and at last the UCN production  $P$  (eq. 2.5):

$$\frac{d^2\sigma}{d\Omega dE_i} \stackrel{1 \text{ phonon}}{=} = 1/2M_{D_2} \left[ 2b \sum_i j_i \left( \frac{qa}{2} \right) \right]^2 \frac{k_f}{k_i} e^{(-2W(\vec{q})q^2)} \frac{Z(\omega)}{\omega} \begin{cases} n(\omega) + 1 & \text{ph. creation} \\ n(\omega) & \text{ph. annihil.} \end{cases}$$

The parameter  $b$  is the bound scattering length of deuterium and  $j_i$  is the form factor of the molecules with the sum over all realized excitation levels inside the target. In the simplest approximation  $j_i$  are the first order spherical Bessel function if one assumes spheres like in the case of 100 % ortho  $D_2$  concentration. The quantity  $a$  describes the mean distance between two deuterium atoms in the deuterium molecule. The population number  $n(\omega)$  is given by Bose-Einstein statistics, while the Debye Waller factor  $e^{-W(\vec{q})}$ , with  $W(\vec{q}) = \frac{1}{6}q^2 \langle \vec{u}^2 \rangle$  (a function of the mean displacement  $\langle u^2 \rangle$  of the nuclei) may be interpreted as the form factor of the crystal. It describes the zero phonon expansion of the cubic lattice. The ratio of the wave numbers takes into account the phase space and finally the phonon density of states  $Z(\omega)$ . This calculation assumes that no internal excitation of the  $D_2$  molecule is generated in the scattering process. A Debye model is usually used to describe the phonon density of states and to calculate the cross section and later the expected production rate [37].

The use of the incoherent approximation may be problematic as outlined in the introduction. In case of UCN production, (final energy 0-200 neV) we are just interested in a thin line on the  $S(q, \omega)$  surface and the necessary integration over the full  $q$  range is suspicious. In our opinion it should be possible to use  $S(q, \omega)$ , eqs. 2.8 and 2.5 for the calculation of  $P$ .

### Losses of UCN in $D_2$ converters

As already shown in eq. 2.7, besides production also losses have to be considered. In case of a deuterium based UCN source two absorption and two up-scattering loss mechanisms have to be taken into account (cf. figs. 2.2 and 2.3).

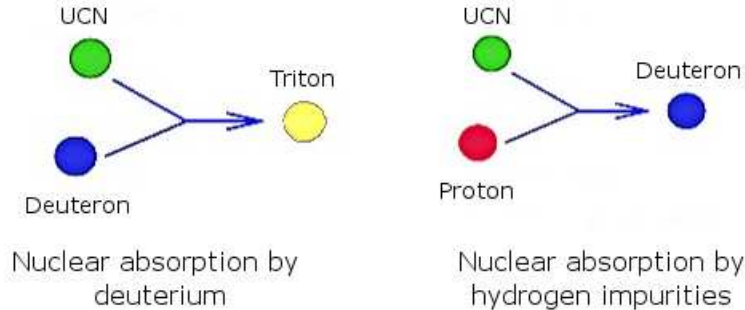


Figure 2.2: Scheme of the two absorption UCN loss mechanisms.

**Nuclear absorption by D<sub>2</sub>** If deuterium is used as converter material nuclear absorption on deuterium atoms ( $d + n \rightarrow t + \gamma$ ) is an intrinsic loss mechanism. It cannot be avoided; hence the minimum attainable loss cross section is  $\sigma_{\text{abs}} = 5.19 \cdot 10^{-4}$  barn.

**Nuclear absorption by impurities.** In highly purified deuterium the most abundant impurities are hydrogen atoms. Due to its large absorption cross section of  $\sigma_{\text{H}} = 0.3326$  barn it is necessary to start with the lowest possible hydrogen content. Any additional contamination from the storage container, the gas handling system or the source wall materials should be avoided by all means.

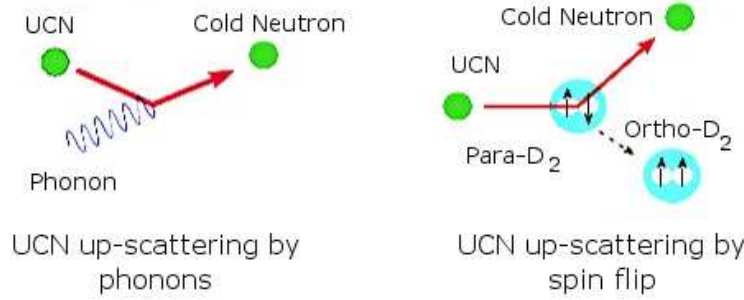


Figure 2.3: Scheme of the two up scattering UCN loss mechanisms.

**UCN up-scattering by phonons.** Up-scattering of UCN via excitations in D<sub>2</sub> leads to acceleration of the neutrons above the UCN range. The occupation of the excited states at a certain temperature is described by the Boltzman factor. The principle of detailed balance, eq. 2.11, describes the correlation between the down- and up-scattering cross sections ( $\sigma_{\text{down}}$  and  $\sigma_{\text{up}}$  respectively) as function of temperature.

$$\underbrace{\sigma(E_{\text{UCN}} \rightarrow \underbrace{E_{\text{UCN}} + \Delta}_{E_{\text{CN}}})}_{\sigma_{\text{up}}} = \frac{E_{\text{UCN}} + \Delta}{E_{\text{UCN}}} e^{-\Delta/k_{\text{B}}T_{\text{conv}}} \underbrace{\sigma(\underbrace{E_{\text{UCN}} + \Delta}_{E_{\text{CN}}} \rightarrow E_{\text{UCN}})}_{\sigma_{\text{down}}} \quad (2.11)$$

Reducing the converter temperature  $T_{\text{conv}}$  and thus the number of phonons inside the crystal suppresses this losses and shifts the balance towards of UCN production.

**UCN up-scattering by D<sub>2</sub> spin flip.** Similar to the H<sub>2</sub> molecule the D<sub>2</sub> also exists in two different configurations. The anti-symmetric configuration is called ortho D<sub>2</sub>, J=even, the symmetric state para D<sub>2</sub>, J=odd. Transitions between ortho and para ground state require an energy of  $E_{\text{spin flip}} = 7.5$  meV and a spin flip. At a scattering process of a neutron with a para D<sub>2</sub> molecule, the spin can be flipped,  $J = 1 \rightarrow J = 0$ , and the neutron gains the spin flip energy and leaves the UCN energy region. Because the para-to-ortho transition requires momentum and spin changes the transition is forbidden and the para state is still occupied to 33% even at lowest temperatures (3 to 1 occupation due to spin spin correlation) for a long time. Increasing the ortho concentration of the D<sub>2</sub> before the use as UCN converter is therefore mandatory.

The heat conductivity of deuterium with 95% ortho is one order of magnitude higher than that of D<sub>2</sub> at normal ortho concentration of 66%. This is important for the extraction of phonons from the converter and thus the previously discussed up scattering loss.

It is useful to express the different losses  $i$  inside the deuterium bulk by neutron lifetimes  $\tau_i$ . The total lifetime  $\tau_{\text{loss}}$  used in eq. 2.7 can be written as the sum of the lifetimes due to the individual loss mechanism  $\tau_{\text{abs D}}$ ,  $\tau_{\text{abs H}}$ ,  $\tau_{\text{up phonon}}$  and  $\tau_{\text{up paraD}_2}$  loss mechanisms<sup>6</sup>. Together with the particle number  $N_i$  and the averaged ultracold neutron velocity  $v_{\text{UCN}}$  the equation can be written as function of the loss cross sections  $\sigma_i$ .

$$\begin{aligned} \frac{1}{\tau_{\text{loss}}} &= \frac{1}{\tau_{\text{abs D}}} + \frac{1}{\tau_{\text{abs H}}} + \frac{1}{\tau_{\text{up phonon}}} + \frac{1}{\tau_{\text{up paraD}_2}} \\ &= \left( \frac{1}{N_{\text{D}}\sigma_{\text{abs D}}} + \frac{1}{N_{\text{H}}\sigma_{\text{abs H}}} + \frac{1}{N_{\text{phonon}}\sigma_{\text{up phonon}}} + \frac{1}{N_{\text{paraD}_2}\sigma_{\text{up paraD}_2}} \right) \cdot \frac{1}{v_{\text{UCN}}} \end{aligned} \quad (2.12)$$

## 2.2 Deuterium characterization

The *cubeD<sub>2</sub>* experiment was designed to characterize D<sub>2</sub> in the gaseous, liquid and solid phase. One challenging task was to try different freezing procedures, characterize the results and determine their possible influence on the UCN production efficiency. The following section introduces the setup that was developed and the techniques that were applied: optical inspection, cold and thermal neutron scattering and UCN production in a cold neutron beam. The results of the various experiments are afterwards reported in the same order.

### 2.2.1 Setup of the *cubeD<sub>2</sub>* experiment

The central part of the *cubeD<sub>2</sub>* experiment was made up of four parts: target cell, cooling system, gas handling system and ortho to para converter.

#### Target cell

The starting point of our investigations was to study the crystal quality for different liquid to solid and gas to solid phase transitions. For this reason a cube of 46 · 46 · 46 mm<sup>3</sup> from AlMg<sub>3</sub> with a machined inner volume of 30 · 30 · 30 mm<sup>3</sup> was used as cell body. On two opposite sides sapphire windows (diameter 14) mm [39] were screwed on the cell using indium sealings. Perpendicular to them, on one side the wall thickness was reduced down to 0.2 mm to form the cold-neutron entrance window and at the opposite side a 0.1 mm thick Aluminum foil was glued with Stycast onto the cell body as UCN extraction window (ø32 mm). The foil was fixed by a stainless steel frame, the first part of the later UCN guide system. The gas supply flange (tube ø 6 mm) was welded to the top of the cell. The different parts can be seen on the right hand side of fig. 2.4.

<sup>6</sup>The  $\beta$ -decay lifetime  $\tau_n$  is neglected here, because it is five orders of magnitude larger.

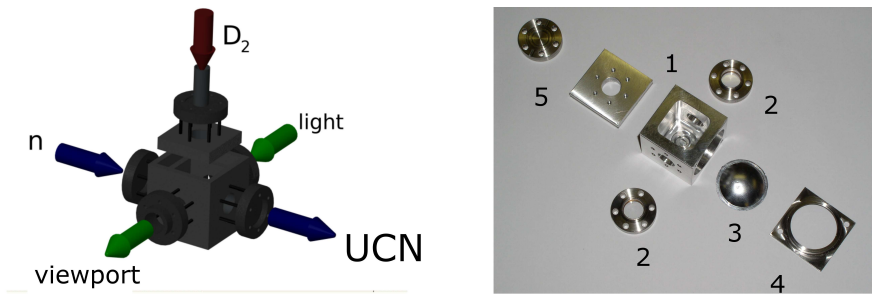


Figure 2.4: Left: Sketch of the *cubeD<sub>2</sub>* experiment to fill a cell with deuterium and use two windows for optical inspection, one for irradiation with cold neutrons and one for extraction the UCN. Right: different single components of the target cell: 1 cell body, 2 sapphire windows, 3 UCN window, 4 steel frame, 5 gas inlet.

To measure the UCN production as a function of the deuterium thickness in the cold neutron beam, cells with 30, 20, 10 and 5 mm extension in beam direction, respectively were built (fig. 2.5). As can be seen (in the back) the critical UCN extraction part is identical for all cells. The 5 mm cell one is not shown on the picture because it was not finished at that time. For technical reasons it was not possible to screw glass windows on the 20, 10 and 5 mm cells.



Figure 2.5: Three of the four deuterium target cells with 30, 20, 10 mm thickness, respectively for the neutron beam. The 5 mm target cell is not shown. The cold neutron entrance window can be seen in the front, the hole for the UCN extraction foil in the back.

All cells were leak tested for several hours with 4 bar He pressure and vacuum at room temperature and 10 K. For temperature monitoring one diode sensor on top and one at the bottom of the cell were mounted.

## Cryogenic system

A two-stage Gifford-McMahon cooling machine cooling power at 4.2 K is 0.25 W [40])<sup>7</sup> was used to achieve cell temperatures around 8 K when the first stage was used as a thermal shield (1 mm thick aluminum cup at approximately 35 K). The stainless steel gas inlet tube was also shielded to a height of approximately 10 cm as shown in fig. 2.6. With a heater at the second stage and a Lakeshore temperature controller [41] it was possible to adjust the cell temperature  $T_{\text{cell}}$  from 8 K to 300 K with a precision of  $\Delta T = 0.5$  K without disturbing the running cooling machine. The whole setup was mounted inside a CF 100 cross with two glass flanges in line with the cell glass windows. To avoid water to freeze on the glass windows an isolation vacuum better than  $10^{-5}$  mbar was mandatory.

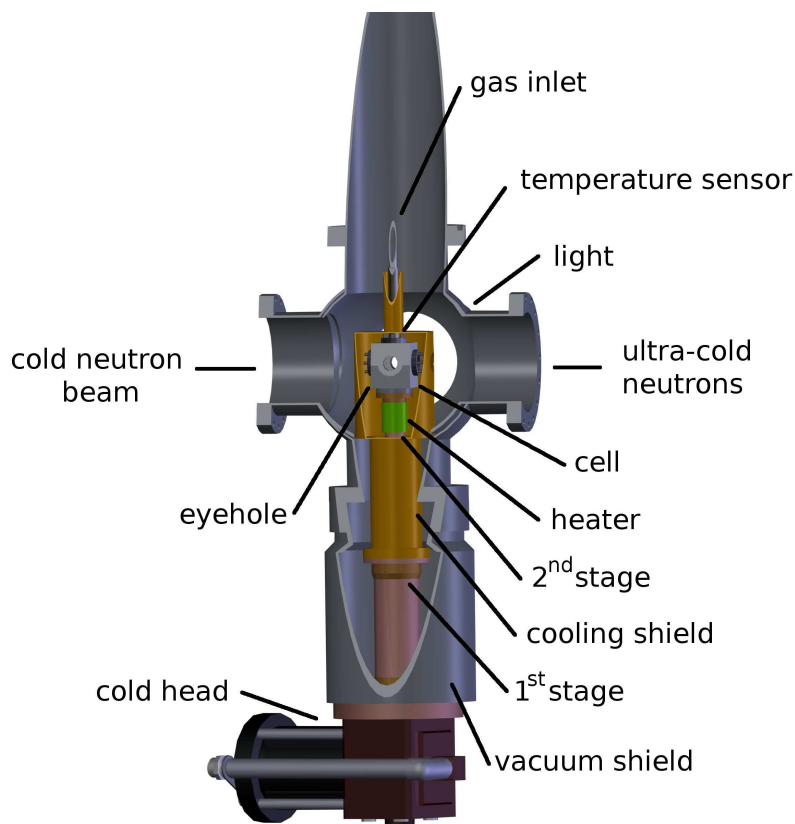


Figure 2.6: *cubeD<sub>2</sub>* scheme with the target cell on top of a two-stage Gifford McMahon cold head. The first stage is used to cool the radiation shield down to 35 K. The gas supply from the top and the CF 100 cross for thermal isolation are also shown. Cell temperature between 8 K - 300 K could be achieved by the use of a the heater. The beam direction is from left to right.

<sup>7</sup>Two-stage Joule-Thomson expansion cooler using He between 25 bar on the high pressure side and 20 bar on the low pressure side for cooling two plates via gas expansion. The first stage at approximately 35 K is usually used as thermal shield for the second stage.

## Gas manifold

The flow scheme of the deuterium gas system is shown in fig. 2.7. One vacuum pump is used to pump gas storage, safety dump and supply tube to the deuterium bottle, the other one for cleaning the gas system itself. Due to the long tubes and their small diameter (6 mm), a vacuum pressure of  $p \approx 1 \cdot 10^{-2}$  mbar was achieved in the gas system. Handling deuterium it was for safety reasons required to just use metal and metal sealed components (Swagelok parts [42]). The dump with a volume of 15 l and permanent pressure control was usually filled with 5 bar deuterium gas<sup>8</sup>. Valves and needle valves were used to fill deuterium into the target cell, the ortho/para converter and afterwards the target cell or the Raman sample cell<sup>9</sup> as shown in the flow diagram fig. 2.7. Depending on the valve settings, the pressure inside the ortho/para converter, target or Raman cell can be changed between 6 bar and  $10^{-9}$  mbar by a combination of pressure and vacuum gauges. To avoid dangerous overpressure inside the system caused by heating (expansion) of low temperature gas and or phase transitions, three overpressure valves and one burst disc were installed. They automatically open the connection to the dump in case of a pressure difference above the adjusted value (fig. 2.7). Pressures above 6.5 bar in the system are avoided by this.

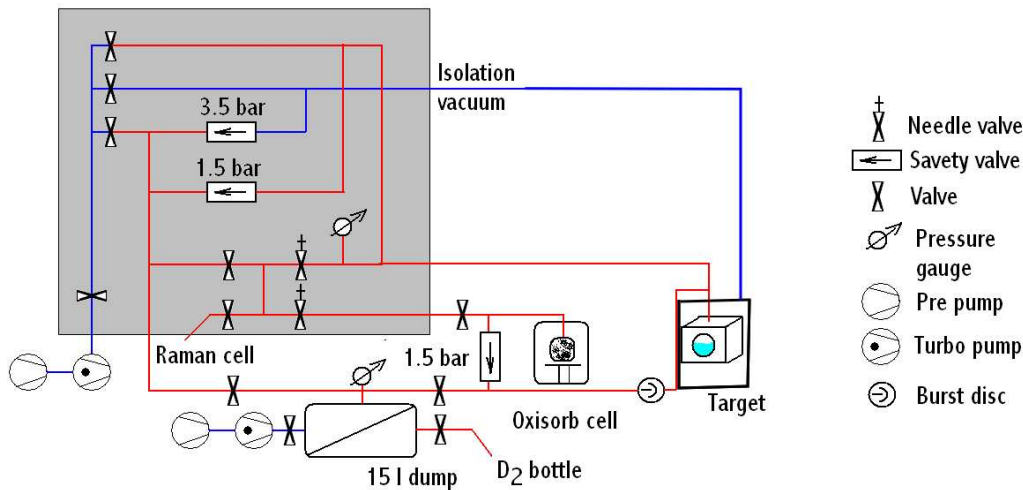


Figure 2.7: Flow diagram of the deuterium gas system for the cube $D_2$  experiments. The red tubes contain deuterium during nominal operation, the blue ones are vacuum connections. Depending on the valve setting, the deuterium may be transferred between the dump, the Oxisorb converter and the target cell.

<sup>8</sup>The dump was positively tested beforehand with He overpressure and a leak tester and finally with 14 bar (air) for several hours.

<sup>9</sup>The Raman sample cell consists of an aluminum container of  $30 \cdot 30 \cdot 30$  mm<sup>3</sup>, four Suprasil glass windows and two tubes connected with metal valves. One is used for pumping, the other to connect to the gas handling system. Usually it is used to measure the ratio of ortho to para  $D_2$  with Raman spectroscopy.

## Ortho/para converter

The aim of the setup was to have a small flexible converter unit to produce high ortho deuterium concentrations within reasonable times. The normal conversion from the 66% concentration at room temperature concentration to the thermal equilibrium at cryogenic temperatures via the forbidden transition takes of the order of 6 months. It is, however, possible to reduce this time by the use of suitable catalysts (PSI [44] and Los Alamos [45]). We used Oxisorb [43] which is just one possible example. A scheme of the converter unit is shown in fig. 2.8, left.

A copper cell of 40 mm diameter and 55 mm height was filled to one third with Oxisorb grains (under argon atmosphere). It is closed at the top by a 2-mm thick deuterium permeable ceramic  $\text{SiO}_2/\text{BeO}$  disc which acts as impurity filter for both sides. This is used to avoid contamination of the gas system with Oxisorb and at the working temperatures of 15-28 K the gas is cleaned from impurities with higher freezing points. The gas connection, the cooling machine and the temperature control is similar to the one described for the target cells before. After characterization measurements the stand alone system was successfully used during the *cubeD<sub>2</sub>* beam times (section 2.5), the miniD<sub>2</sub> test source in Mainz, and for the inelastic n-scattering experiments (section 2.4.3). Further characterizations of the converter material can be found in the appendix.

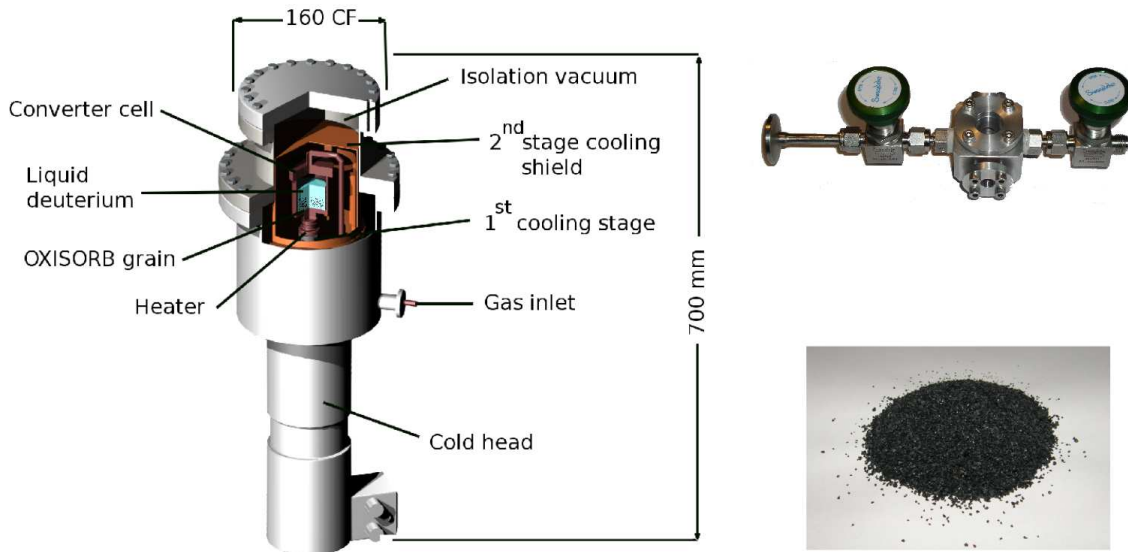


Figure 2.8: Left: scheme of the ortho to para converter using the surface contact of liquid deuterium with Oxisorb grains. Right: the Raman sampling cell used to measure the ortho deuterium concentrations in the Raman setup of the Walter Meißner Institut and the used Oxisorb grain.

### 2.2.2 Visible light inspection

Digital cameras and white or blue light illumination from the opposite side were used to examine the liquefaction, solidification and re-sublimation procedures optically. Inside

the radiation shielding bunker a circuit board camera and a Philips webcam were used during the exposition of the high intense cold neutron beam.

### 2.2.3 Raman spectroscopy

The Raman facility at the Walter-Meißner Institut, Garching was used to specify the ortho to para converter by measuring the o-D<sub>2</sub> concentration,  $c_o$ . For this purpose we made Raman scans of gas samples, as function of the conversion time. In Raman scattering the excited states are populated or depopulated by the laser light itself, as shown in fig. 2.9 left.

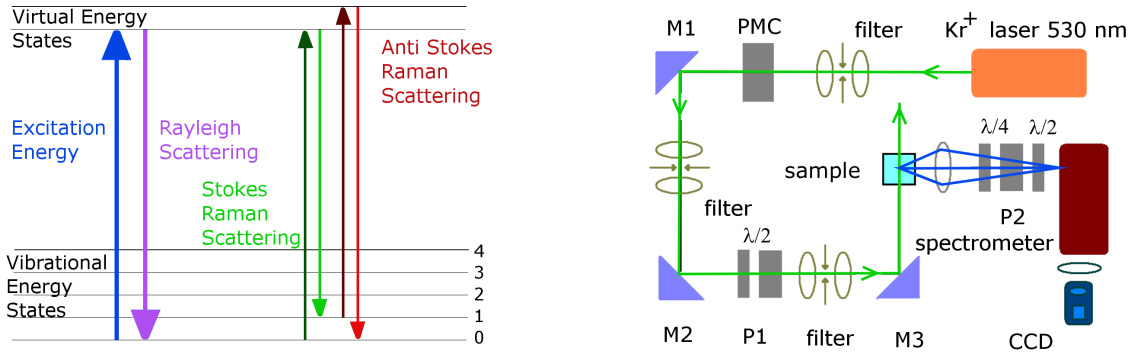


Figure 2.9: Left: excitation-emission scheme for photon scattering. Right: Raman setup at the Walter Meißner Institut.

We used a krypton laser ( $\lambda=530.8$  nm,  $k=1/\lambda=18837$  cm<sup>-1</sup>, power  $P=40$  mW) with the light passing through the windows of the Raman sample cell. The emitted Raman intensity is measured with a CCD camera at an angle of 90 ° to the main laser (fig. 2.9 right). The frequency of the spin transitions for the  $J=0$  ortho D<sub>2</sub> (even transitions) with  $S(0 \rightarrow 2)$  and the  $J=1$  para (odd transitions) D<sub>2</sub>  $S(1 \rightarrow 3)$  are well known, therefore the ratio  $R$  of the intensities can be used to calculate the ortho concentration  $c_o$  [46]

$$R = \frac{S(0 \rightarrow 2)}{S(1 \rightarrow 3)} = \frac{5}{3} \frac{c_o}{1 - c_o} \left( \frac{\omega - \omega_{02}}{\omega - \omega_{13}} \right)^3 \underbrace{\left( \frac{1 + \frac{7}{3}e^{-10B/k_B T} + \dots}{1 + 5e^{-6B/k_B T} + \dots} \right)}_{\tau_{\text{gas}}}. \quad (2.13)$$

The energy of the incident photon is  $\hbar\omega$  and the energy shift caused by the transition is  $\hbar\omega_{02}$ ,  $\hbar\omega_{13}$ .  $B = 29.91$  cm<sup>-1</sup> denotesthe rotational constant for D<sub>2</sub>. At room temperature we obtain  $\tau_{\text{gas}} = 0.447$  for D<sub>2</sub> and  $\tau_{\text{gas}} = 0.597$ ,<sup>10</sup> for H<sub>2</sub>. The concentration of the even  $J$ -species (o-D<sub>2</sub>) is then given by

$$c_o = \frac{R}{R + \frac{5}{3} \{ (\omega - \omega_{02}) / (\omega - \omega_{13}) \}}. \quad (2.14)$$

In table 2.1 the frequency shifts for the lowest rotational states are listed [46] for H<sub>2</sub>, HD and D<sub>2</sub>. Since the efficiency of the Raman spectrometer is, to a very good approximation, constant over the frequency range of interest, we can set  $S$  equal to

<sup>10</sup> $\tau$  is a correction factor taking into account that not all molecules are in the ground state.

	H <sub>2</sub>		HD		D <sub>2</sub>	
J	Expt.	Theory	Expt.	Theory	Expt.	Theory
0	354.38	354.39	267.09	267.12	179.06	179.12
1	587.06	587.07	443.08	443.17	297.52	297.63
2	814.41	814.48	616.09	616.21	414.66	414.78
3	1034.65	1034.75	784.99	785.15	529.91	530.07

Table 2.1: Raman shifts in cm<sup>-1</sup> for the first rotational states  $J$  in H<sub>2</sub>, HD and D<sub>2</sub> [46]. ( $S_0(J) = E_{0,J+2} - E_{0,J}$ )

the line intensity, which may be determined by Gaussian fits of the transition lines. A sample plot is shown in fig. 2.23 right with high and low para concentration.

Besides the concentration  $c_o$  (similar method was used by [44, 45], the intensity of the HD transition can be used to estimate an upper limit of the hydrogen contamination (fig. 2.23), left.

## 2.2.4 Neutron scattering

In order to study the results of different freezing procedures on a microscopic level point of view we used inelastic neutron scattering, at the TOFTOF (FRMII) and IN4 (ILL).

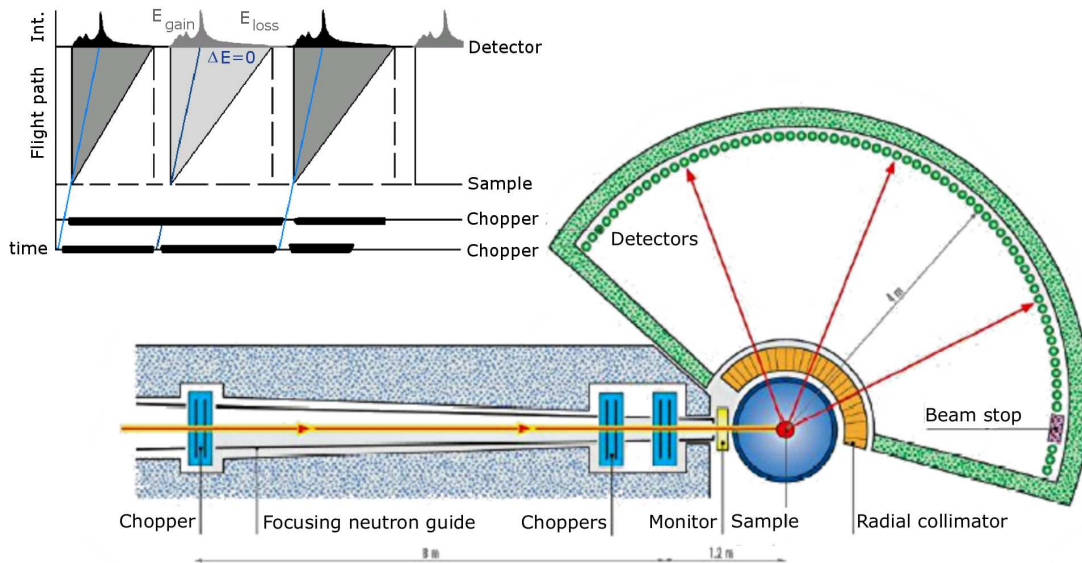


Figure 2.10: Scheme of a neutron time-of-flight instrument to measure the scattering function  $S(q, \omega)$ . The inset on the upper left shows the working principle like explained in the text [49].

The layout of a time of flight instrument is shown in fig. 2.10. Initial position and velocity of the incoming neutrons  $\vec{k}_i$  are fixed by the collimator and the chopper system, and their final  $\vec{k}_f$  is measured via the hit position on the detector bank determining the

scattering angle  $\vartheta$  and the velocity  $v_f$ . The latter is determined from the flight time  $t_{\text{tof}}$  (tof = time of flight) from the sample to the detectors arranged at equal distance  $L$  from the sample. The flight time is compared to the dominant or calculated elastic line (no energy change  $\Delta E = 0$  or  $|\vec{k}_i| = |\vec{k}_k|$ ).

The inset in fig. 2.10 left shows a typical tof pattern. Neutrons relaxing an excitation inside the sample gain this energy, increase their velocity and reach the detector earlier than the elastic scattered neutrons (left side of the blue line in the inset fig. 2.10). Neutrons exciting the sample lose energy and are detected at a later time. Final energy  $E_f$  and final scattering vector  $\vec{k}_f$  of the non relativistic neutrons (mass  $m_n$ ) are calculated via eq. 2.15.

$$E_f = E_i \pm \Delta E = \frac{1}{2}m_n v_f^2 = \frac{1}{2}m_n \left(\frac{L}{t_{\text{tof}}}\right)^2 \quad (2.15)$$

$$|\vec{k}_{(i,f)}| = \frac{2\pi}{\lambda_{(i,f)}} = \sqrt{2m_n E_{(i,f)}/\hbar} \quad (2.16)$$

The scattering process is completely described by with the energy transfer  $\omega$  and the momentum transfer  $q$ . A derivation of  $S(q, \omega)$  from the measured intensity as function of angle and flight time is given in section 10.2). The definition for  $q$  and  $\omega$  were taken from eq. 2.9 and eq. 2.10.

$S(q, \omega)$  can be used to study the structure as well as the dynamics of the investigated sample. We repeated the freezing procedures in a double walled aluminum cylinder. The  $D_2$  thickness was 2 mm to reduce the neutron scattering probability to 10% and suppress multi-scattering events. The gas handling system as well as the ortho/para converter for spin dependent measurements was taken from the *cubeD<sub>2</sub>* setup. The measured doubly differential cross section  $d^2\sigma/d\Omega d\omega$  can now be written with Fermis golden rule, as a function of the scattering vectors  $\vec{k}_{(i,f)}$ , the scattering length<sup>11</sup> and  $S(q, \omega)$  like eq. 2.17 (further details can be found in sec. 10.2).

$$\frac{d^2\sigma}{d\Omega d\omega} = \frac{|\vec{k}_f|}{|\vec{k}_i|} \langle \bar{b}^2 \rangle S(\vec{q}, \omega) \quad (2.17)$$

$S(q, \omega)$  is called the scattering function, response function or dynamic structure factor. The square of the scattering length  $\langle \bar{b}^2 \rangle$  is averaged over all atoms  $i$ , spin configurations and isotope distributions of each element in the sample indicated by the bar:  $\langle \bar{b}^2 \rangle = 1/N \sum_i^N \bar{b}_i^2$ . The sign of the coordinate pairs  $(\vec{q}, \omega)$  used to describe the scattering process may be transformed depending if the momentum and energy changes of the sample or the neutron are meant. The structure factor contains the following necessary information:

### Diffraction patterns $S(q)$ :

One way to analyze the scattering function  $S(q, \omega)$  is to either keep  $\omega = 0$  or to integrate over all possible  $\omega$  values (summing the time slices). The first case leads to the elastic structure factor  $S_{\text{el}}(q)$  which depends on the relative positions at equilibrium states

---

<sup>11</sup>Neutrons in our energy range are scattered at the nucleus  $j$  by the weak nuclear forces without scanning the internal structure. Therefore the scattering process is isotropic and the scattering probability of the nucleus can be described by a scalar number, the scattering length  $b_j$ .

of the sample atoms. In the second case  $S(q)$  depends on the instantaneous relative position of the particles. Both cases are used to describe the structure of the sample. Using the wave behavior of the neutron, the process is identical to standard diffraction patterns with the scattering intensity  $I(\vartheta)$ .

The scattering on atom layers with distance  $d$  leads to constructive interference  $n$  and a peak in the diffraction plot, the Bragg peak:

$$n\lambda_n = 2d_{h,k,l} \sin \vartheta \quad (2.18)$$

For the elastic case ( $\vec{k}_i = \vec{k}_f$ ) the  $\vec{q}$  value of each Bragg peak may be identified with the lattice spacing by the following equation.

$$q = \frac{2\pi}{d} = \frac{4\pi \sin \vartheta}{n\lambda} \quad (2.19)$$

A diffraction pattern contains the following information. The three-dimensional extension of the unit cell (Miller indices  $h,k,l$ ) fixes the position of the peaks in  $I(\vartheta)$ . The intensity of each peak depends on the relative position of the atoms inside the primitive cell (unit cell form factor) and the temperature of the sample. The Bragg-peak intensity decreases with increasing temperature and scattering order  $h, k, l$ . Both is described by the Debye Waller factor. The extraction of UCN from the converter may be affected by different structures.

### Phonon density of states $Z(\omega)$ :

Following the theory of inelastic neutron scattering it is possible to extract the generalized phonon density of states  $GDOS$  from the measured  $S(q, \omega)$  by eq. 2.20 from [48].

$$GDOS^n(\omega) = A \left\langle \frac{e^{2W(q)}}{q^2} \frac{\omega}{n(\omega, T) + 1} S(q, \omega) \right\rangle \quad (2.20)$$

$$GDOS^n(\omega) = B \sum_k \left\{ \frac{4\pi b_k^2}{m_k} \right\} Z_k(\omega) \quad (2.21)$$

In this equation  $2W(q)$  is the Debye Waller factor and  $n(\omega, T)$  the occupation number as function of temperature and energy. The quantity within the brackets  $\langle$  and  $\rangle$  represents the average over all  $q$  values at a given energy.  $b_k$ ,  $m_k$ , and  $Z_k$  are neutron scattering length, mass and partial density of states of the  $k$ th atom in the unit cell.  $A$  and  $B$  are normalization constants. In case of a single component system  $n = 1$  the density of state  $Z(\omega)$  is equal to the generalized phonon density of state  $GDOS(\omega)$  or the partial density of state  $GDOS(\omega)^{n=1}$ .

In this equation the incoherent approximation is used to derive  $GDOS^n(\omega)$  which implies averaging the spectra over the whole scattering angle  $\vartheta$ .

For our discussion we assume that the density of states consists just of single particle excitations leading to the (measured) generalized phonon density of states. In our opinion  $GDOS(\omega)$  is the quantity to be used for UCN because finally it is not necessary for us to separate contributions from roton or phonon excitations or differentiate between ortho or para molecules.

### Direct use of $S(q, \omega)$ :

Due to our doubt on the validity of the incoherent approximation for the deuterium case one may also use  $S(q, \omega)$  in eq. 2.8 to calculate the UCN production cross section without any approximation. The big advantage is that it is measured with neutrons and used for neutrons. Another benefit is that  $S(q, \omega)$  includes all possible scattering processes. Therefore the losses probabilities due to up-scattering, spin flip or other loss cross sections are already included in the data.

We arranged two beam times of five days at the TOFTOF [47] spectrometer with a cold neutron beam from the FRMII [22] and one beam time of six days with the thermal neutrons of the IN4 [49] from the ILL research reactor. We measured  $S(q, \omega)$  for various freezing results (section 2.4.1), temperature treatments and ortho concentrations. The characterization with inelastic neutron scattering [50] was also part of a diploma thesis. Further explanations may also be found in [51].

## 2.3 *cubeD*<sub>2</sub>, a test UCN source at the FRMII

We used our *cubeD*<sub>2</sub> setup at an intensive cold neutron beam to check whether different freezing procedures have an influence on the achievable UCN density<sup>12</sup>.

### 2.3.1 Setup at the FRMII

The *cubeD*<sub>2</sub> setup, used at the MEPHISTO cold neutron beam (FRMII) is shown in fig. 2.11. It was necessary to collimate the beam size of  $4 \times 7$  cm<sup>2</sup> to our cell size diameter of  $\varnothing$  30 mm by lead baffles and polyethylene shielding. The UCN guides on the opposite side were made from electropolished stainless steel (Nokado). An adapter connected the different diameter of the support frame of the target cell (fig. 2.4) to the UCN guides of 66 mm diameter. 10 cm behind the cell a remote controlled foil shutter was installed to estimate the fraction UCN and VCN (very cold neutron as background further explanation are given in section 2.3.2). After a U like guide structure the neutrons were counted with a <sup>3</sup>He detector and the transmitted cold neutron beam is monitored by a uranium fission chamber of 1 mm<sup>2</sup> diameter inside the beam dump. The cameras, the gas handling system as well as the ortho/para converter are also shown. The 2.00 m horizontal part of the UCN guide could be equipped by curves made out of stainless steel bows (flow through mode) or UCN valves (storage mode). Due to the large scattering probability of deuterium it was necessary to surround the experiment with lead and concrete shielding as indicated in fig. 2.11 lower part. The detector was also shielded by lead and polyethylene.<sup>13</sup>

---

<sup>12</sup>A similar test source was successfully operated at the FUNSPIN cold neutron beam at the PSI[52]

<sup>13</sup>One has to mention that the cooling machine, available during the beam times had just 0.125 W cooling power at 4.2 K.

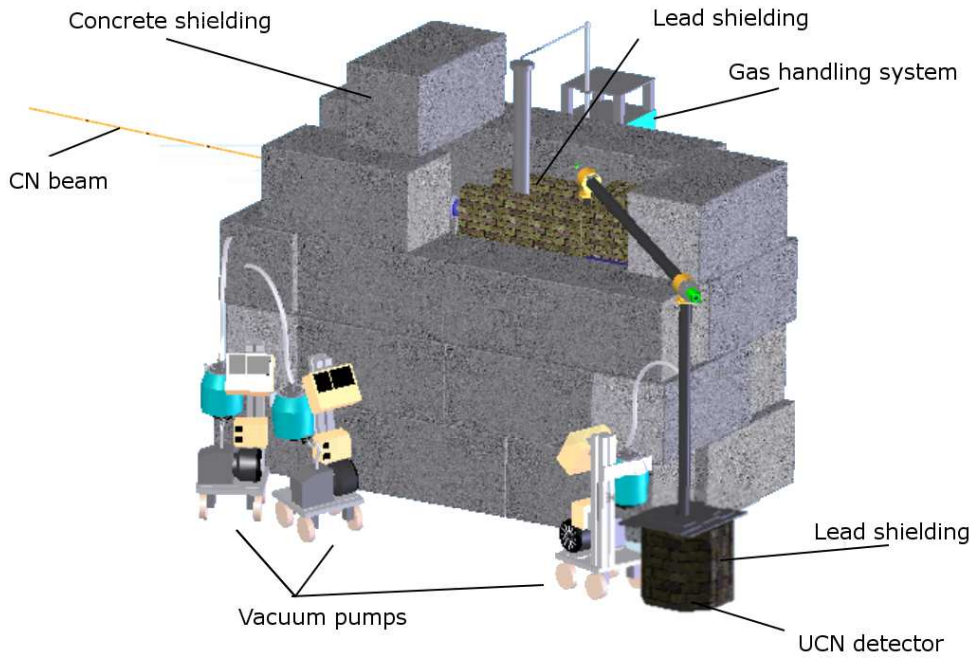
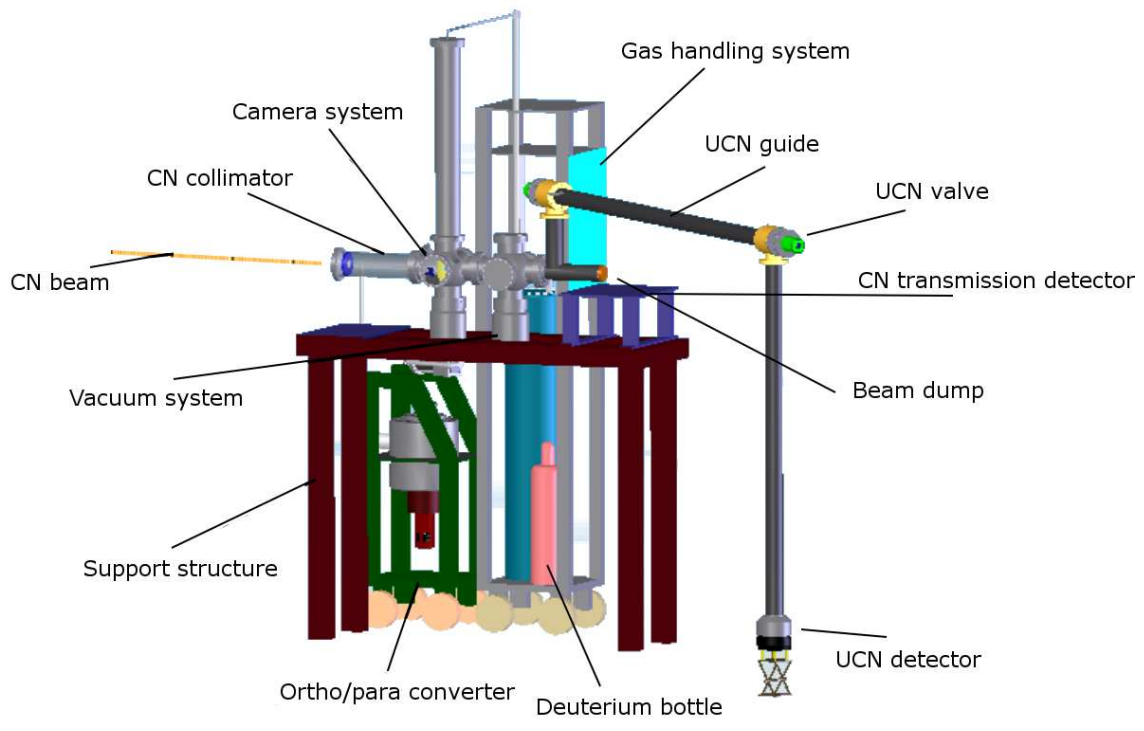


Figure 2.11: Top: layout of central parts. Bottom: *cubeD<sub>2</sub>* shielding as necessary for the use at the MEPHISTO cold neutron beam of the Forschungsneutronenquelle FRMII.

### 2.3.2 UCNs, VCNs and CNs

The three different methods realized to extract the UCN count rate from the very cold (VCN) and cold neutron (CN) background are shown in the following picture:

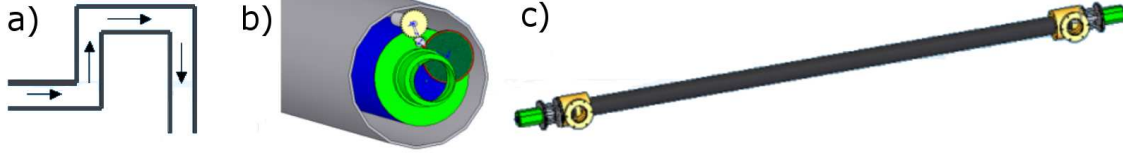


Figure 2.12: Three methods to separate the VCN background from the UCN counts rate realized for the *cubeD<sub>2</sub>* experiment (a) baffle structure of the UCN guide system (b) stainless steel covered foil shutter and (c) storage method (container consisting of valves and UCN guide).

#### a) Separation due to UCN guide structure

The transmission through a "U-baffle" structure between the production area and the detector is close to zero for neutrons with energies larger than the wall Fermi potential.

#### b) Separation due to a foil shutter

The second method uses an aluminum shutter covered with stainless steel ( $V_{\text{Fermi}} \approx 180$  neV). The count rate with open shutter originates from UCN plus possible VCN contributions whereas penetration of UCNs is prevented when the shutter is closed. From the difference, the UCN production rate can be extracted.

#### c) Separation due to storage

The definition of a UCN is, that its kinetic energy is low enough to be reflected by certain materials under all angles of incidence and it may hence be stored. Storing neutrons coming from the converter cell is thus the best way to identify them as UCN. Therefore we designed two UCN valves to close a storage volume of 2m stainless steel tube as shown in fig. 2.12right. For further explanation on the valves and the storage experiment see also chapter 3.

All three methods were used to compare the number of UCN to VCN and CN for different deuterium treatments and source temperatures.

## 2.4 Experimental Results

### 2.4.1 Visible light

First experience with different freezing conditions were made with non explosive neon ( $T_{\text{triple}}(\text{Ne}) = 25$  K), before we investigated deuterium ( $T_{\text{triple}}(\text{D}_2) = 18.7$  K). In the *cubeD<sub>2</sub>* setup, temperature and pressure could be controlled individually and thus different process paths a)-d) in the phase diagram (fig. 2.13) could be realized. The corresponding results are presented after a short summary of the neon freezing tests.

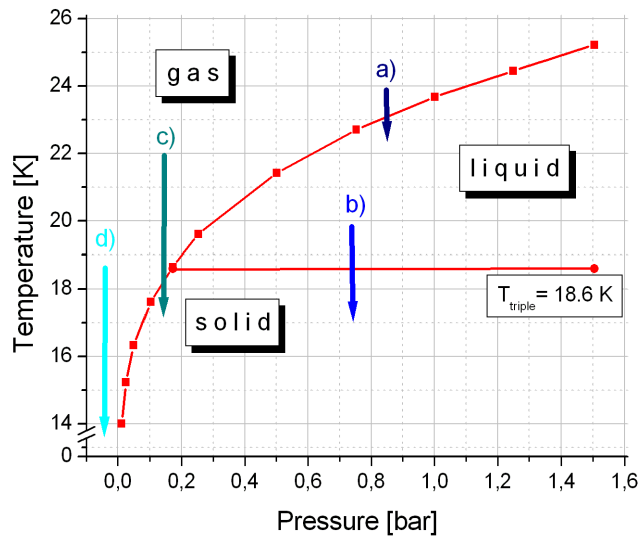


Figure 2.13: Deuterium phase diagram including different process paths of phase transitions studied with *cubeD<sub>2</sub>*: a) liquefaction from the gas phase, b) solidification from the liquid phase, c) re-sublimation at high temperature, d) re-sublimation at low temperature.

### Neon freezing

Besides learning how to fill the cell with liquid or solid neon from the dump, two special experiments were realized using neon: in the first case tiny air contaminations, mainly nitrogen and oxygen were mixed into the gas stream. The impurities acted as condensation seeds where neon started to crystallize above the cold surface. The resulting snow structure is shown in fig. 2.14 on the left side (compared to the freezing model discussed later the dominant step here is step (1)).

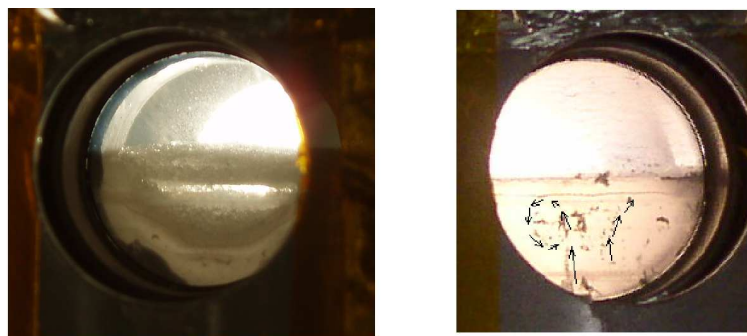


Figure 2.14: Left: solid neon at 20 K frozen in a snow like structure with a gas stream and air impurities. Right: convection zones in liquid neon visible through solid black impurities. The motion along the convection zone is shown by the arrows.

In a second case the air impurities were added to the gas after the cell was half filled with solid neon. Heating up leads to neon liquefaction whereas the impurities stay

solid, swimming in the liquid. They cluster and create visible dark spots. As shown in fig. 2.14, right, these impurities are then used to visualize motion inside the liquid (indicated by the arrows). With these studies one may determine the best settings of temperature and pressure to get maximum convection (motion of the liquid and exchange at the catalyst surface) inside the ortho/para converter (boiling mode).

### Model for crystallization

Following the model of Stranski and Nacke [53] crystal growth can be described in four steps as shown in fig. 2.15: (1) adsorption of the molecules on the surface, (2) diffusion to a crystal edge, (3) diffusion along the crystal line to a crystal corner and (4) fixation into the crystal structure with release of the binding energy.

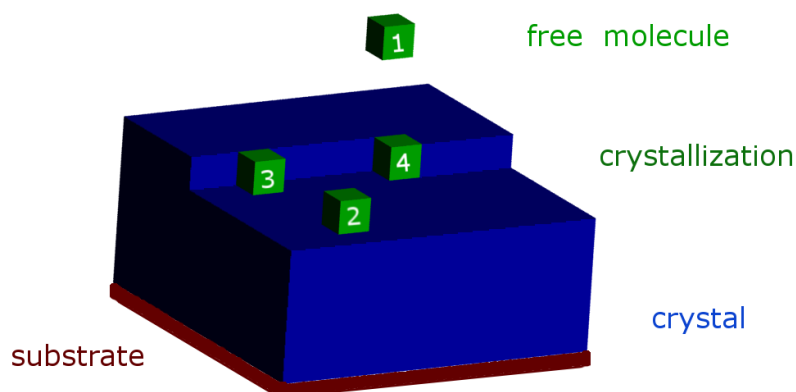


Figure 2.15: Stranski and Nacke model [53] of four step crystallization. Further explanation are given in the text.

The pressure and temperature difference between the molecule reservoir (liquid or gas) and the cold substrate influence the crystallization time and thus determines which of the steps 1-4 dominates: Crystal layer growth, called Frank-van der Merve mode, island growth called Volmer-Weber mode or mixed layer island growth, the Stranski-Krastanov mode [53] are possible.

### Liquefaction of deuterium

The easiest way, with the largest parameter space, is to fill the cell with liquid deuterium indicated as path (a) in the phase diagram fig. 2.13. The fastest filling of our cell took 1.5 hours and is shown in the picture series in fig. 2.16. The steadily rising flat surface marked with a black bar, is an indication for the steady filling with liquid.

### Solidification of deuterium

Keeping the cell temperature  $T_{\text{cell}}$  at around 17 K, which is below the triple point  $T_{\text{triple}} = 18.6$  K, leads to a smooth solidification from the liquid. The deuterium molecules in the liquid have enough time to find the potential minimum at the crystal growing surface. A smooth, curved surface rising with time from the bottom to the top separating both phases is shown as function of time in the picture series of fig. 2.17

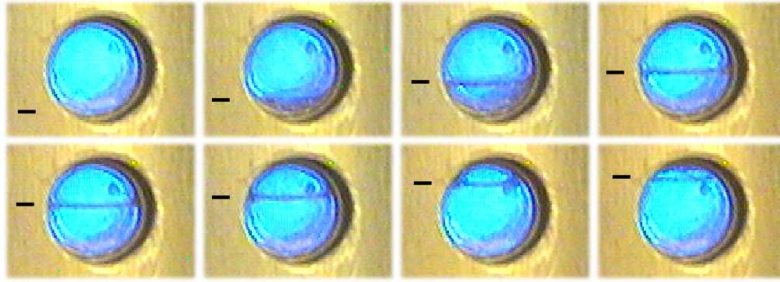


Figure 2.16: Liquefaction: path a) in the phase diagram of fig. 2.13 from the gas phase into the liquid phase. The steadily rising liquid level is marked by the black bar.

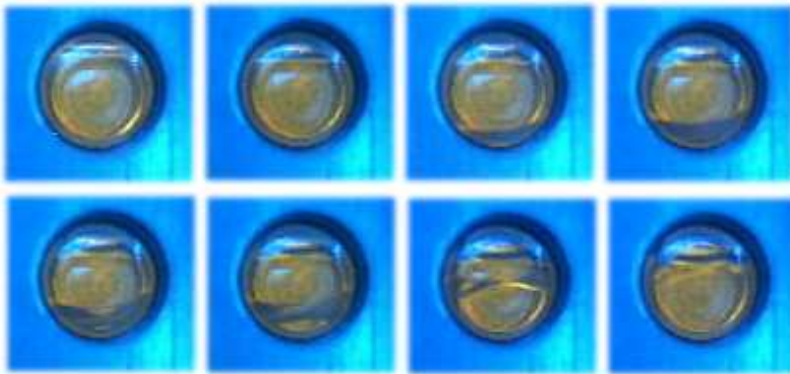


Figure 2.17: Solidification: path (b) in the phase diagram fig. 2.13 from the liquid phase into the solid phase with slight undercooling.

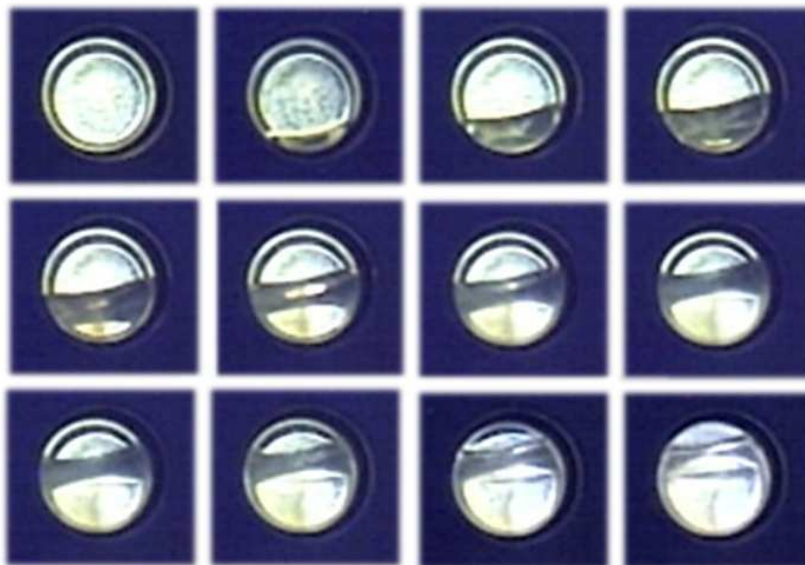


Figure 2.18: Re-sublimation: path (c) in the phase diagram of fig. 2.13 from the gas phase to the solid phase at low gas saturation.

(the time between the first to the last picture  $\approx 3$  h). The dominant step is number four leading to a low defect concentration inside the solid.

At the same time the density difference between solid and liquid are visible by the steady falling liquid level inside the cell. The crystal produced in this way was free from cracks and as transparent as the liquid (fig. 2.19).

When the temperature is raised above  $T_{\text{cell}}=22$  K the solid melts from the top to the bottom. This process can be seen as time inversion of the picture series shown in fig. 2.17 (this time to be read from right to left).

### Re-sublimation of deuterium

Path (c) in the phase diagram shows the direct re-sublimation of the gas to the solid state. The picture series are presented in fig. 2.18. The temperature of the cell was kept at  $T_{\text{cell}} \approx 16$  K and the pressure between 150 and 180 mbar. In this case it took ten hours to fill the 30 mm cell. The heat input from the windows and the different material causes a slightly smaller growth speed and therefore the horse-saddle like surface structure (suppressed condensation on glass)[54]. The conditions in this case are reversed to low supersaturation<sup>14</sup> in the gas condensation literature [53].

Figure 2.19 is used to compare the crystal quality on the right hand side re-sublimated with the liquid-solid sample on the left. In both cases the letters on the paper behind the cell can be easily recognized. A perfect crystal without any visible cracks could be produced from the liquid or the gas phase. Our results are in good agreement with the empirical model published by Dallügge [55]. They proposed a critical growth rate of 3 mm/hour to get transparent crystals for their tested gas crystals  $\text{N}_2, \text{O}_2, \dots$ . This model was extended to hydrogen and deuterium working close to the triple point by Haefler [53]. From our crystallization model step four may also be seen as dominant.

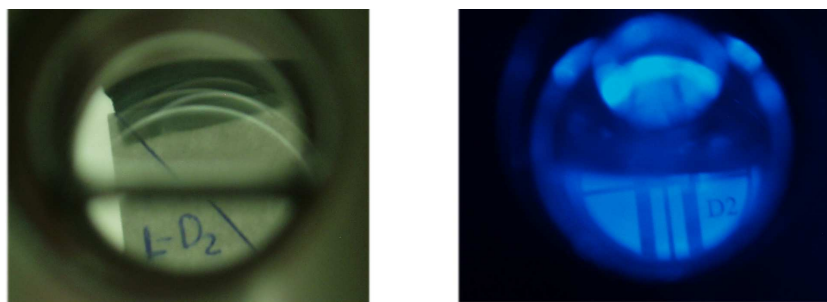


Figure 2.19: Transparent crystal frozen from the liquid phase (left) and respectively a crystal prepared from the gas phase at low oversaturation and low temperature difference to the triple point temperature (right).

### Direct condensation of deuterium

Figure 2.20 left shows a crystal re-sublimated at low temperature  $T=10$  K and thus high supersaturation (path (d) in fig. 2.13). It seems that the high rate of molecules

<sup>14</sup>Supersaturation: the ratio between the equilibrium gas pressure at the substrate temperature and the applied gas pressure.

hitting the surface lead to a rapid island growth. The resulting crystal columns have random lateral size and orientation starting from the cold cell surfaces. This can be seen by light reflexes or from the vertical layer like melting behavior (fig. 2.20right). This sample was not opaque but also not transparent. Taking our model from fig. 2.15 it seems that step 3 is faster than step 4. The freezing took approximately 2-3 hours. Freezing at temperatures well below the triple point is known as direct condensation [54]. The crystal melt in vertical layers as is shown in fig. 2.20 (right).



Figure 2.20: Crystal prepared by direct condensation at lowest temperature  $T_{\text{cell}}=8$  K from the gas phase with high over saturation on the left side. Melting of the gas crystal left as a function of time  $\approx 10$  min at  $T_{\text{cell}}=22$  K. The crystal melts in vertical layers and from the top.

### Turbo freezing of liquid deuterium

Once the cell is filled with liquid "turbo solidification" was also applied. In this case, the heating is suddenly switched off and the sample quenched within ten minutes to the lowest possible temperature ( $T_{\text{celle}} \approx 8K$ ). Here we can assume that step one and two are dominant leading to small crystals with random size, random origin and random orientation. The phase transition from liquid to the grey fine grain structure is shown in the first two pictures of fig. 2.21.



Figure 2.21: Phase transition from liquid (first picture) to solid (second picture) with maximum undercooling: turbo freezing. After moderate turbo freezing, effect of annealing at an intermediate temperature  $T_{\text{cell}}=16K$  shown as function of time (three pictures on the right with a time difference of 1h.)

If the cell temperature is raised above  $T_{\text{cell}}=22$  K the solid melts smoothly from bottom to top.

## Annealing of solid deuterium

At intermediate cooling speeds (tens of minutes) we get similar results as in the case of the turbo freezing (quenching), but by keeping the solid several hours at a temperature of  $T_{\text{cell}} \approx 16$  K it was possible to change the crystal towards a transparent sample. This annealing effect is shown as function of holding time in the pictures of fig. 2.21 (time steps  $\approx 1$  h between the pictures). This fits well to the observation that samples grown faster than with 5 mm/hour become transparent again after storing them close to the triple point as reported in [55]. They explained this fact with a repair of fissures, faults and re-crystallization. Mascher [54] reported that annealing leads to an improvement of a factor of three in the thermal transport coefficient  $\lambda_{\text{th}}$  as well as a significant improvement by the transparency for thermal radiation.

## Under cooling of deuterium

Once the transparent crystal was prepared either from the gas or from the liquid and was cooled below 10 K, dendrites started to grow as shown in fig. 2.22. Their density increased with time or further cool down. Heating above  $T=11$  K stopped their growth but annealing was not observed. The growth continued again below  $T_{\text{celle}} \approx 11$  K. In the empirical model from Dallügge, such a behavior is predicted at a crossing temperature of  $2/3 \cdot T_{\text{triple}}$  ( $D_2 \rightarrow 12$  K). Following his explanation, the reasons are inhomogeneities which arise from inevitable temperature gradients during the growth of the condensate leading to thermal stress. In addition, the condensates are brittle and have comparatively high coefficients of thermal expansion (much higher than for copper for example).

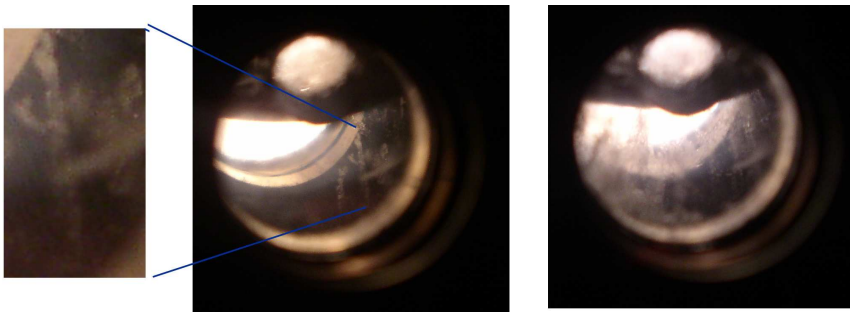


Figure 2.22: Left: dendrite like growth inside the transparent crystal when it is cooled below a critical temperature of 10 K is shown. Right: the dendrite density as function of time seems to increase as shown on the right (picture taken after some minutes).

## 2.4.2 Raman spectroscopy

### Experiment for ortho/para converter characterization

In order to test the ortho/para converter unit, the gas handling system of *cubeD*<sub>2</sub> was used to fill the Oxisorb cell with liquid deuterium. The converter was then operated in two different modes (as the converter cell had no windows the methods have been

developed with neon and the *cubeD<sub>2</sub>* cell from fig. 2.4). In the first mode, the liquid mode, the cell was kept at  $T_{\text{Oxisorb}}=22$  K for one day with the connection to the deuterium reservoir open. Afterwards the ortho concentration  $c_{\text{o-D}_2}$  was measured. For the second mode, the boiling mode the temperature after filling was decreased to  $T_{\text{Oxisorb}}=19$  K before the valves were closed. Afterwards the temperature was increased again to 22 K with the valves to the reservoir closed. In pre-experiments with neon plus impurities to study convection this setting lead to big convection effects as shown in fig. 2.14, right. Every three hours a gas sample was taken and the ortho/para concentration measured every three hours. Raman spectra for high (red) and low (black)  $c_{\text{o}}$  are shown in fig. 2.23 (right) taken at Walter Meißner Institut.

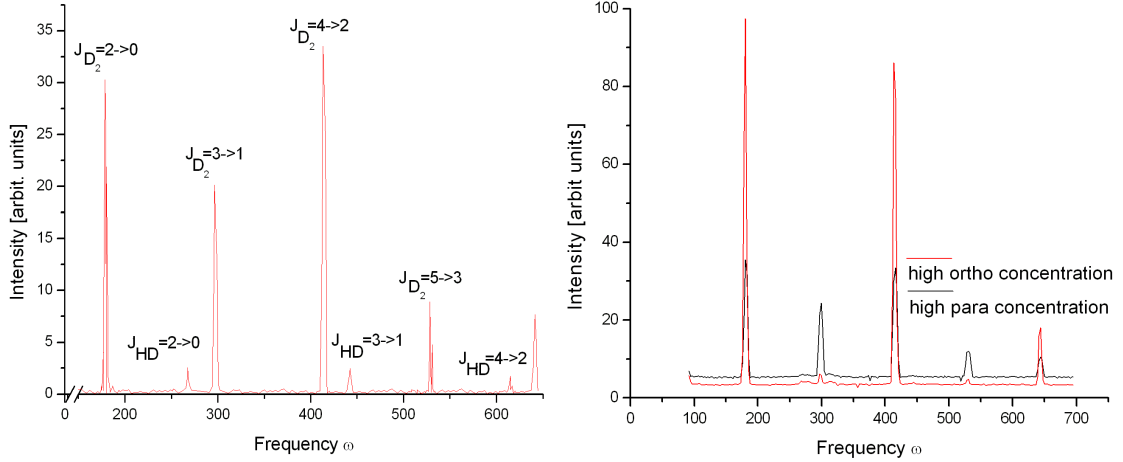


Figure 2.23: Raman spectra: (left) transitions measured and marked with the predicted change in the rotational quantum number  $J$  from table 2.1. One can clearly see the contribution from hydrogen impurities. Right side two spectra with high (red) and low (black) ortho concentration.

## Conversion theory

The development of the p-D<sub>2</sub> concentration  $c_{\text{p}}$  and the o-D<sub>2</sub> concentration  $c_{\text{o}}$  with time  $t$  may be described by two simple linear differential equations.

$$\frac{dc_{\text{p}}}{dt} = -K \cdot [c_{\text{p}} - (1 - c_{\text{o,T}})] \Rightarrow c_{\text{p}}(t) = (1 - c_{\text{o,T}}) \cdot (1 - e^{-K \cdot t}) + c_{\text{p},0} \cdot e^{-K \cdot t} \quad (2.22)$$

and

$$\frac{dc_{\text{o}}}{dt} = K \cdot [c_{\text{p},0} - (1 - c_{\text{o,T}})] \cdot e^{-K \cdot t} \Rightarrow c_{\text{o}}(t) = (1 - c_{\text{o,T}} - c_{\text{p},0}) \cdot e^{-K \cdot t} + c_{\text{o,T}} \quad (2.23)$$

Here,  $K$  is the conversion coefficient,  $t$  the elapsed time,  $c_{\text{p},0}$  the initial para concentration and  $c_{\text{o,T}}$  the equilibrium o-D<sub>2</sub> concentration for a given temperature catalyst

$T$  which is derived from the predicted equilibrium concentration  $c_{p,T}$ . concentration. One may calculate  $K$  by summing over the different interactions leading to conversion. Using Fermi's Golden Rule with the probability  $P_i$  that the system starts in the initial state  $i$  and  $f$  the final state we get [56]:

$$K = \frac{2\pi}{\hbar} \sum_{i,f} (P_i < f | H_{\text{WW}} | i >^2 \cdot \delta(E_i - E_f). \quad (2.24)$$

$H_{\text{WW}}$  is the interaction Hamiltonian consisting of a spin-spin  $H_{\text{SS}}$ , a rotation-spin  $H_{\text{RS}}$  and a quadrupole-quadrupole interaction  $H_{\text{QQ}}$

$$H_{\text{WW}} = H_{\text{SS}} + H_{\text{RS}} + H_{\text{QQ}}.$$

The most important part for the following discussion is the spin-spin Hamiltonian which is linear in the magnetic moment  $\mu_{\text{D}}$  of the deuterium molecule and  $\mu_{\text{B}}$  the magnetic moment of the catalyst

$$H_{\text{SS}} \propto \sum_{i,j=1}^2 \frac{\mu_{\text{D}} \cdot \mu_{\text{B}}}{R_{a_i,b_j}^3}. \quad (2.25)$$

$R_{a_i,b_j}^3$  is the distance of the deuterium molecule to the source of the magnetic gradient field. It is a well known problem [46] that the experimental result,  $K_{\text{natural}} = 6 \cdot 10^{-4} \text{ h}^{-1}$ , is only half the theoretical value<sup>15</sup> (natural conversion as function of time is shown in fig. 2.24 on the left hand side). In this case just the magnetic moment of the neighboring deuterium molecules acts on the spin flip probability.

If a paramagnetic impurity such as  $\text{Cr}_2\text{O}_3$  is present, the  $K$  value changes, due to the higher magnetic moment of the catalyst. Comparing the magnetic moments of  $\text{Cr}_2\text{O}_3$  and hydrogen,  $\mu_{\text{Cr}_2\text{O}_3}/\mu_{\text{H}} = 1487$ , one expects an increase of  $K_{\text{Cr}_2\text{O}_3}$  by at least three orders of magnitude,  $K_{\text{expected}}=0.9 \text{ h}^{-1}$ .

## Determination of the conversion rate

Assuming the ortho  $\text{D}_2$  concentration to approach the equilibrium concentration according to  $[1 - e^{-K \cdot t}]$ , suggested by the theory, we extracted the  $K$  values for the boiling and the liquid mode from the measured data. The change of the  $o - \text{D}_2$  concentration as function of conversion time for the boiling mode is shown in fig. 2.24, right. After 15 h we reached 97.5 %  $o - \text{D}_2$ , close to the saturation level at  $T_{\text{Oxisorb}}=22 \text{ K}$ . Taking a sample during conversion implies, however, that there is always an unknown amount of deuterium gas with lower  $c_o$  concentration than inside the tubes ( $T=300 \text{ K}$ ) flushed into the Raman cell. This amount was estimated to determine the errors. The last measurement showed a higher value at  $c_o = 98 \text{ \%}$  because it was taken after emptying half of the cell. Now the described effect can be neglected due to sufficient flashing of high  $c_o$  gas through the pipes. The conservative conversion rate from a fit to the data of fig. 2.24 is  $0.39 \text{ h}^{-1}$ . This is just a factor two lower than from or simple model expected.

<sup>15</sup>Possible explanation can be found in Ref. [61]: The effective magnetic moment of a para deuterium molecule is just 60% of the free magnetic moment due to the polarisation of nearest neighbours.

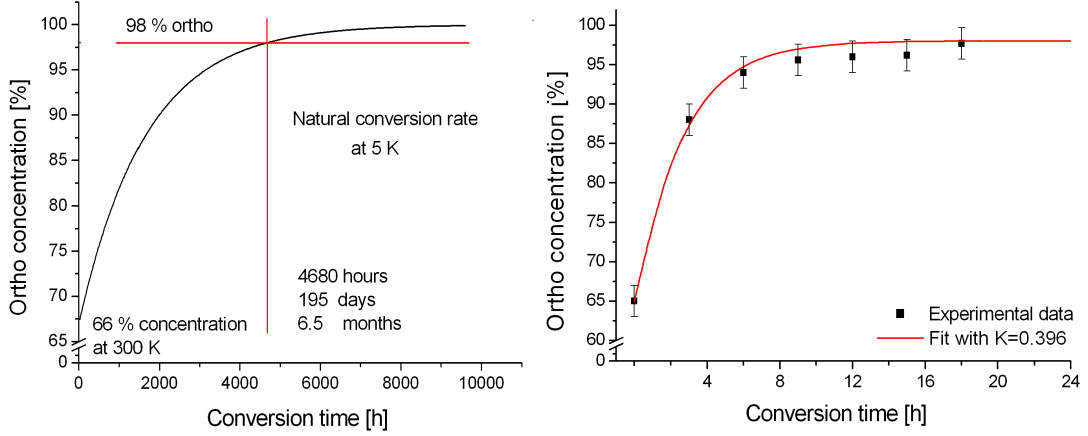


Figure 2.24: Left: natural conversion with a  $K=6 \cdot 10^{-4} \text{ h}^{-1}$ . Right: the measured conversion using Oxisorb catalyst on the right leading to  $K=0.396 \text{ h}^{-1}$  derived from the fit.

For the liquid mode we measured the  $c_o$  concentration once after 24 h and reached only 86 %. This belongs to a rate of  $K=0.13 \text{ h}^{-1}$ . Silvera [46] stated that the catalyst may be covered by converted layers of deuterium and the conversion rate is reduced due to the enlarged distance. We think that the difference to the boiling mode is caused by the large deuterium exchange rate on the catalyst surface caused by the convective motion. Further details on the para to ortho converter can be found in [57].

To summarize, one may say that after 12 h a  $c_o(D_2)$  concentration of  $c_o = 98 \pm 1\%$  can be guaranteed with our Oxisorb unit in the boiling mode.

The successful use of the ortho to para converter as cryogenic impurity filter was tested by comparing the UCN production inside the *cubeD<sub>2</sub>* experiment. Once the Oxisorb cell was filled with pure deuterium, converted and filled into the target cell of the *cubeD<sub>2</sub>* and another time with  $D_2$  and a 10% nitrogen mixture. The UCN production rates were estimated as function of temperature. Due to the large UCN absorption cross section of nitrogen and the identical measured UCN count rates we expect successful filtering by the Oxisorb converter [57].

Analyzing the intensities of the rotational bands of HD in the Raman spectra one can determine the hydrogen contamination  $c_{HD}$ . One spectrum with hydrogen impurities is shown on the left-hand side of fig. 2.23. We know the transition frequency of  $J_{HD} = 2 \rightarrow 0$ . Thus it is than possible to fit the measured intensity there compared with the background to get an estimation on the upper limit of hydrogen impurities in spectra like shown on the right side. At a first try levels of 0.1% and therefore the correlated loss probability from fig. 2.2 could be excluded. Such concentrations are low enough to keep the UCN losses well below the intrinsic loss by the absorption on deuterium:  $\sigma_{\text{abs}}(H)/\sigma_{\text{abs}}(D) \approx 640$ .

### 2.4.3 Neutron scattering data

On the following pages we will present the results of the inelastic neutron scattering. We start with a discussion on the structure  $S(q)$ , followed by the dynamics  $Z(\omega)$  and finally the dynamic structure factor  $S(q, \omega)$  [58].

#### The structure of solid deuterium

Deuterium usually grows in a hexagonal closed packed structure (at the available temperatures of interest for our purpose). The angles between the fundamental vectors  $|\vec{a}|, |\vec{b}|, |\vec{c}|$  ( $|\vec{b}| = |\vec{a}|$ ) in the hcp lattice are  $90^\circ$  and  $120^\circ$  (see fig. 2.27).  $\vec{a}$  and  $\vec{c}$  depend on the ortho/para concentration  $c_o$  [59].

$c_p = 33\%$  para  
 $a = 3,616$  ;  $c = 5,876$

$c_p = 3\%$  para  
 $a = 3,609$  ;  $c = 5,861$

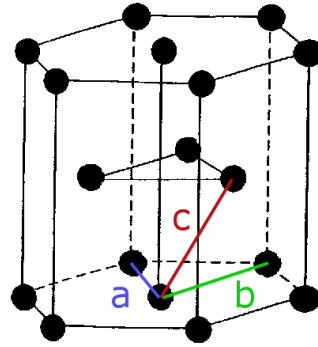


Figure 2.25: Lattice constant and scheme of a hcp deuterium structure.

We used these values to calculate the expected deuterium powder neutron diffraction pattern with the program "powdercell" [60]. The wave length of the incoming neutron  $\lambda_{CN} = 2.178 \text{ \AA} \approx 2.2 \text{ \AA}$  and the scattering angle  $\vartheta$  covered by the detectors of  $20^\circ - 140^\circ$  are taken from the description the IN4 instrument. The result for high and low  $c_p$  is shown on the left-hand side of fig. 2.26 and compared with measured  $S(q, \omega = 0)$  values for similar ortho/para concentrations. The Bragg peaks identified by the Miller indices  $h, k, l$  are correlated via eq. 2.18 with the lattice constants of the solid. The first ten identified distances are listed in table 2.2. The hcp primitive cell fixes the peak position. The distribution of atoms inside the unit cell and domains of texture effects are fixed by the relative height of the peaks. Instead of the expected powder distribution where the grains with small sizes randomizes the orientation of the expected hcp crystal structure in case of texture inside the sample one or some directions are pronounced leading to changes in the relative height of the peaks. In the extreme case (towards a single crystal) there is even a possibility that one hcp Bragg peak misses the detector at all and vanishes from the measured spectrum completely.

Comparing the simulated with the measured results leads to very good agreement for the first ten Bragg peaks. In case of a high para concentration, the first Bragg peaks are slightly shifted. In contrast to the spherical ortho molecule, the para has a quadrupole moment and an elliptical shape (fig. 2.27) [46]. This quadrupole moment influence up to six next ortho neighbors due to polarization [61].

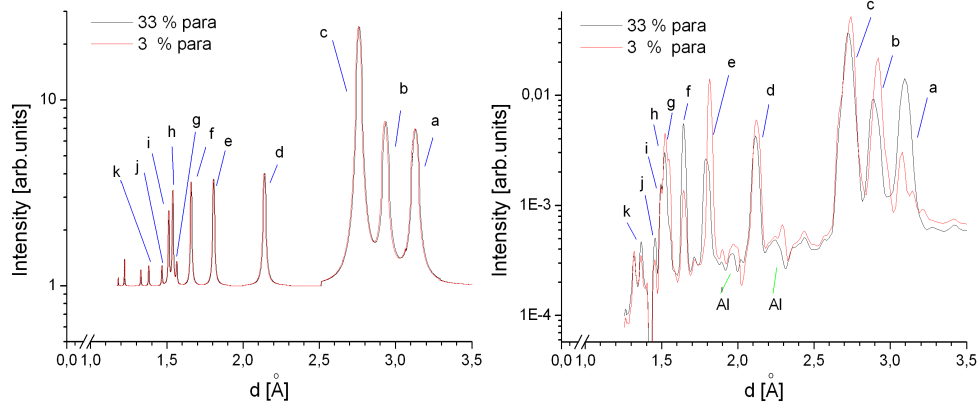


Figure 2.26: Diffraction patterns  $I(\vartheta) \rightarrow I(d)$  as function of the atomic distance  $d$  for deuterium with two ortho/para concentrations in the simulation. A hcp structure is assumed at the simulation (left) which lead to results indistinguishable on the  $c_o$  (different lattice vectors). In case of the measurement (right) the first Bragg peaks are shifted with higher para concentration. Data are taken from  $S(q, \omega = 0)$

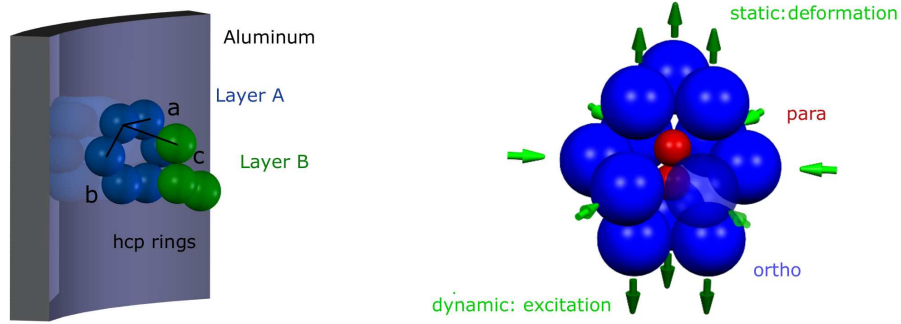


Figure 2.27: Left: preferential crystal direction if the solid is slow grown. Reight: ortho crystal disturbed by a para impurity.

Peak	hkl	simulation powdercell				n-scattering data IN4			
		$d_{33} \text{ \%} [\text{\AA}]$	$I_{33} \text{ \%}$	$d_{3 \text{ \%}} [\text{\AA}]$	$I_{3 \text{ \%}}$	$d_{33} \text{ \%} [\text{\AA}]$	$\frac{d_{\text{sim}}}{d_{\text{exp } 33\%}}$	$d_{3 \text{ \%}} [\text{\AA}]$	$\frac{d_{\text{sim}}}{d_{\text{exp } 3\%}}$
a	100	3.13	25.0	3.13	25.0	3.10	1.15	3.08	1.02
b	002	2.93	27.2	2.94	27.0	2.89	1.02	2.92	1.00
c	101	2.76	100	2.76	100	2.73	0.89	2.73	1.01
d	102	2.14	12.7	2.14	12.7	2.12	1.01	2.12	1.01
e	110	1.80	11.5	1.80	11.5	1.80	1.01	1.82	0.99
f	103	1.66	11.0	1.66	11.0	1.64	1.01	1.65	1.01
g	200	1.56	1.3	1.57	1.3	1.55	1.01	1.58	1.01
h	112	1.54	9.4	1.54	9.5	-	-	1.53	1.01
i	201	1.51	6.4	1.51	1.01	-	-	-	-
k	004	1.47	1.2	1.47	2.2	1.37	1.46	1.46	1.01

Table 2.2: Miller indices for the identification of the hcp Bragg peaks calculated and measured for low and high ortho concentrations

With increasing para concentration both effects, polarization and elliptical shape, lead to a change of the lattice vectors compared to the ideal case of 100 % ortho (hcp from spheres). Above a critical value (still below 1 %) the quadrupole moments of neighboring para molecules are aligned and deform the lattice in one direction. The first three Bragg peaks, mainly 100, 002 and 101 are slightly shifted with increasing para concentration. This was included in the simulation but lead to no significant effect. An improvement would be to consider not only the new lattice-vector ratio but also the structure factor of the non spherical para molecules times their probability. In our data the relative peak heights for the turbo frozen solids agree best with the simulated powder sample.

## Freezing procedure

The structure of solid deuterium produced using different freezing procedures (explained in more detail in section 2.4.1) were investigated in the next step. The  $S(q, \omega = 0)$  plots for slow freezing and "turbo freezing" from the liquid, solidification from the gas ( $T_{\text{cell}} = 12$  K) and an intermediate state, are shown in fig. 2.28. In the latter case, the solid was partially (95%) melted before re-crystallisation<sup>16</sup>. The idea was to freeze from tiny crystals floating in the liquid as nucleation seeds and to avoid freezing dominated by the structure of the wall material. Problems of this kind have been reported for platin or gold foils in ref. [64].

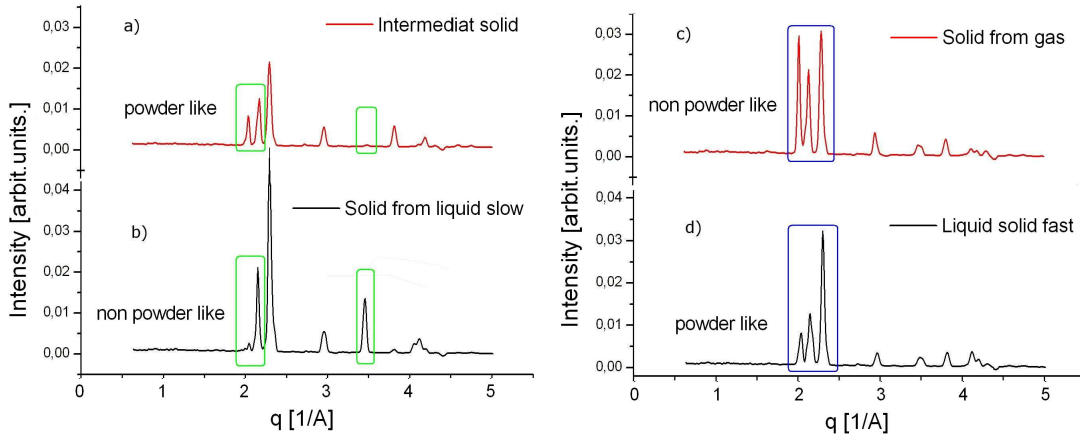


Figure 2.28: Solid deuterium structure  $S(q, \omega = 0)$  as function of the momentum transfer  $q$  and different freezing procedures. The square shows the region of interest.

Independent of the freezing procedure, the position of the Bragg peaks was highly reproducible and the deuterium keeps the hcp structure. The different peak heights indicate however that the mean average orientation was changed (regions of interest inside the squares). As explained before, the turbo frozen solid and the intermediate one reflect best the powder approximation (this fits to the crystallization model in section 2.4.1). In the case of a slow phase transition the absence of the 100 and the strong 110 peak may be an indication that the hcp layers grow perpendicularly to the sample

<sup>16</sup>This is estimated from the in-situ comparison of the intensity versus flight time  $I(\Delta t_n)$  monitored in reference to the liquid intensity  $I_{\text{liquid}}(\Delta t_n)$ .

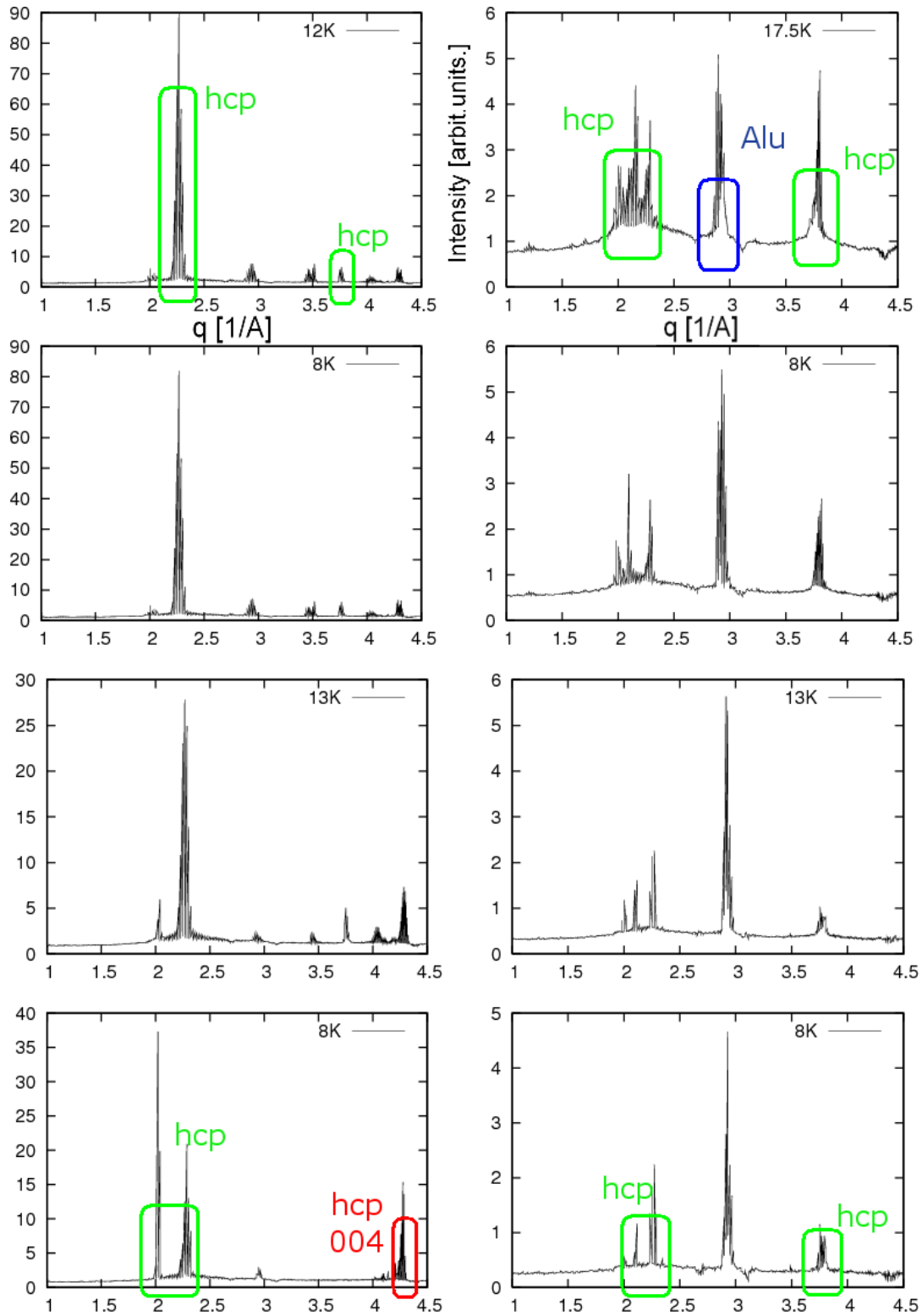


Figure 2.29: Relative intensity versus  $q[1/\text{\AA}]$  for different deuterium temperatures for a solid deuterium sample with  $c_0=66\%$  on the left side and  $c_0=98\%$  on the right side measured at the TOFTOF instrument of FRMII. A possible effect of the annealing on the structure is shown in the colored squares.

container wall as it is shown in fig. 2.27 [65] (green squares). Similar explanations have been published in ref. [59] who found a preferred crystal growth parallel to the walls of the sample holder<sup>17</sup>. The hcp structure of the re-sublimated sample is completely different from the "turbo solid" (blue squares) and therefore consists of larger domains, but it is also different from the liquid, which can be interpreted as more randomly orientated. This is also consistent with the crystallization model used in section 2.4.1

### Temperature treatment

In case of the TOFTOF measurement (sample holder with polished walls instead of machined walls) we got a clear indication that some crystallites change their orientation  $\approx 30^\circ$  when the temperature is raised from 8 K to 13 K. This is shown in fig. 2.29. This change gets even more pronounced when returning to the lowest temperature again. The first Bragg peaks flip their intensity and a new strong 400 Bragg peak shows up. This behavior was much more pronounced for the  $c_o=66\%$  shown on fig. 2.29 left-hand side then for the  $c_o=98\%$  shown on the right.

### 2.4.4 The dynamics of solid deuterium

In the following figures  $GDOS(\omega)$  (cf. eq. 2.21) are shown as function of temperature,  $c_o$ , freezing and sample preparation are shown and the results discussed.

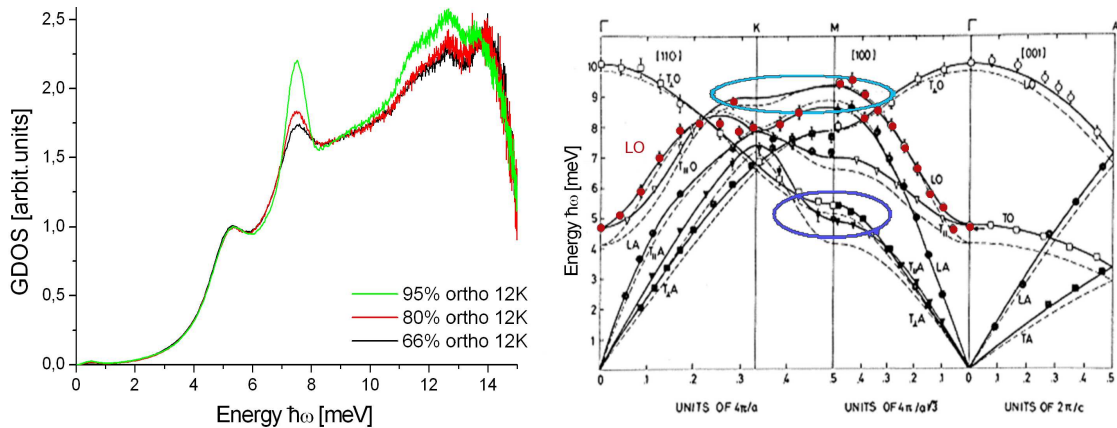


Figure 2.30: Left: generalized phonon density of states  $GDOS$  for solid deuterium measured with three different  $c_o$  of 66% (black), 80% (red), and 95% (green) at 4 K. Right: phonon dispersion curve from, Nielsen [66].

### Ortho/para concentration

Four characteristic features may be identified in all following  $GDOS$  plots. There is a strong excitation at 5 meV and at 7.5 meV which may be identified in comparison with the measured phonon dispersion curve shown on the right side of fig. 2.30 [66] and the different ortho concentrations.

<sup>17</sup>The directions 002 and 101 are the planes with the highest packing density of the hcp crystal.

If the slope of the dispersion curve becomes small (van Hove singularity) a maximum in the phonon density of state is expected. The blue circles are the two phonon excitation modes which we correlated in our *GDOS* data with longitudinal acoustic 5meV and 10 meV longitudinal optical excitation. The rotational excitation from  $J = 0 \rightarrow J = 1$  at 7.5 meV and  $J = 1 \rightarrow J = 2$  at 14.2 meV can be identified by the predicted energy and by their intensity dependence on the ortho concentration (green (95%) red (80%) and black (66%)). The difference at between 10 - 14 meV between the Nielson data and our measurements is very interesting and will be discussed later.

### Temperature dependence

The temperature dependence of the *GDOS* between 16 K and 4 K is shown in fig. 2.31 for fixed ortho concentration. The data have been normalized to the 7.5 meV height. We found a slight shift of the 5 meV phonon excitation towards lower energies and a peak broadening with higher temperatures. Filling up the lowest states in the Lennard-Jones potential approximated by a parabola (cf. right side of fig. 2.31), the mean displacement is shifted to higher values with higher phonon numbers. The shift of the 5 meV peak to higher energies with increasing temperature may be interpreted as a deviation from the harmonic approximation. Nevertheless, the density of occupied phonon states inside the crystal increases with higher temperature. Thus the probability of phonon-phonon interaction increases and the phonon lifetime is reduced. From the uncertainty relation between lifetime and energy we derived the line broadening at higher temperatures. An identical behavior was seen for the sample with high  $c_o$ . In both cases no further change of the solid dynamics has been observed below 8 K, a temperature that fits to the reported lambda temperature  $T_\lambda(D_2) \approx 9$  K where specific heat and diffusion constants of deuterium change rapidly.

### Freezing procedure and annealing

Figure 2.33 shows *GDOS* at 4 K after different freezing histories and annealing at 12 K (measurements at the IN4). In both cases no major difference in the *GDOS* files was seen. The freezing procedures at large ortho concentrations were also investigated but lead to completely identical result.

### 2.4.5 Influence on the design of UCN sources

In a first approximation we took the *GDOS* file from the  $c_o=95\%$  measurement at 4 K and divided it by the energy transfer  $\omega$  and the occupation number  $(n+1)$  to get a quantity proportional to the down scattering cross section (eq. 2.1). Afterwards we multiplied with Maxwell spectra for different cold source temperatures  $T_{\text{cold source}}$  (CN spectrum), as free parameter, to arrive at values proportional to the UCN production rate, as shown in fig. 2.34 left-hand side. The normalized integral number as function of  $T_{\text{cold source}}$  is shown on the right side of fig. 2.34. The best matching and thus ideal cold-source temperature (CN spectrum) was found to be 40 K. This result fits well to the value predicted from theory,  $T_{\text{cold source}} 40$  K in [67] where multiphonons up to order 3 have been taken into account. Another result is, that we have non negligible contributions for UCN production above 10 meV.

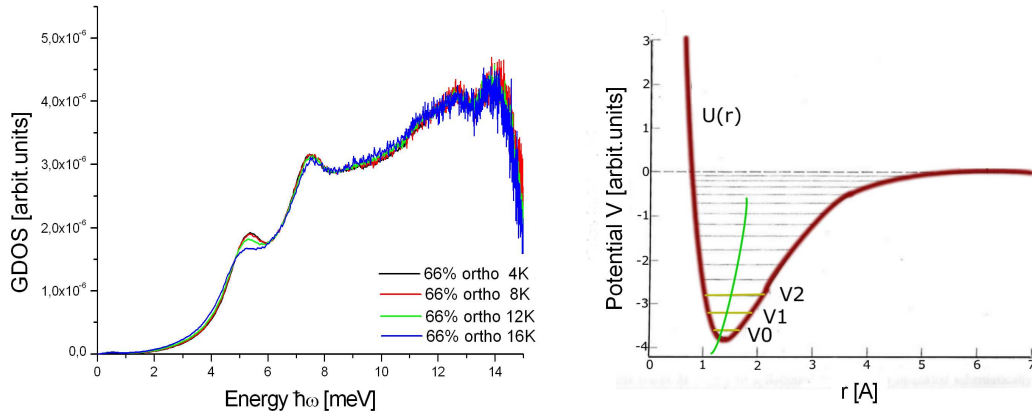


Figure 2.31: Left: GDOS measured at low ortho concentrations for different temperatures  $T$ . Right: Lenard-Jones like potential  $U(r)$  for the molecular force (hydrogen) with the lowest excitation levels  $V_0$ ,  $V_1$ ,  $V_2$ .

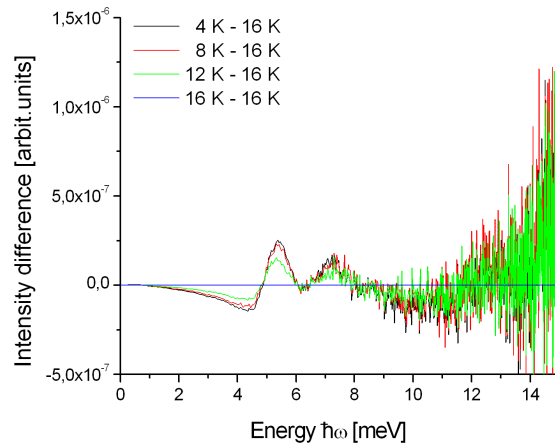


Figure 2.32: Difference between GDOS at 4 K, 8 K, 12 K compared to GDOS at 16 K. The excitation levels below 6 meV are almost equal for 4 K and 8 K.

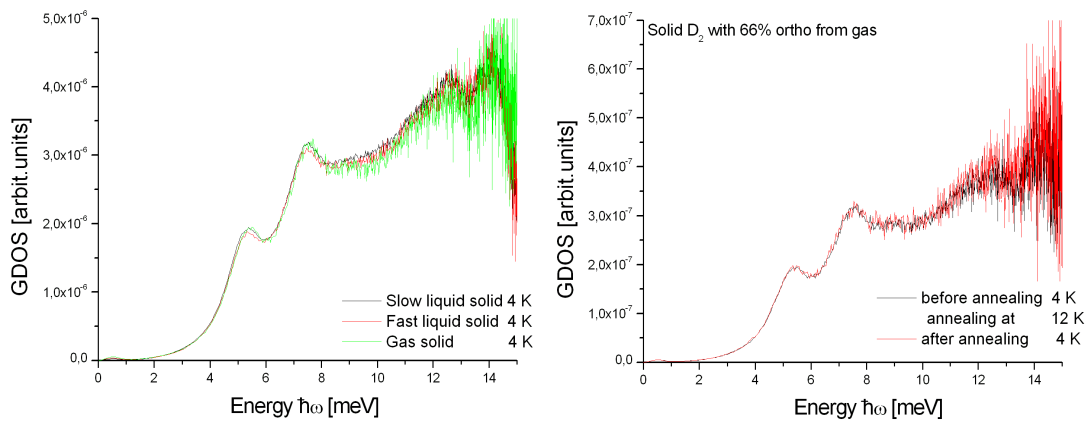


Figure 2.33: Left: GDOS for different freezing processes. Right: for an annealing cycle.

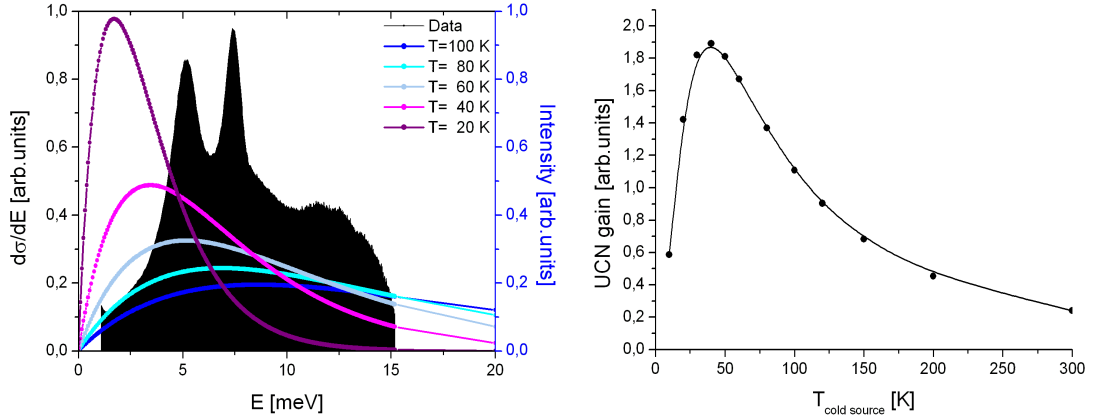


Figure 2.34: Left: relative down-scattering cross section for  $c_o=95\%$  at 4 K compared with different Maxwell spectra expected for different cold source temperatures  $T_{\text{cold source}}$ . Right: integral of the Maxwell spectrum for different cold spectral fluxes multiplied with the  $d\sigma/dE$  function. After normalization the maximum leads to the best cold source setting to achieve the highest UCN production.

## 2.4.6 Phonon and multiphonon contribution

Figure 2.35 shows the relative down-scattering cross section for  $c_o = 66\%$  on the left-hand side and  $c_o = 95\%$  on the right. This time the occupation number  $n + 1$  was linearly approximated leading to a  $GDOS \cdot 1/\omega^2$  term compared to section 2.1. Both curves are shown together with a fit curve consisting of six Gaussians. The center of the Gaussians can be used to get a rough idea on the excitations that are responsible for the UCN production. Peak two at 5.07 meV and peak four at 9.37 meV have already been addressed from the phonon dispersion curve shown in fig. 2.30, right. Peaks number three and six at 7.28 meV and 14.33 meV, respectively belong to rotational excitations, scaling as expected with the ortho para concentration. The very broad peak at 5.69 meV describes the background below the lowest phonon and roton excitations and is necessary to get the Debye like parabola slope for small energie transfers. From our scheme in fig. 2.27 [61], where the para molecule is bound in a cage of ortho molecules we can expect that its motion is not independent. One could argue, that the process of a spin flip with the release of 7.5 meV is coupled to a typical 5 meV phonon excitation. This may be leads to an explanation of peak number 5 as a simultaneous phonon-roton excitation (5.69 meV+7.28 meV= 12.97 meV $\approx$  12.68 meV).

We would like to point out that it is not possible to reconstruct the measured values without this excitation peak at 12 meV. Due to the contradiction between the dispersion curve and our data above 10 meV we made further investigations.

Using the recursion formalism introduced in section 10.2 and the assumption  $GDOS = Z\omega$ , it is possible to calculate higher orders of  $Z_i$  from  $Z_0$  the one phonon density of state. For this purpose we took the  $q$  integrated raw data  $S(E \approx \omega\hbar)$  from our measurement for the 95 % ortho sample at 4 K to apply a multiphonon correction.

As a first step one considers that higher orders do not exist and describes the data by a guess function, in our case the red curve from fig. 2.35. The second step is to fold

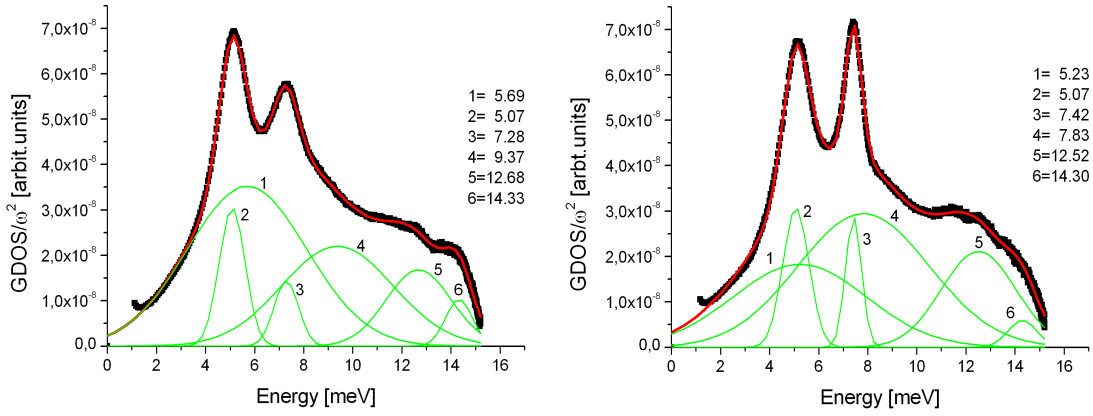


Figure 2.35:  $GDOS/\omega^2$  plus a fit of Gaussians to get an idea on the possible excitations which are responsible for the UCN production. Data are shown for  $c_o = 0.95\%$  (left) and  $c_o = 0.66\%$  (right).

the guess function plus fit parameter (for example the Debye Waller factor) with itself and compare the result with the measured data. The same is then applied with the next order. The fit parameters are tuned to find a convergent series which in total should reproduce the measured function. At the end, the different iteration steps lead to the one-phonon, two-phonon and so on contributions as function of energy. In our case (shown in fig. 2.36) the experimental curve is shown in red, as well as the one phonon contribution  $Z_0$  in black, the two excitation contribution  $Z_1$  in fair blue and three excitations  $Z_2$  in orange. The sum of the single parts is shown in dark blue as an indication on the quality of the analysis. Further explanations may be found in appendix 10.2.

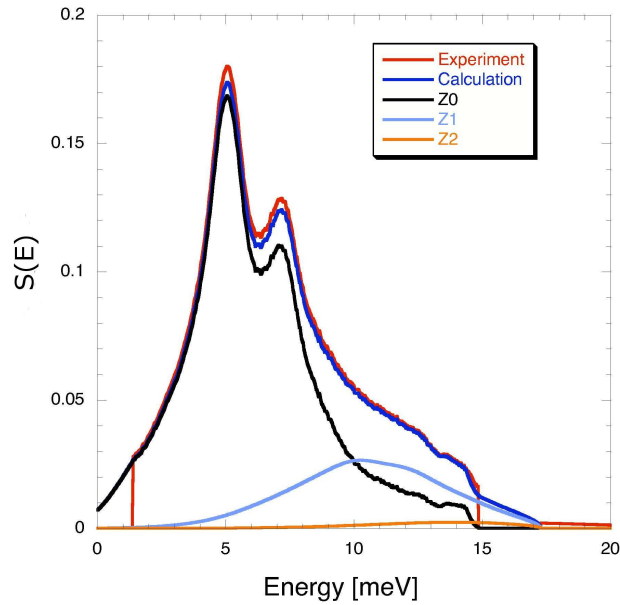


Figure 2.36: Sample with  $c_o = 0.66\%$  and 4 K. Shown are the separated one  $Z_0$ , two  $Z_1$  and three  $Z_2$  phonon contribution. The sum is compared with the experimental value.

One result of fig. 2.36 is that the simultaneous interaction of two excitations start already at energies of 5 meV. Another result is that the origin of the excitation at 12 meV may be explained as double excitation. Concerning UCN production one may say that the two phonon contribution also has to be taken into account, whereas higher orders are negligible.

Nevertheless it is not possible to explain the large intensity between 10 and 14 meV completely with the  $J=1 \rightarrow J=2$  transition and multiphonon contributions. Due to the fact, that even with state of the art correction methods to suppress higher energy contributions [31, 62, 63] it was not possible to get consistent results. One possible reason may be the quantum crystal behavior, another the problem that the mass of the sample atom is comparable to the neutron mass.

### 2.4.7 Estimation of the UCN production from $S(q,\omega)$

Figure 2.37 shows the marked main contributions in a typical  $S(q,\omega)$  plot from the IN4. The energy transfer  $\hbar\omega$  (as defined in eq. 2.10) is plotted on the x-axis, the momentum transfer  $|q|$  on the y-axis and the logarithm of the count rate as color coded histogram in z-direction. The energy gain (left) and energy loss (right) areas of the sample, caused by the inelastic scattering process are separated by the elastic line with  $\omega = 0$  (structure information). In terms of UCN physics we can translate this separation into UCN production (left  $\omega > 0$ ) and UCN losses (right)  $\omega < 0$ .

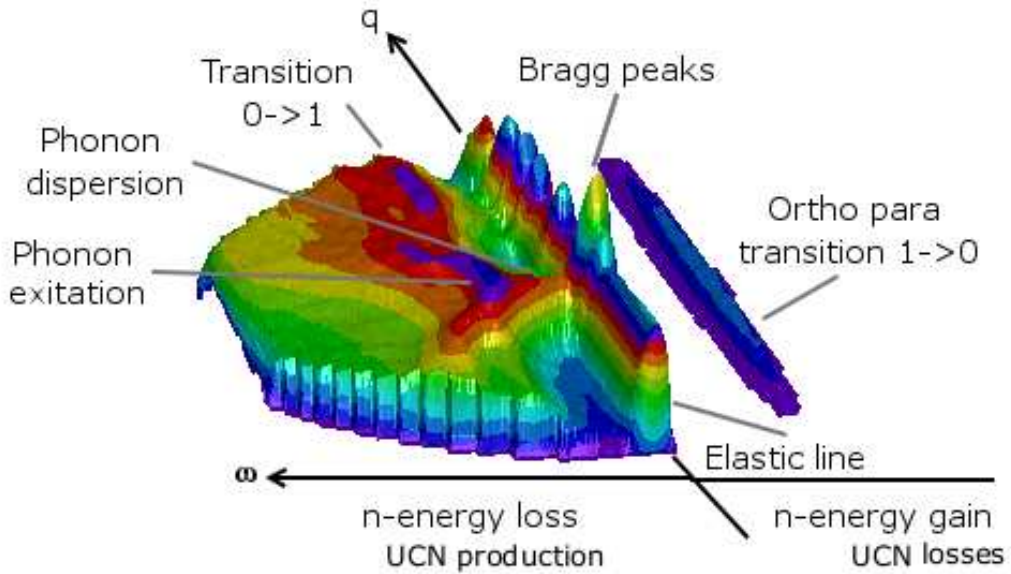


Figure 2.37: Dynamical structure factor as function of energy and momentum transfer. The plot is divided into two regions by the  $q$ -axis:  $\omega < 0$  energy gain of the neutron, UCN loss (right);  $\omega > 0$  energy loss of the neutron, UCN production (left). The sample had  $c_o = 66\%$  indicated by the strong  $1 \rightarrow 0$  transition (forbidden transition) and was measured at 4 K.

As energy and momentum have to be conserved and the final energy of the UCN may be neglected compared with the incident neutron energy, the relevant area for UCN production is reduced to the free-neutron parabola

$$E_i \approx \hbar\omega = \frac{\hbar^2}{2m_n} \cdot q^2 \quad (2.26)$$

In fig. 2.38 we have plotted  $S(q, \omega)$  at 4 K for different values of ortho to para concentrations and freezing procedures. At this temperature the occupation of phonon states is very low and no intensity is seen on the neutron energy gain region  $\omega < 0$ . But in case of the high para (J=1) concentration an intensity band of the spin flip probability is present at -7.5 meV (transition energy of J=1→J=0). Due to the forbidden transition these states are still occupied at 4 K. In n-scattering, due to the spin of the neutron it is not forbidden and therefore seen in the  $S(q, \omega)$  data. In case of large  $c_o$  and low number of para molecules the intensity vanishes (cf. fig 2.38 last four picture). The free neutron parabola is also shown in the other plots in fig. 2.38. Due to the different height of the Bragg peaks, caused by the texture effect in the samples, it is difficult to compare the different color plots as they are.

From eq. 2.8 it should be possible to integrate  $S(q, \omega)$  along the parabola, to get a comparable quantity.

## Coherent UCN production

As mentioned before, coherent scattering (which makes up 2/3 of the total scattering cross section) leads to direction dependent scattering. Looking at fig. 2.38 where the free-neutron parabola was included in the  $S(q, \omega)$  plots, one arrives at the following conclusions:

- The distribution of the free neutron parabola is far away from the Bragg peaks where the dispersion curve is quite horizontal.
- The relevant phonon band for the down scattering process at 5 meV is independent of the  $q$  value.
- The relevant roton band for the down scattering process at 7.5 meV is independent of the  $q$  value.

The band structure of the excitation levels caused by the quantum crystal behavior as well as the gap at low  $q$  values leads to a UCN production rate  $P$  independent from the crystal orientation. In first order a dependence of  $P$  on the freezing technique is not expected [65].

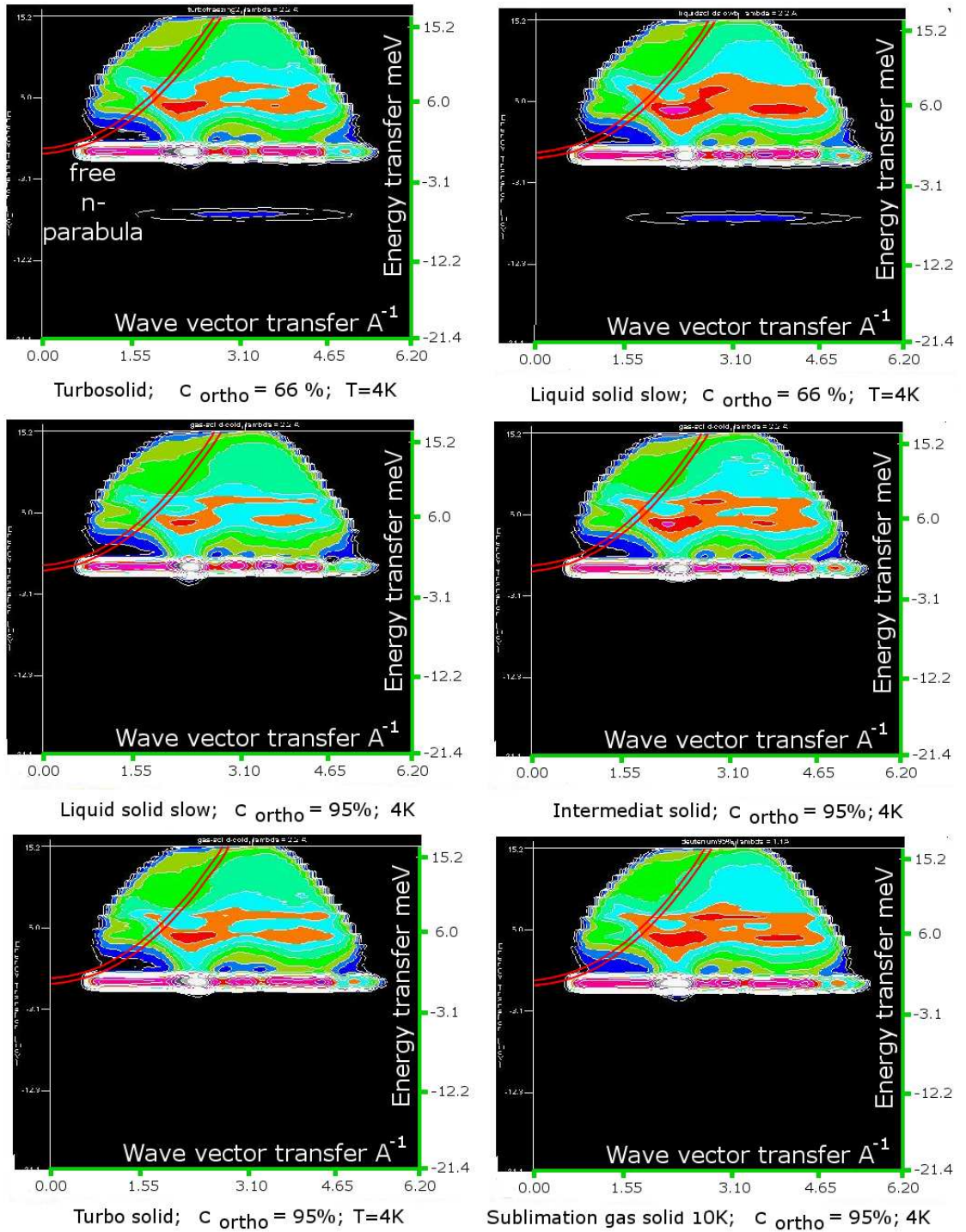


Figure 2.38:  $S(q, \omega)$  for different ortho/para ratios and different freezing procedures. All measurements are taken at 4 K. The free neutron parabola for one phonon down scattering into the UCN region is shown in red.

## Freezing

The two methods to produce transparent crystals<sup>18</sup> were the freezing slowly from the liquid<sup>19</sup> and the re-sublimated crystal from the gas<sup>20</sup>. To avoid an incorrect interpretations due to the color code in fig. 2.38 we introduced a routine to numerically integrate along the free neutron parabola (eq. 2.26) in the  $S(q, \omega)$  data with fixed width  $\Delta q = 0.1 \text{ \AA}^{-1}$  and  $\Delta\omega = \Delta\epsilon = 0.1 \text{ meV}$ , corresponding to the instrument resolution:

$$\frac{d\Sigma_{\text{parabola}}}{dE}(E) = \int_{E-\Delta\epsilon_{IN4}/2}^{E+\Delta\epsilon_{IN4}/2} d\epsilon \int_{q-\Delta q_{IN4}/2}^{q+\Delta q_{IN4}/2} S(q, \epsilon) dq \quad (2.27)$$

Figure 2.39, left for two different ortho concentrations with the sample slow frozen from the liquid and for the two different freezing techniques on the right-hand side shows the result.

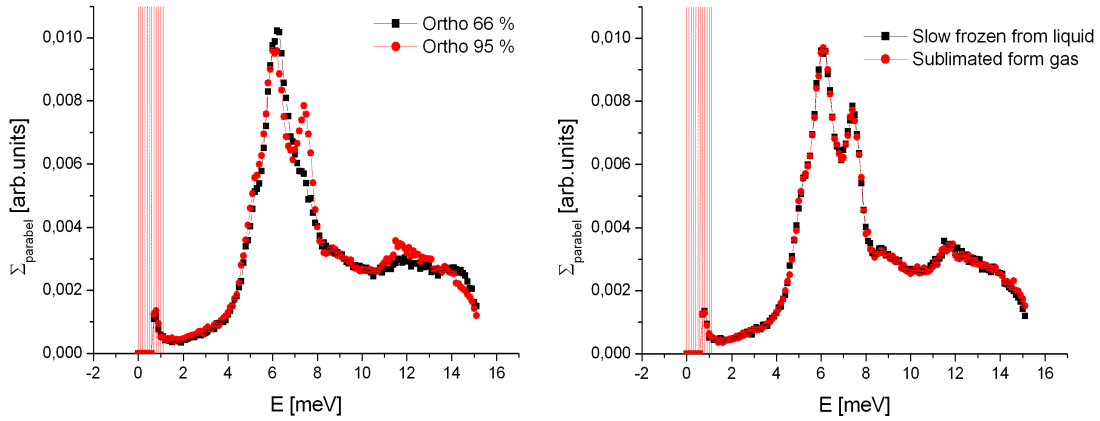


Figure 2.39: Left: Results of the integration of the free neutron parabola for the solid deuterium sample frozen from the liquid with two different ortho concentrations. Right: result for two different freezing methods both with (95% ortho concentration). All data were taken at 4 K.

No drastic difference could be found for the two freezing methods. The best matching Maxwell spectrum was also found for a temperature of  $T_{\text{cold source}} = 40 \text{ K}$ . In this case it was possible to compare the expected production for different ortho concentrations (cf. fig. 2.39, left). From our data we expect a 5% increase in the production rate from the spin flip with larger  $c_o$  of 95%.

<sup>18</sup>Transparent crystals should in contrast e.g. to the turbo solid samples not show small angle scattering of the produced UCN and therefore increase the escape probability of the UCN from the solid  $D_2$

<sup>19</sup>This method is necessary for the planned UCN source (vertical source) at Paul-Scherer Institut PSI [20]. Due to the large size of the solid  $D_2$  (which is used as premoderator and converter) this concept is forced to fill with liquid  $D_2$  before solidification.

<sup>20</sup>This method is necessary for the planned FRMII source where the solid  $D_2$  converter is placed in a horizontal beam pipe (horizontal source). Filling is just possible via direct condensation from the gas phase.

## Absolute production cross section

The integrated spectrum is now used to calculate the absolute UCN production cross section for 95% ortho deuterium at 4 K. The influence of the sample geometry was already considered in the preparation of  $S(q, \omega)$  by the instrument software and by the normalization on the vanadium scattering data (in the same sample holder and sample temperature). The purely incoherent scattering of vanadium is used to correct for the different detector efficiencies. In addition, if the sample thickness corresponds to the assumed 10% scattering, the amount of atoms  $N$  in the beam is considered as well. The data were also normalized to the incoming neutron flux  $\Phi$ . The ratio  $R_i$  may be now interpreted as part of  $S(q, \omega)$  that is covered by the energy and momentum region of the reaktion of interest  $i$ . With this assumption it is possible to calculate  $\sigma_i$ ,

$$\sigma_i = \frac{R_i}{N_i \cdot \Phi}. \quad (2.28)$$

The region of interest for UCN production is the intensity along the free-neutron parabola with an energy width corresponding to the UCN energy range. Instead of integrating over the instrument resolution (meV) we have to correct each value down to the neV range. The problem is roughly indicated in fig. 2.40 left, where the instrument resolution  $\Delta q = 0.1 \text{ \AA}^{-1}$  is shown in blue and the necessary width in the UCN energy range of  $\Delta E = \pm 150 \text{ neV}^{21}$  in red.

The required phase space correction  $K(E)$  derived at a comparison of eq. 2.29 and the wanted equation for the UCN production was calculated for each energy bin (0.1 meV).

$$\frac{d\sigma_{\text{UCN}}}{dE}(E) = \int_{E-\Delta\epsilon_{\text{UCN}}/2}^{E+\Delta\epsilon_{\text{UCN}}/2} d\epsilon \int_{q-\Delta q_{\text{UCN}}/2}^{q+\Delta q_{\text{UCN}}/2} S(q, \epsilon) dq \quad (2.29)$$

Inside the small squares of  $\Delta q_{\text{IN4}}$ ,  $\Delta\epsilon_{\text{IN4}}$  and thus within the instrument resolution the value of  $S(q, \omega)$  is assumed to be constant. With this approximation we can write the integration as a sum of slices ( $q$  value times the  $q$  binning Riemann sum).

$$\frac{d\Sigma_{\text{IN4}}}{dE}(E) = \Delta\epsilon_{\text{IN4}} \Delta q_{\text{IN4}} S(q, \epsilon) \quad (2.30)$$

$$\frac{d\sigma_{\text{UCN}}}{dE}(E) = \Delta\epsilon_{\text{UCN}} \Delta q_{\text{UCN}} S(q, \epsilon). \quad (2.31)$$

From the ratio of both equations we get a method to calculate the necessary correction coefficient  $K(E)$  for each energy bin  $\Delta E$  (0.1 meV):

$$\frac{d\sigma_{\text{UCN}}}{dE}(E) = \underbrace{\frac{\Delta\epsilon_{\text{UCN}} \Delta q_{\text{UCN}}}{\Delta\epsilon_{\text{IN4}} \Delta q_{\text{IN4}}}}_K \cdot \frac{d\Sigma_{\text{IN4}}}{dE}(E). \quad (2.32)$$

Now we can multiply the correction factors on the integrated parabola values of fig. 2.39 and get the absolute down scattering cross section as shown in fig. 2.40 on the

---

<sup>21</sup>The UCN energy of 300 neV was chosen to be able to compare our data with experimental data from the PSI [37] shown in fig. 2.29 in red on the right hand side. The authors used a cut off potential of their UCN guides of 300 neV in their analysis.

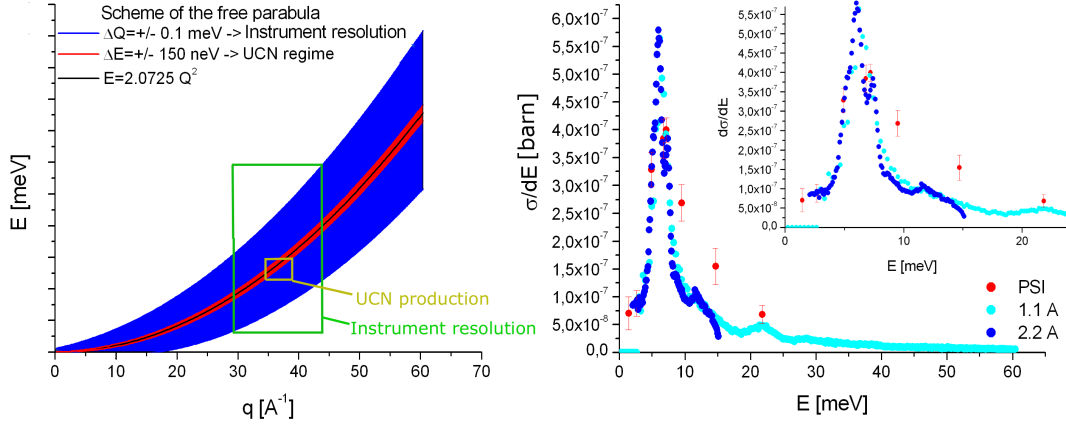


Figure 2.40: Left: scheme of the phase space correction. Right: the absolute UCN production cross section for incident cold neutrons and at the inlet for thermal neutrons. The red points are experimental values from the PSI [37]. The insert shows the extension of the energy range into the thermal neutron spectrum by an additional measurement at shorter wavelength

right hand side<sup>22</sup>. We also compare our results with measured down scattering cross sections [37]. Both show a remarkably well agreement in the energy range below 10 meV. Our data were measured with two different wavelengths ( $2.2 \text{ \AA} \rightarrow 0.15$  meV and  $1.1 \text{ \AA} \rightarrow 0.60$  meV) and are matched asymptotically in the overlapping region to cover the hole energy range.

By multiplying the production cross section with the cold neutron spectrum of a cold source it is possible to calculate the production rate  $P$  in solid deuterium for a given geometry.

For the *cubeD<sub>2</sub>* experiment at the cold beam MEPHISTO we know the beam cross section and the spectrum between 2..15 meV. The second integration over the UCN energy was already performed with the phase space correction factor. Afterwards we multiplied with the number of deuterium particles within  $1 \text{ cm}^3$  to get a predicted production value of  $P \approx 0.44 \text{ cm}^{-3} \text{ s}^{-1}$ . This method is now implemented in the IN4 software and will be used in the future to compare absolute values for converter materials and treatments of converters (e.g.  $\text{O}_2$ ,  $^4\text{He}$ ,  $\text{CD}_4$  [73]).

## 2.4.8 UCN up-scattering losses in deuterium

The use of inelastic neutron scattering and the dynamic structure factor shown in fig. 2.37 also provides a method to look on the energy gain side of the scattered neutrons. Any excitations on this side directly contribute to the UCN loss probability. Due to the low velocity and the large wave length, the UCN stay quite a long time ( $\mu$  s) inside the  $\text{D}_2$  crystal and every excitation leads to significant losses. In principle, at  $4\text{K}$  no excitation except the forbidden  $J = 1 \rightarrow J = 0$  transition should be occupied. Figure 2.41 left shows the intensity projection of the  $q$  values from the TOFTOF as

<sup>22</sup>E. Gutmiedl got similar results by taking the liquid data and the known production cross sections to normalize the solid data at 4 K. The density change have to be known in this case.

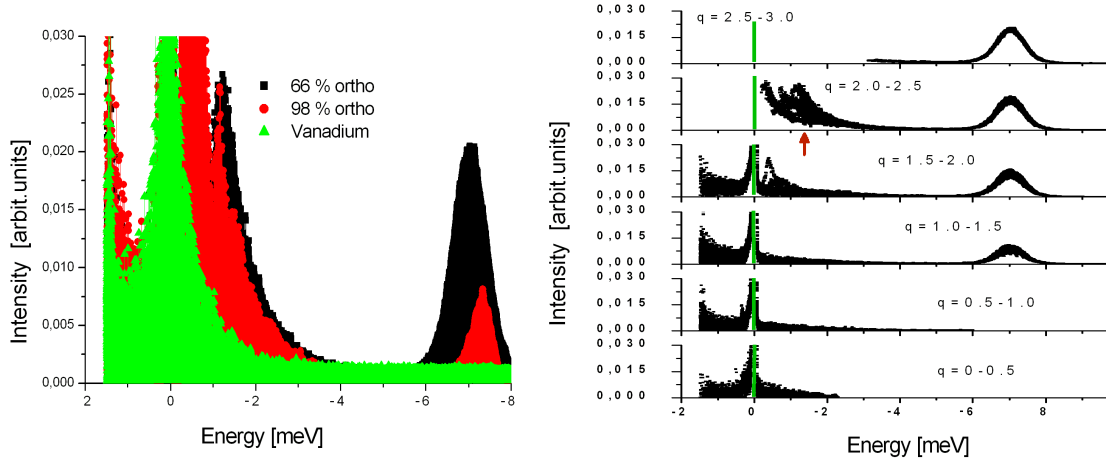


Figure 2.41: TOFTOF time of flight data on the neutron-energy-gain side of the neutron as function of the ortho concentration. Projection in the  $q$  space left and for different  $q$  value cuts on the right. For further explanation see text.

function of energy gain of the neutron ( $E < 0$ ).

We found an additional excitation at 1.8 meV, which was not expected. It is strongly localized at  $q \approx 2.1 \text{ \AA}^{-1}$  as shown in fig. 2.41, right. The excitation seems to be strongly correlated with the para concentration, which is at the -7.5 meV transition. The same behavior was seen in the IN4 data, but due to the limited instrument resolution it is just visible as a shoulder. From the complete data set, we can extract the Boltzmann like temperature dependence of the occupation, as shown in fig. 2.42 left-hand side. The strong coupling to the  $c_0$  was seen at both instruments. The insert of fig. 2.42 shows a color plot (intensity in linear scale) of  $S(q, \omega)$  to illustrate the  $q$  localization (x-axis) compared to the spin flip band structure below.

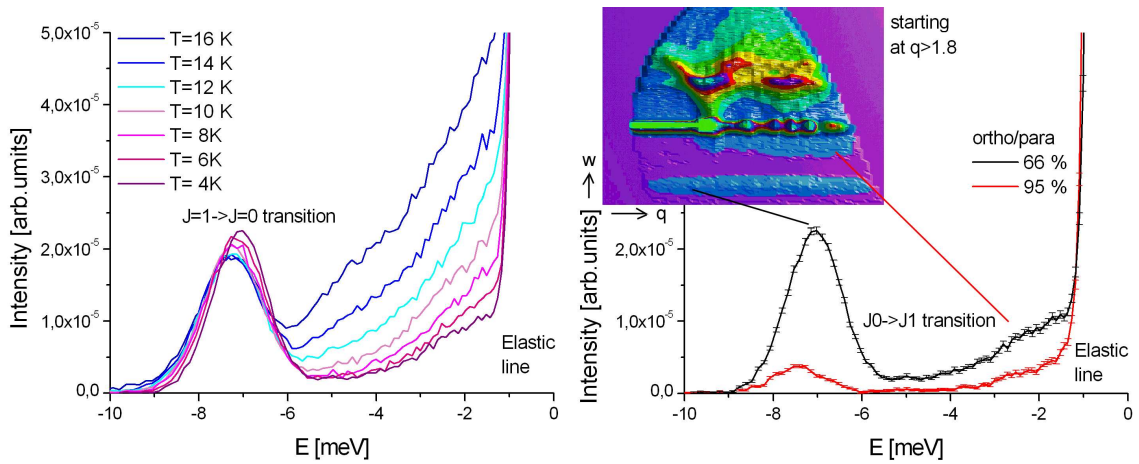


Figure 2.42: IN4 time of flight data for the neutron energy gain side for different temperatures and different  $c_0$  on the right-hand side. The projected  $S(q, \omega)$  insert shows the localization of the additional excitation in the  $q$  space.

## Cross section of the additional loss

For the natural  $c_o$  (fig. 2.43) we used three Gaussians to fit the  $E = -7.5$  meV,  $E = -1.8$  meV and elastic line at  $E = 0$  meV respectively. We know that the rotational excitation should contribute to the losses with a theoretical value at a neutron velocity of  $8 \text{ ms}^{-1}$  of  $\sigma_{J_1 \rightarrow J_0} = 31$  barn. This value has to be corrected for the UCN region,  $\bar{v}=3.4 \text{ ms}^{-1}$ . By comparing the different areas under the peaks we may get an estimate for the expected  $\sigma_x$  loss cross section at 1.8 meV. From our data we also made the assumption that the additional loss scales with the number of ortho particles. Thus, we correct for the number of ortho molecules compared to the number of para molecules responsible for the 7.5 meV peak area. Our result is 8.6 barn.

$$\sigma_x = \frac{2,064 \cdot 10^{-5}}{3,688 \cdot 10^{-5}} \cdot \frac{0.33}{0.66} \cdot 31 \text{ barn} \rightarrow 8.6 \text{ barn} \quad (2.33)$$

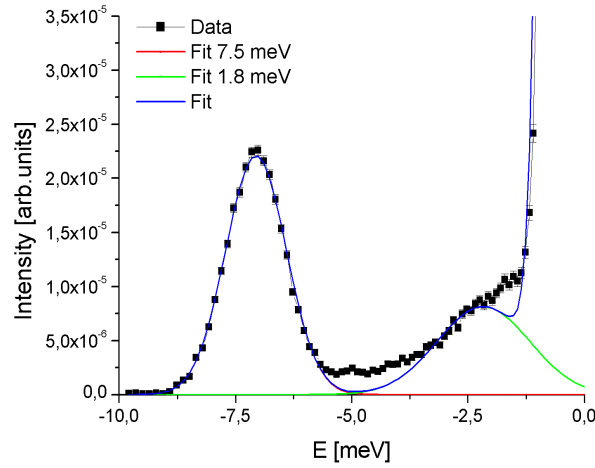


Figure 2.43: The additional excitation level for the normal ortho concentration together with a fit curve in blue. The fit consists of three Gauss functions corresponding to the rotational excitation  $E = 7.5$  meV the new excitation  $E = 1.8$  meV and the elastic line at  $E = 0$  meV

## Cross check

We try now to calculate from our data the cross section of the UCN loss channel  $\sigma_{\text{para}}$  due to the para-ortho spin flip. First we take the data from the 4 K deuterium sample with  $c_o=95\%$  and integrate the area under the -7.5 meV peak, the red curve in fig. 2.42 on the right side. Again we use eq. 2.28 and the interpretation of the reaction rate  $R_{\text{para}}$  as the area  $A_{\text{para}} = 5.31 \cdot 10^{-6}$  [arb.units] below the measured peak. This time there is no restriction on the available  $q$  values and thus the scattering covers all angles in the final state. Hence the area has to be corrected to correspond to a solid scattering angle of  $4\pi$ . Thus the area has to be expected to be a factor 20 times higher. On the other side (energy loss) we have already calculated the production cross section at 7.5 meV by the use of the correction factor  $K_{\text{ortho}}(7.5 \text{ meV}) = 5.026 \cdot 10^{-5}$  from eq.

2.40. Together with eq. 2.28, the correction factor corresponds to the product of the flux times the particle number  $N_{\text{ortho}}$ . Of course the 7.5 meV side scales with the ortho and the -7.5 meV side with the para ratio. Including the known  $c_o$  we can calculate now the expected spin flip loss cross section as follows:

$$\begin{aligned}
\sigma_{\text{para}} &= \frac{R_{\text{para}}}{N_{\text{para}} \cdot \Phi} \\
&= \frac{A_{\text{para}}(-7.5 \text{ meV}) \cdot 20}{N_{D_2} \cdot c_{\text{para}} \cdot \Phi} \\
&= \frac{A_{\text{para}}(-7.5 \text{ meV}) \cdot 20}{c_{\text{para}}/c_{\text{ortho}} \cdot K_{\text{ortho}}(7.5 \text{ meV})} \\
&= \frac{5.31 \cdot 10^{-6} \cdot 20}{0.05/0.95 \cdot 5.026 \cdot 10^{-5}} = 40 \text{ barn} \tag{2.34}
\end{aligned}$$

This fits within 30 % to the theoretical value of 31 barn published in ref. [28]. The presented model requires knowledge of the detector angle and the ortho para concentration. A similar method applied by E.Gutsmiedl uses our liquid  $S(q\omega)$  data and the well known liquid production cross section to get the required scaling factor. Afterwards he applies this factor on the  $S(q, \omega)$  data at 4 K. The prediction on the  $\sigma$  spinflip value is 33 barn (to be published).

### 2.4.9 Interpretation

A possible explanation of the roton and phonon coupling could be as follows. From Silvera [46], we know, that the para  $D_2$  molecules build an ellipsoid structure and need more space due to their quadrupole moment. This fits also well to our diffraction patterns. In addition we know that the quadrupole moment is rather strong and acts via 12 next neighbors to form somehow a super lattice of para molecules within the ortho lake. From Kranendonk, [61] we know that the quadrupole moment polarizes the neighboring ortho spheres. The quadrupole moment has to be described with a static and a dynamic part [61]. Our assumption is that also the dynamically part causes a dynamic induced fluctuation inside the ortho molecules. The resulting vibrational excitation is indicated at dark and fair green arrows in fig. 2.27. A change of a rotational excitations (para $\rightarrow$ ortho) releases  $\pm 7.5$  meV energy but also has to influence the ortho phonon system in the neighborhood (leading to the peak at 5.6 meV). In the opposite way for an excitation (ortho $\rightarrow$ para), compared to a cage effect also simultaneously phonons can be created, leading to the 12.4 meV peak.

## 2.5 UCN production results

The extended *cube* $D_2$  setup with the different sample cells (fig. 2.5) was used at the cold neutron beam Mephisto ( $\Phi_n = 1.52 \cdot 10^9 \text{ n cm}^{-2} \text{ s}^{-1}$ , measured by gold activation) at the FRMII. The goal was to measure the UCN production in deuterium varying several parameters, like  $D_2$  thickness, temperature, freezing procedure etc.<sup>23</sup>.

---

<sup>23</sup>Due to a later calibration of the used  $^3\text{He}$  UCN detector by Igor Altarev at the ILL the efficiency of 50% was considered in the following data.

## 2.5.1 UCN versus VCN

At first we will discuss the three methods to separate the UCN from the CN background from section 2.3.2. In fig. 2.44 the count rate with open foil shutter is shown in black (UCN plus VCN) and with closed shutter in red (just VCN). The difference, shown in green, are UCN. The left and right parts of fig. 2.3.2 plot show the count rate during cool down and warm up, respectively.

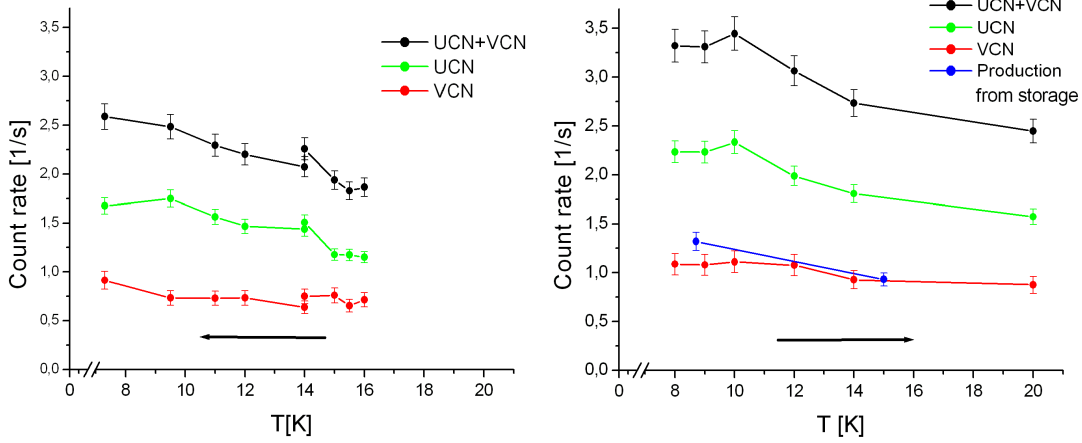


Figure 2.44: UCN-VCN count rates from the *cubeD<sub>2</sub>* test source. Shown are data for the three different schemes to separate a possible VCN background from the UCN events. Further explanation can be found in the text and at sec. 2.3.2. Shown are the statistical error bars. Left during cool down, right during warm up phases.

A ratio of  $0.654 \pm 0.13$  UCN/CN, almost independent of the temperature, was found by analyzing more than  $10^4$  UCN events from different source settings. This result is in good agreement with the ratio published at [68]. A possible spectral change in the UCN over VCN contribution with the converter temperature was not observed. In addition, two production values at 15 K and 8 K (fig. 2.44 right in blue) were estimated data taken from the storage method in the following way: the neutron count rate  $N_{\text{stored}}$  as function of filling time  $t_{\text{filling}}$  can be described with ( $t_{\text{stored}} = \text{const.}$ )

$$N_{\text{stored}} = P_0 \tau_1 (1 - e^{-\frac{t_{\text{filling}}}{\tau_1}}). \quad (2.35)$$

$\tau_1$  describes losses caused by the guide system (source to storage bottle) and is used to estimate the sufficient filling time ( $t_{\text{filling}} = 2 \cdot \tau_1$  [s]) to reach an equilibrium of UCN density between the production and the losses in the guide system (entrance valve open). The production rate  $P_0$  and  $\tau_1$  can be extracted from plotting the count rate versus filling time  $t_{\text{filling}}$  shown in fig. 2.45, left. Equation 2.36 describes the time development of the neutrons  $N_{\text{stored}}(t_{\text{stored}})$  ( $t_{\text{filling}} = \text{const.}$ )

$$N_{\text{stored}}(t_{\text{stored}}) = N_{\text{stored}}(t_{\text{stored}} = 0) \cdot e^{-t_{\text{stored}}/\tau_{\text{bottle}}}. \quad (2.36)$$

Besides the final proof of the production of UCN, the neutron lifetime  $\tau_{\text{bottle}}$  as a characteristic loss value for the 2 m NOKADO<sup>24</sup> storage volume was extracted from

<sup>24</sup>Nokado is a company which produces stainless steel tubes of fine quality by electro polishing for the food industry.

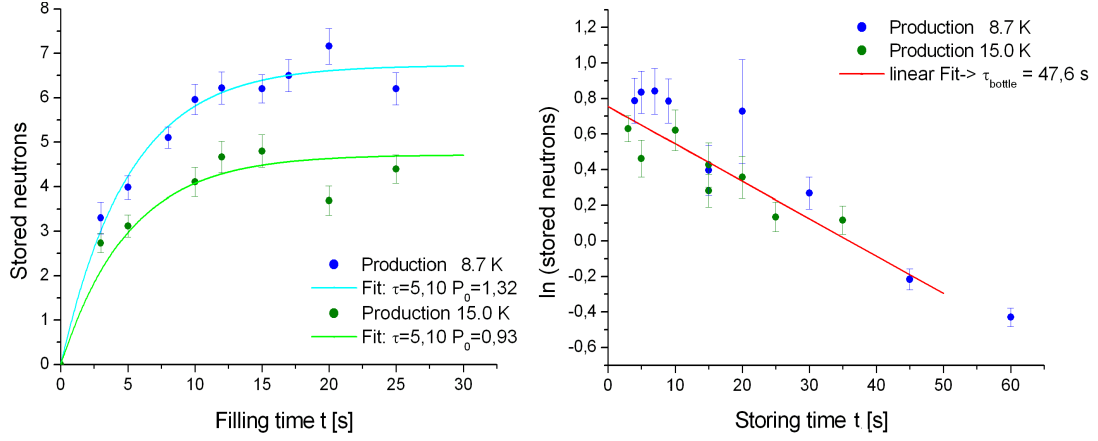


Figure 2.45: Left: variation of the filling time to get the production  $P$ . Right: variation of the storing time to get the loss probability  $\mu$  per bounce coefficient. Shown are the statistical error bars.

fig. 2.45, right. A value of  $\tau_{\text{bottle}} = 47.5$  s fits well to the values discussed in section 3 ( $\mu = 3 \cdot 10^{-4}$  with a Fermi potential of stainless steel and a cut-off velocity of  $4.5 \text{ ms}^{-1}$ ).

The three different methods (geometry, foil shutter and storage), in the order described, cut more and more into the UCN spectrum thus the discrepancy between them, shown in fig. 2.44, becomes understandable. Due to the fixed ratio UCN/CN we took the geometry method (black points) for the following UCN data.

## 2.5.2 UCN production in gaseous, liquid and solid $D_2$

The UCN count rate  $N_{\text{UCN}}(\text{gas})$  was measured for different deuterium-gas conditions. In a first measurement we changed the pressure between 175 and 1720 mbar and kept the temperature constant at 25 K. For the measurements with constant pressures of 300 mbar and 1000 mbar respectively we changed the temperature between  $\approx 40$  K and 130 K. In two additional measurements, both temperature and pressure were changed and the UCN production measured (fig. 2.46, left). All data were taken with the 3 cm sample cell. The ideal gas equation was used to calculate from the temperature, pressure and volume the number of deuterium molecules  $N(D_2)$  [mol] interacting with the collimated cold neutron beam  $A_{\text{beam}}$ .

Figure 2.46 shows the UCN count rate  $N_{\text{UCN}}$  as a function of  $N(D_2)$ . Together with the measured CN flux we calculated the scattering cross section  $\sigma_{\text{CN} \rightarrow \text{UCN}}$  using eq. 2.37. The expected loss rates from the extraction foil  $\eta_{\text{foil}} \approx 0.5$  and from simulations (*FRED* sec. 3.4)  $\eta_{\text{guide}} \approx 0.5$  in the UCN transport system to the detector have also been taken into account. We compare our result with a value from the PSI group [69], where the UCN production cross section for gaseous deuterium as a function of the incoming energy spectrum of the cold beam was given. The red cross corresponds to a 5 meV incident neutron spectrum similar to the MEPHISTO beam. The agreement confirms our estimation of the extraction losses.

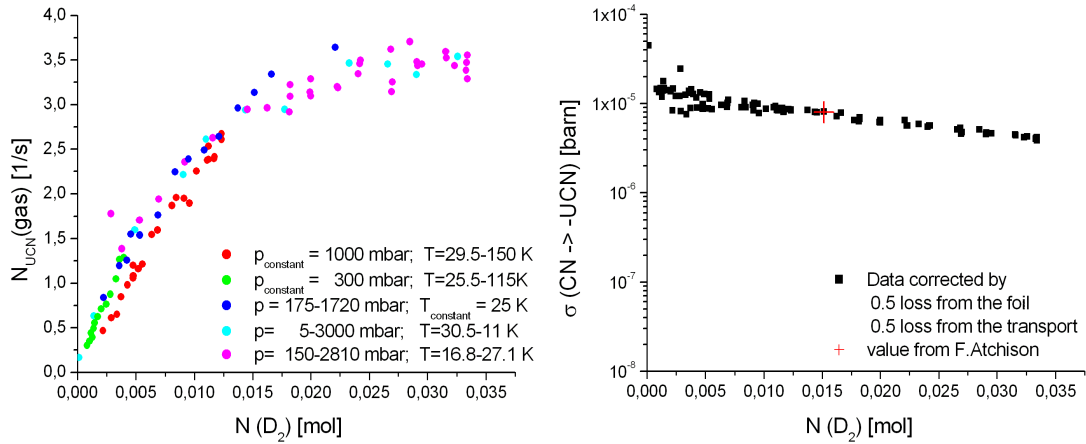


Figure 2.46: UCN count rate from deuterium gas under different conditions like isobar and isothermal together with the UCN count rate as function of deuterium particle number.

$$\sigma_{\text{CN} \rightarrow \text{UCN}} = \frac{N_{\text{UCN}}}{\Phi_{\text{CN}} A_{\text{beam}} N_{\text{D}_2} \eta_{\text{foil}} \eta_{\text{guide}}}. \quad (2.37)$$

Figure 2.47 shows the development of the UCN count rate for the two phase transitions from gas (green) to liquid (red) and from liquid to solid (black). In contrast to the expected gain factor of 10 due to the change in particle density from warm to cold gas<sup>25</sup>, we measured only a factor five between room temperature and 30 K. At first glance, it was surprising that the count rate saturates at 25 K. It seems that the gain caused by the increase in particle density from gas to liquid (factor 6.4) was somehow compensated. Due to this reason, the count rate was normalized to the transmitted cold neutron beam to include an attenuation of the cold neutron beam (elastic scattering). The result is shown on the left hand side. As can be seen, we got just a factor of two difference. In addition to the increased probability for elastic scattering of the CN beam, elastic scattering of the produced UCNs is also increasing with higher particle density. For our source geometry with completely transparent walls, just a forward cone out of the produced UCNs inside the deuterium volume is able to exit through the extraction system. In addition, within this cone, the cold neutron beam itself is degraded by elastic scattering. In the following analyzes only relative changes between liquid and different solids are discussed.

The drop in UCN count rate at 18.5 K may be explained with imperfect filling of the cell. The density increase at the phase transition from liquid to solid causes the  $\text{D}_2$  probe to shrink. The collimated CN beam is no longer completely covered by the solid  $\text{D}_2$  beam and the produced UCN count rate drops. From the cell geometries together with the calculated amount of deuterium, or the pictures from the webcam we may consider this effect in the range of 30%. After correction we get the expected asymptotic connection between liquid<sup>26</sup> and solid.

<sup>25</sup>Gas  $\rho_{\text{D}_2}(1 \text{ bar}, 300 \text{ K}) = 2.5 \text{ kg/m}^3$  ( $25 \text{ kg/m}^3$  at  $T=30 \text{ K}$ ) to liquid  $\rho_{\text{D}_2}(1 \text{ bar}, 20 \text{ K}) = 162.4 \text{ kg/m}^3$  [70].

<sup>26</sup>Another proof was to apply a second filling at the solid stage to have again 100% filling and the described effect disappeared.

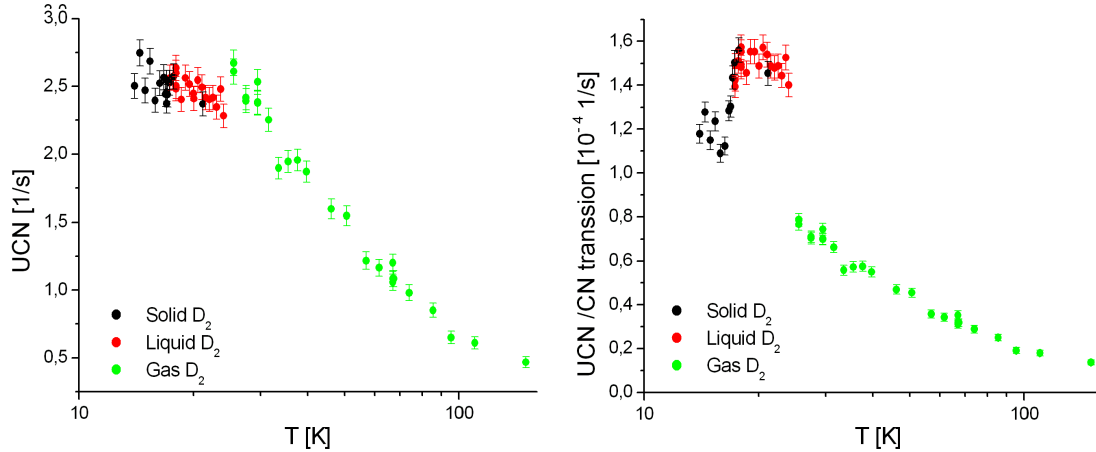


Figure 2.47: Left: UCN count rate as function of temperature during the phase transitions from gas to liquid and liquid to solid. Right: UCN counts normalized to the transmitted CN beam. Shown are the statistical error bars.

If we divide the cell thickness (30 mm) by the change in density by a factor of 6.5, we arrive at a lower limit on the ideal layer thickness for our special geometry (parallel incident cold beam and UCN extraction in the same direction as transmission) of 0.46 cm. This is a compromise between the ideal production and the extraction.

The count rate scaled to the transmitted CN flux is in good agreement with data from the PSI experiment at the FUNSPIN (target thickness 40 mm [71]) beam of  $\Phi_{\text{CN SINKQ}} = 4.5 \cdot 10^7 \text{ n cm}^{-2} \text{ s}^{-1}$ . The results do not reproduce a gain factor five between 20 and 18 K published by Serebrov et al. [72].

### 2.5.3 Effects of freezing and annealing

Figure 2.48 show the influence of the four freezing techniques and of temperature cycling (annealing) on the UCN count rate. Every annealing step (vertical green arrow) took about 10 h. Those from the slowly frozen sample and fast from the liquid are shown on the upper two plots and sublimated samples at 16 K and 10 K preparation temperature in the lower plots. The time sequence is always marked with green arrows. For the slowly prepared crystals annealing did not lead to significant changes<sup>27</sup>. In contrast to this result, the turbo solid crystal showed a 60% improvement. The samples grown from the gaseous showed an improvement of 30 – 40% after the first annealing. Subsequent temperature treatments at various temperatures did not increase the UCN output. Overall, we measured an increase of 73% between 18 K to 10 K, which is similar to the gain of 80% published by PSI [71] but far away from the factor 15 improvement reported by Serebrov [72].

From our model (cf. fig. 2.15), it seems that the size of the produced crystallites and thus the crystallization speed has an influence on the UCN extraction from the deuterium solid. Bigger crystals, as expected after slow freezing from the liquid, tend to

<sup>27</sup>The sample cells with 20 mm, 10 mm and 5 mm have all be filled by the slow freezing procedure from liquid and none of them showed a measurable effect due to annealing.

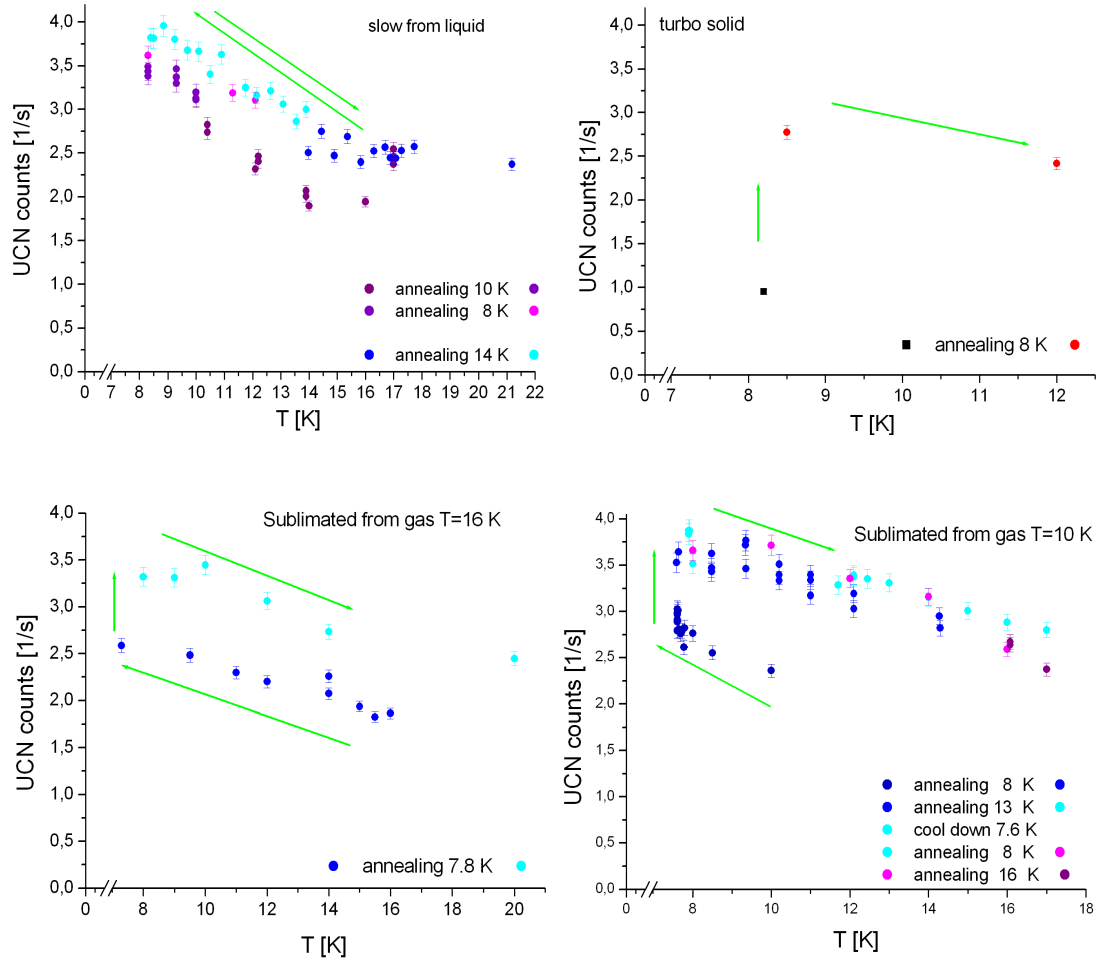


Figure 2.48: UCN count rate for upper left slow freezing from the liquid upper right turbo freezing; lower left re-sublimations at 16 K and lower right re-sublimated at 10 K. The time is indicated by green arrows, vertical arrows mark 10 h annealing. Shown are the statistical error bars.

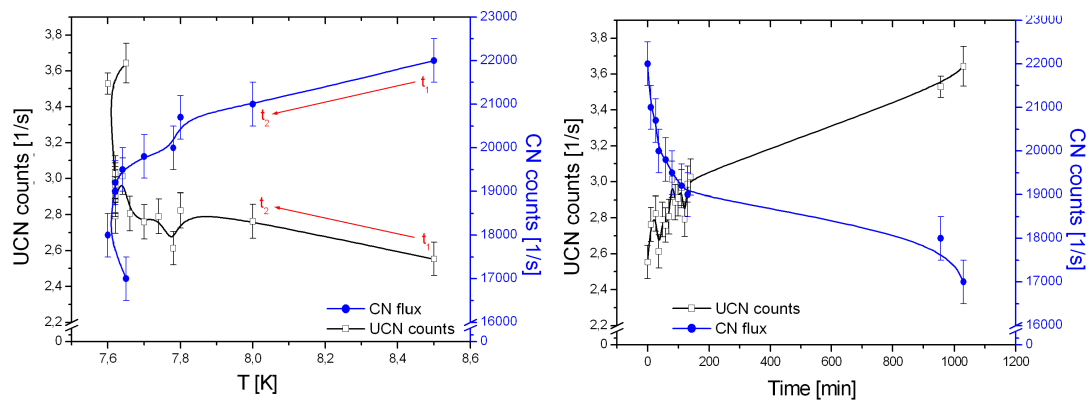


Figure 2.49: Left: time resolved annealing for the sublimated sample (10 K) visualized by the CN and UCN count rate for as function of temperature and right as function of holding time. Shown are the statistical error bars.

be better for extraction than the smaller crystals from the turbo solid . The latter may increase its crystal size by re-crystallization above an activation temperature with a positive impact on the UCN count rate; this could be an explanation for the improvement after annealing. The results with the sublimated gas sample are somewhere in between these two cases.

In fig. 2.49, the time-resolved annealing process for one re-sublimated solid sample is shown. On the left-hand side the UCN count rate and the rate of transmitted CNs rate is plotted as function of temperature and on the right as function of time. The changes in the CN beam intensity may be interpreted as changes of the sample in scattering probability due to structural changes which may occur with time. The UCN increase indicates a positive net effect. An influence on the production side is excluded from our  $S(q, \omega)$  data.

## 2.5.4 UCN production as function of ortho/para concentration

From the measured temperature dependent UCN count rate as function of the ortho concentration, it is possible to test the expected loss channels. The UCN count rate  $I_{\text{measured}}$  may be calculated from the production  $P \approx 0.44 \text{ cm}^{-3} \text{ s}^{-1}$  from section 2.4.7 times the deuterium volume seen by the beam  $V_{2 \text{ cm}}(\text{D}_2)$  (deuterium particle density  $n$ ). This value has to be corrected by transmission losses in the foil and the guiding system,  $\eta_{\text{guide}} = 0.5$  and  $\eta_{\text{foil}} = 0.5$  (estimated from simulations and cross checked in fig. 2.46). The internal losses inside the deuterium are now described by the exponential reduction factor.

$$I_{\text{measured}} = P \cdot V_{2 \text{ cm}}(\text{D}_2) \epsilon_{\text{guide}} \epsilon_{\text{foil}} \cdot e^{-x_{\text{active}} n \sigma_{\text{tot}}}$$

$x_{\text{active}}$  is a predicts an averaged active distance from the deuterium surface where the UCN can escape. The loss cross section  $\sigma_{\text{tot}}$  is then split into the known losses (from section 2.1) as function of temperature and ortho/para dependence [28] and an additional, unknown cross section  $\sigma_x$ . The known cross sections for absorption  $\sigma_{\text{abs D}_2} = 0.157$  [barn] and  $\sigma_{\text{para J1} \rightarrow 0} = 0.157$  [barn] as well as the temperature dependent  $\sigma_{\text{para}}(T)$  and  $\sigma_{\text{ortho}}(T)$  are taken from Liu [28].

$$\sigma_{\text{tot}} = \underbrace{c_{\text{para}}[\sigma_{\text{para J1} \rightarrow 0} + \sigma_{\text{para}}(T)] + \sigma_{\text{abs D}_2} + c_{\text{ortho}} \sigma_{\text{ortho}}(T)}_{\text{standard}} + \underbrace{\frac{1}{c_{\text{ortho}}} \sigma_{x_{\text{active}}}(T)}_{\text{added loss}} \quad (2.38)$$

From our previous results (fig. 2.41 and fig. 2.42) we expect  $\sigma_x$  to depend on the ortho concentration, indicated by the factor  $c_{\text{ortho}}^{-1}$ . From our data at 66%, 80% and 98% (shown in fig. 2.50 left), together with parabola fits, it is possible to find graphic solutions for  $\sigma_x(T)$  and  $x_{\text{active}}(T)$  from eq. 2.38<sup>28</sup> as crossing points of the different concentrations  $c_{\text{ortho}}$  and variation of  $x_{\text{active}} = 0.1 - 10 \text{ cm}$ .

The cross points for each temperature of  $\sigma_x(T)$  is shown on the right hand side side of fig. 2.50 together with an exponential fit. This could correspond to a Bose temperature

<sup>28</sup>Eq. 2.38 is rewritten as function of  $\sigma_x$  and plotted as function of  $x_{\text{active}}$  in the range of 0.1-5 cm.

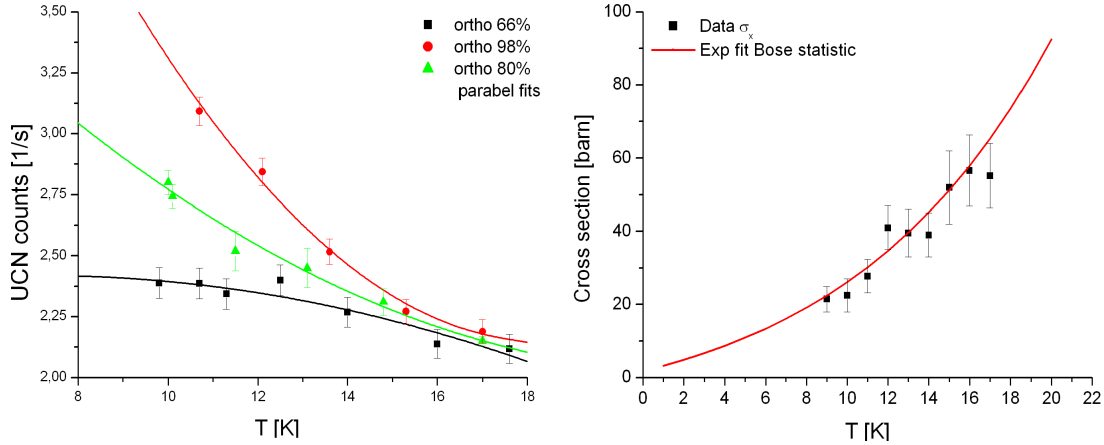


Figure 2.50: Left UCN count rate as function of temperature for different ortho/para ratios measured with the 20 mm cell and samples slowly grown from the liquid phase. Shown are the statistical error bars. Right: extraction of the necessary loss cross section to compare experimental with theoretical values.

occupation behavior like that measured for the additional excitation level from fig. 2.42. The loss cross section measured at an experiment can be derived from fig. 2.50 at the corresponding deuterium temperature divided by the ortho concentration of the experiment.

Experiment	$c_o$ [%]	T(D <sub>2</sub> ) [K]	$\sigma_x(\text{exp.})$ [barn]	$\sigma_x(\text{th.})$ [barn]
miniD <sub>2</sub>	98	4.5	8.5	9.5
cubeD <sub>2</sub>	98	10	21	21
LANSCE	98	4.5	8-9	9-10
PSI test	98.7	6	17	14

Table 2.3: Comparison of  $\sigma_x$  values estimated from three different UCN ( $v=3.4 \text{ ms}^{-1}$ ) production experiments from different deuterium solids. Data were taken from [36, 74].

This result also agrees well with the estimate from the IN4 data of 9.5 barn at 4 K from eq. 2.33. The average value for the active layer  $x_{\text{active}}$  from the fit was found to be  $1.1 \pm 0.4 \text{ cm}$ .

In table 2.3, our source setting and the setting of other UCN test sources are listed. The method of the additional loss cross section  $\sigma_x$  with its  $c_o$  dependence is used to predict the expected  $\sigma_x(\text{th})$  for other UCN sources. The value is compared with the measured misalignments between theory and experiment  $\sigma_x(\text{exp})$ .

From our storage measurements from fig. 2.45 we get also a measured value for the production rate. One has to mention that this value describes the number of UCN entering the guide system. That means that in this case  $P^*=1.34 \text{ UCN cm}^{-2}\text{s}^{-1}$  belongs to a surface source. Normalized to  $1 \text{ cm}^2$  and assuming an average production along the 3 cm length we get  $P=0.29 \text{ UCN cm}^{-3}\text{s}^{-1}$  (in this case the losses are already considered).

## 2.5.5 Cell thickness

Four different cells with a deuterium thickness of 30 mm, 20 mm, 10 mm and 5 mm exposed to the cold neutron beam of the FRMII to measure the UCN count rate as function of temperature and moderator thickness. In all cases, the samples were slowly frozen from the liquid. The data from the 20-mm cell was multiplied by 30% to correct for incomplete filling (section 2.5.2).

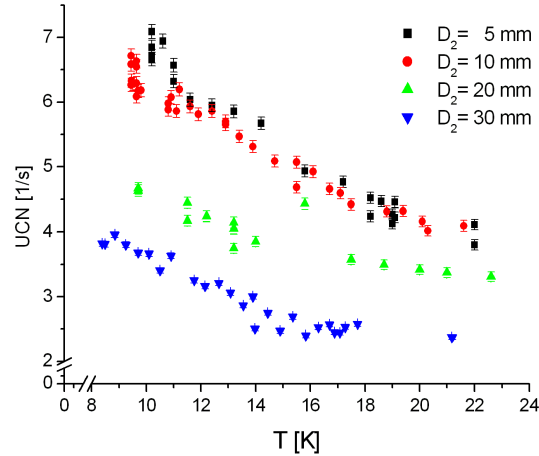


Figure 2.51: UCN count rate as function of temperature and deuterium thickness in the cold neutron beam. Data were taken with different target cells. Shown are the statistical error bars.

Figure 2.51 may be interpreted that the net production of UCN (within our source geometry) saturates at a deuterium thickness of the order of 5-10 mm. It seems that the effective UCN production thickness, for our UCN production from a collimated cold neutron beam in transmission is around 1 cm. A count rate of 7 UCN s<sup>-1</sup> was reproducibly achieved.

## 2.6 miniD<sub>2</sub> converter

Based on the results obtained from the presented measurements a new design of the miniD<sub>2</sub> source for ultra cold neutrons was developed (cf. fig. 2.53). It is specially designed to fit into the tangential, through-going beam tube SR6 of the FRMII. A schematic view may be seen in fig. 2.52.

Converter (deuterium), moderator (hydrogen) and cooling system (with supercritical helium) are all from one side supplied. Thus, the complete tube diameter on the opposite side is available for UCN extraction. On a scale of a few ten centimeters, the source position will be flexible inside the tube to find the best distance to the fuel element and an optimum compromise between the thermal neutron flux and heating input.

Thermal neutrons penetrating the source from all directions are transmitted almost lossless inside the deuterium layer. After down scattering inside the solid hydrogen

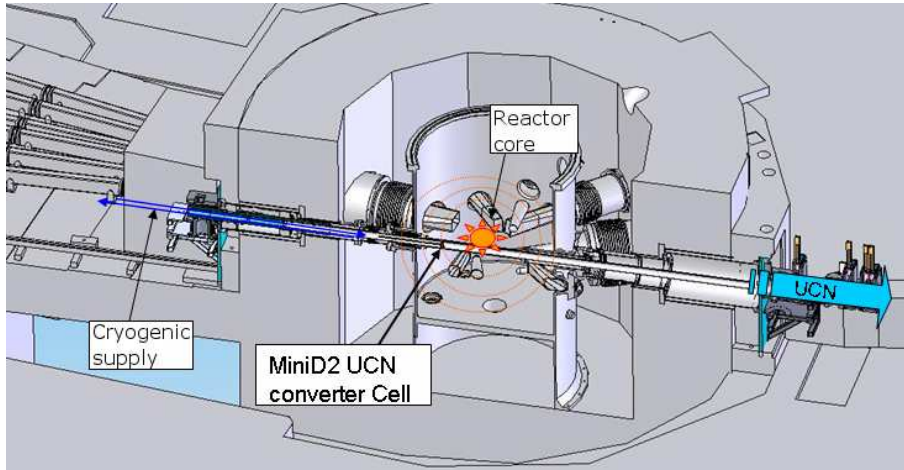


Figure 2.52: Scheme of the FRMII reactor building showing the location of the planned UCN source  $miniD_2$  and the UCN extraction direction.

frozen in the inner shell most cold neutrons have to pass the deuterium frozen on the outside surface of the donut skin. With its high probability to be scattered into the UCN energy region they will escape through the large surface area into the UCN guide. Both layers are cooled by liquid He flushed steadily in between (maximum cooling efficiency). The large deuterium surface leads to a high probability to extract the UCN into the UCN guide.

The concept described above has the following advantages:

- flexible deuterium thickness  $\rightarrow$  variable UCN flight path inside the converter material
- flexible hydrogen thickness  $\rightarrow$  tunable cold neutron spectra
- simple cooling circle  $\rightarrow$  only one He cooling cycle/large contact surface
- highly effective cold spectrum  $\rightarrow$  ideal solid angle between CN flux and UCN converter
- freezing on the outer shell  $\rightarrow$  close to maximum extraction area/tube diameter
- compact source  $\rightarrow$  source position variable in the SR6 tube
- support from opposite direction  $\rightarrow$  whole UCN guide diameter used for extraction
- possible use as VCN or CN source

## 2.7 Conclusion

We learned a lot about freezing and handling deuterium in the laboratory as well as the reactor environment. A systematic study of the structure and the dynamics was performed by inelastic neutron scattering. As a result, we were able to show that the production should not depend on the deuterium preparation. A method to compare different converter materials, by integrating over the free neutron parabola in  $S(q, \omega)$ , was developed. It was also possible to study the UCN loss sector from the  $S(q, \omega)$  data. An additional spin dependent loss channel could be identified and compared with different production experiments. The  $cubeD_2$  experiment lead to first UCN production at the FRMII and informations on the conversion efficiency as function of

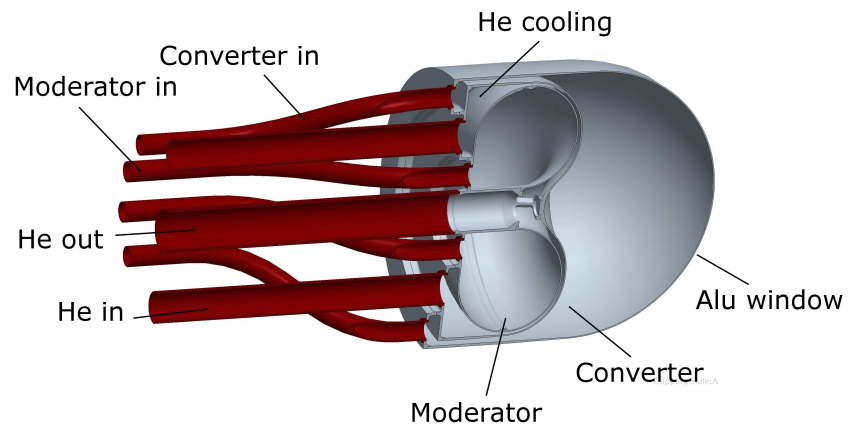


Figure 2.53: Scheme of a new concept for the miniD<sub>2</sub> UCN source at the FRMII. The cold neutron CN moderator is frozen inside, the ultra cold neutron UCN converter outside of the donut shape.

different deuterium parameters. Finally, a new concept for the new FRMII UCN source was developed based on the results.



# Chapter 3

## UCN guides

Efficient guiding of ultra cold neutrons (UCN) from source to experiment is crucial for all experiments using UCN. The transport of UCNs through guides depends mainly on two physical properties: the loss probability per wall collision  $\mu$  and the probability  $f$  for diffuse scattering from the wall. In the past it was popular to use stainless steel tubes as UCN guides as they are commercially available and rather easily adapted to the experimental requirements. Tubes have good transport properties for UCN when their inner surface is of fine quality. This low roughness can be achieved by mechanically polishing (sapphire [75]), by replica technique [76] or by electro polishing. Further improvement were achieved by coating the inner tube surface with weakly absorbing materials of high Fermi potential, like beryllium [77], nickel or diamond-like carbon(DLC) [78, 79]. In our case, where the tubes should be used at the high-radioactivity environment close to the FRMII neutron source leads to additional requirements limiting the number of possible materials. For this reason surface coatings on aluminum tubes have been developed.

At room temperature a significant portion of the UCN losses may be caused by incoherent up-scattering, which should be reduced with decreasing temperature. However, up to now an essential part of the losses can not be explained, neither by absorption nor by up-scattering and they are defined as "anomalously high losses". So far no commonly accepted model exists for their explanation [80].

A correct comparison of specially coated tubes should involve the determination of the two essential parameters  $\mu$  and  $f$ <sup>1</sup>. In this chapter the "*storage method*" [81] is presented to estimate  $\mu$  for a sample tube.

Our completion [80] of an alternative method "*two hole technique*" or "*constant flow method*" [81] to estimate  $\mu$  and  $f$  simultaneous is introduced next. Afterwards experimental values extracted from both methods for a 2 m electro polished stainless steel tube will be used to compare both methods. The latter was then used to get information on the temperature dependence of  $\mu(T)$  and  $f(T)$  for aluminum tubes with stainless steel, stainless steel plus beryllium coating, for a raw and electro polished stainless steel tube (the tubes have been coated by I. Altarev). In addition, the influence of different temperatures and of discharge cleaning was tested. The results will be presented and discussed. UCN transport was simulated using the "FRED" software to estimate the diffuse scattering probability.

---

<sup>1</sup>For the definition of  $f$  the assumption is made that the scattering process can be split into a spectral and a diffuse part. It is just an approximation of the far more complicated real neutron-surface interaction.

### 3.1 Methods to evaluate the transmission probability of UCN guides

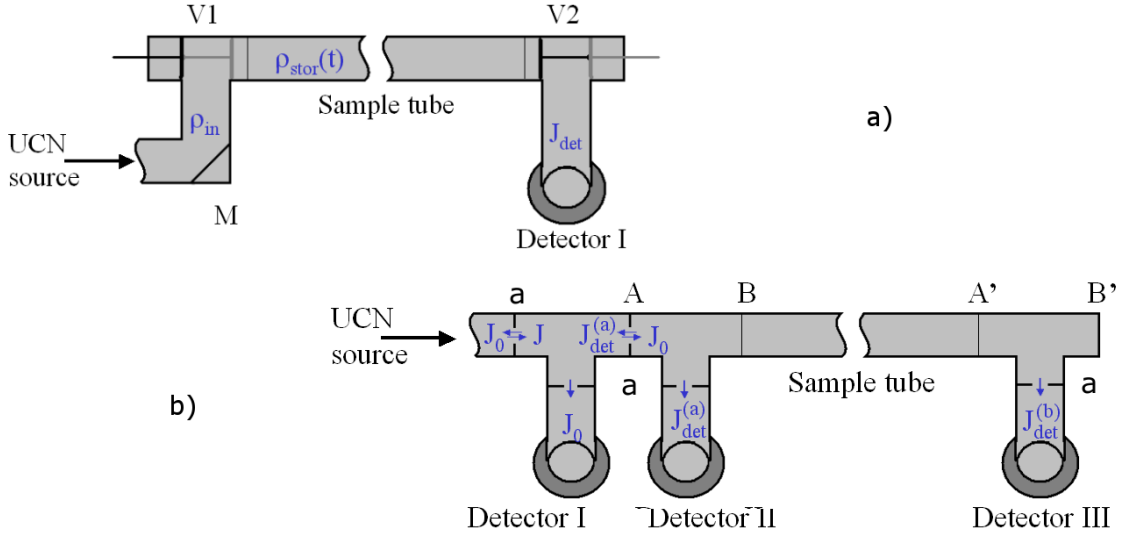


Figure 3.1: Top scheme of a) the storage method and b) below two hole method b) to characterize UCN guides by estimating  $\mu$  in the first case,  $\mu$  and  $f$  in the second case.

#### 3.1.1 The storage method

##### Theorie

In the *storage method* (fig. 3.1 a)) the change of the UCN density  $\rho_{\text{sample}}$  inside the sample tube as function of time  $t$  is measured. After a sufficient filling time  $t_{\text{filling}}$  with valve V1 open and valve V2 closed the UCN density reaches an equilibrium between number  $P$  of UCN entering from the source (production) and the losses caused by i) UCN leaving the volume through the open valve V1 and ii) UCN lost by wall collisions. The total losses can be described by a mean lifetime  $\tau$ . After V1 is closed (with only wall losses) UCN are stored for a certain time  $t_{\text{stor}}$ . Because the production drops to zero the decrease of the UCN density  $\rho_{\text{sample}}$  can be described by the following equation [8].

$$\underbrace{\frac{d\rho_{\text{sample}}}{dt}}_{dt \rightarrow dt_{\text{stor}}} = \underbrace{P}_{P \rightarrow 0} - \underbrace{\frac{\rho_{\text{sample}}}{\tau}}_{\tau \rightarrow \tau_{\text{loss}}} \quad (3.1)$$

The number of surviving neutrons  $N_{\text{stor}}(t_{\text{stor}})$  after different time periods  $t_{\text{stor}}$  are counted when V2 is open. Equation 3.1 can be multiplied by the storage volume  $V_{\text{stor}} = V_{\text{sample}}$ . The loss life time for short storage times is related to the loss probability per wall collision, which can be calculated using kinetic gas theory. The equations for the mean free path can be approximated  $\lambda_{UCN} = 4 V_{\text{stor}}/A_{\text{stor}}$  and the mean velocity  $\bar{v} = \lambda_{UCN}/\tau_{\text{loss}}$  where used. The surface  $A_{\text{stor}}$  is split into the cylinder surface  $S_{\text{sample}}$  weighted with the loss probability  $\mu$  and twice an unknown area  $h$  corresponding to the losses at the closed valves with absolute loss probability  $\mu_{V1,V2} := 1$  (black area).

Both valves are assumed to be identical with the short storage times used ( $< 100$  s) the decay lifetime  $\tau_n \approx 874$  s has no significant influence.

$$\frac{d\rho_{\text{sample}}}{dt_{\text{stor}}} = -\rho_{\text{sample}} \frac{\bar{v}}{4V_{\text{sample}}} \left( \mu \cdot S_{\text{sample}} + \underbrace{1}_{\mu_{V1}} \cdot h + \underbrace{1}_{\mu_{V2}} \cdot h \right) \quad (3.2)$$

This differential equation is solved by eq. 3.3 which describes the development of the UCN density. After translating to absolute neutron numbers with the initial amount of neutrons  $N_0$  this equation can be used to get  $\mu$  from a set of measurements (e.g. with different sample length).

$$\rho_{\text{sample}}(t_{\text{stor}}) = \rho_0 \cdot e^{-\frac{t_{\text{stor}}}{\tau_{\text{loss}}}} \Leftrightarrow N_{\text{sample}}(t_{\text{stor}}) = N_0 \cdot e^{-\frac{t_{\text{stor}}}{\tau_{\text{loss}}}} \quad (3.3)$$

Using eq. 3.2 and eq. 3.3 leads to the final equation eq. 3.4. The lifetime  $\tau_{\text{loss}}$  is extracted as the slope of the number measured stored neutrons on a logarithmic scale as function of storage time  $t_{\text{stor}}$ . This model was derived from discussions with Igor Altarev [86]. The  $\mu$  value of the sample tube can be measured by this method. The value of  $f$  is not directly extracted but can be extracted, from simulations, as shown later.

$$\frac{1}{\tau_{\text{loss}}} = \frac{\bar{v}}{4V_{\text{sample}}} \cdot (\mu \cdot S_{\text{sample}} + 2 \cdot h) \quad (3.4)$$

In our case we assume an energy independent wall loss coefficient  $\mu$ .

## UCN valves

A scheme of our UCN valves is shown in its open position in fig. 3.2.

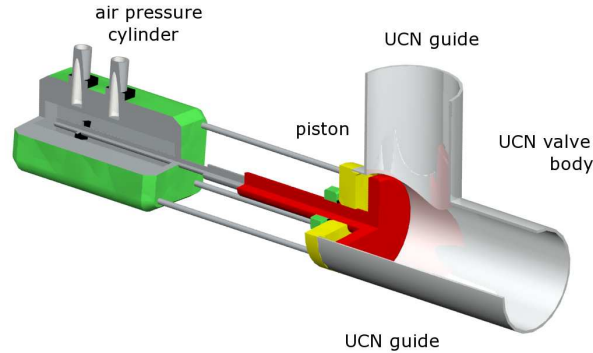


Figure 3.2: Scheme of the UCN valve in open position. The red piston is moved to the left when the UCN valve is closed.

The valves are machined from stainless steel cylinders. The inner diameter of  $\varnothing$  66 mm was selected to fit to the standard Nocado tubes [82] used in our group. The inner surface, which is a part of the UCN guiding system has been cleaned in an ultrasonic bath (with distilled water plus alcohol) and electro polished [83]. The two valves were also used in the *cubeD<sub>2</sub>* experiment and in the *Abex* experiment<sup>2</sup> [108].

### 3.1.2 The two hole method

A detailed introduction of the theory of the *twoholemethod* is given in the appendix section 10.3 or by 3.1.2. How the loss probability  $\mu$  and the diffuse scattering factor  $f$  is extracted from the setup shown in fig. 3.1 is explained there in more detail.

## 3.2 Sample tubes

### 3.2.1 Samples for UCN valve characterization

Tubes of different length  $l_{\text{sample}}$  from stainless steel (Nokado)<sup>3</sup> with inner  $\varnothing$  66 mm and  $\varnothing$  70 mm outer diameter were used for the *storage method* (section 3.1.1) to measure the amount of stored neutrons as function of storing time and storing volume  $N_{\text{sample}}(t_{\text{storing}}, V_{\text{sample}}(l_{\text{sample}}))$ . The length of the tubes were:

$$l_{\text{sample}} = 200 \text{ mm}, 400 \text{ mm}, 800 \text{ mm}, 1300 \text{ mm}, 2000 \text{ mm}$$

We can extract the loss lifetime  $\tau_{\text{loss}}(l_{\text{sample}})$  as function of length from eq. 3.3 and afterwards with the help of eq. 3.4 the values  $\mu$  and  $h$ .

### 3.2.2 Possible UCN guide materials

In order to evaluate possible UCN guides for the *miniD<sub>2</sub>* UCN source at the FRMII the values  $\mu$  and  $f$  have been measured for the following 2 m sample tubes with the *two hole method* sec. 3.1.2. From the data of the 2 m long samples it may be possible to address the questions listed in table 3.1.

The coated aluminum tubes were prepared at a dedicated and unique sputtering facility which permits the inside coating of tubes. Not only single layers can be produced but also multi-layers of suitable materials are feasible. Two aluminum tubes were coated with 500 nm stainless steel,  $V_{\text{Fermi Fe}} = 180 \text{ neV}$ , before one tube got an additional layer of 250 nm Be  $V_{\text{Fermi Be}} = 250 \text{ neV}$  [85]. The aluminum tubes had inner diameter of 57.2 mm.

---

<sup>2</sup>Experiment to estimate the absorption efficiency of different absorber materials for the later *PENeLOPE* lifetime experiment as function of temperature inside a UCN storage vessel.

<sup>3</sup>Nokado tubes of Hygieneklasse4 have electropolished inner surface and are up to now commonly used tubes for standard applications as UCN guides at experiments from TUM, PSI and ILL.

	raw st. st.	el.pol.st. st.	st.st. on Al	Be on st.st. on Al
roughness	x	x	-	-
coating	-	-	x	x
wall potential	-	x	-	x

Table 3.1: Different samples prepared for the *two hole method* to measure  $\mu$  and  $f$  values to evaluate their guide properties.

### 3.2.3 Electro polishing and discharge cleaning

An introduction about electropolishing and discharge cleaning is given in the appendix section 10.4. The different surface effects are listed together with the possible influence on their use to improve the properties of UCN guides. Some of the described information will be used for the interpretation on our data.

## 3.3 Beam measurements

The data presented on the following pages were taken during a beam time 2006 at the "beam PF2-test" at the UCN turbine of the research reactor ILL, in Grenoble, France. The results were then compared with the tube characterization measurements performed at the *cubeD<sub>2</sub>* UCN source at FRMII.

### 3.3.1 "UCN valve" and "storage method results"

The number of stored neutrons  $N$  as a function of  $t_{\text{stor}}$  and sample length  $l_{\text{sample}}$  is shown in fig. 3.3. The data have been corrected for the leakage through the closed valves and the dark count rate. The first one was estimated from the ratio between the count rate for open and for closed valves to be about 3 %, the later from the count rate with the shutter between source and experiment closed.

Equation eq. 3.3 can be written in the following way:

$$\ln\left(\frac{N}{N_0} \cdot \frac{1}{\tau_{\text{loss}}}\right) = -\frac{t_{\text{stor}}}{\tau_{\text{loss}}}$$

$$\ln(N) = -\frac{1}{\tau_{\text{loss}}} \cdot t_{\text{stor}} - \ln(N_0 \cdot \tau_{\text{loss}}) \quad (3.5)$$

The loss time  $\tau_{\text{loss}}$  for the sample is the negative reciprocal slope from fig. 3.3 (eq. 3.5) when the counted, stored, neutrons are plot on a logarithmic scale for the different storing times. The linear fit to extract this slope is also shown in the fig. 3.3 right.

$$\ln(N) = a + b \cdot t_{\text{stor}} \quad (3.6)$$

$$\rightarrow -\frac{1}{\tau_{\text{loss}}} = b \quad (3.7)$$

The calculated  $\tau_{\text{loss}}$  as function of  $l_{\text{sample}}$  is shown in fig. 3.4 together with a rational fit function with the fit parameter A and B.

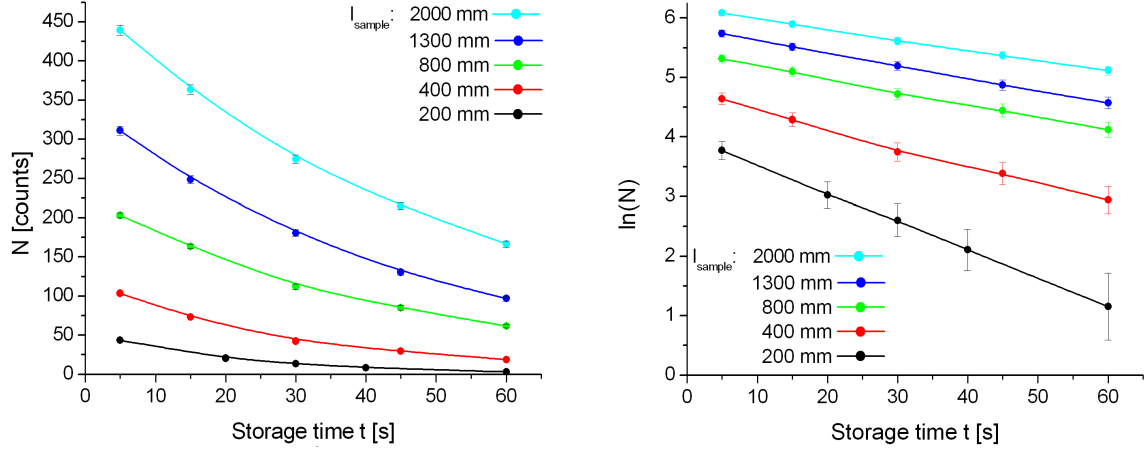


Figure 3.3: Left: the corrected count rates as function of storage time and sample length. Right: the logarithmic plot to extract the corresponding lifetimes  $\tau_{\text{loss}}$ . Full lines are used to guide the eye.

$$\tau_{\text{loss}} = \frac{4\pi r_{\text{sample}}^2 l_{\text{sample}}}{\bar{v}(2\pi r_{\text{sample}} \mu l_{\text{sample}} + 2h)} = \frac{B \cdot l_{\text{sample}}}{A + l_{\text{sample}}}$$

From eq. 3.4 we get the correlation between A and B and the wanted  $\mu$  and  $h$  value. But we also need an assumption on the mean velocity<sup>4</sup> for our setup of  $\bar{v} = 4.5 \text{ ms}^{-1}$ . From our measurements we got a  $\mu = 2.18 \pm 0.34 \cdot 10^{-4}$  for the Nokado tube and for the black surface of the valves  $h=0.99 \pm 0.14 \text{ cm}^2$ .

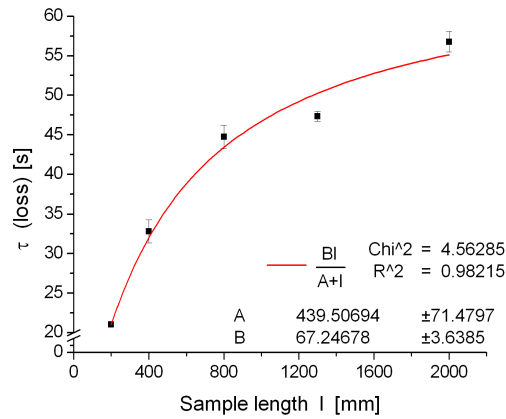


Figure 3.4: Calculated  $\tau_{\text{loss}}$  as function of sample length together with the fit to get the  $\mu$  and  $h$  value.

<sup>4</sup>Turbine spectrum corrected by the energy loss due to the height of the sample tube and the steel Fermi potential cut off  $v_{\text{max}} = 5.44 \text{ ms}^{-1}$ . The mean velocity assuming a Maxwellian like distribution is the calculated  $\bar{v} = 4.5 \text{ ms}^{-1}$ .

### 3.3.2 Surface roughness, machined versus electro polished

In the following subsections the data of our measurements are presented. The results for the different materials used as well as the temperature dependence of the transmission probability will then be used to discuss possible reasons. The results for  $f$  and  $\mu$  for different surface roughness; due to different stainless steel surface treatments, are shown in fig. 3.5 A) and B). This may be seen as the surface roughness after electro polishing (section 10.4.1) may be related to the probability for diffuse scattering  $f$  of UCN. Assuming a typical finishing process for the normal stainless steel tube of  $\leq \approx 1.14 \mu\text{m}$  (polished Nr.4 table 10.2) and comparing this value with the surface roughness of  $\leq 0.13 \mu\text{m}$  expected from an electro polished tube like Nokado (polished Nr.8 table 10.2) leads to an improvement by a factor of eight. This is in extremely good agreement with our experimental value from fig. 3.5 B).

No temperature dependence off was observed.

The difference in shown in fig. 3.5 A) may be correlated with the higher amount of impurities inside the rough structure as well as the change in the chemical composition of the surface (section 10.4.1).

### 3.3.3 Efficiency of discharge cleaning

The numbers on the plot in fig. 3.5 indicate the history of the data points. Between 1 and 2 room temperature and between 4 and 5 low temperature discharge cleaning was applied. The other numbers are values measured after cooling or heating periods. Some progress, (far from the expected factor of 10 published by Ignatovitch [?]) was achieved due to impurity reduction at the stainless steel surface. The situation even increases for the electro polished surface indicated as increase of the loss coefficient. Up to now the reason is not clear. A failure of the realization of the cleaning method (impurities inside the Ar gas for example, sputtering of impurities released during breakthroughs on the surface) is one possibility. An additional ground electrode like the one used in [91] to get controlled breakthrough was not installed. Comparing the two applied cleaning methods electropolishing (fig. 10.2 left) (work piece as anode) and discharge cleaning (fig. 10.4) (work piece as cathode), one notices that the applied electric potential is reversed. The first process leads to the growth of an oxide surface layer whereas the second one can be used for its reduction. This could be another explanation for our measured increase in  $\mu$  for the electropolished tube after discharge cleaning.

Both samples show the same very low temperature behavior. We can compare our results with experimental values and theory of Korobkina [92], where  $\mu(T)$  for a copper surface was studied. They were able to explain the decrease of the loss coefficient  $\mu$  from  $2.5 \cdot 10_{T=300\text{ K}}^{-4} \rightarrow 0.5 \cdot 10_{T=100\text{ K}}^{-4}$  with the up-scattering probability (described by the ice phonon density of state) of water molecules or clusters on the surface. Due to our effort to reduce this water concentration by pumping, heating, discharge cleaning, electropolishing and cooling (indirect cooling by double wall cryostat) one may not expect any temperature effect in agreement with our data of  $\mu = 3.1 \cdot 10_{T=300\text{ K}}^{-4} \rightarrow 2.2 \cdot 10_{T=100\text{ K}}^{-4}$ .

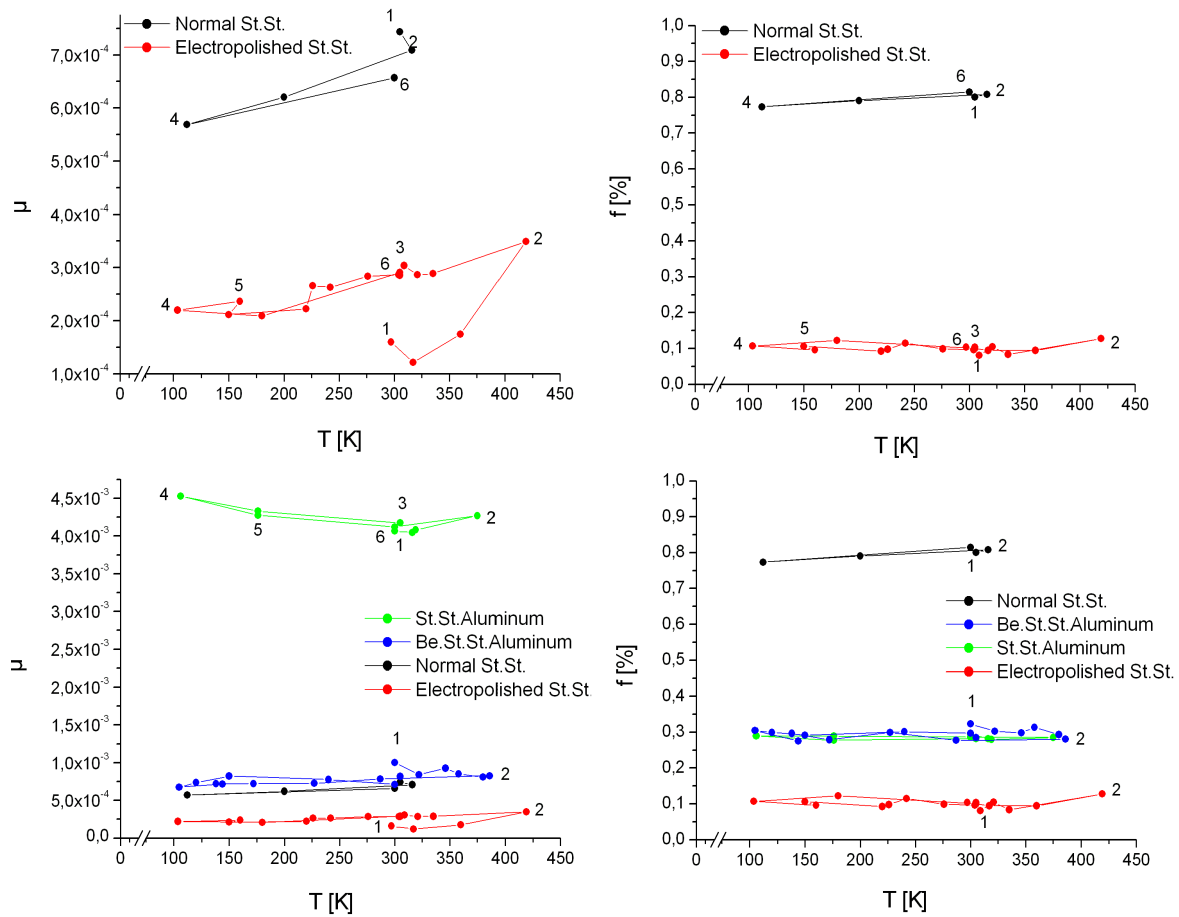


Figure 3.5: Left: experimental  $\mu$  value for the 2 m Nokado UCN guide and the coated aluminum tubes. Right:  $f$  value measured with the *two hole method*.

### 3.3.4 Different wall coatings on aluminum tubes

The temperature dependence of  $f$  and  $\mu$  for different coatings with large Fermi potential coatings in aluminum tubes is shown in fig. 3.5 C) and D). Obviously the same substrate roughness leads after sputtering to the same  $f$  value. The absence of any temperature dependence was explained before. The factor four difference of the  $\mu$  values can be used as an indication for the imperfectness of the sputtered surface layer. Holes in the St.St. coating directly on Al leads to losses due to the small Fermi potential of Al whereas holes at the Be plus St.St. on Al sample, the neutrons are still reflected by the underlying st.st. layer. The absence of a temperature effect may be explained also by the absence of surface water.

### 3.3.5 Temperature dependence

The coating of surfaces with gases like oxygen or nitrogen leads to a low-pass or high-pass filter for the phonons of the metal substrate [54]. If the electro polishing process creates an oxygen layer (from the electro polishing process) (discussed in section 10.4.1) and in fig. 10.3 this could be an additional explanation of the absence of any temperature behavior for our electropolished tube as well as other experimental data like these from [92]. Phonons are reflected on the inside of the surface layer and are not seen by the ultracold neutrons reflected from the other side. The occupation of the phonon states and thus the material temperature has no influence on the up scattering loss rate. The expected increase by a factor of ten by cooling the guides, as well as the expected factor ten from discharge cleaning could not be seen.

## 3.4 UCN transport simulation

The ray tracing program *FRED* [94] was used for UCN transport simulations. A big advantage of this program is that it works with step files from 3D construction programs like Solid Works or Pro Engineer.

Figure. 3.6 shows a screen shot of the *FRED* software. The tool bar with the parameters characterizing the surface, source and interaction properties is shown on the left side. The surface interaction between four UCNs emitted by a source part in yellow and two plates shown in fair blue was used to get the right settings of the software to correspond to UCN wall interactions. In the case shown the source emitted four UCNs with a fixed angle. The properties of the two plates were set to  $f = 50\%$  specular reflection and  $\mu = 0.5$ . For better visualization, the red rays change to green ones after a diffuse reflection. Absorbed UCN are shown as blue lines transmitted through the walls. Broken lines indicate UCN trajectories which out further interactions. With all important properties included<sup>5</sup>, the software was then used for some preliminary tests.

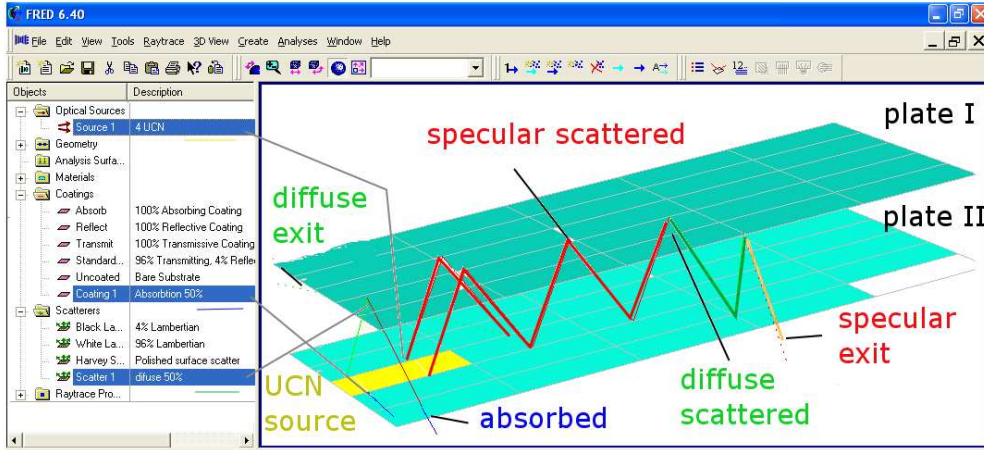


Figure 3.6: Screen shot of the *FRED* software used for the simulation of UCN transport. Four UCNs are emitted from the yellow source. The properties of the plates have been set to 50 % specular reflection and 50 % loss probability.

### 3.4.1 The U shaped baffle

An U shaped baffle (fig. 3.7), usually used to separate cold neutrons (too high energy for reflection) from ultracold neutrons, was used for some consistency checks of the simulation. The transmission of UCNs starting from an otherwise absorbing source ( $\phi$  20 mm) on the left side through the structure and towards the black absorbing detector on the right was studied as function of  $\mu$  and  $f$ . For the simulation the dimensions and diameter of the *cubeD<sub>2</sub>* experiment ( $d_{\text{tube}} = 66$  mm) were used.

In fig. 3.8, left the transmission probability was calculated for  $f = 10$  %, 20 % and 30 %. The loss probability per bounce in this case was taken into account through the limitation on the total number of wall collisions (shown by the different colours). It

<sup>5</sup>The effect of gravity can be included in the FRED calculation but it was not, at the presented data.

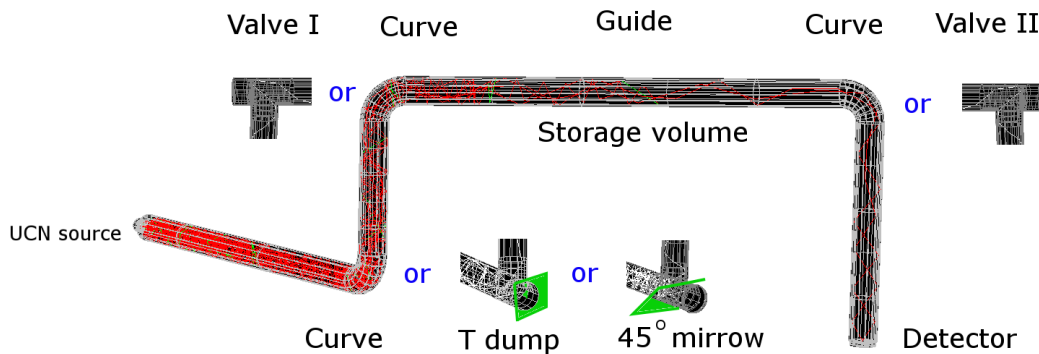


Figure 3.7: U shaped baffle for UCN transport simulation corresponding to the *cubeD<sub>2</sub>* geometry. The curve pieces can be replaced by valves and mirror pieces to get the dump mode, mirror mode and valve mode realized during the beam time at the FRMII.

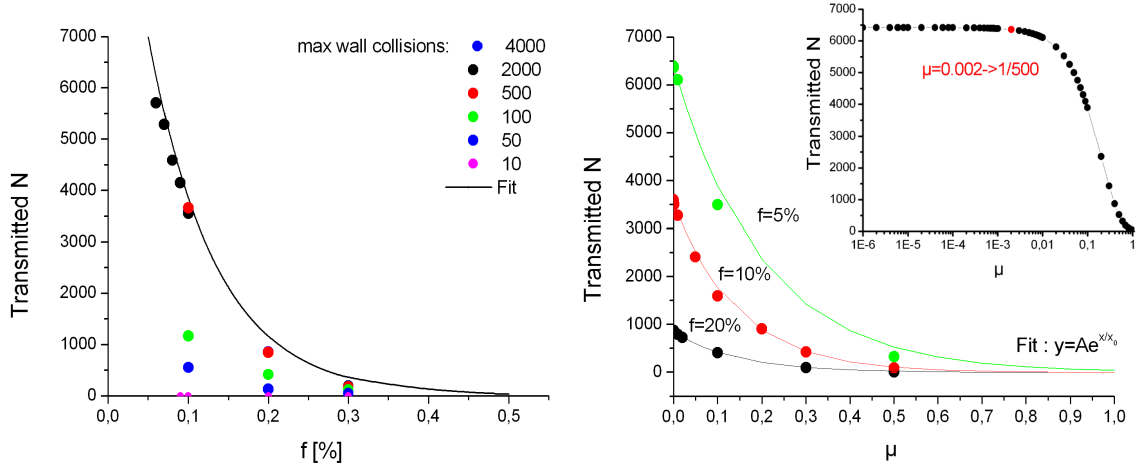


Figure 3.8: A systematic parameter study for a cross check to use the *FRED* simulations for UCN transport. The transmission of 10000 UCNs from a source through the U shaped baffle from (cf. fig. 3.6) is shown as function of  $f$ , and  $\mu$ , right.

can be seen that a minimum number of approximately 500 wall collisions is necessary to reach the absorbing detector or source area. A second result is that the number of transmitted neutrons  $N_{\text{UCN}}$  drops down when the diffuse scattering parameter  $f$  and therefore the backscattering possibility becomes too high ( $f \rightarrow 1$ ). On the right hand side of fig. 3.8 the count rate was estimated as function of the loss coefficient  $\mu$ . The rapid drop down of  $N_{\text{UCN}}$  is shown together with exponential fits [81] for different  $f$  values. The inlet of the figure shows the same calculation on a logarithmic scale down to the more realistic  $\mu$  values (see also table 3.3). The saturation level, beyond no further  $\mu$  dependence can be seen was 0.02. That fits to our previous result of necessary 500 ( $=1/0.02$ ) wall collisions for the UCN to hit either the black absorbing source area or the black absorbing detector. This can be interpreted as cut off value for this geometry. For smaller values a variation on the  $\mu$  does no longer effect the transport problem. This special point was marked red in the inlet of fig. 3.8 where the transmission property was studied as function of  $\mu$ .

### 3.4.2 Calibration of the simulation

The transmission of a stainless steel and an electropolished stainless steel tube of 36 mm inner diameter as function of its length  $l$  were measured by Kosovintsev [12, 97]). The results are presented in fig. 3.9 together with our simulated results using the *FRED* software for the same sample settings. Kosovintsev then used experimental data to calibrate his Monte Carlo simulations. Beside the diffuse scattering parameter  $f$  he also modeled different definitions for the angular distribution of the diffusely scattered neutrons. By simulating the given experiment we were also able to calibrate our simulation software. Our  $f$  values with the best fit to the experimental data are in good agreement with expected values for raw stainless steel tubes  $f = 0.5$  and electro polished stainless steel tubes  $f = 0.03$  [8]<sup>6</sup>.

<sup>6</sup>The value found for  $f$  is lower than our measured value for the NOKADO sample tubes. This may

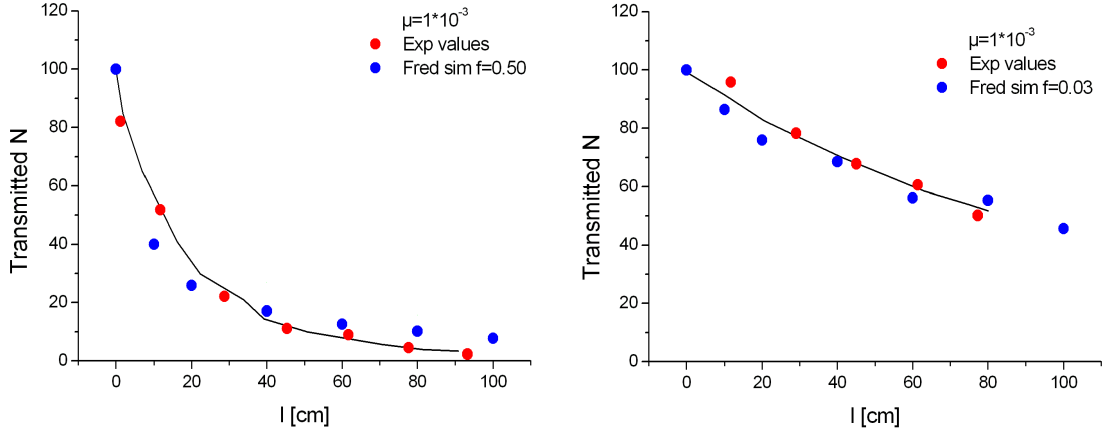


Figure 3.9: Left: measured transmission of a regular stainless steel tube. Right: electropolished tube [97]. The results of the corresponding FRED calculation are shown as with blue dots. Solid lines are shown to guide the eye.

### 3.4.3 *cubeD<sub>2</sub>* data to extract $f$

The *FRED* software was then used to simulate the transmission through the *cubeD<sub>2</sub>* experiment at FRMII. With identical source settings we have transmission data  $N$  (UCN counts) at two different source temperatures (9 K, 16 K) and the following setups: **Dump mode:** in the baffle setup (fig. 3.7b) the first bow was replaced by a T piece with a beam reflecting iron coated foil in front of the beam stop, the other two bows were replaced by UCN valves  $N_{\text{dump}}(T = 16 \text{ K}, 9 \text{ K})$ ; **Valve mode:** the dump foil was replaced by a  $45^\circ$  angle stainless steel coated mirror  $N_{\text{valve}}(T = 16 \text{ K}, 9 \text{ K})$ ; **Curve mode:** still with the mirror the two valves are replaced by  $90^\circ$  bows as drawn in fig. 3.7 b)  $N_{\text{curve}}(T = 16 \text{ K}, 9 \text{ K})$ .

We started with  $10^6$  UCN and determined the number  $N_i$  of transmitted particles at the different experimentally realized modes  $i$ . The  $\mu$  value of  $2.5 \cdot 10^{-4}$  was taken from our measurements. The diffuse scattering probability of the commercial Nokado parts  $f_{\text{Nokado}}$ , and the electropolished self made stainless  $f_{\text{stainless steel}}$  was varied using the following grids:

The ratio of the difference between the experimental ratios and the simulation was then used to find the combination of  $f_{\text{Nokado}}$  and  $f_{\text{stainless steel}}$  which reproduced the experimental values the best. Because we have three different configurations and two different source power (converter temperature at 9 K and 16 K) we took the sum of the differences. <sup>7</sup>

---

be explained by the fact that we took commercial tubes whereas the sample used for this experiment went through a cleaning and electro polishing process special investigated for high UCN transport.

<sup>7</sup>To reduce the systematic errors in case of the fine grid just the valve and curve mode were taken. They have been measured during the same beam time, where the bunker was opened just to replace the described parts.

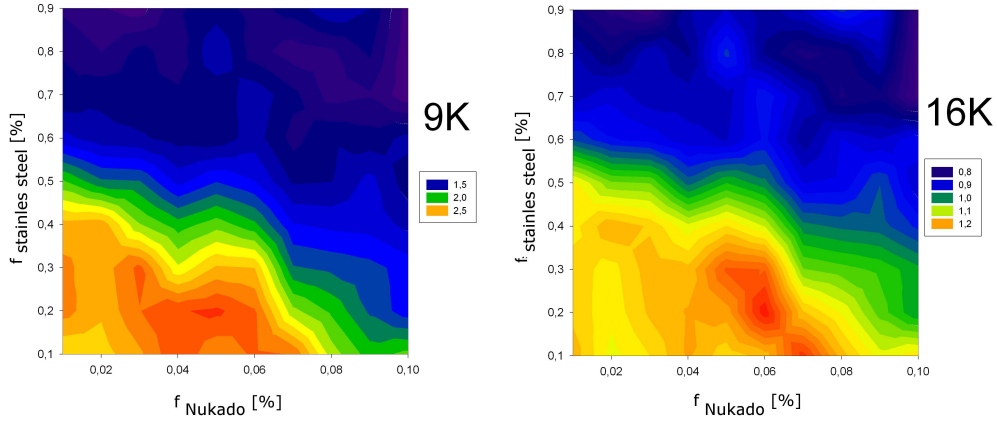


Figure 3.10: Deviation coefficient  $Z$  from eq. 3.8 between the ratio of the measured count rate from the different  $cubeD_2$  setups and the simulated transmission parameter from the  $FRED$  simulated ratios. Rough grid with three structures (dump,curve, valve)

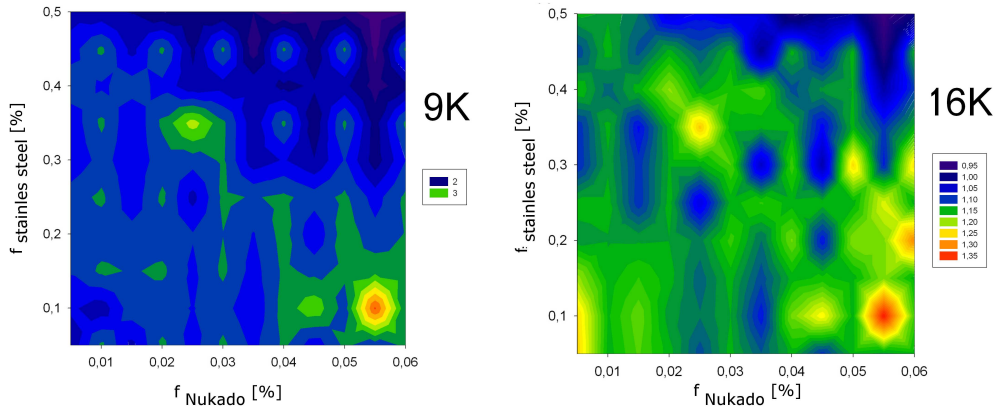


Figure 3.11: Comparison of  $Z$  from eq. 3.8 between the measured count rate of the  $cubeD_2$  setups and the simulated transmission rate from the  $FRED$  simulation. Fine grid of  $f_i$  for the structure (curve, valve).

	dump,curve, valve			
	rough		fine	
$f_m T_n$	9 K	16 K	9K	16 K
$f_{Nokado} [\%]$	5	6	5.5	5.5
$f_{valve} [\%]$	20	20	10	10

Table 3.2: The parameter  $f_i$  from fig. 3.10 and fig. 3.11 with the highest value  $1/z$  between experiment and simulation to extract the diffuse scattering probability for the Nokado electro polished stainless steel and the self made electro polished wall material.

$f_{\text{Nokado}}$	0.01 - 0.1	$\Delta$ 0.01	and	0.005-0.06	$\Delta$ 0.005
$f_{\text{stainless steel}}$	0.1 -0.9	$\Delta$ 0.1	and	0.05-0.5	$\Delta$ 0.05

$$Z_{9K,16K}(f_{m,n,m',n'}) = \sum_j^{\text{valve curve}} \sum_i^{\text{valve curve dump}} \frac{N_i^{\text{Exp.}}}{N_j^{\text{Exp.}}} - \frac{N_i^{\text{Sim.}}(f_{m,n})}{N_j^{\text{Sim.}}(f_{m',n'})} \quad (3.8)$$

The value for the reciprocal deviation  $Z(T_n, f_m)^{-1}$  is shown in the color code plot of fig. 3.10 as function of the  $f_{m,n}$  grid. The simulation was done first with a rough grid (fig. 3.10) to find the region of interest and afterwards with a fine grid repeated fig. 3.11.

The combinations of  $f_{\text{Nucado}}$  and  $f_{\text{valve}}$  leading to the lowest discrepancy to the experiment at the two temperatures are listed in table 3.2, obtain the result may be averaged to

$$f_{\text{Nocado}} = 5.5 \pm 1\%$$

$$f_{\text{Valve}} = 15 \pm 5\%.$$

The Nokado value is close to the result of the *two hole method*, section 3.1, from the beam times in 2005 and 2006 (fig. 3.5 red points) as well as the value from [97]. The  $f$  value for the machined and electro polished stainless steel parts are larger by a factor of three.

### 3.5 Storage method and two hole method results

Both methods have been used to characterize the identical 2-meter Nokado electropolished stainless steel tube. The extracted  $\mu$  and  $f$  value are listed in table 3.3.

	Storage method		Two hole method	
Beam time	2005 FRMII	2006 ILL	2005 ILL	2006 ILL
UCN source	<i>cubeD<sub>2</sub></i>	Turbine	Turbine	Turbine
$\mu$ [ $10^{-4}$ ]	$2.4 \pm 0.5$	$2,2 \pm 0.3$	$2.1 \pm 0.2$	$2.5 \pm 0.2$
$f$ [%]	$5.5 \pm 1$	-	$7.0 \pm 2$	$9.3 \pm 3$

Table 3.3: Summary of the results on the diffuse-scattering probability  $f$  and loss coefficient per wall collision  $\mu$  for the electropolished 2 m stainless steel tube extracted from different UCN sources with the *storage method* and the *two hole method* 3.1.2.

The good agreement of both values within the uncertainties may be seen as indication of the reliability on the developed *two hole method*.

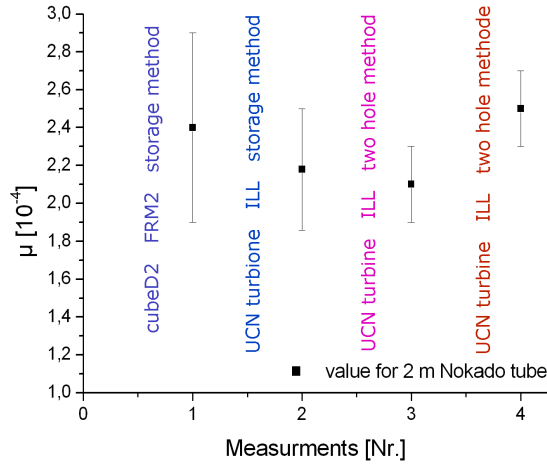


Figure 3.12: Comparison of the  $\mu$  values for the 2 m Nokado tube measured with the two different methods at two different UCN sources

### 3.6 Conclusion on the characterization of UCN guides

Two methods for experimental extraction of the loss probability per bounce  $\mu$  for possible UCN guides (shown in fig. 3.12) were presented. From the *two hole method* we also got the diffuse reflection probability  $f$ . The necessary UCN valves have been build and completely characterized. Data taken from different sample tubes and wall coatings could be used for discussions on the anomalously large losses. However a clear conclusion requires more systematic studies. The ray trace program *FRED* was used to simulate the UCN transport through a UCN guide system. The results from the *FRED* simulation may be compared in the future with self made Monte-Carlo-Codes like reported in ref. [95] or upgrades of *Geant4* [96]. The results were compared with the experimental data.



# Chapter 4

## UCN storage for n-lifetime measurement

After a short introduction about lifetime experiments using storage bottles with high Fermi potential materials and their problems, the basic principle of our planned magnetic storage experiment *PENeLOPE* will be described. The advantages of this storage principle are outlined. A new method to measure  $\tau_n$  via the detection of the decay protons during a storage cycle is shown. The requirements for the proton detector are listed and used as input parameter for the next chapter, where it will be developed step by step.

### 4.1 UCN trapping using material bottles

As stated above, the reflection of neutrons with kinetic energies lower than the Fermi potential of a suited wall material can be used to store the neutrons for a certain time. The number  $N(t = 0)$  of UCN are filled in a bottle and the surviving neutrons  $N(t)$  after the storage time  $t$  is measured. With the assumption that the UCN flux from the source stays constant the lifetime  $\tau_n$  can be extracted (eq. 4.1) from measurements with different storage times.

$$N(t) = N(t = 0) \cdot e^{-t \cdot (1/\tau_n + 1/\tau_{\text{capt}} + 1/\tau_{\text{scat}})} \quad (4.1)$$

The neutron number decreases by the free neutron decay (mean lifetime  $\tau_n$ ) as well as due to the two loss mechanisms described by  $\tau_{\text{capt}}$  (absorption of neutrons on the wall or rest gas atoms) and  $\tau_{\text{scat}}$  (losses due to kinetic energy gain above the Fermi potential of the wall material caused by inelastic up scattering). The two loss coefficient have to be known with high precision to extract a precise neutron lifetime value  $\tau_n$ .

**Absorption:** Even in the case where the kinetic energy of the neutron is smaller than the Fermi potential of the wall, an exponentially decreasing part of the wave function is penetrating into the material. Due to the absorption cross section of the wall material the neutron can still be captured. For example hydrogen, which is very likely deposited on the walls, has a high  $\sigma_{\text{capt}} = 0.33$  barn [98] cross section.

**Inelastic scattering:** Absorbed hydrogen on the surface of the trap walls is also a major cause for inelastic up-scattering of UCN ( $\sigma_{\text{scat}}^H = 80.3$  barn). The UCN gain in one scattering process or in the sum of the huge amount of wall collisions ( $\approx 10^4$  hits) transfers enough energy to the UCN, so that they may penetrate the walls and escape from the trap [98].

Knowing and assessing these sources of losses is the main challenge for material-bottle storage experiments. The leakage through the walls can be dealt with e.g. by changing the surface to volume ratio of the trap and then extrapolate to infinite storage volumes [99]. Another method is to measure the neutrons leaving the storage container with neutron detectors [100]. Also numerous systematic studies of different wall coatings and different bottle temperatures were performed e.g. [101]. Nevertheless, it was concluded that, with the latest results, the precision limit of material bottles was nearly reached [100].

In order to increase the accuracy further, another method has to be applied: Magnetic storage of ultra-cold-neutrons (UCN), which allows trapping of UCN without any wall collision.

## 4.2 UCN trapping in magnetic bottles

### 4.2.1 Basic theory

The principle of magnetic storage of ultra-cold neutrons is based on the magnetic moment,  $\mu_n = -60.3$  neV T<sup>-1</sup> of the neutron. Inside an inhomogeneous magnetic field  $B(\vec{r}, t)$  which leads to a force [102]. Two coupled equations govern the interaction

$$\frac{d^2\vec{r}}{dt^2} = -\frac{\mu_n}{m_n} \vec{\nabla}(\vec{\sigma}_n \cdot \vec{B}) \quad , \quad \frac{d\vec{\sigma}_n}{dt} = \gamma \vec{\sigma}_n \times \vec{B},$$

where  $\gamma = 2\mu_n/\hbar = 1.832 \cdot 10^8 \text{s}^{-1} \text{T}^{-1}$  and  $\sigma_n$  is the unit vector parallel to the magnetic moment  $\vec{\mu}_n$  of the neutron [103]. The equation of motion can be simplified, when the projection of  $\vec{\sigma}_n$  on  $\vec{B}$  stays constant.

$$\frac{d^2\vec{r}}{dt^2} = \pm \frac{\mu_n}{m_n} \nabla |\vec{B}|.$$

The acceleration of the neutron caused by the changing magnetic flux density  $\vec{B}$  depends on the sign of the spin projection. Neutrons with a spin parallel to  $\vec{B}$  are called low-field seekers because they are repelled from high flux densities. Neutrons, with the opposite spin configuration, the so called high-field seekers, are attracted by large magnetic fields. This is described by the potential  $U$ .

$$U = -\mu \cdot |B|$$

A gradient field with a maximum value of, e.g. 2 T is sufficient to reflect neutrons with  $E_{\text{kin}} = 120$  neV. In a magnetic field only the projection of the spin on the  $\vec{B}$  direction is a good quantum number with the values  $M_s = \pm 1/2$ . Perpendicular to the field

lines, the magnetic moment has the phase angle  $\Phi$  as a degree of freedom. Thus, the magnetic moment precesses around the  $\vec{B}$  vector with the Larmor frequency

$$\omega = \frac{2\mu_n}{\hbar}|\vec{B}|.$$

Changes in the magnetic field have to be smooth enough to avoid a possible spin flip. The spin has to be able to follow the changing magnetic field everywhere in the trap as described by the adiabatic condition

$$\omega_L \gg \frac{d\vec{B}/dt}{|\vec{B}|}.$$

It can be seen from this equation that for storing low-field seekers in a volume surrounded by a strong magnetic B field, zero field regions have to be avoided. Otherwise, a spin-flip may occur, changing the neutron into a high-field seeker, which is afterwards accelerated towards the walls.

## 4.2.2 Previous magnetic storage experiments

In order to confine neutrons, one has to create a magnetic field configuration where a region with a very low (but not zero) field is surrounded by a high field "cage".

The first experiments applying this storing concept used different approaches. Wolfgang Paul et al. [13] designed a sextupole magnetic storage ring, whereas Abov et.al. [104] constructed a cup trap where gravity confinement was also exploited to close the trap to the top. A magnetic trap consisting of permanent magnets leading to a flux density of  $\approx 1$  T was successfully realized by Ezhov et.al. [105]. A superconducting ioffe trap with decay electron detection was built at Nist [106, 107].

## 4.3 The *PENeLOPE* project

### 4.3.1 *PENeLOPE* storage container

The new neutron-lifetime experiment *PENeLOPE* (*P*recision *E*xperiment on *N*eutron *L*ifetime *O*perating with *P*roton *E*xtraction[22]) shall improve the accuracy by one order of magnitude over the world average lifetime value  $\tau_n = 885.7 \pm 0.8$  s. The goal is to store UCN with  $E_{\text{kin}} < 110$  neV by magnetic and gravitational confinement. A field of 2 T at the periphery generated by superconducting coils is necessary. The height shall reach 1.1 m to store a large number of UCN. A scheme of the planned setup is shown in fig. 4.1.

The basic geometry of the magnetic bottle is a cylinder of 21 superconducting NbTi solenoidal coils with alternating current directions (indicated in red and green respectively). The coil cross section was optimized to get the required magnetic density of 2 T with a feasible current density of 360 A/mm<sup>2</sup>. The magnetic field between two coils adds up due to the opposite current directions but decreases rapidly inside the storage volume (the required gradient field). To avoid regions with very low absolute magnetic field and to guarantee the adiabatic condition an additional field component is mandatory. The  $\vec{B}$  field of the yellow race track coils is sufficient for this purpose.

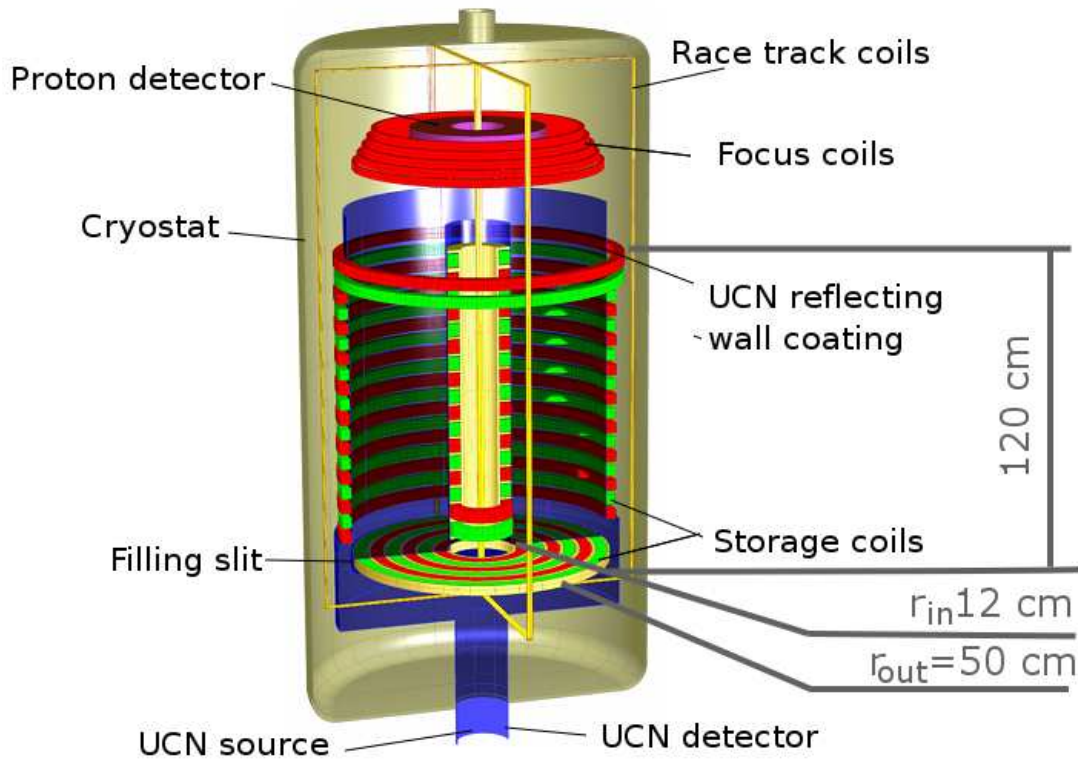


Figure 4.1: Schematic cut-away view of the magnetic storage device.

Because the azimuthal magnetic field from the center current rod is always perpendicular to the field from the solenoid coils, the  $\vec{B}$  field seen by the neutrons does not vanish. With a current of  $I = 10$  kA through the race track coils a minimum  $\vec{B}_{min} \approx 10^{-3}$  T is guaranteed. To avoid absorption of the UCN on the rod material it is necessary to create an additional magnetic shielding. The 2 T repelling field from the 17 inner solenoids with alternating current in the middle of fig. 4.1 are inserted for this purpose. The bottom of the storage vessel consists of 6 concentric coils. With a height of 1.1 m a coverage on the top is not necessary, because of the gravitational confinement. A storage volume of  $700 \text{ dm}^3$  is achieved by the double cylinder geometry with an inner radius of 12 cm and an outer radius of 50 cm. Together with the expected UCN production rate of the next-generation UCN sources, e.g. the *miniD*<sub>2</sub> source at the FRMII, the storage of  $10^8$  UCN per filling should be achievable. During filling and emptying, the bottle the magnetic field has to be ramped down. At this time period the confinement will be provided by a neutron reflective coating of the walls (indicated in blue in fig. 4.1).

There are two possibilities to extract the neutron lifetime from a storage experiment. The first one, following eq. 4.1, counts the surviving neutrons after different storage times  $t_{stor}$ . Counting one of the decay products during the storage phase is the second choice. Using the gravitational confinement, the bottle can stay open to the top and

a detector for in-situ lifetime measurement during storage cycle can be placed there. The energy spectrum of the protons on the left and the electrons on the right from the free neutron decay is shown in fig. 4.2. Different to electrons, protons with their much lower kinetic energy starting in a direction opposite to the detector may still be guided towards the top with a manageable electric potential applied between the bottom and the uppermost coils. Focusing coils surrounding the planned proton detector increase the collection efficiency and reduce the necessary active detector area. It is mandatory to post-accelerate the protons towards the detector to achieve a sufficient detection efficiency.

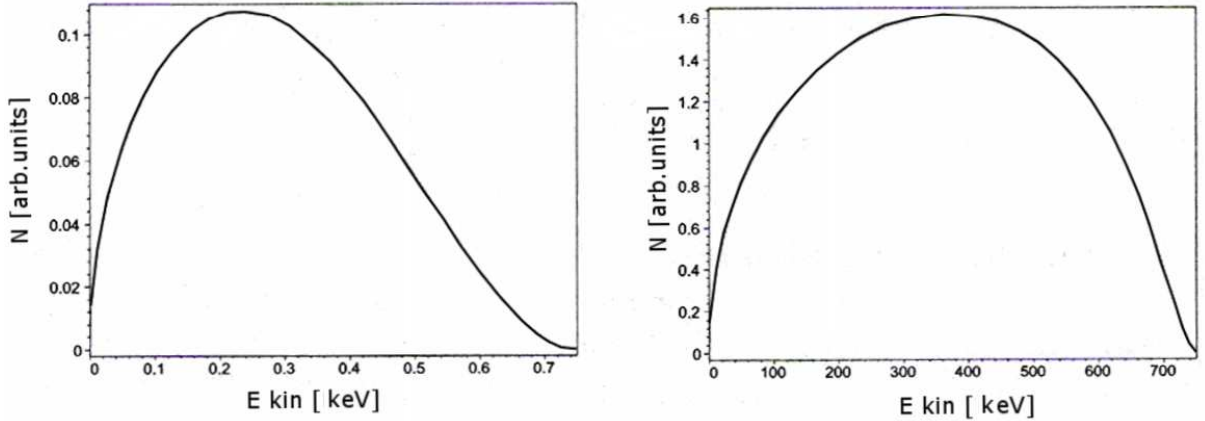


Figure 4.2: Energy spectrum of protons and electrons from the free neutron decay [108].

### 4.3.2 *PENeLOPE* neutron detection

In order to count the survived number of ultra-cold neutrons after the storage time, the current through the coils has to be ramped down to extract the UCN through the filling/emptying slits at the bottom. Afterwards, they are guided to a UCN counter. To accelerate the UCN to energies high enough to penetrate the entrance window of this counter the latter is located approximately one meter lower than the storage vessel.

### 4.3.3 *PENeLOPE* proton detection

In principle, both charged particles are useful to directly determine  $\tau_n$ , but due to their different energy spectra shown in fig. 4.2 (caused by their mass difference) it is much easier to collect and guide the low energetic protons than the electrons. A potential difference of 10 kV from the top to the bottom in the storage volume is already sufficient for this purpose. Some proton trajectories inside the magnetic and electric extraction field shown in fig. 4.3. Data is taken from ref. [84].

On the other hand, to detect these low-energy protons a post acceleration to 30-40 keV is mandatory. The expected energy spread of protons hitting a detector at  $-40$  kV potential difference to the storage container and their angle of impact (end of proton trajectory at the detector surface) at the detector surface is shown in fig. 4.4.

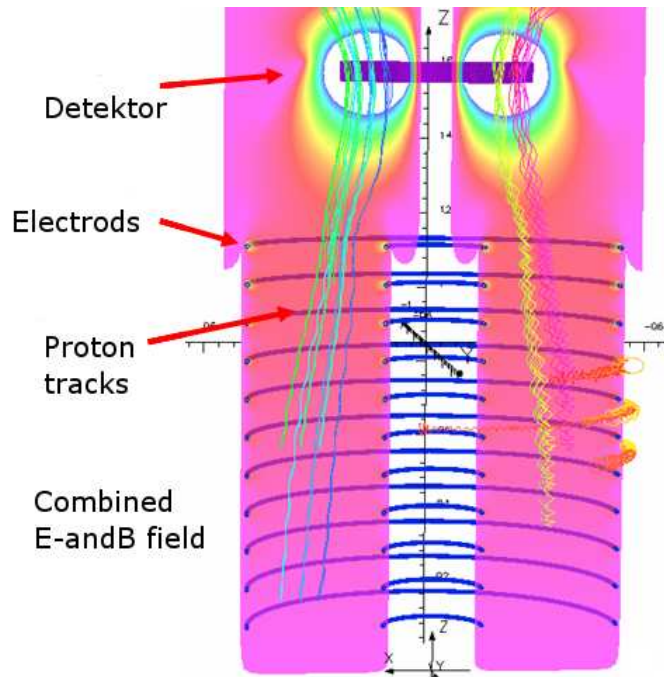


Figure 4.3: Proton trajectories starting inside the storage container with the extraction E- and B field towards the proton detector on the top.

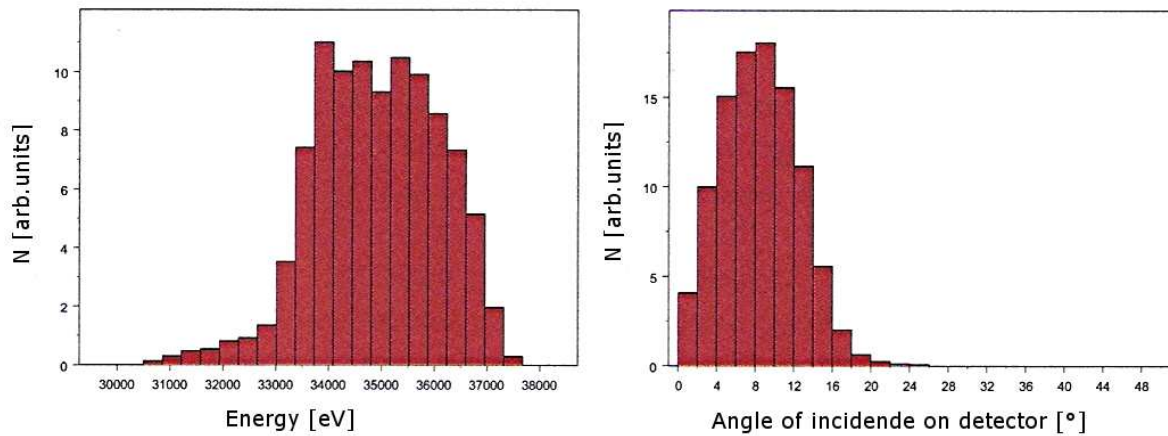


Figure 4.4: Left: simulated energy spectrum of protons extracted from the storage volume by 10 kV potential difference and guided by the focusing  $\vec{B}$  field (detector held at -40 kV). Right: angular distribution of protons on the detector. The angle is defined between the surface normal of the detector and the momentum vector [108].

Besides the different storage method, the expected improved statistics we may expect due to higher UCN densities and the direct measurement are the big achievements on this planned experiment. The much shorter measuring times necessary to reach sufficient statistics open the possibility of systematic studies on storing conditions and much more. The *PENeLOPE* setup just described leads to following requirements for the proton detector: a high efficiency detection of low energy protons in combination with a low efficiency for electrons, the major background (electrons from the decay hitting the detector). The extension of the ring shape detector area is limited on one side by the focusing coils and on the other side by the race track coils fig. 4.1. The required active area is 2500 cm<sup>2</sup>. The superconducting environment makes it necessary to run the detector next to the liquid helium cryostat at low temperatures and high magnetic fields.

To avoid any contamination deposited on the wall coating all materials should be suited for ultra high vacuum expected at these temperatures. Overall the price of the complete detector system should be realistic.

The goals of the planned detector are listed below:

- high efficiency for the detection of low energy protons
- low efficiency for the decay electron detection
- detector dimensions between the focusing and racetrack coils
- largest possible detector surface
- detector suitable for cryogenic temperatures
- detector suitable in high magnetic fields
- detector working at low vacuum conditions (outgasing)



# Chapter 5

## Proton detection

Proton detection is one of the key issues of the planned neutron-lifetime experiment *PENeLOPE*[sec. 4]. As the maximum energy of the decay protons is only 720 eV, proton acceleration is mandatory. Nevertheless, the detection of 30-40 keV protons is not trivial.

It was shown [108] that in *PENeLOPE* one may guide 65% of the protons onto a ring of 10 cm inner and 30 cm outer radius. The protons may be detected either by solid-state detectors or by scintillation counters. As solid-state detectors are rather expensive, a suitable scintillation counter had to be developed. After a list of requirements, the basic detector principle, different simulations and experimental results will be presented to develop the detector will be part of the following section.

### 5.1 Requirements

The proton detector for the *PENeLOPE* lifetime experiment has to fulfill the following requirements.

i)	Detection of protons with an energy of	$\approx 30$ keV
ii)	Discrimination against decay electrons with energy	0...750 keV
iii)	Area	$\approx 2500$ cm <sup>2</sup>
iv)	Diameter	$< 630$ mm
v)	Temperature	$\ll 300$ K
vi)	Vacuum	$\approx 10^{-8}$ mbar
vii)	Magnetic field	$\approx 3$ T

### 5.2 Basic detector idea

The basic idea is to cover the area with a thin film scintillator evaporated on a light-guiding structure and to count the photons from the (much smaller) side. These scintillator has to be thick enough to stop the accelerated protons, but thin enough to keep signals from the electrons small. Counting the photons from the side reduces the amount and size of necessary photon detectors and electronics significantly.

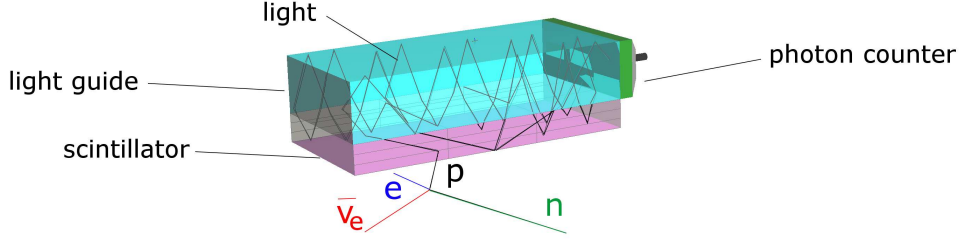


Figure 5.1: Basic idea for the proton detector of the *PENeLOPE* lifetime experiment.

As, this geometry is not very favourable for the light transport from the scintillator to the detector a poor photon rate per incident proton is expected. For this reason we considered CsI(Tl) with the high light output of  $65\,000$  photons/MeV<sup>-1</sup> (at room temperature) as the first-choice scintillator material.

For the light guide it is obvious to use material transparent at the short wavelength of the emitted light (quartz or plastic).

## 5.3 Simulation

A variety of software programs were used to find solutions for the requirements i)-vii) (section 5.1). Questions like the interaction between protons, electrons and the scintillator substrate, the material and geometry of the light guides, the expected temperature and possible support realizations were covered. The still open questions beyond standard knowledge results in a list of necessary experimental data presented in section 5.5.

### 5.3.1 Active area

Starting with a randomly distributed proton gas inside the superconducting storage volume and taking the designed proton extraction systems into account, the trajectories of 65% of the protons finally hit the for seen area between race track coils and focusing coils. Besides the optimized extraction efficiency  $\eta_{\text{extr}} \approx 65\%$  [84] to the later proton detector area, one gets also the distribution of the proton hits on the detector area (shown in red in fig. 5.2) as a function of the detector radius. The geometric boundaries shown in blue are caused by the focusing coils ( $r_{\text{focus}}$ ) on the outside and the race track coils ( $r_{\text{racetrack}}$ ).

With a fixed inner radius  $r_{\text{in}}=10$  cm the integrated collection efficiency (of the 65% extracted protons) is shown on the right side of fig. 5.2. At  $r_{\text{out}} = 30$  cm  $\eta_{\text{coll}} \approx 100\%$  is reached. This leads to an active area of  $A_{\text{det}} = 2500$  cm<sup>2</sup>, of  $r_{\text{in}} = 10$  cm and  $r_{\text{out}} = 30$  cm as input parameter for the simulations. If necessary  $r_{\text{out}}$  could be reduced to 25 cm still keeping a detection efficiency of  $\eta_{\text{coll}} = 0.95$ .

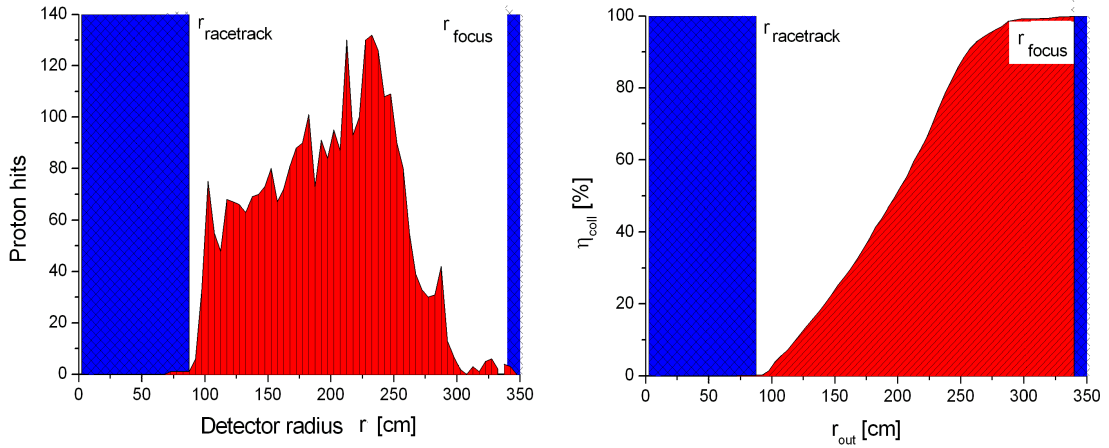


Figure 5.2: Left: radial distribution of the proton hits on the detector. Right: collection efficiency  $\eta_{\text{coll}}$  as function of the outer detector radius  $r_{\text{out}}$ .  $\eta_{\text{coll}}=100\%$  means that all of the extracted protons (65% of the extracted particles) are collected.

### 5.3.2 Proton interaction

The interaction between the protons and the scintillator was calculated using SRIM [110]<sup>1</sup>. As introduced before, CsI(Tl) turned out to be the favorite scintillator material and was used in the following calculations. Relevant properties are listed in table 5.1. The low concentration on Tl doping was here not considered.

material	index of refraction	$\lambda$ [nm]	%/Anthracene	%/NaI	hygroscopic
NaI(Tl)	1.85	415	230	100	yes
CsI(Tl)	1.79	550	95	110	slightly
CsI(Tl)*	1.79	-	0	0	slightly
CsI(Na)	1.84	420	150	85	slightly
CsI	1.80	315	-	6	slightly
CsI*	1.80	315	500	-	slightly

Table 5.1: Scintillator materials and its properties. The values denoted with \* correspond to  $T = 70$  K [130, 132].

#### CsI as scintillator

In order to estimate the necessary thickness of the scintillator layer, the trajectories of  $10^5$  protons hitting perpendicular a CsI bulk material was calculated as a function of their incident energy. A typical ray-tracing plot for 40-keV protons is shown in fig. 5.3 (left), indicating how the beam widens inside the material. Figure. 5.3 (right) depicts the penetration-depth distribution.

The penetration range was calculated for proton energies  $E_p = 20 - 40$  keV in  $\Delta E_p = 2$  keV steps; the result is shown in fig. 5.4 (left). At a fixed beam energy of 30 keV

<sup>1</sup>SRIM: Stopping and Range of Ions in Matter.

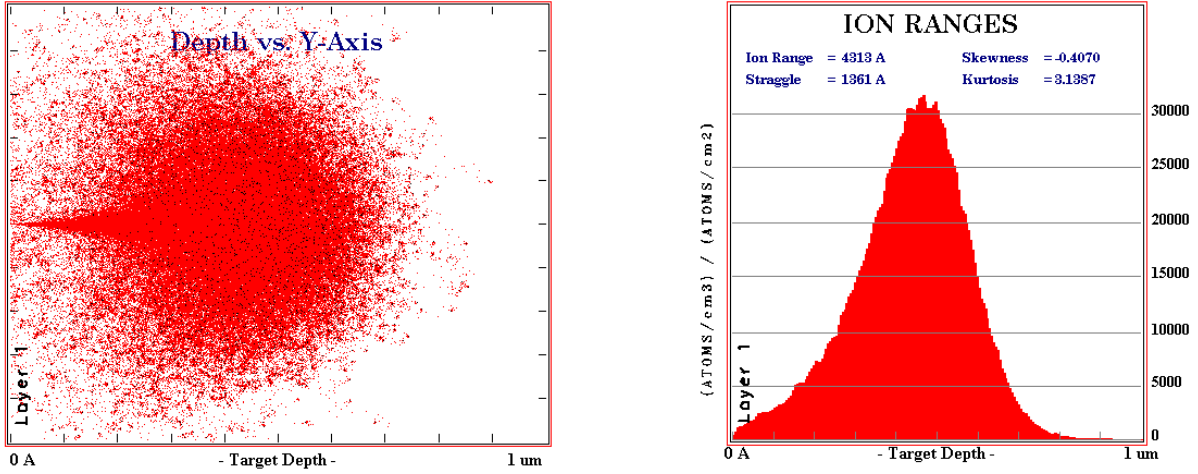


Figure 5.3: Left: proton trajectories inside a CsI scintillator layer. The proton energy is 40 keV. The beam spread is shown. Right: the distribution in penetration death.

the angular distribution was studied by varying the angle  $\phi_{\text{beam}}$  between beam and scintillator surface in  $\Delta\phi_{\text{beam}} = 5^\circ$  steps. The result is shown in fig. 5.4 (right). This was important as the protons gyrating around the magnetic-field lines of the storage volume of PENELOPE and may hit the detector with rather low angles (the simulated angular distribution can be seen in fig. 4.4). Another reason is that we cannot expect to grow a flat surface in the evaporation process (fig. 5.27).

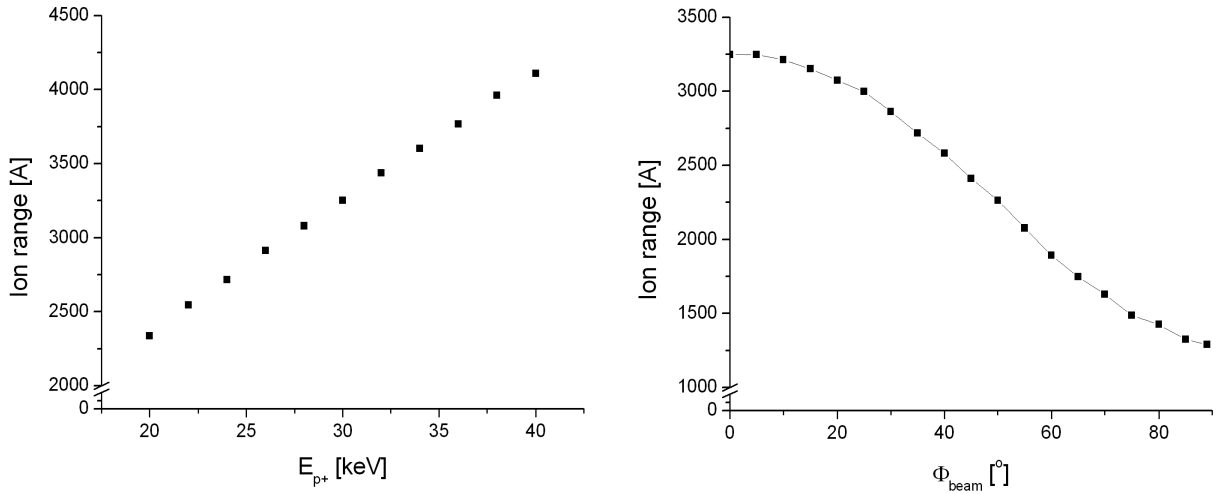


Figure 5.4: Left: penetration depth in a CsI scintillator as a function of proton energy. Right: maximum penetration depth as function of incident angle for 40-keV protons.

For the proton energies envisaged (30-40 keV) a most probable penetration depth of  $3250 \text{ \AA}$  for  $E_p(30 \text{ keV})$  and  $4313 \text{ \AA}$  for  $E_p(40 \text{ keV})$  was extracted. A layer thickness of less than  $1 \text{ }\mu\text{m}$  was found to be sufficient. From the angular plot (fig. 5.4, right) we see that up to an angle of  $50^\circ$  no major negative impact on our detection efficiency  $\eta_{\text{det}}$  is expected.

## Water cover on the CsI scintillator

CsI is known to be at least slightly hygroscopic. Nevertheless, for our evaporated polycrystalline structure with its large surface one has to expect strong absorption or adsorption<sup>2</sup> of water from the surrounding environment. The proton loss probability and the energy loss as a function of the water film thickness  $d_{\text{water}}$  is shown in fig. 5.5 for a simulation of 30-keV protons.

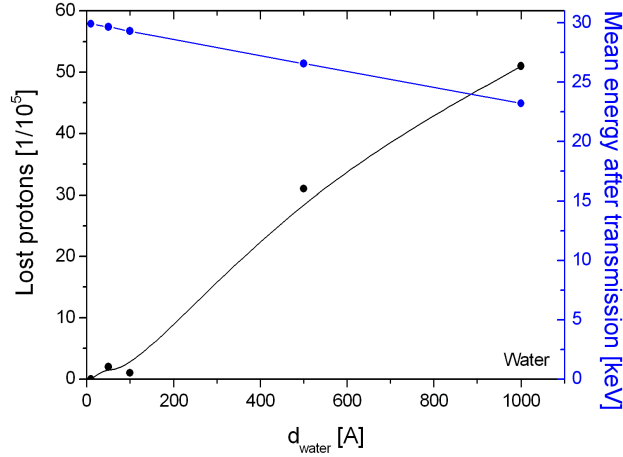


Figure 5.5: Proton loss fraction and mean energy loss of 30 keV protons in a surface layer of water with thickness  $d_{\text{water}}$ .

Hygroscopic layers of up to some  $\mu\text{m}$  thickness have been reported and as our simulations show this may be a problem for low energy particle detection.

Absorption of water can be avoided by keeping the detector in vacuum ( $< 10^{-5}$  mbar) or storing it in an inert gas atmosphere (water concentration  $\leq 10$  ppm), as it has been reported for CsI photocathodes [112]. Due to our complex main experiment and the large implemented detector this is not possible in our case. Once contaminated, the surface water can be partially removed by heating inside a vacuum system. Cusanno et al [113] reported for CsI layers to get  $\approx 50\%$  of the initial performance back after baking at  $60^\circ\text{C}$  for 12 hours. Due to the large UCN absorption cross section of  $\text{H}_2\text{O}$  special care has to be taken where the evaporated water will be deposited. Contamination of the storage walls must be avoided. Another way is to evaporate a thin non hygroscopic protection layer on the surface [114]. The influence on the transmission and energy loss for low-energy protons by such an additional surface protection layer has to be studied experimentally.

### 5.3.3 Light guiding structures

The optical ray tracing program *FRED* [94] was used to find the best segmentation of the active area and to ensure sufficient light collection.

---

<sup>2</sup>Absorption: the molecules are taken by the bulk; Adsorption: the molecules are bound at the surface.

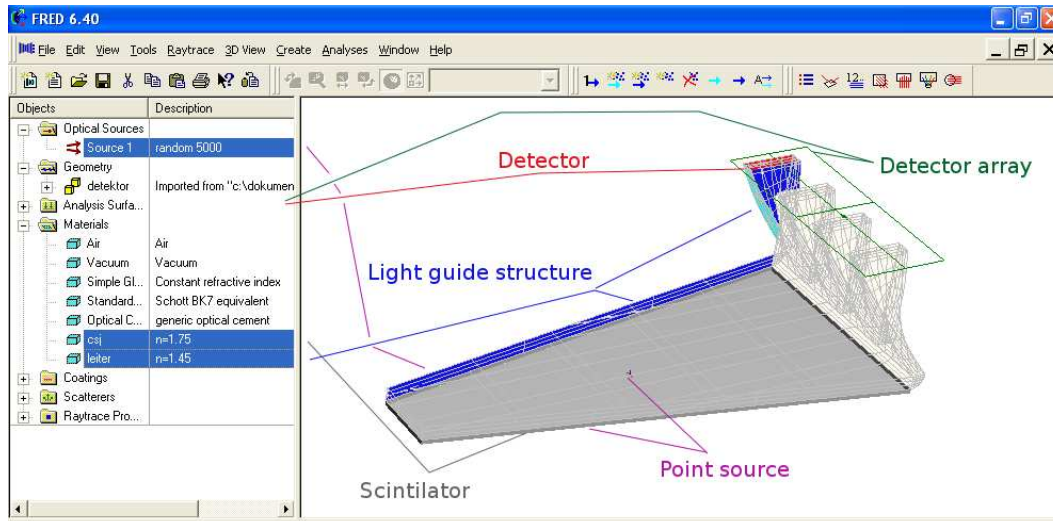


Figure 5.6: Screen shot of the used *FRED* software used for light transport simulations.

A typical screen shot of the *FRED* worksheet is shown in fig. 5.6. Using simple geometries, the results of the simulations agreed with simulations done with the *guide7* [116]. The problem of a scintillator bar irradiated by an  $\alpha$  source with the light read by a photomultiplier at the side was addressed by Niederberger [117]. He compared experimental values with an analytical model. We simulated the experiment and found agreement on the 20% level. Further explanations may be found in the appendix. Our simulations fit also to experiences from a group from the Michigan State University [118] working on similar questions concerning scintillation light transport [119].

### Basic geometry

Many different possibilities to cover the required  $r_{\text{in}} = 10$  cm and  $r_{\text{out}} = 30$  cm ring-shaped area with smaller pieces have been considered. Collecting light from one side makes additional space for photon counter and front-end electronics necessary. Our simulations showed that cuboids are the easiest geometry with sufficient light output and excellent homogeneity but the circular boundary conditions imposed by the focusing coils (cf. fig. 5.2) rules out an easy way of covering. An improvement is achieved by the combination of triangle and cuboids read out from the circumference. The light collection from these two basic geometries differs by a factor of two at least. A compromise is achieved by a solution with trapezoidal structures as shown in fig. 5.6. Increasing the amount of trapezoidal pieces, in the following called panels, drives the trapezoidal angle towards  $90^\circ$  and the good homogeneity again. Good light output and homogeneity can be realized. Further important advantages will be discussed in detail in this section. The solution with segments of a circle showed dead areas with hardly no light transport to the photon counters and was excluded. Using the CsI layer as source for  $10^5$  rays with randomly origin and direction of emission the average transmission to the side was calculated for various geometries, thicknesses and light-guide materials. The simulation results for different other investigated geometries are shown in the appendix.

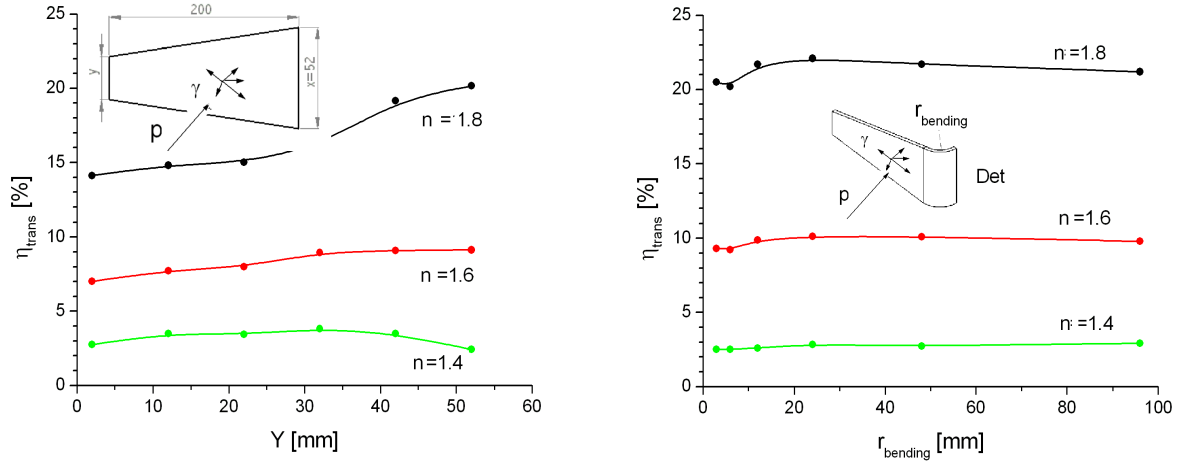


Figure 5.7: Left: Transmission to the longer lateral side as a function of the trapezoidal angle indicated by a change in the shorter length  $y$ . Calculated with the scintillator surface as area source. Right: Efficiency  $\eta_{r,trans}$  as function of the bending radius for  $90^\circ$  bending and different refraction indices.

### Light-transport efficiency

Focusing on the trapezoidal geometry the *FRED* software [94] was used to analyze the light-transport efficiency  $\eta_{trans}$  as a function of the trapezoidal angle.  $10^6$  photons were emitted randomly from the CsI-scintillator surface ( $n=1.75$ ) and the trajectories passing the long side of the 3 mm high, 200 mm long trapezoidal side counted. The simulation was performed for two suitable materials (transparent at the emitted wavelength of  $\lambda_{CsI}$ ) quartz glass  $n = 1.8$ , lucite  $n = 1.4$ , and at an intermediate index of refraction  $n = 1.6$ , as cross check. The results are shown in fig. 5.7.

As predicted by earlier simulations, the rectangular shape, with equal side lengths  $x$  and  $y$ , respectively, leads to the highest  $\eta_{trans}$ .

A second result is that the material with the highest refractive index leads to the best light transport. This can be understood as the refractive index becomes close to the refractive index of the scintillation layer. Thus the limiting angle of total reflexion becomes larger and the coupling between the two materials becomes better. This means that we gain in efficiency with an increasing number of trapezoidal pieces and the use of high  $n$  material.

In order to have enough space for the photon counting units it may be necessary to bend the last part of the light guide panel by  $90^\circ$ . The influence of the bending radius on  $\eta_{trans}$  was simulated with a rectangular guide and a surface source, as shown in fig. 5.7, (right). The influence on the bending radius predicted by the simulation was small.

### Photon counters

As explained in more detail in section 5.5.3, we specialized our detector modeling on two commercially available large area avalanche photodiodes (LAAPDs). The reasons will be pointed out later and by our own measurements presented in chapter 6. The interesting input for the present analysis is the active size of  $10 \cdot 10 \text{ mm}^2$  for the LAAPD

S8664-1010 from Hamamatsu Photonics (called Hamamatsu) and  $13 \cdot 13 \text{ mm}^2$  for the LAAPD S1315P from Radiation Monitor Devices (in the following called RMD). To match the long rectangular shape to the square a twisted light guide shown in fig. 5.8 with the lowest transmission losses is used [124].

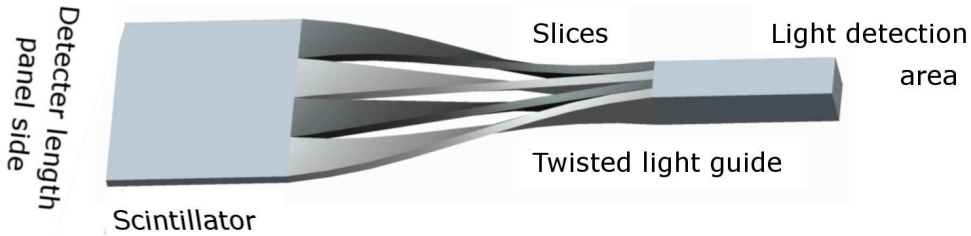


Figure 5.8: Twisted light-guide structure as an efficient way to transform the rectangular light-guide surface to the square shape of the photon counting units.

The light guide thickness was fixed to 3 mm as compromise between light transport, self stability and necessary photon counters. With this thickness, three slices with a length of 10 mm can be used for the Hamamatsu  $10 \times 10 \text{ mm}^2$  diode which then covers a trapezoid length of 30 mm. In case of the RMD  $13 \times 13 \text{ mm}^2$  LAAPD we can use four 13 mm slices and cover a trapezoid length of 52 mm.

Figure 5.9, left, shows the number of needed detectors as function of the outer radius and number of polygon edges for the Hamamatsu LAAPD in red and the RMD solution in blue.

On the right-hand side of fig. 5.9 the maximal outer radius  $r_{\max, \text{out}}$  of the polygons is shown as function of the required radius  $r_{\text{out}}$  of the active area. The limit set by the radius  $r_{\text{focus}}$  of the focusing coil support is shown in black. Polygons with more than 30 single trapezoidal pieces will be necessary to cover the proton collection area with 300 mm radius. This leads to a needed number of 62 Hamamatsu detectors or 36 RMD detectors. For the moment this is equivalent to two LAAPD's for each trapezoidal panel. A possible coincidence condition that a proton event is identified when only both LAAPD's gave a signal above noise was ruled out by the simulations. The variation of the photon collection efficiency onto the two LAAPD's for different point sources on the trapezoid surface were too high (factor 50). The upper limit on the trapezoidal pieces is reached when each trapezoidal gets its own photon counting unit. Due to the results from fig. 5.7 we can expect the highest efficiency  $\eta_{\text{trans}}$ , when this maximum number is used. Avoiding photon sharing between LAAPD's facing the same trapezoidal light guide leads to better light transport as well as a better signal to noise ratio with the same total amount of photon counting units.

### Homogeneity of $\eta_{\text{trans}}(x, y)$

A typical panel optimized for the RMD detector solution consisting of a trapezoid ( $x = 52 \text{ mm}$ ,  $y = 17 \text{ mm}$ ,  $h = 200 \text{ mm}$ ) with CsI coating, a  $90^\circ$  bending and a twisted

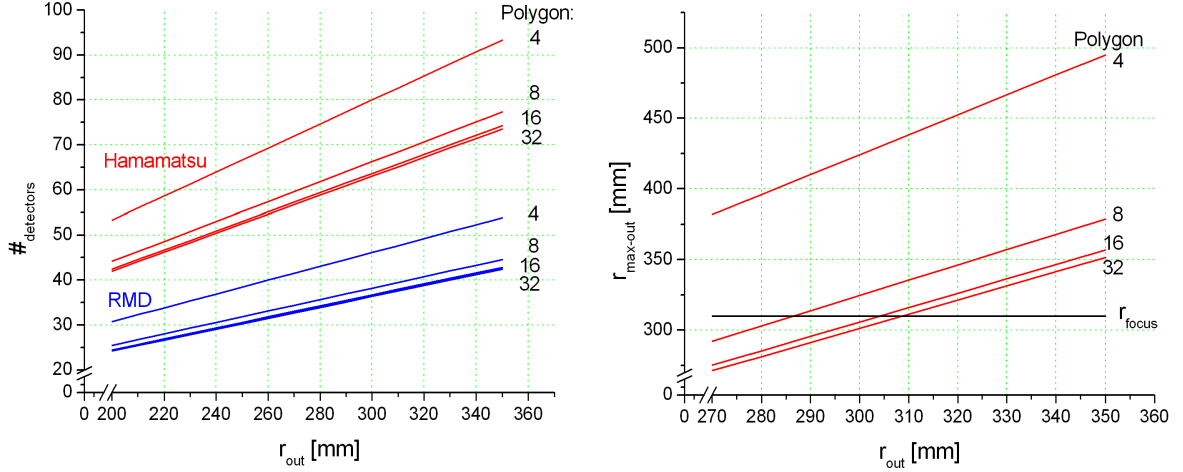


Figure 5.9: Left: number of Hamamatsu  $A = 1 \text{ cm}^2$  or RMD  $A = 1.69 \text{ cm}^2$  LAAPD detectors needed as a function of the outer detector radius  $r_{\text{out}}$  and number of polygon edges. Right: possible polygon realization based on the geometrical constraints and the task to cover an outer radius of 300 mm is shown.

light guide, as shown in fig. 5.6, was used to calculate the homogeneity  $\eta_{\text{trans}}(x, y)$  (light collection as function of hit position of the proton). A point source was moved across the CsI surface along a x-y grid and the number of photons  $N_{\text{photon}}(x, y)$  out of 5000 ejected directions reaching the detector surface of  $4 \cdot 13 \text{ mm} \cdot 3 \text{ mm}$  were determined. The individual count rate from the four different slices were available, but due to the homogeneous performance of the LAAPD area [121] (shown in the inlet of fig. 5.10 with the dimension of the active LAAPD area x and y) this is of minor interest in our case.

For this geometry only 6% of the produced photons will reach the RMD detector. The simulation was made with quartz as light guide. For lucite one has to expect about a factor of two less photon numbers.

### 5.3.4 Stress calculations

#### Stress through bending

The CsI scintillator will be evaporated on a relatively long trapezoidal light guide. How to support this structure without drastic bending by its weight and hence a higher risk of scintillator peel off was addressed next.

The same panel model used for the previous simulation (cf. fig. 5.10) was equipped with the material parameters, supported at one side, on both sides and with a complete frame (green arrows in fig. 5.11) and the deformation due to its own weight was calculated with a finite element program [122]. The results are shown in fig. 5.11. The maximum stress at the scintillator surface can be reduced from  $8.5 \cdot 10^5$ ,  $9 \cdot 10^4$  to  $5.8 \cdot 10^4 \text{ Nm}^{-2}$ . The corresponding elongation  $\Delta y_1$  was calculated to be  $9 \cdot 10^{-2} \text{ mm}$ ,  $2 \cdot 10^{-3} \text{ mm}$  and  $2 \cdot 10^{-3} \text{ mm}$  respectively (from left to right).

The support from two end sides seems to be sufficient.

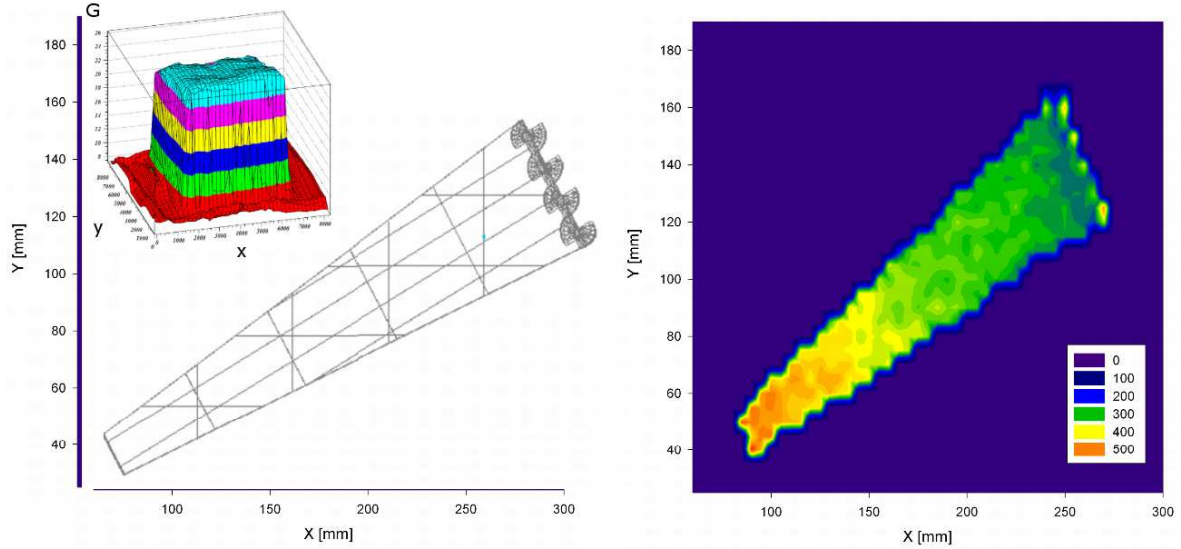


Figure 5.10: Left: one of the 36 detector panels for the RMD solution. The LAAPD homogeneity is shown in the inlay. The point like response on the active area of the LAAPD is shown here in false color code. Right: Number of photons reaching the detector as function of the point of origin. 5000 photons were emitted under random directions for each point.

### Thermal stress

Shrinkage of the 200 mm long bulk material due to a temperature change from 300 K to 25 K can be estimated from the thermal expansion coefficient  $\alpha$  and the initial length  $L$ .

$$\alpha = \frac{1}{L} \cdot \frac{\Delta L}{\Delta T}.$$

The bulk material (light guide thickness 3 mm) forces then the thin layer (CsI) to follow the shrinking process; this lead to thermal stress. Because both are connected we can assume in first order approximation that the flat structure becomes curved. The height of the elongation  $\Delta y_2$  in the middle can be calculated from the length of the CsI layer at room temperature  $L$  and the expected length at the cold temperature  $L - \Delta L$ .

$$(L + \Delta L) \approx \sqrt{L^2 + \frac{16 \cdot \Delta y^2}{3}}$$

A rough idea of the results when the thermal stress is translated into a change in geometry is given in table 5.2.

The expected bending  $\Delta y_1 + \Delta y_2$  effect on the layer may be tested with a setup shown in fig. 5.12. The peel off risk for the thin evaporated scintillation layer may be reduced by such tests. Similar rough calculations and tests can also be applied to a possible reflection layer.

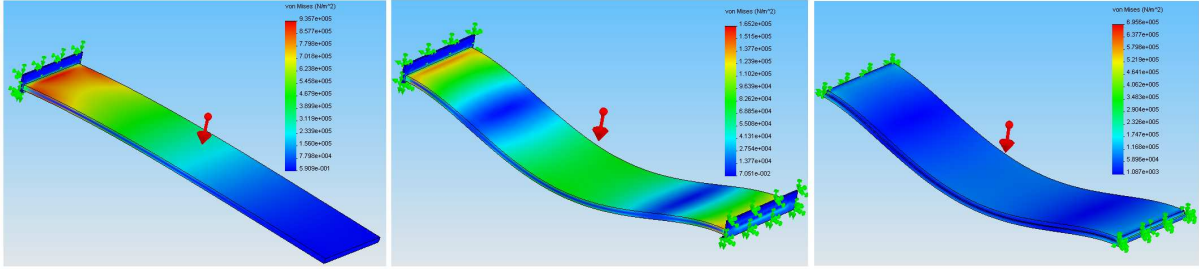


Figure 5.11: Study of the necessary support structure of the thin detector panels. Left: one sides Middle: two sided. Right: complete frame. The maximum of stress is reduced from  $8.5 \cdot 10^5$ ,  $9 \cdot 10^4$  and  $5.8 \cdot 10^4 \text{ Nm}^{-2}$ .

material	$\alpha [10^{-6}] 1/K$	$E$ [GPa]	$\Delta L$ [mm]	elongation $\Delta y_2$ [mm]
CsJ	0,54	75	0,03	0
Quartz	0,50	75	0,03	1.0
PVC	50	3,2	2,8	15.3
Lucite	85	3,2	4,6	17.8

Table 5.2: Calculated stress due to cool down to  $T=25 \text{ K}$  for CsI layers on various light-guide materials.

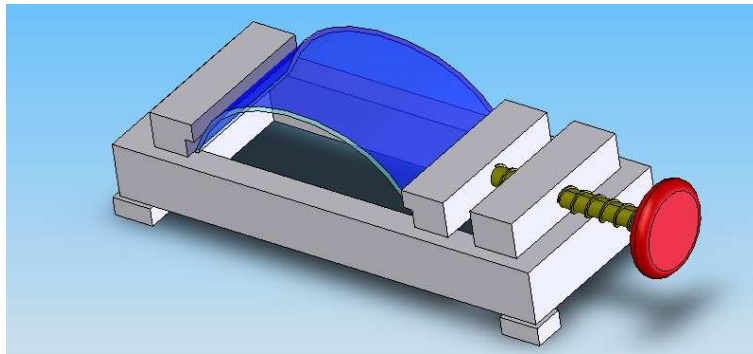


Figure 5.12: A possible setup to measure the risk of scintillator peel off. The light guide material is shown in fair blue, the evaporated scintillator in dark blue.

### 5.3.5 Temperature mapping

Together with an aluminum support frame (support from two sides) the panel was now placed between the superconducting focusing and racetrack coils, as shown in fig. 5.13. The dimensions used are the ones according to the PENELOPE setup. The temperature of the neighboring coils are fixed to the necessary He bath cryostat, 4.5 K. The frame itself was connected to the nitrogen shield. The figure shows the temperature distribution after reaching the equilibrium conditions between radiation from the He cryostat and the heat flow through the aluminum structure (simulation performed with Cosmos works [123]).

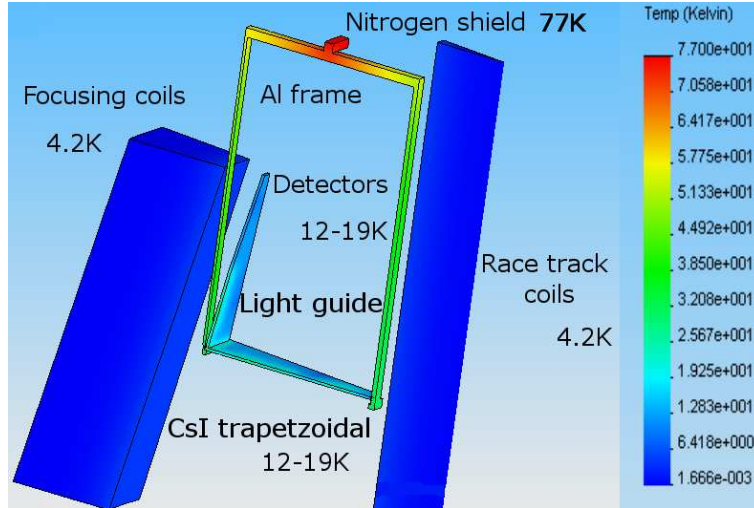


Figure 5.13: Simulation of the expected temperature distribution caused by radiation cooling from the focusing coils with a connection of the support cage to the nitrogen shielding.

A detector temperature in the range between 12 – 19 K can be expected without active regulation. A possible heat input from the LAAPD's, the preamplifiers and the cables were not included. It seems that no additional active heating or cooling will be necessary.

## 5.4 Material requirements

### 5.4.1 Scintillator

Some common scintillators with their properties are listed in table 5.1. Data are taken from [130, 132] and [124].

Due to the somewhat exotic read-out geometry and expected low photon number we started with the scintillator of the highest expected light output CsI(Tl). New compound products with a factor of two more light output than NaI(Tl) and CsI(Tl) like BrillanCe from Saint Gobain Crystals have not been considered due to their complicated structure. Due to its temperature dependence, discussed in details in section 5.5.2, it was mandatory to switch to pure CsI with its low wavelength of maximum emission,  $\lambda_{\text{CsI}} = 320 \text{ nm}$ .

## 5.4.2 Light guides

The transmission curves for light with  $\lambda_{\text{CsI}} = 320$  nm of possible light-guide materials are shown in fig. 5.16, right. The transmission curves for lucite is shown in green (maximum transmission 90 % [125]), that of Herasil [126], a clean amorphous quartz glass shown in blue, has a slightly higher transmission, but is much more difficult to machine. The required twisted shape may rule out the quartz based solutions.

## 5.4.3 Photon counting units

As a result from the simulations we will expect a small number of photons at our detector for each incident proton. Therefore, it is mandatory to use detector units capable to detect for single-photon events. Photomultipliers with their large entrance windows and large internal gain would be a good candidate, but had to be ruled out due to the magnetic field and low temperature at the detector area. Long light guides with a length of 2-3 m would be necessary otherwise and hence increase the transmission losses unacceptably. The use of self-amplifying semiconductor detectors, APDs or LAAPDs inside high magnetic fields has been reported by Fernandes et al. [127]. Their performance at low temperatures will be discussed in chapter 6.

## 5.5 Experimental data

The experimental data presented in the following were taken at the *PAFF* accelerator (for a detailed description see section 7.1).

Low-energy proton detection with scintillators will be the first topic before the discussion will be expanded to the temperature dependence of CsI(Tl), CsI scintillators and LAAPD's. Preparation of thin CsI layers, their characterization and their hygroscopic behavior is the topic of the next part and finally first measurements with a small prototype of our detector concept with protons and electrons will be presented.

### 5.5.1 Low energy proton detection with scintillators

A CsI(Tl) crystal of  $10 \cdot 10 \cdot 10$  mm<sup>3</sup> size, optically coupled to a Hamamatsu photomultiplier R3292 was irradiated by a proton beam. The signal was amplified by a factor of 100 and fed into a multi channel analyzer (MCA). The kinetic energy of the protons was changed between  $E_{\text{kin}} = 10$  and  $E_{\text{kin}} = 35$  keV in steps of  $\Delta E_{\text{kin}} = 1$  keV. The spectra are shown in fig. 5.14 on the left hand side (2 keV steps up to 30 keV, one spectrum at 35 keV is also added). Each spectrum  $F(E_{\text{kin}})$  could be fitted by an exponential background plus a Gaussian with the fit parameters  $a_1 \dots a_6$  as follows.

$$F(E_{\text{kin}}) := \underbrace{a_1 e^{-a_2 E_{\text{kin}}}}_{\text{Background}} + \underbrace{a_3 e^{-a_4 (E_{\text{kin}} - a_5)^2}}_{\text{Gauss}} + a_6. \quad (5.1)$$

Different gamma-ray sources were used for energy calibration (<sup>241</sup>Am, <sup>133</sup>Ba, <sup>137</sup>Cs, <sup>57</sup>Co, <sup>55</sup>Fe) shown with the green crosses in fig. 5.14, right-hand side, together with the peak position of the proton spectra, full circles. Both fit very well and show the expected linear behavior. The error bars of 1 keV are caused by the spread in beam

energy from the accelerator setting at that time (double peak structure caused by two acceleration potentials; further explanations are given in section 7.1).

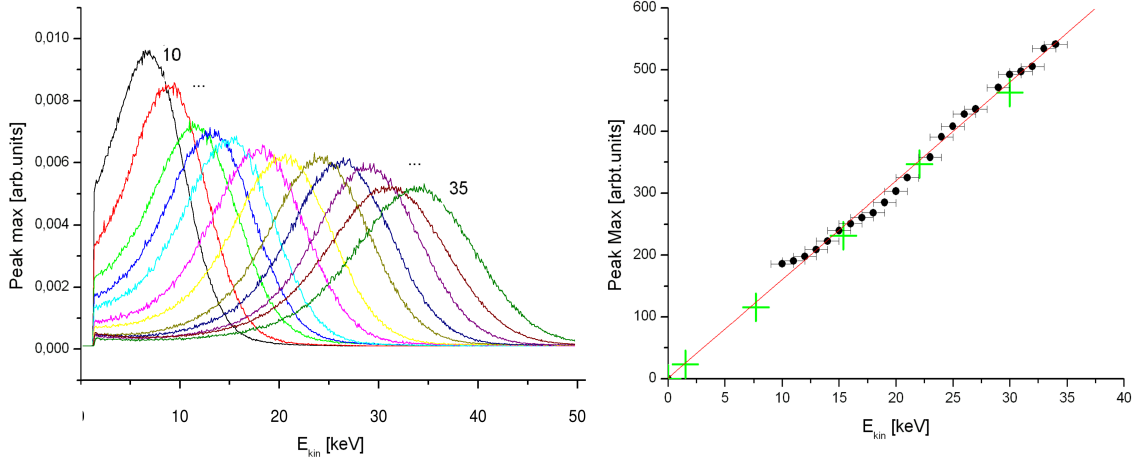


Figure 5.14: Left: Pulse height spectra for different proton beam energies from the *paff* accelerator. Right: channel number of the peak maximum as function of the beam. Also shown are the peak maxima from  $\gamma$  ray and x-ray lines (green crosses) which have been used for the channel to energy calibration.

The signal-to-noise ratio for the 30 keV beam energy was approximately 100:1. Protons down to  $E_{kin} = 10$  keV can still be identified and detected. Assuming a typical conversion factor of 64000 photons/MeV [130], an emission wavelength of  $\lambda = 550$  nm and a decay time of approximately  $\tau_s = 650$  ns [130] for our CsI(Tl) crystal, we get (at a transmission probability of 25%),  $N = 480$  photons per 30-keV proton. Including the quantum efficiency 7.5% [129] of the used photomultiplier this number is reduced to  $N_{e\gamma} = 36$  electrons at the first dynode. The gain  $G$  at the used working voltage between cathode and anode is  $G(U = 1750 \text{ V}) = 2.5 \cdot 10^6$  and the resistance of the voltage divider  $R = 1000 \Omega$ . Using the theory for estimating signals from photomultiplier tubes (eq. 5.2) from [124] with  $\tau = RC$  and  $C = 10$  pF for typical photomultiplier tubes, one can calculate the expected voltage signal as function of time from our scintillator signals.

$$V(t) = \frac{GNeR}{\tau - \tau_s} (e^{-\frac{t}{\tau_s}} - e^{-\frac{t}{\tau}}) \quad (5.2)$$

$$V_{\max}(30 \text{ keV}) \approx 2100 \text{ mV}.$$

With the conversion range factor 4 used at our MCA for this setup the result is close to the measured value of about 500 mV for the 30 keV signals.

## 5.5.2 Low-temperature characterization

### CsI(Tl) and CsI scintillators

The temperature dependences of the light output of  $5 \cdot 5 \cdot 5 \text{ mm}^3$  CsI(Tl) and CsI [133] crystals were studied with the setup shown in fig. 5.15. The crystals were connected without grease to a  $5 \cdot 5 \cdot 100 \text{ mm}^3$  Herasil light guide with  $n \approx 1.7$ . The other

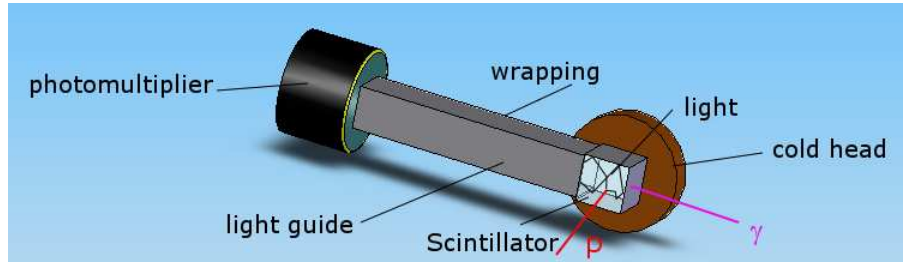


Figure 5.15: Setup for the first temperature dependence measurements and test of the wrapping materials. The photomultiplier stayed always at room temperature.

end was viewed by a low-noise Hamamatsu photomultiplier R2801 coupled to the light guide with optical grease. The signal was amplified by a shaping amplifier  $G = 2000$ ,  $\tau_{\text{shape}} = 2 \mu\text{s}$ , before being analyzed with the MCA.

In order to get a stable crystal-light-guide configuration it was necessary to wrap both of them. Wrapping was also necessary to get thermal contact to the surface of the cold head without creating a light sink through a dark surface. Different materials were used and the spectrum of an  $^{241}\text{Am}$  source measured with almost identical configurations. The comparison of the results is shown in fig. 5.16, left.

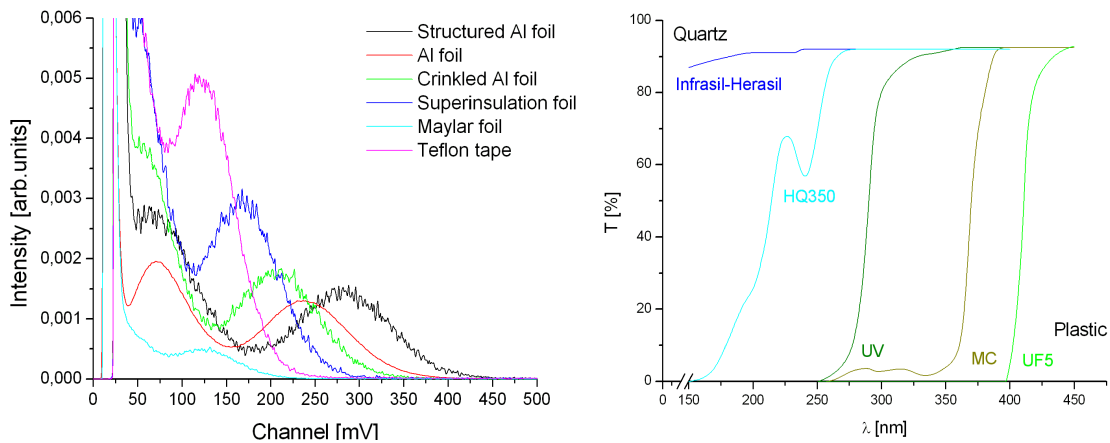


Figure 5.16: Left:  $^{241}\text{Am}$  spectra with CsI(Tl) connected to the quartz light guide structure as a function of different wrapping materials. The Al wrapped sample was measured with much more statistic. Right: transmission curves for plastic (green) and quartz (blue) as possible candidates for the light guides. Data have been taken from Herasil and Altuglass. Quartz samples 10 mm, plastic sheets had 6 mm thickness.

An aluminum foil with a pressed grid structure lead to the best light transmission, shown in black, but the smooth aluminum foil had the best signal-to-noise ratio and the best reproducibility. Similar observations may be found in reference [130] or [134]<sup>3</sup>.

<sup>3</sup>The maximum in light transmission through a light-guiding structure depends on the refraction index and on the coupling of the photon counter to the light guide. In the case of a refractive index  $n \approx 1.7$  and a coupling with optical grease a specular reflection at the foil that is in direct contact with the light guide is better than diffuse reflection at the wrinkled foil.

The scintillator-light guide package was then fastened on the cold head of the *pafl* facility ( $T = 15 - 400$  K) and illuminated by a  $^{57}\text{Co}$  source ( $E_\gamma = 136$  keV). The peak position from eq. 5.1 as function of temperature  $T_{\text{crystal}}$  is shown on the left-hand-side of fig. 5.17.

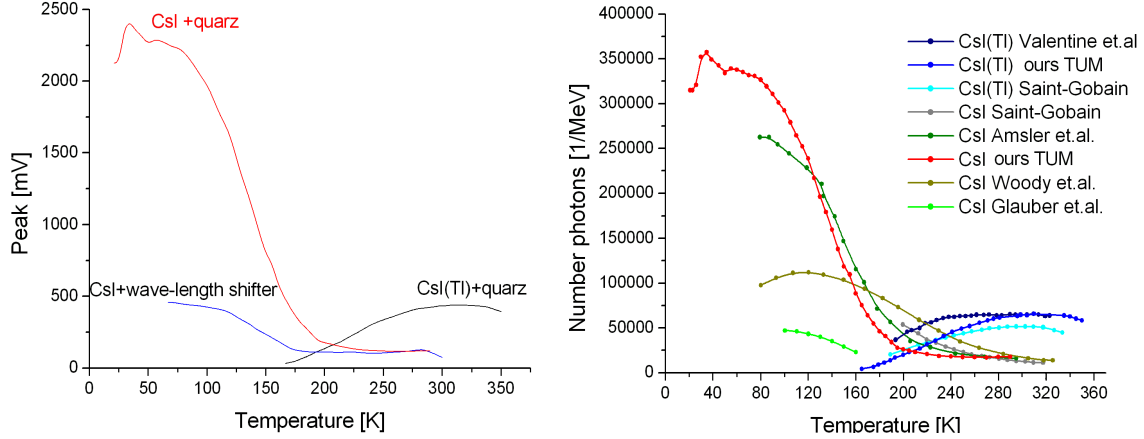


Figure 5.17: Temperature dependence of the light output from CsI(Tl) and CsI. Left: peak position as function of crystal temperature from this work. Right: number of photons per MeV calculated from our data and compared with other publications. The data from Saint-Gobain [135], Glauber [138] and Valentine [141] were already given in photons/MeV. Relative data from Amsler [137] and Woody [139] were normalized to the room temperature value.

To get the absolute light output as a function of the crystal temperature, as seen in fig. 5.17 right-hand-side, the conversion factor for CsI(Tl) at room temperature of 64 000 photons/MeV [130] and [131] (the extensively studied with crystals from four different manufacturers) was used to normalize our CsI(Tl) and CsI data. Also shown are other published data for comparison. The Saint-Gobain values were taken from the data sheet [135] of CsI-based scintillators 54 000 photons/MeV for CsI(Tl)<sup>4</sup>. The relative data for CsI from Amsler [137] and Woody [139] were normalized to the expected room-temperature value of CsI, 16 800 photons/MeV<sup>5</sup>, from Spectra physics [140]. The values from Glauber [138] and Valentine [141] were already published as photons/MeV.

For the CsI(Tl) measurement our data agree very well with the results from Saint Gobain and Valentine. The CsI values are consistent with those of ref. [137]. From this result we can expect an increase of a factor of four in the relative light output between CsI(Tl) at room temperature and CsI at low temperature. The low emission wavelength  $\lambda = 320$  nm, may be a disadvantage due to the quantum efficiency of the photon counter and for the transmission probability through the guide material.

Nishimura et al. [142] measured the luminescence spectra (LS) for pure CsI at various temperatures. One can see from fig. 5.18, left, how the energy of the emitted photons

<sup>4</sup>The light output of CsI(Tl) depends above all from the Tl doping concentration [136] which is not easy to find out for the special crystals.

<sup>5</sup>This value agrees very well with our measurement.

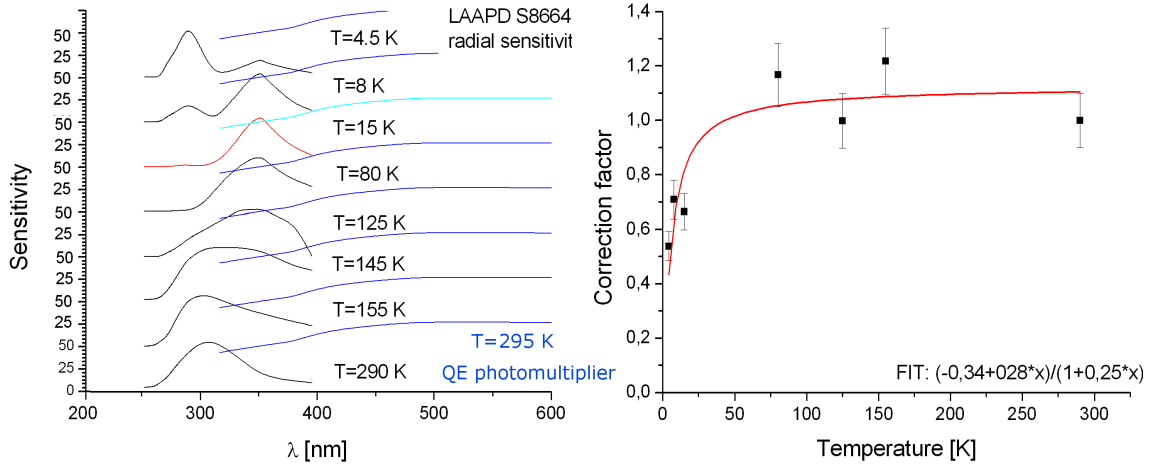


Figure 5.18: Left: excitation spectra from illumination of CsI with laser light as function of temperature [142] (black) together with the spectral quantum efficiency of the used photomultiplier (blue) which stays at room temperature. Right: the correction factor for the overlap of the spectral excitation of CsI and the quantum efficiency shown on the left side as a function of temperature. The integrated convolution of both curves, left, is normalized to the room temperature value.

changes with temperature. To exclude, that our measured temperature dependent light output (cf. fig. 5.17) was caused by the frequency shift towards higher photomultiplier quantum efficiency (QE) both, LS (at various temperatures) and QE were fitted by two Gaussians and folded. The integrated value of the folded equation  $H_{\text{fold}}$  is a measure on the overlapping of both quantities and thus the expected temperature behavior from this effect. The fit functions requires the following fit parameters  $A_{\text{LS}}(T) \dots F_{\text{LS}}(T)$  and  $A_{\text{QE}} \dots F_{\text{QE}}$ :

$$N_{\text{QE}}(\lambda) = \frac{A_{\text{QE}}}{B_{\text{QE}}\sqrt{\frac{\pi}{2}}} e^{-2\frac{(\lambda-C_{\text{QE}})^2}{B_{\text{QE}}^2}} + \frac{D_{\text{QE}}}{F_{\text{QE}}\sqrt{\frac{\pi}{2}}} e^{-2\frac{(\lambda-E_{\text{QE}})^2}{E_{\text{QE}}^2}},$$

$$M_{\text{LS}}(\lambda, T_{\text{CsI}}) = \frac{A_{\text{LS}}}{B_{\text{LS}}\sqrt{\frac{\pi}{2}}} e^{-2\frac{(\lambda-C_{\text{LS}})^2}{B_{\text{LS}}^2}} + \frac{D_{\text{LS}}}{F_{\text{LS}}\sqrt{\frac{\pi}{2}}} e^{-2\frac{(\lambda-E_{\text{LS}})^2}{E_{\text{LS}}^2}}.$$

Figure 5.19, left shows the raw data, the single Gaussians in green and the corresponding fit curve in red for the luminescence spectra (example at room temperature) taken from [142]. For the photomultiplier quantum efficiency the same is shown on the right. The values were normalized to the room-temperature value to get the relative correction factor  $K_{\text{correction}}$  as function of temperature shown in fig. 5.18, right.

$$H_{\text{fold}}(\tilde{\lambda}, T) = \int_{-\infty}^{\infty} M_{\text{LS}}(\lambda, T) \cdot N_{\text{QE}}(\tilde{\lambda} - \lambda) d\lambda$$

$$K_{\text{correction}}(T) = \frac{\int_{\mathfrak{R} \neq 0} H_{\text{fold}}(\tilde{\lambda}, T) d\tilde{\lambda}}{\int_{\mathfrak{R} \neq 0} H_{\text{fold}}(\tilde{\lambda}, T = 295\text{K}) d\tilde{\lambda}}$$

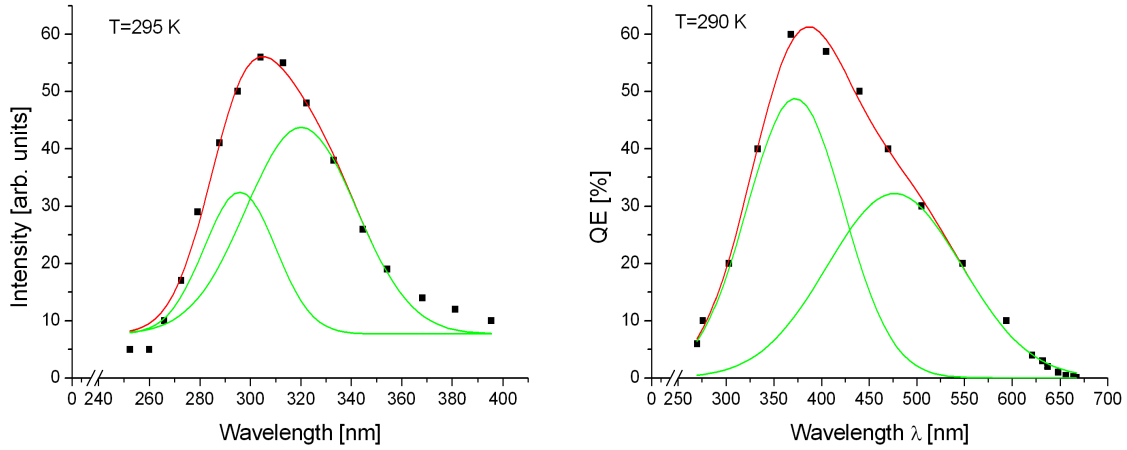


Figure 5.19: Left: example of the CsI excitation spectrum at 295 K [[142]] in black together with two Gaussians green lines to get the fit function shown as red. Right: quantum efficiency of the photomultiplier used in black and two Gaussians in green to get the fit function red curve. The fit functions are necessary for a later analysis, see text.

The 20% increase between  $T=300$  K and  $T=100$  K effected by the wavelength shift cannot explain the factor of four gain in the light output. Thus, we may expect that more light per incident deposited energy is created or extracted at lower temperatures. The onset of the steep drop of the scintillation efficiency, at  $T=30$  K can be linked however to the intensity shift from the 350 nm excitation level to the 280 nm band [142] and the much lower QE of our photomultiplier at this wavelength. The data at  $T=125$  K were excluded due to the sudden drop to zero of the excitation spectra which leads to unrealistic Gaussian fit functions compared to the neighboring curves. From our data we extract a desired working temperature between 25 K and 50 K.

Also shown in fig. 5.17 is the temperature dependence of the light output using a wavelength shifting bar [143] as light guide ( $\lambda_{\text{absorption}} = 340$  nm  $\rightarrow$   $\lambda_{\text{emission}} = 425$  nm) (values from the data sheet). The measured intensity in our case was a factor of five lower. Comparing the typical excitation wavelength from fig. 5.18 at  $T=100$  K with the absorption band leads to just 45% overlap. Another point to consider is that the wave shifting centres act as new point like sources emitting the light in  $4\pi$  direction [144]; thus half of the shifted light is emitted in the direction opposite to the photomultiplier and is lost. Both factors lead to an expected saturation at  $\approx 0.22$  times the quartz results (the naively expected saturation at 510 mV can be compared to our measured result fig. 5.17).

### Estimation of the scintillation light

The results from the Al-foil wrapped CsI(Tl) system with the  $^{241}\text{Am}$  source (shown in red in fig. 5.16) and the results from the  $^{57}\text{Co}$ -source measurement shown in fig. 5.17 were used to calculate the expected signals from proton illumination. The energy  $E_\gamma$  of the incident  $\gamma$ -ray times the conversion factor for the CsI(Tl) crystal, 64 pho-

tons/keV, leads to the number of created photons. This number has to be reduced by the transmission losses of about 25% and the quantum efficiency of the photomultiplier to get the number of primary electrons from the photocathode. From eq. 5.2 and the values for the photomultiplier used we get the raw signal  $E_{\text{photo}}$ . The influence of the shaping amplifier (typically with  $n=4$  differential integration stages and a shaping time  $\tau_s = 2 \mu\text{s}$  is taken into account by eq. 5.3 from [130], leading to the measured spectra  $E_{\text{spectra}}$ .

$$E_{\text{signal}} = E_{\text{photo}} \left( \frac{t}{\tau_s} \right)^n \cdot e^{-\frac{t}{\tau_s}} \quad (5.3)$$

Calculated and measured peak positions are listed in table 5.3. These results lead to predictions for the spectra to be expected when the CsI crystal is illuminating at  $T=35$  K with 30 and 45 keV protons. The decrease of light output (by a factor of four lower deposited energy) as well as the reduced light transmission (10%) due to the perpendicular illumination from the proton beam instead of the straight configuration (source, crystal, light guide, photomultiplier in one line), shown in fig. 5.15 was considered.

Data in [ch.]	$^{241}\text{Am I}$	$^{241}\text{Am II}$	$^{57}\text{Co}$	30 keV $p$	45 keV $p$
expected peak	320	120	640	155	240
measured peak	250	90	500	80	190

Table 5.3: Calculated channel number for the different energy spectra from the listed radioactive sources compared with the measured ones.

Together with the known signal-to-noise ratio the prediction was to see the 30 keV protons as shoulder and the 45 keV protons separated from the exponential noise. The measured spectra are shown in fig. 5.20.

The gap between scintillator and light guide as well as that between light guide and photomultiplier was taken into account by the simulation. This, together with the non-perfect wrapping may explain the 30% difference between expected and measured value in table 5.3.

### The temperature-dependent transmission of the light guides

A pulsed LED, emitting light with a wavelength  $\lambda = 325$  nm, close to the expected light emission maximum of CsI, was used to measure the transmission function of quartz and the wavelength shifter [143] down to  $T=20$  K. The small decrease (of the order of 5%) for the wave shifting bar and the 3% decrease for the quartz light guide may be easily explained by thermal expansion and inverse change of gap width (crystal  $\leftrightarrow$  lightguide, light guide  $\leftrightarrow$  wrapping, light guide  $\leftrightarrow$  photomultiplier).

### 5.5.3 The photon counting unit

The use of low-noise photomultipliers was ruled out by the low temperature and the high magnetic field in the PENeLOPE setup. Both would require long light guiding systems with increased light transportation losses, a more complicated construction and

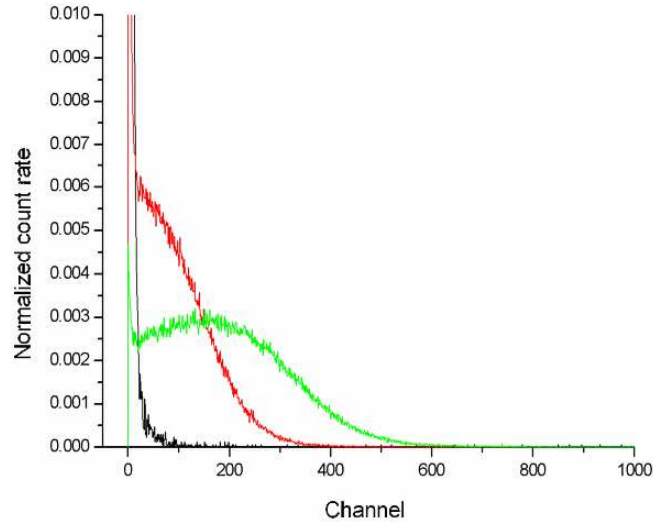


Figure 5.20: Pulse-height-spectra measured with the CsI crystal at  $T=34$  K. Shown in black are the data without beam, in red and green those with 30 keV and from 45 keV protons respectively.

a higher heat input to the He-bath cryostat. The second choice mentioned in section 6 is to use semiconductor detectors as closely as possible coupled to the scintillator. Extensive studies on their temperature behavior have been performed and are presented in a separate section ???. The promising result is that we can use LAAPDs down to 20 K. The gain is still  $G = 300$  for the Hamamatsu S8664-1010 and  $G = 1000$  for the RMD LAAPD respectively. The low noise in the primary signal is a big advantage for our low photon counting mode.

### 5.5.4 Thin film CsI scintillation counter

A film of  $600 \frac{\mu\text{g}}{\text{cm}^2}$  CsI was evaporated in vacuum (thermal deposition [145]) at the target laboratory of the Physics Department on an area of  $5 \cdot 10 \text{ mm}^2$  of two Herasil quartz tubes of  $5 \cdot 5 \cdot 25 \text{ mm}^3$ . Besides the experimental proof that they may be used as low-energy proton detectors, a possible change in the evaporated structure after storing the hygroscopic CsI layer in air was another topic. Thus, one sample was used for surface inspection with a scanning electron microscope SEM.

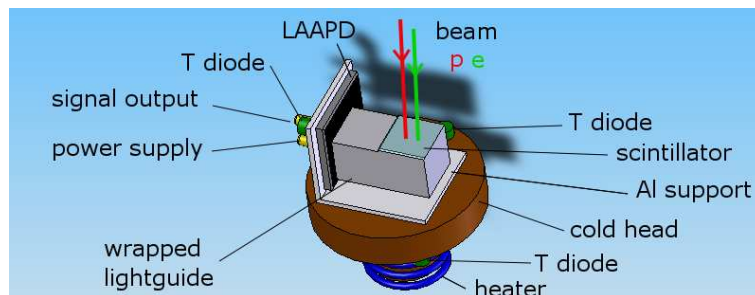


Figure 5.21: Setup to measure at 50 K the efficiency of the thin film CsI layer detector.

The other sample was mounted on the cold head to measure the light output when illuminated by protons (fig. 5.21). The photon counter was an RMD LAAPD held at the same temperature. Pictures of the surface and spectra were taken after different exposition times  $t_{\text{exp}}$  to air at a relative humidity of 50%.

### Crystal characterization

The SEM (Scanning Electron Microscope) pictures (cf. fig. 5.22) were taken after exposition times  $t_{\text{exp}}$  of 0.1 h, 3 h, 6 h and 20 h. Four different model grains were used at each picture to get the size distribution of each picture and the grain size evolution as function of exposition time. The spread of the grain sizes is shown as the error bars. The average grain size  $d_{\text{grain}}(t_{\text{exp}})$  increased during this time from 150 nm diameter<sup>6</sup> to 1.3  $\mu\text{m}$ .

It turned out, that the mean crystal diameter  $d_{\text{grain}}$  as seen in fig. 5.22 can be described as function of exposition time  $t_{\text{exp}}$  by a rational fit. The result of the picture analysis together with a rational fit eq. 5.4 on the crystal growth is shown in fig. 5.23

$$d_{\text{grain}} = \frac{1.44 \cdot t_{\text{exp}}}{3.31 + t_{\text{exp}}} \quad (5.4)$$

Our results from the SEM measurements are consistent with atomic force microscopy (AFM) pictures, also taken from evaporated CsI layers [146]. Their results are shown in fig. 5.24. The left picture was taken right after evaporation, the right one after 24 h storage in air. In this case, the crystal growth was less pronounced than in our case. From two different CsI evaporation speeds they got humidity driven growth rates between 430 nm and 860 nm per 24 h when the crystal was grown at a slow rate 0,04 nm/s, and 475 nm to 616 nm at a (fast) deposition rate of 1 nm/s.

### Scintillation characterization

As described, the second quartz tube was fixed on the cold head faced by an RMD LAAPD at an angle of  $90^\circ$  to the proton beam. Spectra for 40 keV-protons were taken with scintillator and detector kept at  $T=50$  K, as function of exposition time  $t_{\text{exp}}$  to air. After exposition to the beam, the test detector was always warmed up to  $T = 300$  K and kept there for at least ten hours before the vacuum was broken.

An example spectrum of a 30 keV proton beam after 10 h exposition is shown in fig. 5.25. The background shown in red in the figure is surprisingly high. This beam correlated background is caused by protons charging the aluminum wrapping leading to a current along the LAAPD surface or by direct hits of the LAAPD with beam-halo protons. Both contribute to the LAAPD dark current discussed at section 6. This effect was studied in detail more by scanning e.g. with the beam along the light guide LAAPD setup.

The fit function  $G_{\text{fit}}$  shown in the following equation was used to get the peak positions shown in fig. 5.26 as a function of exposition time.

---

<sup>6</sup>At the first picture the structure was smaller than the resolution of the SEM. The 150 nm are an upper limit from the measurements.

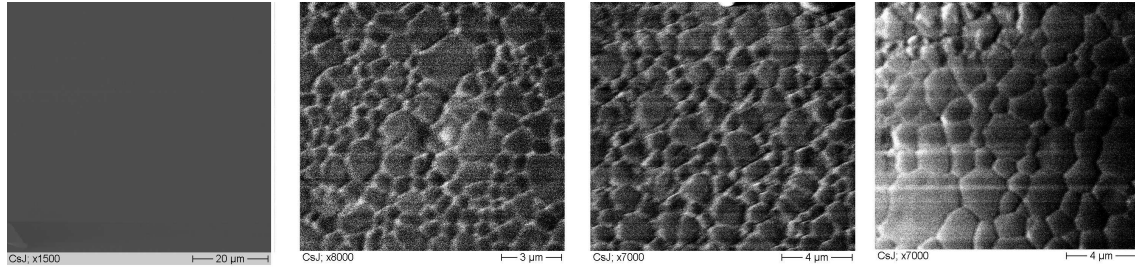


Figure 5.22: SEM pictures of the evaporated crystal structure as a function of the exposition time  $t_{\text{exp}}$  to air at an average humidity of 50%. From left to right:  $t_{\text{exp}} = 0.1$  h, magnification  $x=8000$ ,  $t_{\text{exp}}=3$  h  $x=8000$ ,  $t_{\text{exp}}=6$  h  $x=7000$ , and  $t_{\text{exp}}=20$  h  $x=7000$ .

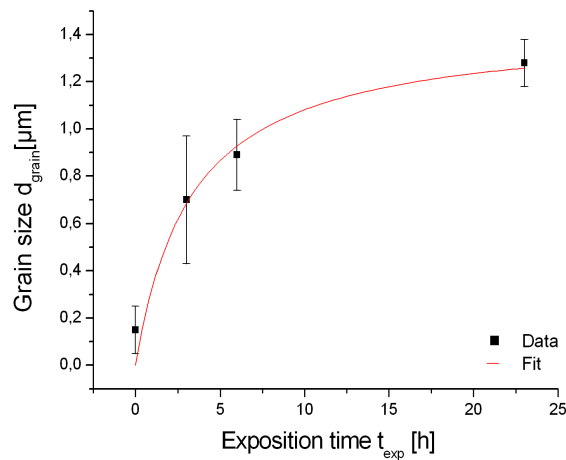


Figure 5.23: The average crystal diameter  $d_{\text{grain}}$  as estimated from the SEM pictures as a function of the exposition time  $t_{\text{exp}}$  to air with relative humidity of 50%.

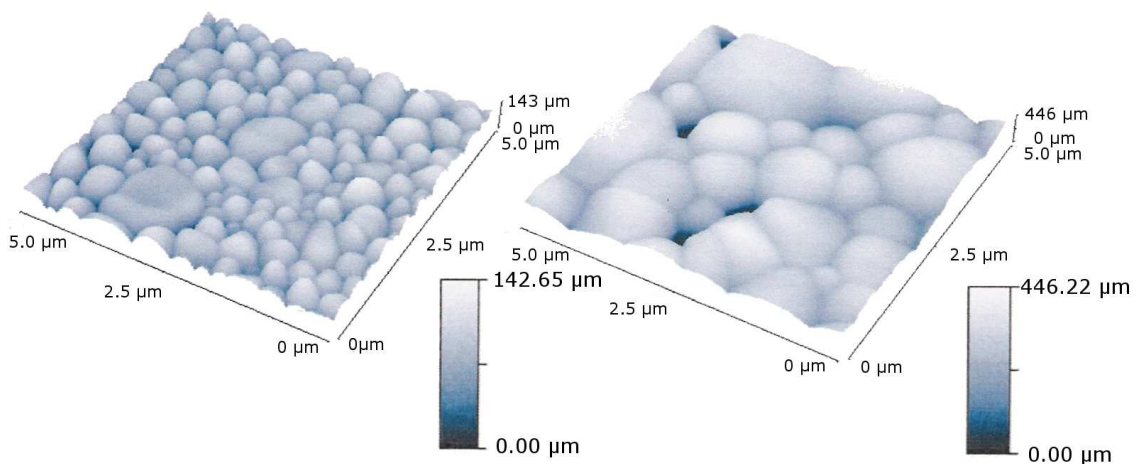


Figure 5.24: Atomic force microscopy pictures of an evaporated CsI layers directly after evaporation and after 24 h exposure to air [146].

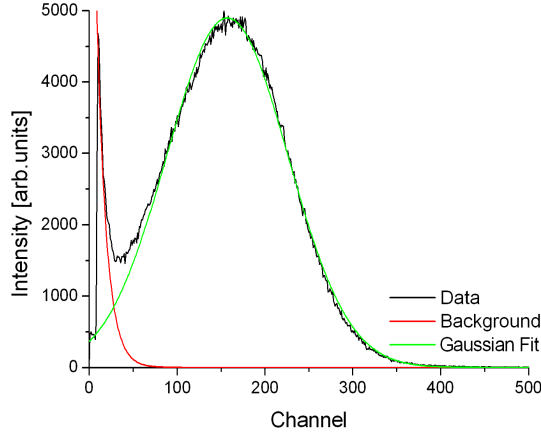


Figure 5.25: Pulse height spectrum of 30 keV protons from a 1.5  $\mu\text{m}$  evaporated CsI layer on a quartz light guide, read with a RMD LAAPD from the side. Detector temperature was 50 K. The scintillator was exposed 10 h to air (50 % relative humidity).

$$G_{\text{fit}}(t_{\text{exp}}) := M_{\text{amplifier}} \cdot \left( \underbrace{A(t_{\text{exp}}) \cdot e^{\frac{-t}{B(t_{\text{exp}})}}}_{\text{background}} + \underbrace{\frac{C(t_{\text{exp}})}{D(t_{\text{exp}}) \sqrt{\frac{\pi}{2}}} e^{-2 \frac{(t-E(t_{\text{exp}}))^2}{D^2}}}_{\text{signal}} \right) \quad (5.5)$$

The development of the peak position as function of exposition time is shown in fig. 5.26. The scintillation efficiency increased rapidly during the first 10 h and decreased over the next 30 h towards zero. This observation is in contradiction with the reduction of the quantum efficiency of CsI layers by 90 % when used as photocathode after 24 h exposition to air [147].

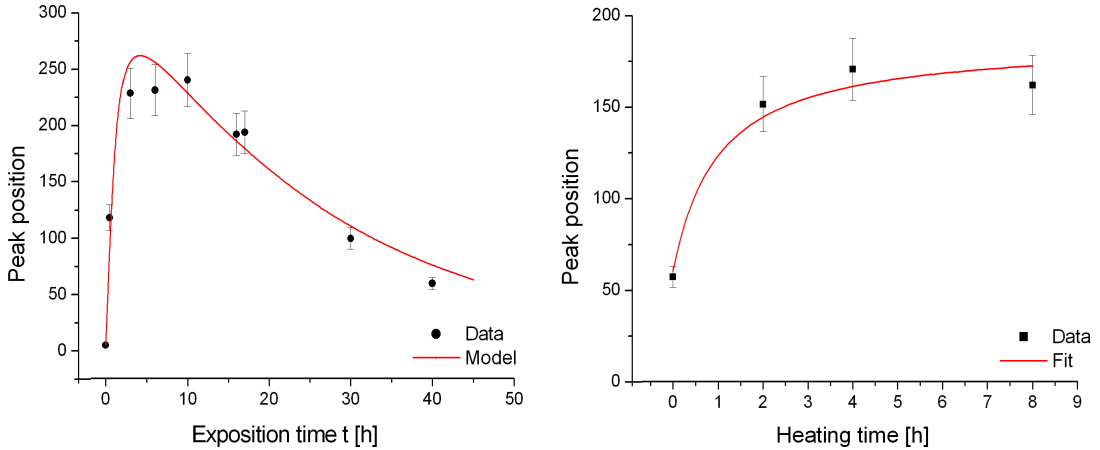


Figure 5.26: Left: measured peak positions for 40 keV proton spectra taken with the thin layer CsI detector and RMD LAAPD at 50 K as function of air exposition time (relative humidity 50%). Right: measured peak position as function of holding time at  $T = 353$  K, measured at 50 K. Results of a heoretical model are shown in red.

We assume that the water bound to the hygroscopic crystallites can be separated into two categories. In the first 10 h the situation is dominated by water entering the column-shaped CsI crystals (crystal water). Bigger crystals grow by decreasing smaller ones. Thus, the homogeneity and the average crystal size is increasing, as indicated in figs. 5.23 or 5.24. If all crystals have the same size the system reaches thermodynamic equilibrium and the process saturates after approximately 10 to 15 h. From this point on, the second process the build-up of water layers on the surface, becomes important.

The diameter of the crystal will increase with time  $t_{\text{exp}}$  as described by the fit function of fig. 5.23. The inverse of the typical crystal diameter (eq. 5.4) may be used as an indication of the number of surfaces per 1  $\mu\text{m}$  unit length (equal to the thickness of the layer). At each surface boundary we can assume to lose a fraction  $P_2$  (a fit parameter) of photon intensity which are lost by scattering during non perpendicular transmission through the evaporated layer. A gain effect on the light transport occurs with a power law of the surface density (transmission of light through glass plates). At the same time the continuously growing water layer on the surface reduces exponentially the energy of the protons reaching the scintillator ( $e^{P_3/t_{\text{exp}}}$ ). The number of created photons decreases, leading to a reduction in the peak position. Additional losses due to the evaporation process and the unknown quantum efficiency of the used LAAPD are taken into account by the fit parameter  $P_1$ .

The expected peak position leading to the red line can be calculated now by the following equation:

$$C_i = M_{\text{amplifier}} \cdot C_{40 \text{ keV}}(T_{\text{CsI}} = 50 \text{ K}) \cdot P_1 \cdot \underbrace{P_2^{\frac{1}{d}}}_{\text{gain}} \cdot \underbrace{e^k}_{\text{loss}}$$

$$C_i = M_{\text{amplifier}} \cdot C_{40 \text{ keV}}(T_{\text{CsI}} = 50 \text{ K}) \cdot P_1 \cdot P_2^{\frac{3,31+t_{\text{exp}}}{1,44t_{\text{exp}}}} \cdot e^{-\frac{t_{\text{exp}}}{P_3}}$$

$$P_1 := 0.042 \quad P_2 := 0.75 \quad P_3 := 25$$

The factor  $M_{\text{amplifier}}$  consists of the known gain (sector 6) of the LAAPD at 50 K, preamplifier, main amplifier and light transport losses.

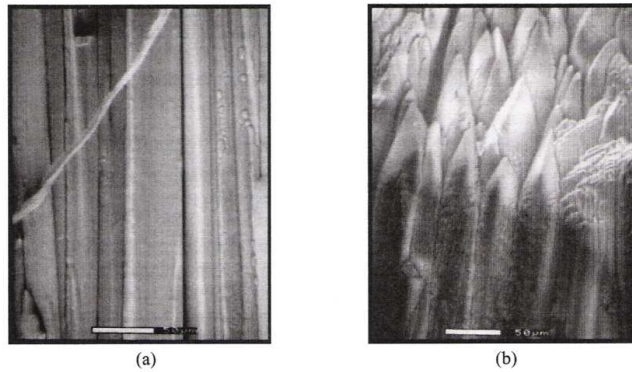


Figure 5.27: SEM pictures of a cut through an evaporated CsI crystal with a column-like growth [114, 148].

A necessary assumption for our model is that the crystals are growing in a column-like structure. This can be seen from the pictures where the evaporated layers have been cut perpendicularly to the substrate (shown for example in fig. 5.27, published by [114, 148]).

Our curve describes the experimental value for the signal height as function of exposure time quite well. The three extracted fit parameter  $P_1$ ,  $P_2$  and  $P_3$  have the following physical meaning. Together with the *SRIM* simulations (fig. 5.5)  $P_3$  leads to a rough estimation for the water growth rate on a hygroscopic material, by comparing the energy loss as function of layer thickness with the signal reduction as function of time. The fit parameter  $P_1$  leads to an estimation of the quantum efficiency of the RMD LAAPD at  $\lambda = 320$  nm. The 4.2% are in good agreement with the extracted value estimated at section 6. from the comparison of the RMD LAAPD with the Hamamatsu LAAPD. The quantum efficiency of the Hamamatsu LAAPD, which is stated in the data sheet with 45%, was measured to be ten times larger than that of the RMD LAAPD under the same experimental conditions ( $\text{RMD}_{\text{expected}} \rightarrow \approx 4.5\%$ ).

The fit parameter  $P_2$  describes the transmission probability of the scintillation light at a crystallite surface boundary.

One prediction of this theory is that the surface water should be partially removed by heating the substrate and pumping inside a vacuum chamber. The predicted increase of light output as a function of  $t_{\text{heating}}$  at  $T = 353$  K is shown in fig. 5.26, left. The spectra have been taken under the same beam and detector conditions as before. About 50 % of the maximum light output could be recovered. A further increase of temperature is not possible without the risk of changing the doping profile inside the semiconductor,  $T_{\text{semiconductor}} \leq 80^\circ \text{C}$  detectors.

## Electron background

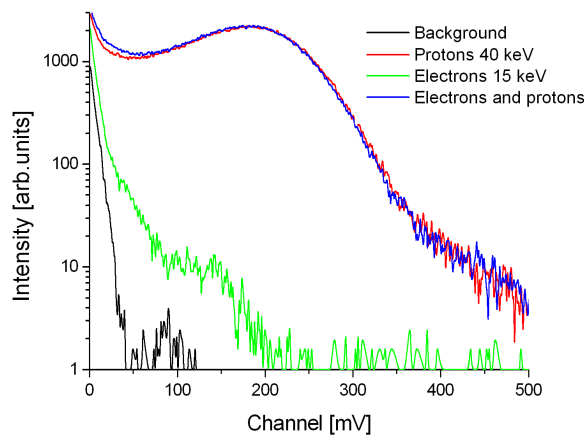


Figure 5.28: Puls-height spectra taken without beam (black), 40 keV protons (red), 15 keV electrons (green) and electrons and protons together (blue) measured with the test detector CsI layer on a light guide viewed by a RMD LAAPD at 50 K.

In order to check a possible response of the thin-layer scintillation counter to the neutron decay electrons, different spectra were taken: 40 keV protons and 15 keV electrons hit the detector at rates of  $3 \cdot 10^4 \text{ s}^{-1}$  and  $1 \cdot 10^4 \text{ s}^{-1}$  respectively, either alone or together. The result is shown in fig. 5.28. The background spectrum without beams is shown in black, the proton and electron beams are shown in red and green, and the combined spectrum is shown in blue. All spectra were measured for 5 min at a temperature of 50 K for both, crystal and LAAPD. One has to keep in mind that still a number of halo electrons may hit the LAAPD or the wrapping contributing also to the measured spectra.

As expected from earlier simulations, the electrons cause a negligible increase of the background, well separated from the proton signal.

## 5.6 Main detector concept

The result of the investigations presented so far led to the following possible realization of the proton detector for the *PENeLOPE* neutron lifetime experiment. It is shown in fig. 5.29. Just for simplicity, the detector was constructed using the RMD LAAPD's. It is easy however to incorporate the Hamamatsu LAAPDs.

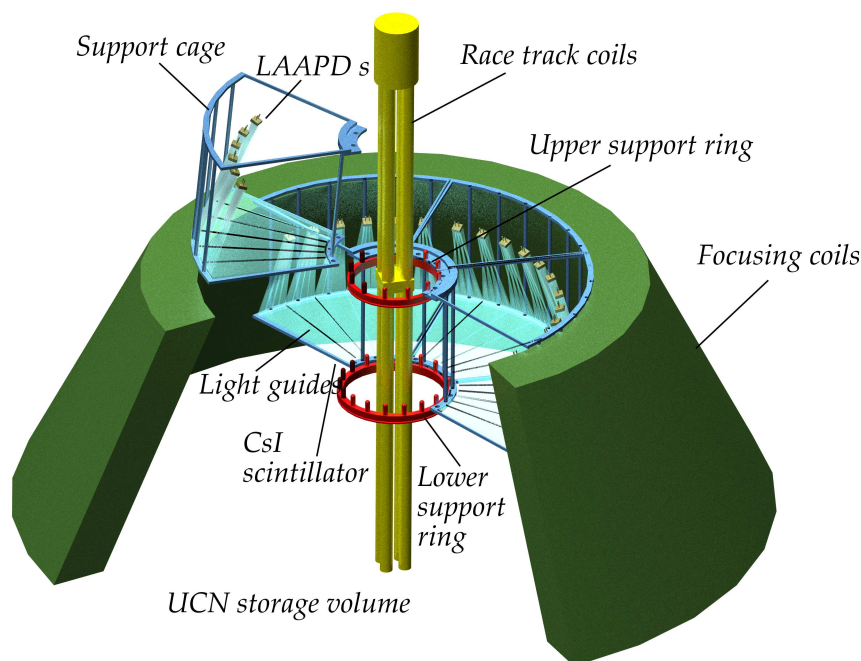


Figure 5.29: Scheme of the proton detector for the PENeLOPE lifetime experiment.

The detector area is covered by 36 trapezoidal light guides with a  $1\mu\text{m}$  CsI layer

evaporated on the bottom side. After ten hours exposure to air another reflective isolating layer of a thickness in the nm range may be evaporated. The long side of each trapezoid will be connected via a twisted light guide to one LAAPD. The preamplifiers will be placed close to the photon counters at low temperature. Six detector panels could be mounted onto one frame. The six segments are then connected by a plug-in system on two support rings in the middle of the cryostat. Behind the panels, will be enough free space for the ring shape accelerating electrode not shown in fig. 5.29. The amplified signals from the 36 detectors are then guides through the nitrogen shield and through the vacuum-tight connectors to the main amplifier outside the experiment.

## 5.7 Evaluation

**CsI layer** The detection of low-energy protons with evaporated CsI scintillators at low temperatures was proven. This may open the possibility to produce large-area evaporated detector systems in different shapes. Background signals from electrons do not play a role as long as the CsI layer is sufficiently thin.

**Trapezoids** The trapezoid solution has the advantage that it consists of 36 identical detector panels. They can be produced easily and tested separately even in larger numbers than later needed for possible exchanges. The corresponding electronic settings can be fine tuned outside with calibration sources to finally give identical performance of all units.

**Sections** The combination of six panels to one segment makes it easier to mount them into the neutron storage bottle on a rotatable support rings. Due to a lack of space just an angle of for example  $100^\circ$  is necessary for plugging one segment after the other onto the rings. This rotating system can be used later to test the symmetry of the storage and extraction B fields. A fixed reference LED below the focusing coils can be used for in-situ calibration of the actual facing panel.

**Acceleration electrode** In our case the photon counting unit as well as the electronics stays at ground potential. Therefore, it should be possible in principle to keep enough distance between the acceleration electrode and some safety lightning rod to avoid any breakthrough to the LAAPD or the electronics. Besides the higher electric field it is also possible to guide the protons towards the race-track coils where the light transmission through the guide seems to be better.



# Chapter 6

## Large area avalanche photodiodes (*LAAPDs*)

The large-area avalanche photo diode (LAAPD) is a good candidate as photon counting unit for the planned proton detector in the *PENeLOPE* experiment. Its well known good performance in high magnetic fields [149], its non problematic use in ultra high vacuum and its sensitivity to a small number of photons due to the avalanche process solves three of our requirements. The alternative, photomultipliers, are problematic due to low temperature and high magnetic fields in *PENeLOPE*. We have however to extend the working temperature range defined by the manufacturer,  $T > -30$  °C to cryogenic temperatures,  $T \approx 10$  K, which is another prerequisite for our planned detector. After an introduction to the working principle of PiN diodes and avalanche photodiodes APDs, followed by a description theory on the avalanche process and noise, the two most common realizations for LAAPDs are described. Both types were used for temperature studies and the data are presented in this chapter. Some of the mentioned differences will then be used to give a hint on their low temperature behavior.

### 6.1 Basic information

Some equations from the theoretical description of the amplification and the noise are introduced for later use to understand the experimental data.

#### 6.1.1 PiN diode

APDs are semiconductor photon/particle detectors with an internal current amplification mechanism. The underlying basic principle of a PiN diode with its scheme, doping profile and resulting electric field distribution is shown in fig. 6.1.

A PiN diode consists of a thick n-doped silicon layer with a relatively small p-doped entrance layer. The charge free area between the highly doped regions is called the depletion zone. A voltage applied between the electrodes on both sides of the junction increases the depletion zone and leads to the shown potential. Ionizing particles (radiation) which deposit sufficient energy  $E_\gamma$  in the depletion zone create primary electron hole  $e^-h^+$  pairs. For Si 3.6 eV are necessary <sup>1</sup> per pair. The free charges are accelerated

---

<sup>1</sup>The necessary energy for Si at room temperature is 3.62 eV which is about a factor of three higher than the band-gap  $E_\Delta = 1.1$  eV. This means that less than a third of the energy deposited

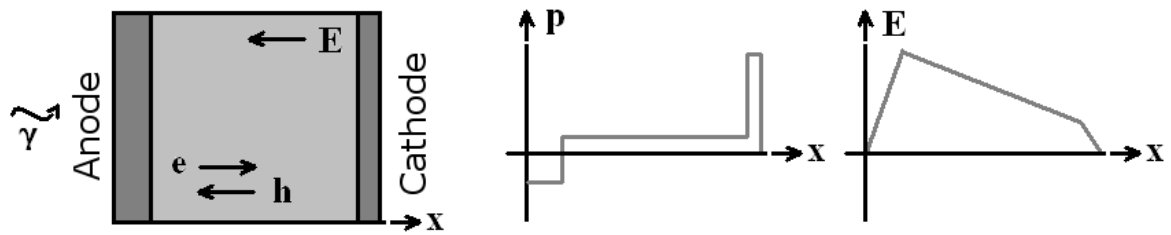


Figure 6.1: Structure of a PiN diode (left-hand side) with the p-doping profile (middle) and the resulting potential profile (right-hand side). The motion of the charge carrier electrons  $e$  and holes  $h$  are shown inside the electric field  $E$ .

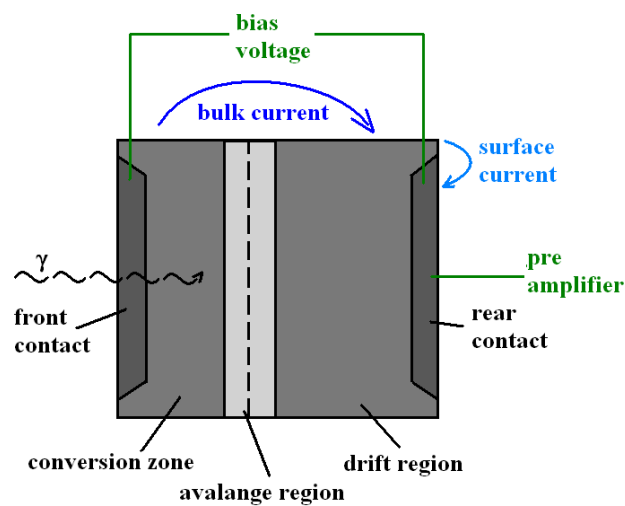


Figure 6.2: The five different zones of a typical LAAPD structure together with the most important noise currents [150].

by the applied  $E$  field and drift in opposite directions to the electrodes. The charge accumulated is proportional to the deposited energy  $E_\gamma$ .

### 6.1.2 APD diode

If the charge carriers gain enough kinetic energy to create secondary electron-hole pairs, an avalanche reaction is started. The signal from the APD is still proportional to the incoming  $E_\gamma$  this time however multiplied by the internal gain  $M$ .

Different schemes to optimize the internal gain have been realized for different purposes and to enlarge the detector size to get large area avalanche photon detector *LAAPD*. Reverse and beveled edge types are the most common ones. Their different doping profiles, doping concentrations, layer thicknesses and overall shape are shown in fig. 6.2. All LAAPD have the following in common:

**Front contact:** In order to reduce the entrance resistance, the front contact is rather thick. A few tenth of an Ohm would start to influence the white noise of the detector significantly but the absorption in thick entrance dead layers for low energy photons ( $\lambda < 500$  nm) is not negligible. A compromise is found at a thickness of  $\approx 200$  nm.

**Conversion zone:** In this region the deposited energy  $E_\gamma$  leads to the number of primary  $e^-h^+$  pairs. The quantum efficiency of the detector is a measure for the conversion rate from the deposited energy into the number of  $e^-h^+$  pairs. A typical depth of a few  $\mu$  m is sufficient and fits to the attenuation length of light ( $\lambda = 500$  nm in Si  $1\mu\text{m}$ ). To reduce the amount of thermally excited electron-hole pairs, which scales with the volume, is the main reason to keep this layer as thin as possible. Another reason is to avoid signals caused by other particles flying through the detector.

**Avalanche region:** The avalanche region is the highly doped part next to the PN transition (dashed line). The electric field caused by the applied bias voltage  $U_{\text{bias}}$  reaches gradients of  $1 \cdot 10^2 - 1 \cdot 10^4$  Vcm $^{-1}$ . These high fields are necessary to accelerate the primary charge carriers fast enough ( $E_{\text{kin}}(e^-h^+) > 3.6$  eV) to create secondary  $e^-/h^+$  pairs which are again accelerated by the  $E$  field to produce the chain reaction.

**Drift region:** The majority of the charge carriers, in our case electrons, drift through the  $\approx 1$  mm thick low resistance zone to the rear contact. Because the diode capacity contributes linearly to the noise (eq. 6.5) its very high value at the PN edge is reduced to a lower value by this drift region.

**Rear contact:** This contact is used to collect the produced charge and transport it to the preamplifier. Similar to the front contact, this one is also highly doped to get low resistance. As the absorption problem of incident gamma rays does not exist the thickness is negligible.

---

by radiation is actually spent to produce  $e^-h^+$  pairs. The other two thirds go into exciting lattice vibrations [124].

## 6.2 Theoretical description

### 6.2.1 Internal gain

The internal gain  $M$  is the ratio of the electron number created by the incident radiation  $E_\gamma$  and the number of electrons at the rear contact. We define the probability per unit length  $W_e$  that an additional electron-hole pair is created inside the avalanche zone (thickness  $x=0..w$ ). It is a function of the ionization coefficient  $\alpha_e$ ,<sup>2</sup> the incident electron current  $I_e$  and its charge  $e$ . In a similar way, the corresponding probability  $W_h$  for holes is introduced (hole ionization coefficient  $\beta_h$ ):

$$W_e = \alpha(v_e) \frac{I_e}{e} \quad W_h = \beta(v_h) \frac{I_h}{e}.$$

It is important to point out that both coefficients  $\alpha_e$  and  $\beta_h$  depend strongly on the particle velocity  $v_{e,h}$  and thus on the temperature and the applied electric field  $E$  (cf. eq. 6.1).  $\mu_e$  and  $\mu_h$  are the mobilities of electrons and holes, respectively. The latter strongly depend on the diode structure and the doping profile [151]. The velocity is

$$v_e = \mu_e(T) \cdot E \quad v_h = \mu_h(T) \cdot E. \quad (6.1)$$

Let us assume that an electron is injected at  $x = 0$  into the avalanche zone; the gain  $M$  from higher order pair generations after a distance  $[0 \leq x_0 \leq w]$  can be written as:

$$M_e = e \int_0^{x_0} \alpha_e(v_e) dx.$$

For a more realistic case also the holes are assumed to participate in the multiplication process ( $\beta \neq 0$ ) and the equation for the gain becomes more complicated [153, 152]:

$$M_e = \frac{1 - k_1}{e^{-\delta(1-k_0)} - k_1} \quad (6.2)$$

$$\delta := \int_0^w \alpha dx, \quad k_0 := \frac{\int_0^w \beta dx}{\int_0^w \alpha dx}, \quad k_1 := \frac{\int_0^w \beta e^{\int_0^{x_0} (\beta - \alpha) dx'} dx}{\int_0^w \alpha e^{\int_0^{x_0} (\beta - \alpha) dx'} dx}.$$

Due to the dependence of  $\alpha_e$  and  $\beta_h$  on the position, the equation presented above are, in general, quite complicated. However, to demonstrate the dependence of the avalanche gain from the ionization coefficient, we will consider the two extreme cases illustrated in fig. 6.3 (middle and right).

i)  $\beta_h = 0$  :

Without any ionization due to the holes and a sufficiently strong  $E$  field, the formula for the gain simplifies to  $M = e^{\alpha_e \cdot w}$ . Under these conditions no avalanche breakdown exists and  $M$  increases exponentially with increasing values of  $\alpha_e \cdot w$ . The built-up of the chain reaction as a function of time and space is shown in the middle of fig. 6.3 and as function of applied  $E$  field as blue line in fig. 6.4.

---

<sup>2</sup>The energy dependent probability for an excitation ionization inside a semiconductor.

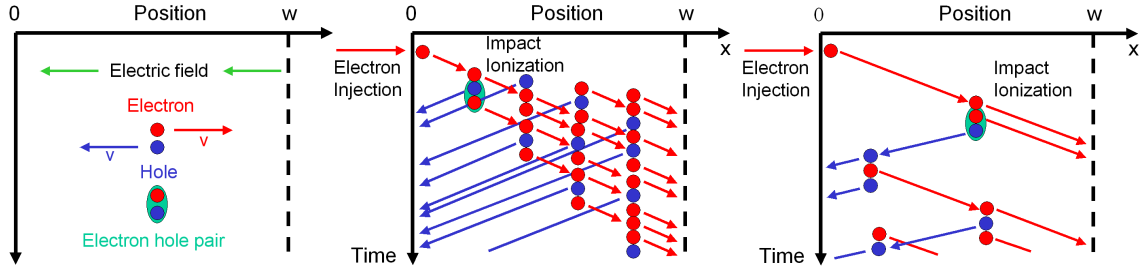


Figure 6.3: Schematic diagram of the avalanche multiplication process. Left: definition of the boundary conditions, middle: avalanche process with i)  $\beta = 0$ ; right: avalanche process with ii)  $\alpha = \beta$  [151].

ii)  $\alpha_e = \beta_h$  :

Now both, holes and electrons, contribute in the same way to the avalanche process. The  $E$  field leads again to an acceleration and the chain reaction. The gain equation simplifies to  $M = 1/(1 - \alpha_e \cdot w)$ . The break down voltage (gain  $\rightarrow \infty$ ) can be identified as  $\alpha w \rightarrow 1$ . On the average, every generated charge carrier generates another  $e^- h^+$  pair during its transition. This built-up of the avalanche gain is also shown in fig. 6.3 left and the dependence on the applied electric field as red line in fig. 6.4. This is the worst case for an APD.

The intermediate cases, when both electrons and holes contribute to the ionization process with different ionization probabilities, are the normal operation modes of APDs. The ratio  $k$  between the ionization coefficients<sup>3</sup> defined in eq. 6.3, is used to describe different LAAPD realisations or temperature dependences<sup>4</sup>. The gain  $M$  as function of the electric field  $E$  and therefore of the applied voltage  $U_{\text{bias}}$  for different values of  $k$  is shown in fig. 6.4 [154].

$$k = \frac{\beta_h}{\alpha_e} \quad (6.3)$$

## 6.2.2 Noise

The noise from the APDs can be separated into two categories:

**Serial noise:** The serial noise is the sum of the thermal noise from the preamplifier and that from the highly doped contacts of the semiconductor.

**Parallel noise:** The parallel noise current  $I_D$  consists of the surface (superficial) current  $I_{DS}$  and the bulk (volume) leakage current  $I_{DV}$  (cf. fig. 6.2). Impurities, dirt or covers for protective purpose cause a current flow across the surface. In contrast, the

<sup>3</sup>Silicon has the lowest  $k$  value and is best suited for such detectors;  $k_{\text{Si}} = 0.035$  compared for example to  $k_{\text{GaAs}} = 0.5$ .

<sup>4</sup>Values for pure Si at room temperature:  $\mu_e = 1350 \text{ cm}^2\text{V}^{-1}\text{s}^{-1}$  and  $\mu_h = 480 \text{ cm}^2\text{V}^{-1}\text{s}^{-1}$  [124].

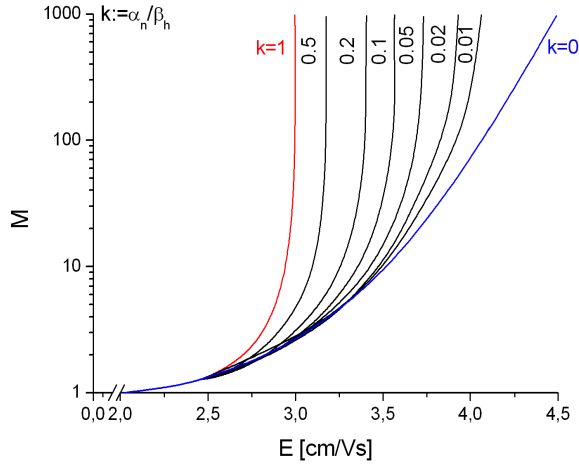


Figure 6.4: Calculated electron multiplication as a function of electric field for a  $1 \mu\text{m}$  thick PiN diode with  $\alpha = 3.36 \cdot 10^6 e^{(-1.75 \cdot 10^6/E)}$  for various  $k = \beta/\alpha$  [154].

bulk current is based on charge diffusion through the diode. The major contribution comes from impurities providing energy levels within the band gap that are already excited at lower temperatures. Spontaneously created electron hole pairs inside the depletion zone, travel through the avalanche zone and are amplified as well. The big advantage of the APD structure is, that the usually dominant surface current is not amplified with the internal gain  $M$ . Equation eq. 6.4 describes the separated noise contributions:

$$I_D = I_{DS} + M(U_{\text{bias}}) \cdot I_{DV}. \quad (6.4)$$

**Excess noise factor:** The output signal fluctuates, as dark current, production of  $e^-h^+$  pairs from the incident particle and avalanche chain reaction are random processes. The excess noise factor  $F(M)$  is a measure for this statistical noise.  $F(M)$ <sup>5</sup> depends strongly on the gain as well as on the ratio  $k$  between the ionization coefficients. Following McIntyre [152], one gets the following expression [155]:

$$F(M) \approx k \cdot M + \left(2 - \frac{1}{M}\right)(1 - k).$$

The equivalent noise charge  $ENC$  is one way to characterize a semiconductor detector. This quantity shows the charge that is equivalent to the final noise level:

$$ENC = \frac{1}{\sqrt{8}} \cdot \sqrt{\underbrace{2e \cdot \left(\frac{I_{DS}}{M^2} + I_{DV} \cdot F\right) \cdot \tau}_{\text{parallel noise}} + \underbrace{\frac{4k_B T R C_{\text{tot}}^2}{M^2 \tau}}_{\text{serial noise}}} \quad (6.5)$$

with  $\tau_s$  the shaping time constant,  $k_B$  the Boltzmann constant,  $T$  the absolute temperature and  $C$  the sum of the capacity from the diode, the preamplifier and the read out electronics.

<sup>5</sup>The excess noise factor for a good quality photomultiplier tube is 1.2 [153].

## 6.3 LAAPD structures

Figure 6.5 shows the two most common LAAPD structures, the "beveled edge" and two versions (normal and reverse) of "reach through" structures. One of each kind was used for the measurements presented in this thesis. Beside the similarities described above there are also differences. Some will be used later for the data interpretation.

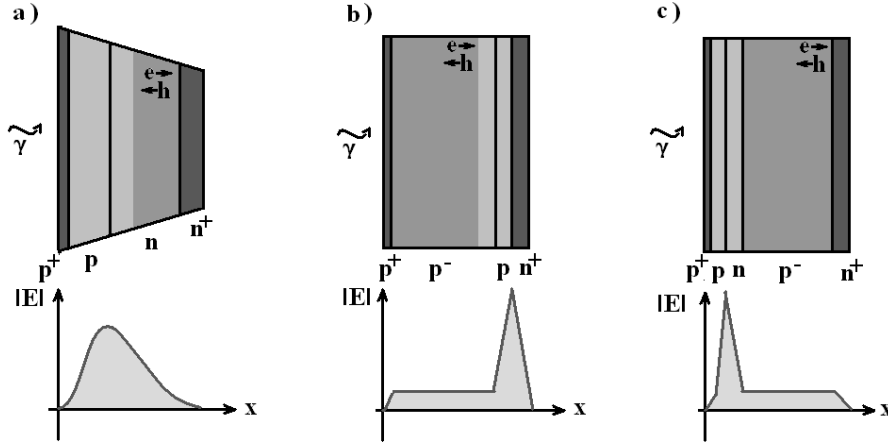


Figure 6.5: Structure, doping profile and corresponding electric field distribution of the a) beveled-edge, b) reach-through and c) reverse reach-through LAAPD types.

### 6.3.1 Beveled edge type

This structure can be produced by gallium diffusion into high-resistivity Si to form the  $p^+n$  profile. This doping structure allows much higher voltages ( $U_{\text{bias}} \approx 2000$  V) and higher gains ( $M \rightarrow 10000$ ). Etching the sides is necessary to avoid breakthroughs where the pn junction meets the surface [157]). The etching can be avoided, with high working voltages and high gains guaranteed if the doping concentration towards the surface is modulated in a similar way is the edged shape. Both devices have large depletion widths ( $\approx 100 \mu\text{m}$ ), but do not deplete the hole conversion area. The dark current which is generated in the wide n-type depletion region is multiplied less than the photo current and thus contributes less to the noise. Part of the  $p^+$  layer is removed to reduce losses inside this relatively thick layer. Beveled-edge types are the detectors from Radiation Monitoring Devices (RMD) [157]) which we used.

### 6.3.2 Reach through type

The reach through structure can be produced by epitaxial growth on a low-resistivity silicon substrate [156]. The complicated doping profile with a sharp PN junction divides the depletion zone into two regions. The necessary electric field is already reached at a moderate typical bias voltage of  $U_{\text{bias}} = 400$  V with a maximum gain of  $M \approx 1000$ . The large depleted conversion zone provides a signal that is independent of the penetration depth of the photon ( $E_\gamma$ ). At approximately  $M = 10$ , the drift zone is completely depleted and the multiplication varies much slower with  $U_{\text{bias}}$ . The operation of such

devices is much more stable. The disadvantage is a higher noise level caused by the amplified dark current component (larger conversion zone). There are two types: i) the reach through LAAPD with a long drift and short avalanche zone and ii) the reverse reach through LAAPD with a short drift and a long avalanche zone. The spectral quantum efficiency can be tuned by varying the dimensions of this zones. Perkin Elmer Instruments (PKI) and Hamamatsu photonics have specialized in this type of detectors [157].

## 6.4 Characterization

One reverse-reach-through LAAPD from Hamamatsu and one LAAPD beveled edge type from RMD have been used for our measurements. Typical data are listed in table 6.1

	Nr.	Active area [mm <sup>2</sup> ]	$U_{\text{breakdown}}$ [V]	$I_{\text{breakdown}}$ [nA]	$T_{\text{working}}$ [K]	$U_{M=1}$ [V]
RMD[158]	S1315P	13×13	1700-2300	500	270-300	250
Hamamatsu [159]	S8664-1010	10×10	300-400	100	250-330	50

Table 6.1: List of specified operation parameters.

This section is divided into two parts. First, the measurement of the working parameters as function of temperature is described. Afterwards, the temperature dependence of the achievable gain  $M$  and the noise down to 15 K is discussed.

### 6.4.1 Measurement of the working parameters as function of temperature

The two-stage cold head from the *paiff* accelerator was used for all temperature dependent experiments. As will be described in section 7.1, the temperature of the LAAPDs coupled to the second stage, can be varied between 15 K and 400 K. The dark current  $I_D$  was measured as a function of the bias voltage  $U_{\text{bias}}$  with a high-voltage nA and pA meter for different temperatures. The result is shown in fig. 6.6. Below approximately 240 K for the Hamamatsu and 220 K for the RMD diode, the exponential increase was too steep to get further information with the limited voltage resolution<sup>6</sup>.

The linear behavior on a logarithmic scale shows the exponential growth of the current with the applied voltage as expected for diodes. The data shown in blue were taken with the nA setting, the data shown as green lines with the pA settings and the dark yellow lines represent the intermediate one. The data in black shows values from the data sheets as the diode characteristics at room temperature in the Hamamatsu case and the break-down voltages  $U_{\text{break}}(T = 300 \text{ K})$  and  $U_{\text{break}}(T = 70 \text{ K})$  for the RMD. Whereas our Hamamatsu values agree very well with the data given by the manufacturer, the

---

<sup>6</sup>The high voltage step size was limited to  $\pm 2.5 \text{ V}$  for the Hamamatsu (nominal voltage of break down where  $M=\infty$   $U_{\text{breakdown}}(T = 300 \text{ K}) = 450 \text{ V}$ ) and  $\pm 12 \text{ V}$  RMD ( $U_{\text{breakdown}}(T = 300 \text{ K}) = 1900 \text{ V}$ ).

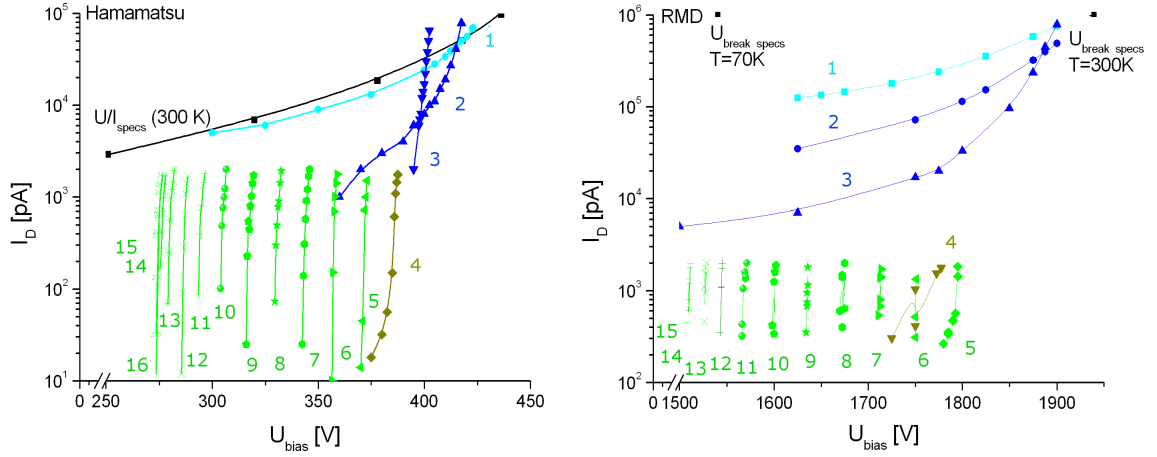


Figure 6.6: The measured  $U - I$  working function for the used LAAPD's (Hamamatsu right and RMD left) as a function of temperature. The black line and points are values from the data sheets. 1) 300 K, 2) 280 K, 3) 260K 4) 240 K, 5) 220 K, 6) 200 K, 7) 180 K, 8) 160 K, 9) 140 K, 10) 120 K, 11) 100 K, 12) 80 K, 13) 60 K, 14) 40 K, 15) 20 K, 16) 15 K.

extrapolated curves in the RMD case indicate an offset between set and applied voltage. This misalignment was measured and  $U_{\text{bias}}$  was corrected before the data analysis.

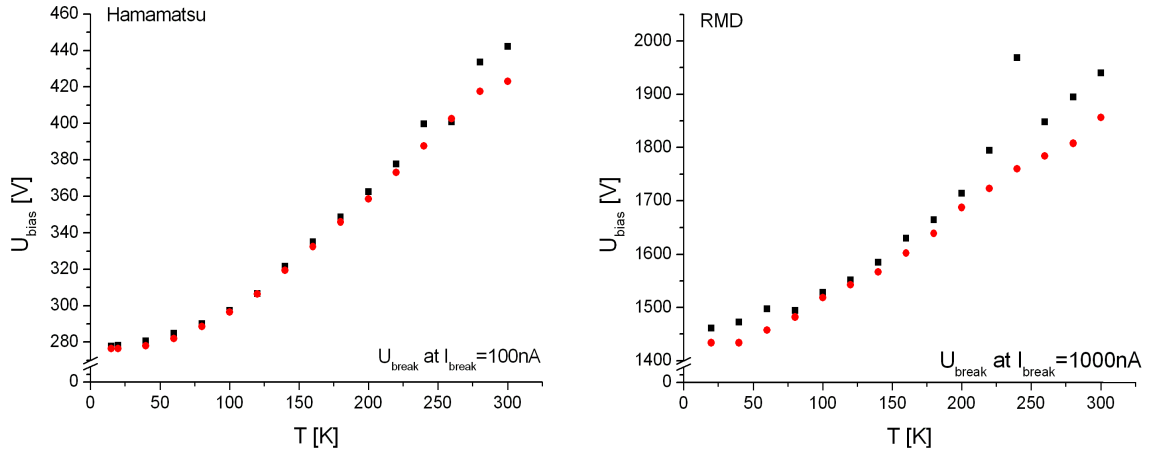


Figure 6.7: Calculated break-through voltage  $U_{\text{break}} \leftrightarrow I_{\text{break}}$  in black compared with the maximal applied bias voltage  $U_{\text{bias max}}$  in red as function of temperatures.

From the room-temperature curve and the known  $U_{\text{break}}(T = 300 \text{ K})$  we were able to calculate the corresponding break through current as  $I_{\text{break}} = 100 \text{ nA}$  for the Hamamatsu and  $I_{\text{break}} = 1000 \text{ nA}$  for the RMD diode. The results are in very good agreement with typical values [159, 160, 161]. Together with exponential fits to the data shown in fig. 6.6 and these  $I_{\text{break}}$  value it was possible to calculate the break-through voltage  $U_{\text{break}}$  for each temperature. The results are shown in fig. 6.7 (black points). The temperature dependence will be discussed in section 6.5. From fig. 6.7 we get the im-

portant information, how far we can go with the applied  $U_{\text{bias}} < U_{\text{break}}$  for the ongoing systematic studies. The red points indicate the actual  $U_{\text{bias max}}$  voltage, we used.

## 6.4.2 Gain and noise as function of $T$

### Gain

The LAAPD signal was fed into an Canberra preamplifier (Model 2003 B) and a Tennelec main amplifier (TC 243). A shaping time of  $\tau_{\text{shape}} = 2 \mu\text{s}$  led to the best signal-to-noise ratio. The signal was monitored with an oscilloscope and fed into a multi-channel analyzer (Amptek MCA). Spectra from a radioactive  $^{55}\text{Fe}$  source,  $E_\gamma = 5.8$  keV were measured as a function of  $U_{\text{bias}} \leq U_{\text{bias max}}$  and temperature  $T$  in steps of  $\Delta T = 20$  K. A Gaussian plus exponential background function was used to fit the spectrum and determine the peak center  $C_i$ .

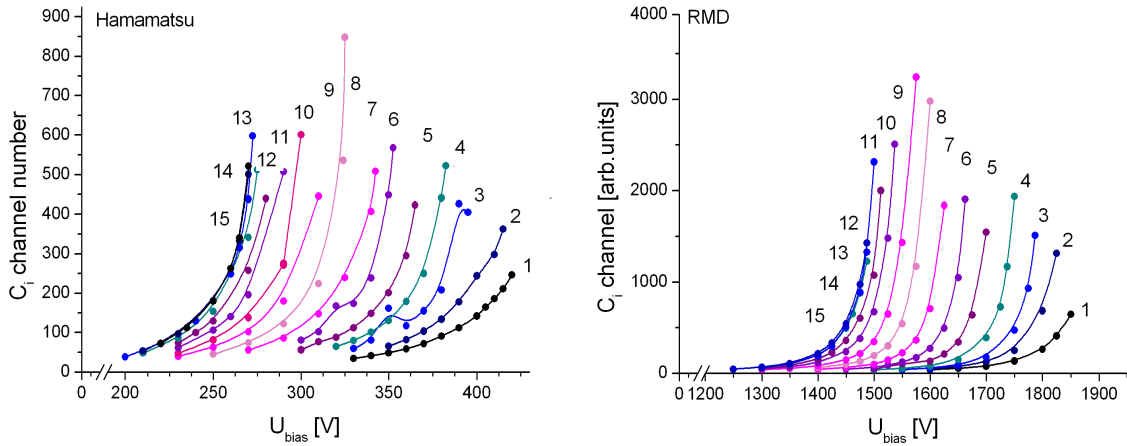


Figure 6.8: Peak position of the 5.9 keV line from a  $^{55}\text{Fe}$  source as function of bias voltage and temperature for the Hamamatsu LAAPD left and the RMD LAAPD right. 1) 300 K, 2) 280 K, 3) 260K, 4) 240 K, 5) 220 K, 6) 200 K, 7) 180 K, 8) 160 K, 9) 140 K, 10) 120 K, 11) 100 K, 12) 80 K, 13) 60 K, 14) 40 K, 15) 20 K, 16) 15 K.

The ratio between the peak position  $C_i$  and the channel number corresponding to the peak position  $C_0$  ( $C_0 = C_i(M=1)$ ) is defined as the gain factor  $M$ , eq. 6.6. This definition corresponding to the theoretical one from eq. 6.2.

$$M(U_{\text{bias}}, T, \dots) = \frac{C_i(U_{\text{bias}}, T, \dots)}{C_0(M=1)}. \quad (6.6)$$

From our data we can extract the gain dependence as function of bias voltage  $U_{\text{bias}}$  and temperature  $T$ . In addition we can compare the results from the two LAAPD's: The peak position  $C_0(M=1)$  corresponds to the  $U_{\text{bias}}$  where only the primary electron is transported through the avalanche zone. With the poor signal to noise ratio from the  $^{55}\text{Fe}$  source it is impossible to measure down to this region, but it is possible to increase the number of photons by a fixed factor when using a pulsed LED with  $\lambda = 560$  nm. This method was applied earlier by Karar et al. [156]. In our case we adjusted the light output from the LED to increase the number of primary  $e^-h^+$  pairs by a factor 45 for the Hamamatsu and of 41 for the RMD LAAPD.

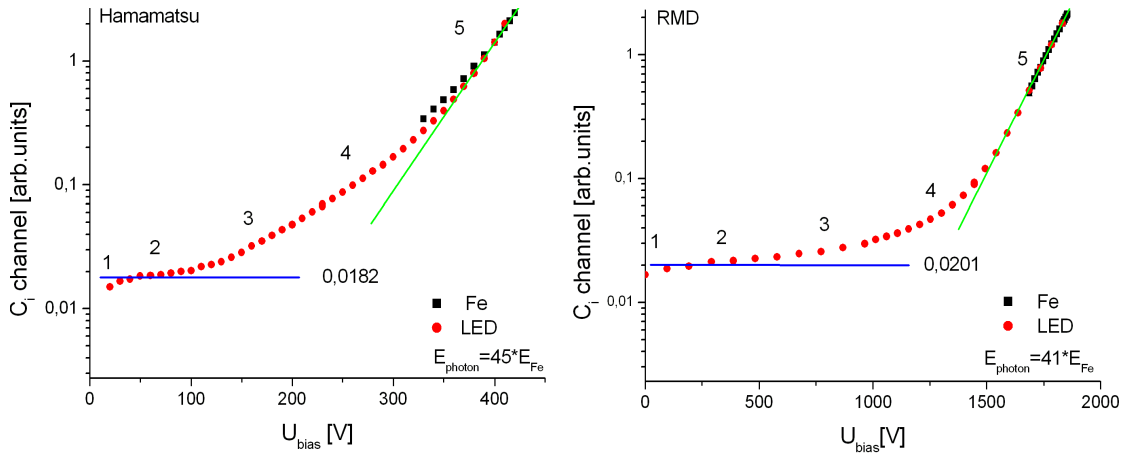


Figure 6.9: Current from the LAAPD as function of bias voltage illuminated by an LED and normalized to the  $^{55}\text{Fe}$  spectrum.

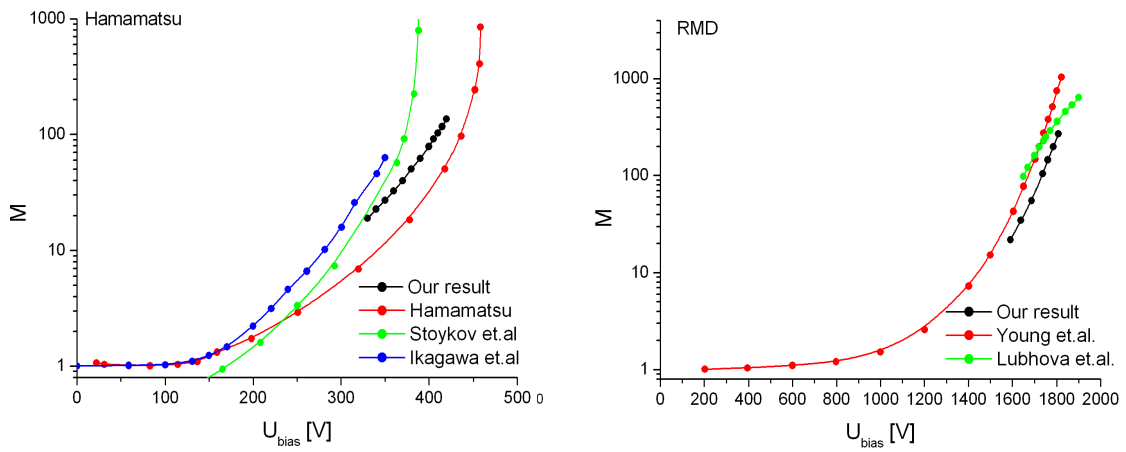


Figure 6.10: Room temperature gain as function of voltage compared with published data. Left: Hamamatsu [159, 166, 165], right: RMD [162, 177]

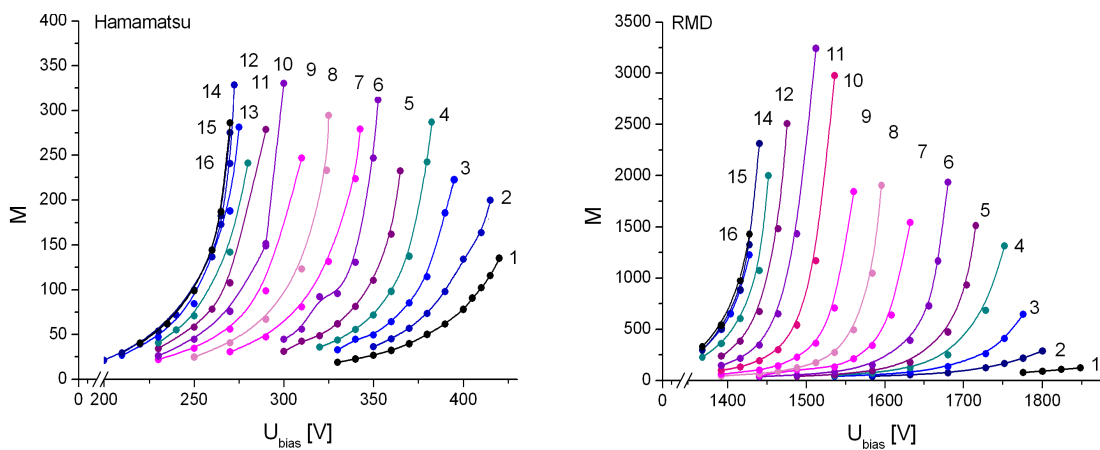


Figure 6.11: Gain  $M$  as function of  $U_{\text{bias}}$  and temperature  $T$  (the numbers have the same meaning like in fig. 6.8)  $M(U_{\text{bias}}, T)$ .

These values were extracted from the normalization factor necessary to match the peak positions  $C_i$  from  $^{55}\text{Fe}$  and LED at high  $U_{\text{bias}}$  values, (cf. fig. 6.9). The asymptotic matching between the LED and the gamma signal is used at highest amplification levels and thus large  $U_{\text{bias}}$ . In this area many of electron hole pairs are rather quickly generated and the signal becomes dominant compared to the noise contributions. This effect can be seen in the difference between the red and black points for  $U_{\text{bias}} < 350$  V in case of the Hamamatsu LAAPD. It corresponds with its known high noise level at room temperature. Repeating this measurements at reduced temperature would be an improvement, but then we would lose the possibility to compare our results with published data. Afterward it was possible to extend the LED signal analysis down to  $U_{\text{bias}} \approx 0$  V. The expected  $^{55}\text{Fe}$  values presented at fig. 6.9 have been corrected by the fixed gain factor of the main amplifier and the Fe/LED ratio.

The steadily growing peak position with increasing  $U_{\text{bias}}$  for both LAAPD's can be separated into 5 sections: **1)** The electric field is not high enough to push all created electrons through the depletion zone to the rear contact and the signal is dominated by recombination effects inside the front contact and the conversion zone. **2)** The plateau predicted to start at  $U_{\text{bias}}(\text{Hamamatsu}) = 50$  V [163] and  $U_{\text{bias}}(\text{RMD}) = 200$  V [177], respectively with almost constant peak position indicates efficient electron transport without significant multiplication. The onset value of this region is defined as signal for unity amplification  $M = 1$  (blue line). **3)** In this part the electron multiplication due to the increasing accelerating potential  $E$  applied through  $U_{\text{bias}}$  leads to an exponential signal growth. The Hamamatsu diode shows a little bump at the point when the diode is completely depleted at **4)**. In region **5)** the slope is changing where also the holes contribute significantly to the gain. This area with voltages close to the point when irreversible damage occurred the LAAPD, is called Geiger mode<sup>7</sup> (green line).

The extracted value for  $M = 1$  (Hamamatsu 0,018, RMD 0,020) are then used to rescale the results shown in fig. 6.8 into gain factors  $M(U_{\text{bias}}, T)$  (fig. 6.11). Our rescaled gain values at room temperature agree well with published values [162, 177] for the RMD LAAPD and [159, 165, 166] and for the Hamamatsu device shown in ref. 6.10.

In order to compare the temperature dependence of the two LAAPD detectors we made exponential fits to each curve in fig. 6.11. Using the extracted fit parameters it was then possible to separate the pure temperature dependence  $M(T)$  for fixed  $U_{\text{bias}}(T_{20\text{ K}})$  voltages. For comparison the data of  $U_{\text{bias}}(T_{20\text{ K}}) \pm 10\%$  are shown in fig. 6.12. The dashed blue line belong to the quantitative influence on the charge mobility on the phonon occupation number. This point will be discussed in detail in section 6.5.1.

## Noise

Following eq. 6.4 noise from the measured dark current  $I_{\text{D}}$  can be separated into a gain dependent volume part  $I_{\text{DV}}$  and a gain independent superficial one  $I_{\text{DS}}$ . With our gain levels  $M(T, U)$  from fig. 6.11 and the diode characteristics  $I_{\text{D}}(U_{\text{bias}})$  from fig. 6.6 we even can extract the temperature dependence of the superficial and volume noise contributions introduced in section 6.2.2. For each temperature, the lower part of

---

<sup>7</sup>Some diodes are built to run in this Geiger mode. The proportionality of the signal to the incident energy is lost for very high gain factors.

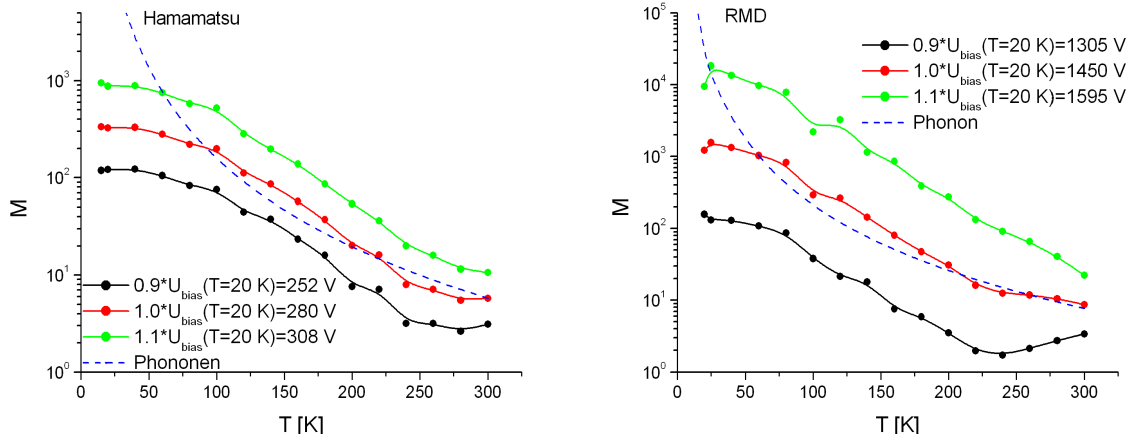


Figure 6.12: Gain as a function of temperature for fixed  $U_{\text{bias}}(T = 20 \text{ K})$  red,  $0.9 \cdot U_{\text{bias}}(T = 20 \text{ K})$  black and  $1.1 \cdot U_{\text{bias}}(T = 20 \text{ K})$  green. The quantitative influence on the charge mobility due to the phonon occupation number used later in the text for an explanation is shown in blue.

$I_D(U_{\text{bias}})$  was rescaled into an  $I_D(M)$  plot. The parameter from the linear fit are then plotted as a function of temperature in fig. 6.13. In both cases, the noise contributions vanished below 220 K, in perfect agreement with results from [167].

One of the differences between the LAAPDs is that the RMD is covered by a transparent reflective plastic coating, whereas the Hamamatsu LAAPD was specially treated to remove such a coating. Otherwise the different thermal expansion coefficient caused the LAAPD to break during cool down to below 180 K. It was possible to get one LAAPD without the cover from HAMAMATSU or to remove it by carefully bathing the LAAPD in acids alcohol and water (further explanations can be found in the appendix). Both LAAPDs showed the same results. In the Hamamatsu case one could expect an effect on the noise level due to different isolation vacuum, caused by freezing gas impurities on the surface at low temperature. We therefore measured  $I_D$  at the cross point between liquid nitrogen  $T = 77 \text{ K}$  and re-sublimation of nitrogen  $T = 40$

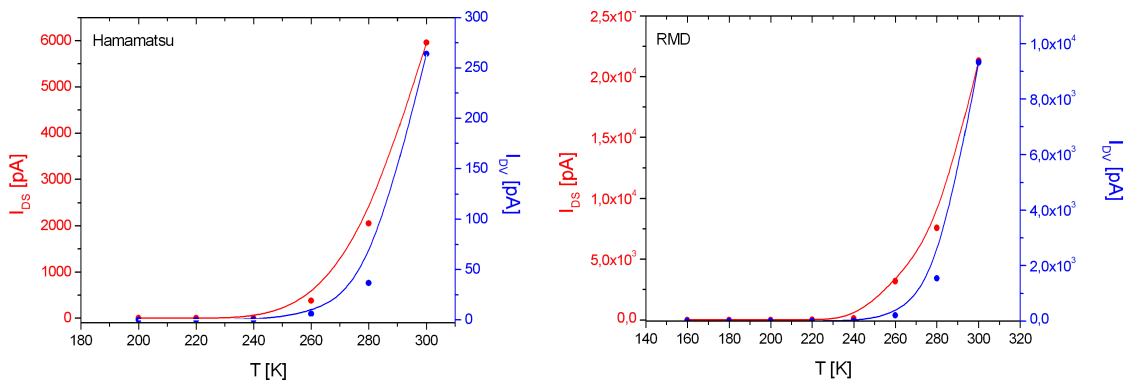


Figure 6.13: Temperature dependence of the dark current  $I_D$  components superficial  $I_{\text{DS}}$  and volume  $I_{\text{DV}}$ .

K at  $10^{-4}$  mbar and  $10^{-6}$  mbar. The dependence of  $I_D(U_{\text{bias}})$  is shown in fig. 6.14, left. Both noise components become worse when the vacuum gets worse. No irreversible impact on the LAAPD itself was measured but one can expect that the signal-to-noise ratio will be drastically affected by bad vacuum at low temperature as function of time.

### 6.4.3 Spectral response

The main purpose of our investigation was to find a photon counting unit working with a low level of scintillation light from CsI at low temperatures ( $\lambda = 320$  nm). The CsI test detector system (fig. 5.21) was connected to both LAAPDs and irradiated in both cases by 40 keV protons. The spectra measured at 50 K, at highest possible  $U_{\text{bias}}$  voltage are shown at the right-hand side of fig. 6.14.

From our detailed studies on the scintillator and the light guide system we roughly know, how many photons  $N_\lambda$  reach the LAAPD's conversion zone. Together with the measured peak-position ratio  $C_{\text{RMD}/\text{HAM}} = S_{\text{RMD}}/S_{\text{HAM}}$  (the peak position  $S$  from fig. 6.14 right) and the set main amplifier gain  $M_m$ , the preamplifier gain  $M_p$  and the LAAPD gains (cf. fig. 6.11)  $M_{\text{RMD}}$  and  $M_{\text{Hamamatsu}}$  we can try to calculate the amount of produced primary  $e^-h^+$  pairs. With the assumption that the incident deposited energy was in both cases the same, this ratio leads to an estimate of the relative quantum efficiency of the LAAPDs at  $\lambda = 320$  nm.

$$\eta = \frac{EQ_{\text{RMD}}}{EQ_{\text{HAM}}} = \frac{S_{\text{RMD}}}{M_m M_p M_{\text{RMD}}(T, U)} \cdot \frac{M_m M_p M_{\text{HAM}}(T, U)}{S_{\text{HAM}}}$$

$$\eta = \frac{134}{1440} \cdot \frac{285}{336} = 0.08$$

From the Hamamatsu data sheet we get a rough estimation of 45% which would lead to a prediction for the RMD LAAPD in the range of 4%. A possible explanation why the efficiency of the RMD LAAPD is an order of magnitude lower than for the Hamamatsu will be given in section 6.5.

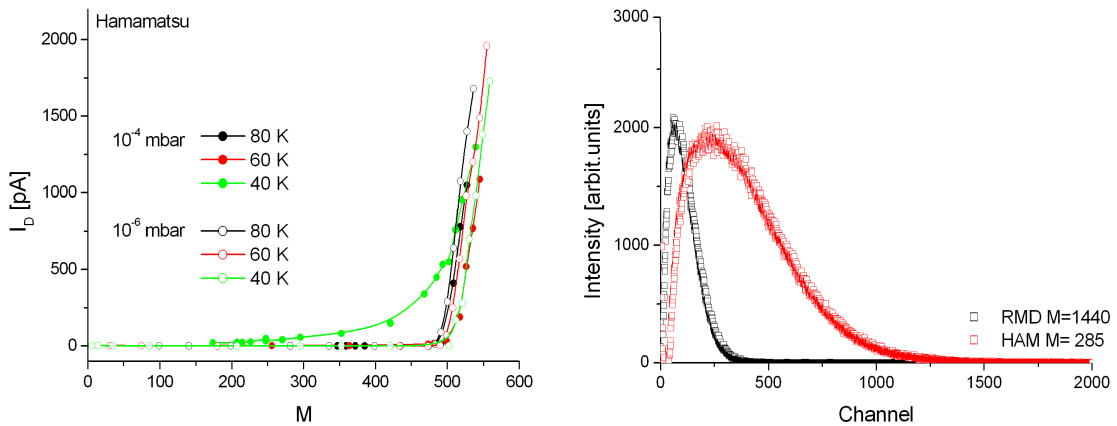


Figure 6.14: Left: diode dark current as a function of  $M$  for three different temperatures. The different symbols indicate different pressures. Right: a spectrum of 40 keV protons with both LAAPDs at identical conditions and maximal possible  $U_{\text{bias}}$ .

## 6.5 Interpretation

### 6.5.1 LAAPD performance at low temperature

The operation of LAAPDs relies on the high electric field for the amplification process. The ability of their depletion and avalanche zone to withstand high voltages without break through is mandatory. A break down occurs when the internal gain reaches "infinity". The multiplication process begins when an initial charge carrier gains enough kinetic energy to create additional electron hole pairs on its way through the avalanche zone.

The major resistance against acceleration of electrons and holes is caused by charge carrier phonon scattering where in principle the increased kinetic energy is transformed into heat. As the temperature of the device is lowered, the amount of phonons is decreased. The occupation number of the density of phonon states  $Z(\omega)$  can be described by a  $T^{3/2}$  distribution (Debye model). On the other hand this should have an effect on the mobility  $\mu_{e,h}$  of the electrons and holes. At a temperature of  $1/10 \cdot \Theta_{\text{Debye}}$ , (for Si:  $\Theta_{\text{Debye}} = 628 \text{ K}$ ) all phonons can be seen in first approximation as frozen [168] and further increase of the described effect with cooling is not expected.

If this is the case, some predictions on our experimental values are possible. First of all this effect is independent on the origin of the first generation charge carriers (signal or noise). Thermal excitations and the diode counter effect are determining the breakdown voltage  $U_{\text{break}}$ . The amount of excitations is reduced by the decreasing temperature, but from the increase in mobility one would expect that the usable  $U_{\text{break}}$  is decreasing with reduced temperature  $T$ . A saturate at about 60 K could be expected. Whereas the onset of this effect as an intrinsic behavior of Si should be similar for both LAAPDs, the slope may depend on the structure, doping profile, noise level and others. This result fits well with the data shown in fig. 6.7.

In case of normal operation the first generation of charge carriers are created by an incident particle and the bias voltage is below the break-down voltage. The increase in mobility with decreasing temperature leads to an improved acceleration efficiency and thus to an increase in the number of created electron hole pairs and usable gain. This result can be seen on the envelope of fig. 6.11. The temperature effect is extracted from fig. 6.12 where the gain is shown as function of  $T$  and fixed acceleration potential. The blue broken line indicates the effect from the phonon occupation with the  $1/T^{3/2}$  [155] function normalized to the room temperature value of the experimental curve. The slope in the logarithmic plot describes quite well our experimental results. As described above, also here we could expect a saturation at about 60 K for both LAAPD's.

No indications for a sudden drop-down of the efficiency of the RMD LAAPD due to carrier freeze-out as reported in [177] was seen. The working temperature of the LAAPD's can be extended to at least  $T = 20 \text{ K}$ , which was the lowest temperature in our setup.

## 6.5.2 Beveled edge type versus reach through type

### Temperature dependence:

Besides the listed differences between the RMD and the Hamamatsu LAAPD we found qualitatively similar but quantitatively different temperature behavior. Following our interpretation, it is obvious that the temperature behavior of both LAAPD types are similar but in detail the different diode structure has to be considered. Comparing the result of fig. 6.12, we see that at the lowest temperature the maximum applicable  $U_{\text{bias}}$  changes for the Hamamatsu diode to 60% and for the RMD diode to 76% of the room-temperature value. This can be understood by the different noise levels due to the thicker conversion zone of the reverse reach-through type. On the other hand, a change of 10% in the applied bias voltage reduces the gain at 50 K by a factor of three in the case of the Hamamatsu and by a factor of ten for the RMD LAAPD. The increase in gain as a function of temperature between room temperature and 50 K is 60 for the Hamamatsu, compared to 15 for the RMD LAAPD. All values have been derived from the data shown in fig. 6.12.

In the following figure the charge carrier mobility as function of doping concentration and temperature is shown on the left hand and the ratio between these two for low and high doping is shown on the right side. In lowest approximation, we can consider the mobility ratio  $\mu_h/\mu_e$  to be proportional to the ratio  $k$  of the ionization coefficient (eq. 6.3).

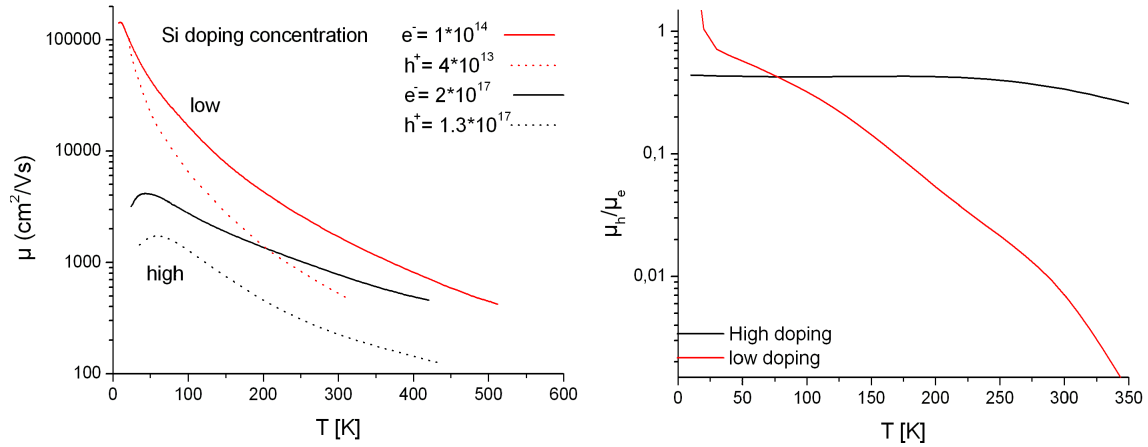


Figure 6.15: Mobility for holes and electrons as a function of doping concentration and temperature. The ratio  $\mu_n/\mu_h$  for the low and high doping case is shown on the right hand side [155].

From fig. 6.15 we see that the doping level has a strong impact on the temperature dependence of the mobility ratio  $k$  and its behavior towards the critical  $k_{\text{break}} \rightarrow 1$  value from section 6.2. If we use a linear approximation between the accelerating  $E$  field and the applied voltage  $U_{\text{bias}}$  and the connection between the mobility, ionization ratio and temperature we can rescale  $M(E, k)$  fig. 6.4 to our  $M(U, T)$  in fig. 6.11. We can also assume that due to the sharp pn junction and the lower required working voltage the doping density for the reverse reach through diode is higher (black squares).

From fig. 6.15, right and we may conclude that the intrinsic break through voltage temperature relation at equal hole and electron mobility is much less pronounced than for the beveled edge LAAPD. This leads to an additional limitation on the usable gain ratio of 60/15 as function of temperature linked now maybe to the doping profile of the LAAPD's.

### Spectral response

There are several reasons for the reduced amount of quantum efficiency of the RMD detector. The entrance window is thicker and free of any electric drift field <sup>8</sup> compared to that is the completely depleted Hamamatsu LAAPD. The reach through LAAPD's are optimized for light detection [160] (cf. fig. 6.5). The increase of the recombination rate with decreasing temperature causes additional losses that scale with the drift length through the non-depleted zone. The much lower noise at room temperature for the RMD indicates a thicker entrance contact leading to a higher absorption for low wavelength light before the conversion zone is reached, see section 6.1. The primary amount of photons may also be strongly reduced by the transmission losses of the  $\lambda = 330$  nm radiation in the plastic coating of the RMD LAAPD. In case of the Hamamatsu the light guide is directly coupled to the silicon surface.

### Noise

The noise from both LAAPDs is reduced to a negligible level, even at a (moderate) temperature of  $-50$  °C. The noise in the spectra is caused by noise from the preamplifier (in a latter stage of the experiment this will be also cooled to the working temperature of the main detector) and not yet optimized read-out electronics and in the case of fig. 6.14 from the proton source itself.

---

<sup>8</sup>RMD: Due to the longer drift length these detectors are usually used for direct particle detection.



# Chapter 7

## *paff* accelerator

To measure precisely the decay products of the free neutron decay is the goal of some experiments to measure the free neutron lifetime or correlation coefficients from the theoretical description of the decay. Beside the antineutrino with its by far to low interaction cross section with any detector material there are the protons ( $E_{\text{kin}}=0\dots750$  eV) and the electrons ( $E_{\text{kin}}=0\dots750$  keV). They can be guided, collected and accelerated towards sufficient energy to produce detectable signals by their charge. The lower necessary potentials favors in some cases the protons. A list of experiments using the detection of one or both decay products is given in the following table 7.1.

n-decay experiments	location	goal	detection	source
PENeLOPE	TU-Munich FRM II	$\tau_n$	$p$	Picker et al. [172]
Lifetime	Harvard NIST	$\tau_n$	$p$	Huffman et al. [173]
aSPECT	Mainz FRM II ILL	$a$	$p$	Zimmer et al. [174]
aCORN	NIST	$a$	$p$	Wietfield et al. [175]
PERKEO I,II,III	Uni Heidelberg	$A$	$e, p$	Reich et al. [176]
UCNA	LANSCE	$A$	$e, p$	Young et al. [177]
...	...	...	...	...

Table 7.1: Experiments for fundamental particle research dealing with proton detection from the free neutron decay.  $\tau_n$  the neutron lifetime and the correlation coefficients from the parameterized neutron decay  $a, A$ .

Besides the *PENeLOPE* project to measure  $\tau_n$ , the *aSPECT* spectrometer to derive  $a$ , the correlation coefficient (electron antineutrino asymmetry) from the energy spectrum of the neutron decay protons from a passing neutron beam needs well known proton detector. After acceleration towards the detector a high efficiency in detection of 30 keV protons is mandatory. Both projects are under development at E18 at the Technische Universität München. The requirements of both detectors are listed in table 7.2. For the detector principle as well as later calibration before, during and after the beam time a dedicated proton source with tunable kinetic energy up to 30 keV and an intensity on the target corresponding to the expected count rate is mandatory. An electron beam in addition would provide us with the opportunity on systematic studies of the possible background caused by the decay electrons also hitting the detector.

Another beam position allows to change the angle between detector and beam for angular resolution measurements.

Requirements	PENeLOPE	aSPECT
Energy [keV]	$\leq 30$	$\geq 30$
Area [cm <sup>2</sup> ]	2500	3
Temperature [K]	$\geq 70$	$\geq 270$
Vacuum [mbar]	$\geq 10^{-4}$	$\geq 10^{-9}$
B-field [T]	3	
resolution	$e^{-}, p^{+}$ signal	angular/spatial

Table 7.2: Requirements on the *pafl* facility from the two experiments *PENeLOPE* and *aSPECT*. Detector development for both experiments is done at E18 in Munich.

Proton accelerators for the test of detectors to be employed in neutron-decay studies have been devised earlier [179] as well as special developments exactly for this purpose as can be seen by [180]. *pafl* however has some special features:

- The accelerator provides protons of up to 45 keV.
- *pafl* produces a beam of narrow spatial dimensions.
- The beam intensity can be varied over a wide range.
- It is possible to apply a background free proton beam.
- There is access to the target position at ground potential.
- Additional electron beam.
- Simultaneous electron and proton beams.

The scheme of this accelerator together with its working principle as well as characterization measurements are presented in the following chapter. Finally, some results already achieved with the *pafl* setup are shown on the last pages.

## 7.1 Setup

The *pa<sub>ff</sub>* accelerator (*proton accelerator working with femto ampere flux*) is divided into four sections: the source, diagnostic, e-beam and target part, as can be seen in fig. 7.1. Each section uses its own vacuum system.

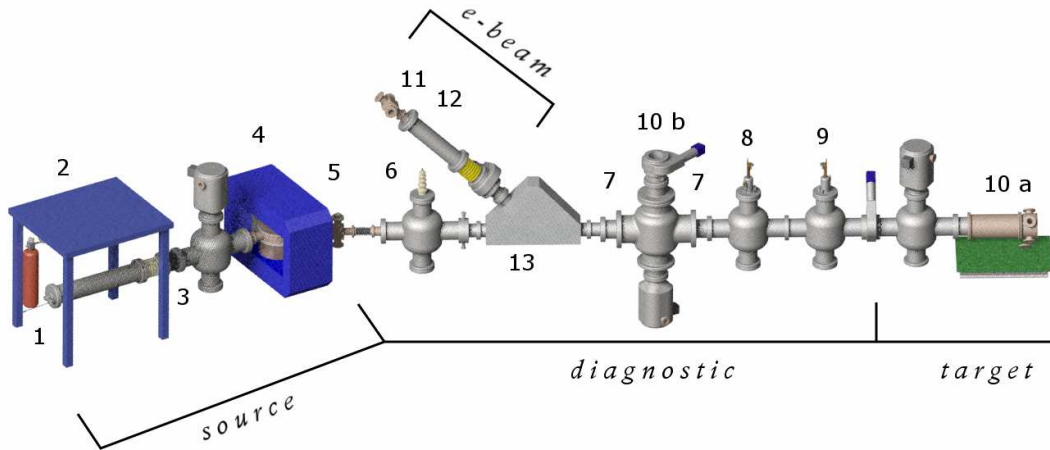


Figure 7.1: Scheme of the *pa<sub>ff</sub>* accelerator with the four different sections.

- |              |                      |          |
|--------------|----------------------|----------|
| • Source     | Ion source           | (1)      |
|              | High-voltage cage    | (2)      |
|              | Insulator            | (3)      |
|              | Separation magnet    | (4)      |
| • Diagnostic | Four-sector aperture | (5)      |
|              | Einzel lens          | (6)      |
|              | Iris collimators     | (7)      |
|              | Faraday cup          | (8)      |
|              | MCP detector         | (9)      |
| • $e^-$ beam | Electron gun         | (11)     |
|              | Steering Magnet      | (12)     |
|              | Bending magnet       | (13)     |
| • Target     | Targets              | (10 a/b) |

### 7.1.1 Source part

#### Ion source

The extractor-type ion source IQE 11/35 [178] is normally used to clean the surface of silicon wafers passing at small distance by ion sputtering.

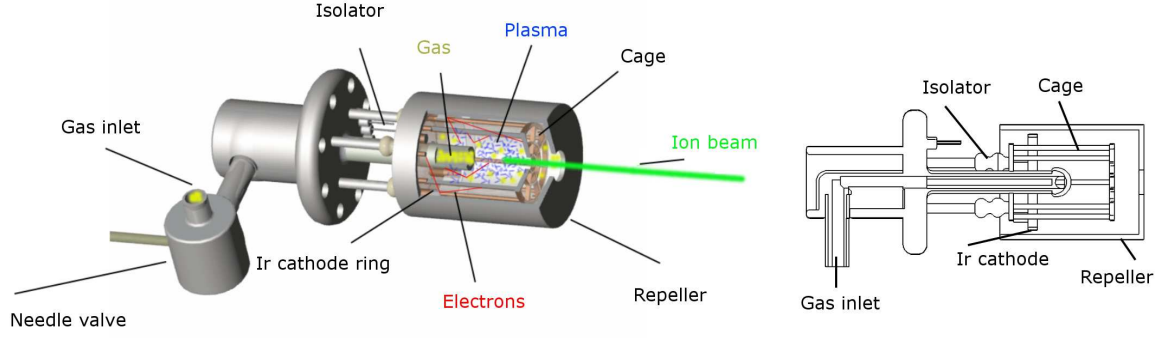


Figure 7.2: Scheme of the extractor-type ion source[178].

**Plasma source:** The source consists of three main components, the iridium coated filament, a wire frame and the repeller, as shown in fig 7.2. During the operation, the ring-shaped filament is heated with a fixed current of 5.5 A to a temperature above  $T = 2200$  K.

$$j(T)/A = -\frac{em}{2\pi^2\hbar^3}(k_B T)^2 e^{-\frac{k_B T}{E_A}} \quad (7.1)$$

According to the Richardson-Dushman equation eq. 7.1 with the work function  $E_A$ , the filament surface  $A$ , filament Temperature  $T$ , ion mass  $m$  and the Boltzmann constant  $k_B$  we may expect an electron current  $j(T)$  in the mA range is evaporation. The iridium coating with its higher  $E_A$  value decreases the current, but it is necessary to avoid fast filament break down due to plasma etching, when hydrogen or oxygen ions are produced. The free electrons are accelerated to the wire frame in the center (potential +30 V). The repeller with the gas inlet and the extraction hole covers the source. A needle valve is used to adjust the gas pressure in the repeller cup to reach values below  $10^{-4}$  mbar inside the vacuum chamber. This leads to a pressure inside the source approximately one order of magnitude larger. Part of the neutral atoms are ionized by the electron bombardment, creating a low-temperature plasma, which may be described by the Saha equation [181]. A potential difference  $U_{\text{source}}$  (cf. fig. 7.3) between the source and the vacuum chamber (0 to 5 kV) can be applied, leading to a separation of the charges and to plasma oscillations [181]. With the source control unit one can adjust the electron current  $I_{\text{plasma}}$  escaping through the wire frame from the plasma between 0 and 10 mA. The plasma has to be neutral, therefore the same amount of positive ions are extracted, in the opposite direction  $I_{\text{extract}} = I_{\text{plasma}}$ . The kinetic energy ( $E_{\text{kin}} = 0..5$  keV) corresponds to the applied voltage  $U_{\text{source}}$ .

**Acceleration cage:** The source, mounted inside a CF100 ( $\phi$  100 mm) vacuum pipe, is connected to the beam tube by a ceramic isolator; and an additional high-voltage  $U_{\text{cage}} = 0..45$  kV is applied to the source. This gives the ions the required and adjustable kinetic energy of  $E_{\text{kin max}} = 50$  keV and focuses them slightly towards the separation magnet. Without this effect, the strongly divergent ion beam would drop from 10 mA to  $225 \mu\text{A}$  at 5 cm and to  $75 \mu\text{A}$  at 10 cm distance from the extraction hole [178]. The positively charged walls of the vacuum pipe create a drop-like beam shape leading to

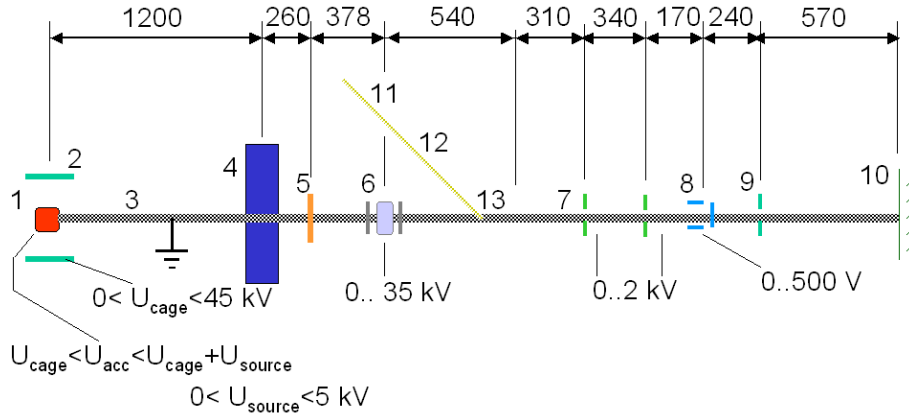


Figure 7.3: Dimensions in mm and potentials at the different parts of the *paff* accelerator.

low-loss transport of the beam into the beam tube. Section 7.2 and section 7.3 will describe results from simulations and from measurements.

A separation magnet ( $B = 0 \dots 270$  mT) is used to bend the right ion species with the correct velocity to mass ratio into the next beam tube that is horizontally tilted by  $30^\circ$  (cf. fig. 7.1). For better differential pumping of source and diagnostic part this section has a reduced diameter of only 30 mm.

The  $30^\circ$  bend is also necessary to avoid direct view from the detectors to be tested to the plasma source. Thus, light from glowing filament and plasma [182] as well as neutral particles do no harm to the sensitive devices.

## 7.1.2 Diagnostic and monitoring part

Three detectors are used to check quality and quantity of the ion beam.

### Four-sector baffle

The first monitor detector is a four-sector baffle consisting of Ta plates framing the beam, as sketched in fig. 7.4. The beam is localized by simultaneously measuring the current from the four plates. This baffle also acts as a first collimator after the bending magnet, cutting the beam down to  $1 \text{ cm}^2$  area.

This detector works fine in the nA region without blocking the beam and provides the user, with steady information on the beam. In future, this information may be used to correct the main data for source instabilities, e.g. caused by pressure variations.

### Faraday cup

The Faraday cup shown in fig. 7.5 collects the protons on a Ta plate. It covers the beam only during a current measurement. The current into this cup is measured by a femtoamperemeter. Special care has to be taken to avoid secondary electrons from the proton bombarding the cup, thus leading to a higher positive charge and to an overestimation of the true beam current. The conducting aluminum cylinder reduces this escape probability. A ring at a negative suppression voltage pushes the electrons

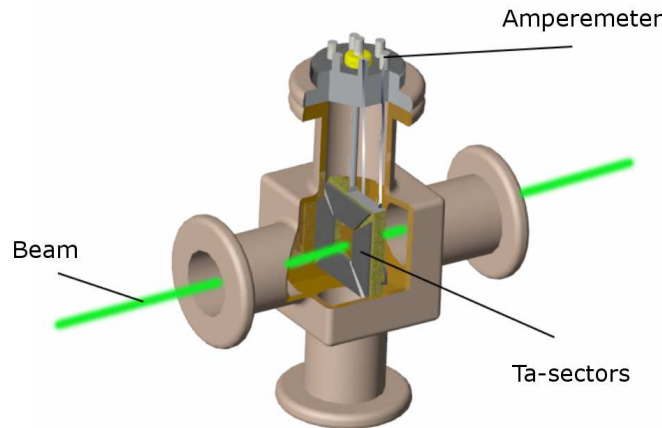


Figure 7.4: Scheme of the four-sector baffle detector used for beam tuning. The beam charges four Ta-plates framing the beam; the current is measured with amperemeters.

back to the Ta plate. With the triple shielding, the noise current may be reduced to  $\leq 1$  pA [183]. (Shielding 1rs is an iron tube inside, shielding 2sd is the vacuum cross isolated from the other accelerator parts and shielding 3rd is a grounded aluminum foil wrapping.) Beam intensities from mA to pA can be measured.

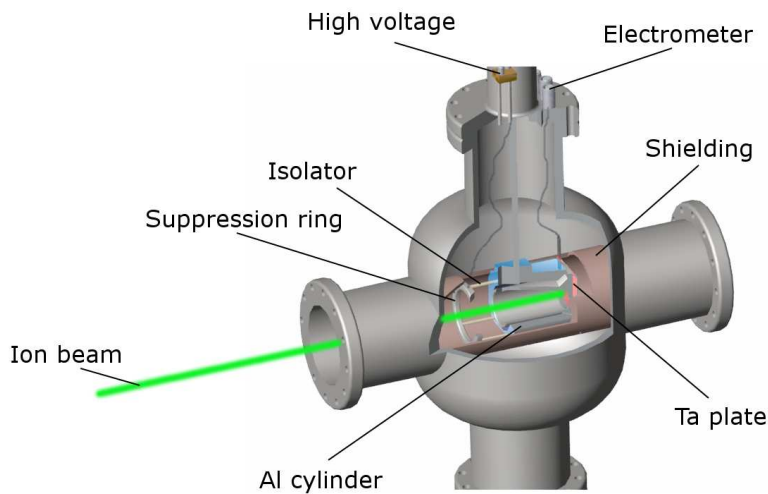


Figure 7.5: Faraday cup for measuring the beam intensity for currents between pA and mA.

### MCP detector

A double MCP (multi channel plate) detector in chevron geometry is used to measure intensities below the pA region. The signal from an anode doublet behind the MCP are counted and a corresponding ion current reading derived. The dynamical range is limited to count rates from  $1 \text{ s}^{-1}$  to  $1 \cdot 10^8 \text{ s}^{-1}$ . As the electron cloud collected on the anode, keeps the spatial information, it is possible to use this detector to get

information about the beam profile. We use a ring shaped outer anode of 21 mm inner and 40 mm outer diameter and a center anode of 20 mm diameter to localize the beam and determine the halo (fig. 7.6). Also this detector is moved into the beam when to be used, otherwise it is removed inside the vacuum cross well above the beam.

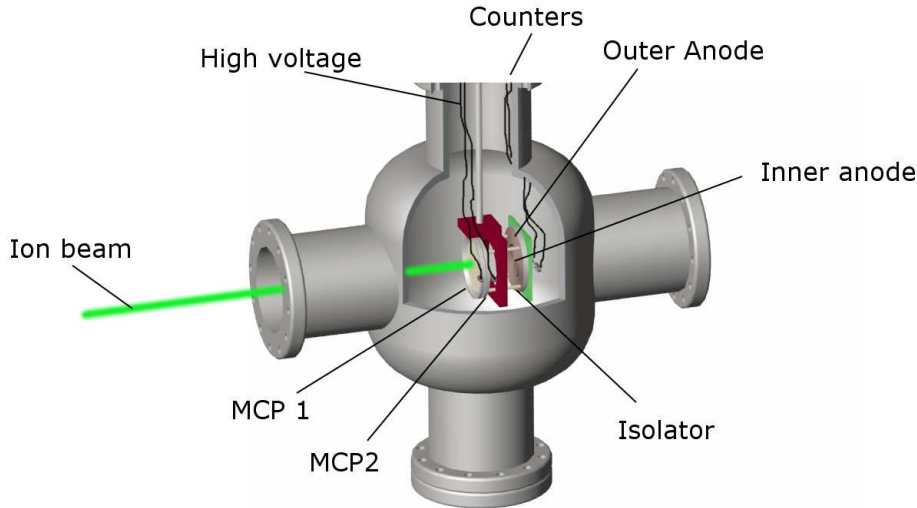


Figure 7.6: Scheme of the MCP (micro-channel-plate) monitor detector for single event counting.

Using the two monitor detectors moved into the beam from time to time allows to compare the beam intensity at monitor and target position. The reproducibility of the source settings, especially the vacuum and gas pressure gets much less important. Fine tuning to the required count rate can always be achieved via the plasma current.

### 7.1.3 Diagnostic and beam-reduction part

Reducing the applied gas pressure is the easiest and most effective way to reduce the beam intensity by orders of magnitude. At a pressure of  $10^{-7}$  mbar it becomes challenging to adjust to the right pressure and still guarantee a stable gas flow. The large pressure at the reduction valve of the gas bottle and the almost closed needle valve causes fluctuations. Another way is to use the control unit to reduce the extraction current  $I_{\text{extract}}$  to  $50 \mu\text{A}$ . Below this level, the self-regulating source control system is no longer stable or switches off. With both methods it is possible to adjust an ion flux in the range of  $10^9 \dots 10^4 \text{ s}^{-1}$ . An iris collimator, together with an electrostatic Einzel lens (cf. fig. 7.7) is used to achieve count rates down to a few events per second.

#### Einzel lens

The electrostatic Einzel lens consists of three conducting steel cylinders (cf. fig. 7.7) two on ground potential and the middle one on an adjustable high voltage (cf. fig. 7.3). The first gap acts as a defocusing, the second as a focusing lens with an overall refractive index depending on the ratio of beam energy and applied lens voltage  $U_{\text{lens}}$  [184, 185].

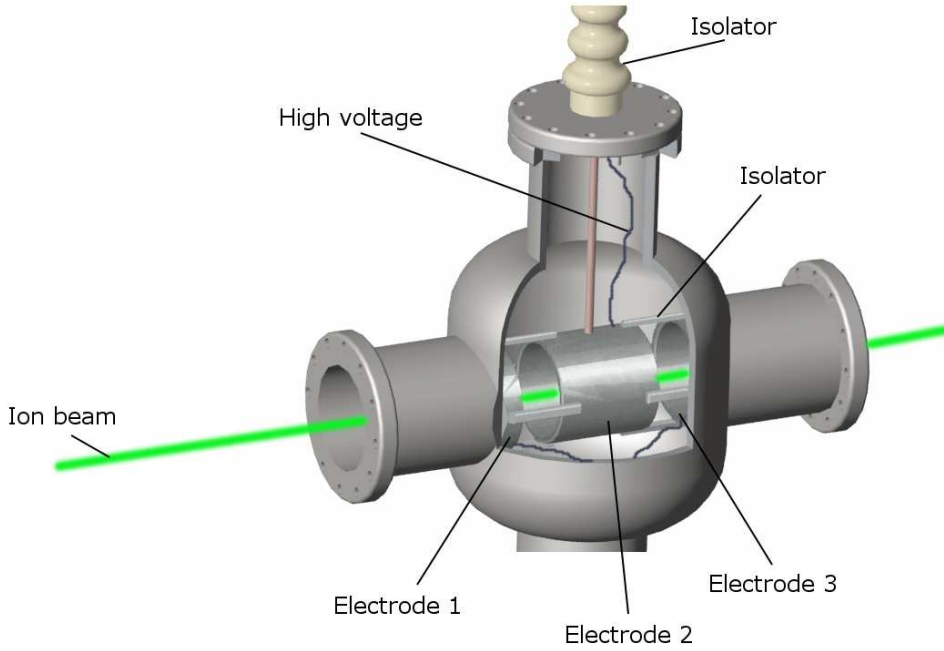


Figure 7.7: Einzel lens system used to focus and defocus the beam at the target position.

The effect of  $U_{\text{lens}}$  on the beam is described in table 7.3.  $U_{\text{lens}}$  may be used to set the beam intensity at the target position.

- $U_{\text{lens}} = 0 \text{ V}$	just the divergent beam on the target
- $U_{\text{lens}} < U_{\text{focus}}$	focus behind the target: slow increase of intensity
- $U_{\text{lens}} = U_{\text{focus}}$	focus at the target: maximum count rate
- $U_{\text{lens}} > U_{\text{focus}}$	focus between target and lens: again count rate reduced
- $U_{\text{lens}} > U_{\text{accelerate}}$	focal point inside the lens: divergent beam again
- $U_{\text{lens}} \cong U_{\text{accelerate}}$	focus at the target: increased count rate again
- $U_{\text{lens}} \geq U_{\text{accelerate}}$	no intensity

Table 7.3: Influence of the lens voltage  $U_{\text{lens}}$  on the beam focus position.

Once the lens voltage is very close to the acceleration voltage the lens leads to double reflection. The beam becomes parallel and crosses the target position again. The reason lays in the velocity change between the lens parts (see ref. [186] for details).

## Collimator

In contrast to a usual accelerator, which focuses on high intensities, our facility with the purpose of very low, well known intensities we have to take special care on beam halo effects. Hitting the wall or some of the equipment inside the beam guides, even a 30 keV proton releases tens of secondary electrons. These electrons are the main contribution to the background in later measurements and obviously have to be removed to allow the detection of few proton events.

The collimator is made of two computer controlled circular irises with an aperture between 2 and 40 mm. One purpose is to reduce the beam size and to produce a parallel beam. The second task is to reduce the number of background events due to electrons created upstream. A potential of +200 V is applied to an aluminum cylinder behind each iris to suppress electrons created at the edge of the iris as well as filtering electrons otherwise flying parallel to the axis of the positive ion beam. An influence on the proton beam can be neglected (or focusing effect).

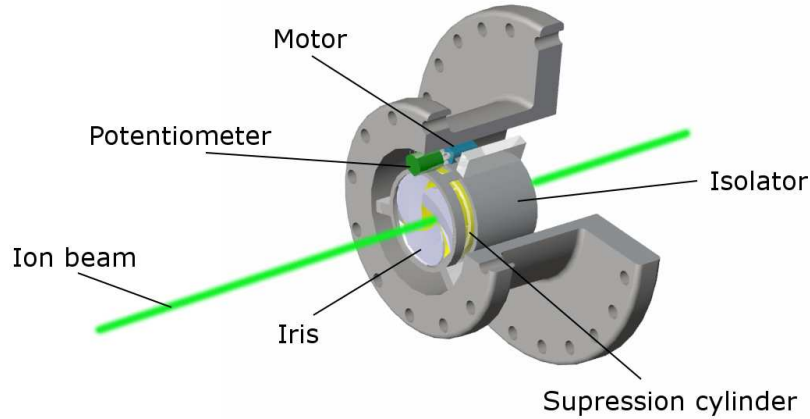


Figure 7.8: Scheme of one of the two irises building the collimator system of the accelerator.

#### 7.1.4 e-beam part

The largest contribution to the expected background in the *PENeLOPE* proton detector will be caused by electrons from neutron decay with energies between 0 and 780 keV, that hit this detector. It is highly desirable to know the response under halfway realistic conditions. For this reason, *pafl* is equipped with an electron source. A scheme of the used  $e^-$  gun, which is usually used in television picture tubes, is shown in fig. 7.9. A vacuum of  $< 10^{-6}$  mbar is essential to run the source and once it has been used, it has to be stored always under vacuum. The cathode is indirectly heated. The electron current from the surface, eq. 7.1, is influenced by the voltage at the grid G1 (control grid)<sup>1</sup>.

Grid G2 (extraction grid) and G3 (focusing grid) are normally used to adjust the beam intensity on the screen. In tubes the electron source is on ground potential and the screen on high voltage. In the *pafl* facility the beam tube stays at ground potential and the acceleration voltage is applied to the  $e^-$  gun. In contrast to our ion source, the lens effect from the cage voltage is lost. It is hardly possible to adjust the  $e^-$  source with the needed precision to the center of the tube. Therefore, an extra steering element is needed (shown cf. fig. 7.10) consisting of twice times two coils with homogeneous fields perpendicular to each other. Similar to the TV screens, the electron beam can be scanned with the applied  $B_x, B_y$  field across the whole vacuum tube aperture.

<sup>1</sup>For the first operation one has to change the surface of the cathode from BaO to Ba. This requires a ten-step procedure of applying a heating voltage for certain periods.

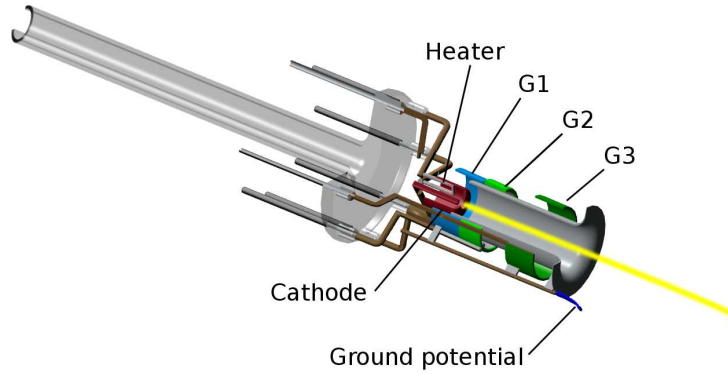


Figure 7.9: Scheme of the electron gun used for background studies.

### 7.1.5 Target part

Up to now, four different setups were realized and successfully used at the target position. i) with a reference Faraday cup<sup>2</sup> we characterised the beam and cross-checked the monitor detectors. ii) a phosphor screen served to visualize the beam. iii) the performance of the silicon strip detector and the cylindrical drift detector for the *aSPECT* spectrometer was investigated there as well as iv) the concept of the *PENeLOPE* large area proton detector. Further discussions may be found in the section 7.4. A cold head together with a heater allows us to adjust the temperature of the target between 15 – 400 K.

## 7.2 Simulations

The ray-tracing program *Simion 7.0* [188] for charged particles in electrostatic and magnetic fields was used for the following calculations. Besides a particular study on the source part and the Einzel lens, the complete setup was modeled to estimate the losses caused by the beam divergence. Some of the results were cross-checked with *OPTIC-II* simulations [189] with good agreement .

### 7.2.1 The effect of the potential distribution in the source

The source cup and the first vacuum pipe in front of the isolator were modeled. In fig. 7.11 the influence of the two acceleration voltages on the beam intensity is shown. The green mesh visualizes the different potential heights in  $z$  direction, the red lines the equipotential lines (potential is indicated by the height in  $z$  direction) and the black

<sup>2</sup>The Faraday reference detector was a long 1.2 m cup  $\phi 100$  mm detector with 100% efficiency, a small entrance hole of  $\approx 10$  mm and a triple shielding. Due to the black box like geometry no extracted electrons from the closed back of the tube leave the reference cup.

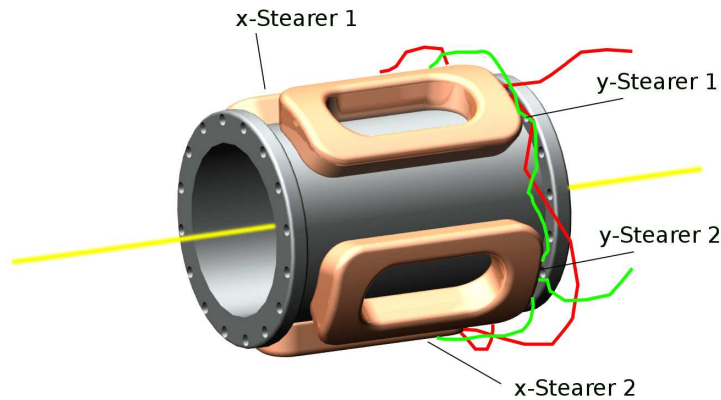


Figure 7.10: Steerer with two correction coil used for the alignment of the electron beam.

lines the proton trajectories resulting from a point source and different acceleration conditions. Starting with  $U_{\text{source}} = 5 \text{ kV}$ ,  $U_{\text{cage}} = 0 \text{ kV}$ ;  $U_{\text{source}} = 0 \text{ kV}$ ,  $U_{\text{cage}} = 30 \text{ kV}$  and  $U_{\text{source}} = 5 \text{ kV}$ ,  $U_{\text{cage}} = 30 \text{ kV}$  are shown from left to right. The last two simulations clearly show the additional cage focusing effect. A narrow beam can be produced with a small source and a large cage voltage. Depending on the ratio  $U_{\text{source}}/U_{\text{cage}}$  the beam gets some halo. The huge intensity drop within a distance of some cm is strongly underestimated when modeling the point source instead of a plasma volume source.

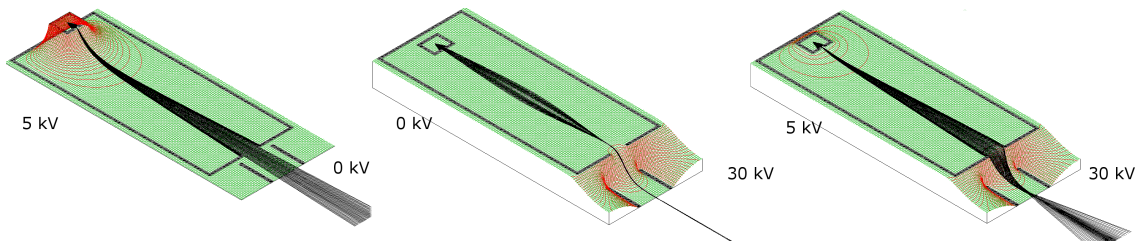


Figure 7.11: Simulation of the ion trajectories inside the source part from a point like proton source and different  $U_{\text{source}}(0..5 \text{ kV})/U_{\text{cage}}(0..30) \text{ kV}$  ratios. The potential is marked in z direction by the green grid. Red are the equipotential lines and black the particle trajectories.

## 7.2.2 The Einzel lens

The focusing effect of the three-cylinder Einzel lens was modeled starting with a parallel beam of 30 keV protons, . On the left-hand side of fig. 7.12, the proton trajectories are shown for four different values of  $U_{\text{lens}}$ ; the potential is shown in green and the trajectories in red. The right-hand side shows the focal length  $f_{\text{focal}}$  (distance from the lens to the cross point of the trajectories) as a function of  $U_{\text{lens}}$ . The exponential fit curve is just used to guide the eye. The expected reduction of the beam mentioned in

sec. 7.1.3 was proved and quantitatively understood. The mentioned effects of double focusing close to the beam energy are not included in this software.

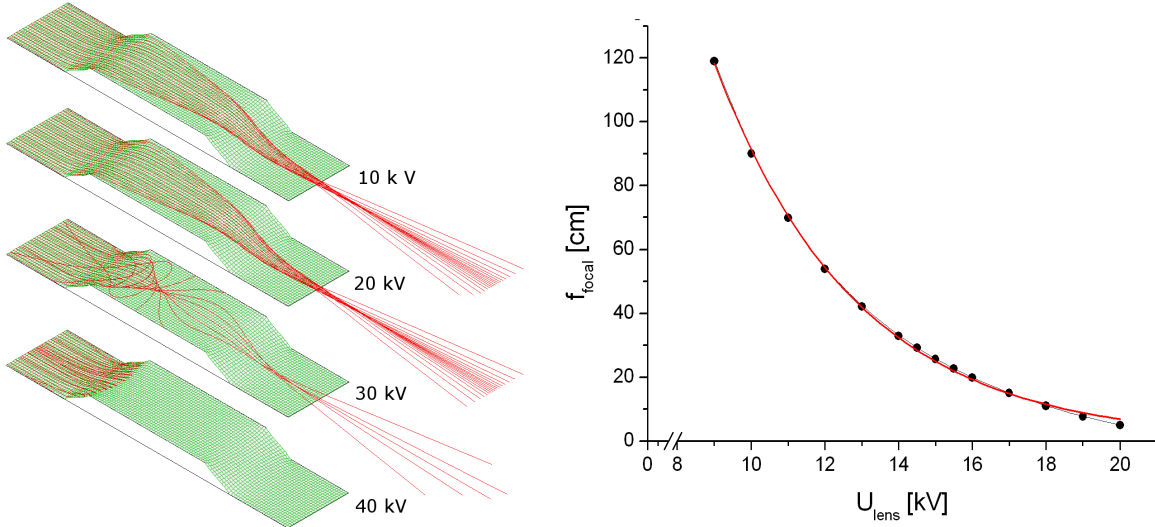


Figure 7.12: Left: Simulation of 30 keV proton trajectories through the Einzel lens for four voltages of the center electrode; right: focal length  $f_{\text{focal}}$  as a function of  $U_{\text{lens}}$ .

### 7.2.3 Beam transport properties

In order to derive a number for the divergence of the beam, the ion losses up to different positions along the beam. The whole *paff* setup was simulated together (with a spherical emitting point source in the middle of the plasma area) and the trajectories ending in the Faraday cup and the target were calculated. Later the real source and the count rates were compared to the used source strength ( $\cdot 10^6$  30-keV) protons and simulation results shown in table 7.4. These correction factors will be used later together with the measured data.

	Faraday cup	target position
simulated ions	$\approx 2000$	$\approx 1000$
relative correction factor	$\approx 0.002$	$\approx 0.001$

Table 7.4: Relative correction factor for the intensity loss due to the divergent beam calculated with *Simion* simulations. Source power for the simulations were  $10^6$  protons of 30 keV energy.

The first step from the source to the monitor is used as reliability check on the simulation. The second value is then used for the correction between the fixed monitor and the expected count rate at the target.

## 7.3 Characterization

In order to characterize the proton accelerator, a series of measurements were performed. Standard equipment like the Faraday cups, the MCP detector and a prototype

detector, a cubic CsI(Tl) crystal  $10 \times 10 \times 10 \text{ mm}^3$  on top of a Hamamatsu R1490 photomultiplier were used. In addition, a thin-layer phosphor screen at the target position was employed to visualize the ion beam.

### 7.3.1 Beam composition

Starting point of the following measurements was a source current of  $I_{\text{extract}} = 400 \mu\text{A}$  and a gas pressure of  $2 \cdot 10^{-5} \text{ mbar}$  (typical values from the Specs manual [178]). The acceleration potentials were set to  $U_{\text{source}} = 2 \text{ kV}$  and  $U_{\text{cage}} = 30 \text{ kV}$ . The current  $I_{\text{Faraday}}$  on the Faraday cup was measured as a function of the magnetic field  $B_{\text{bending}}$  of the separation magnet (calibrated with a Hall probes from Lakeshore) leading to the mass spectrum of the produced positive ions shown in fig. 7.13.

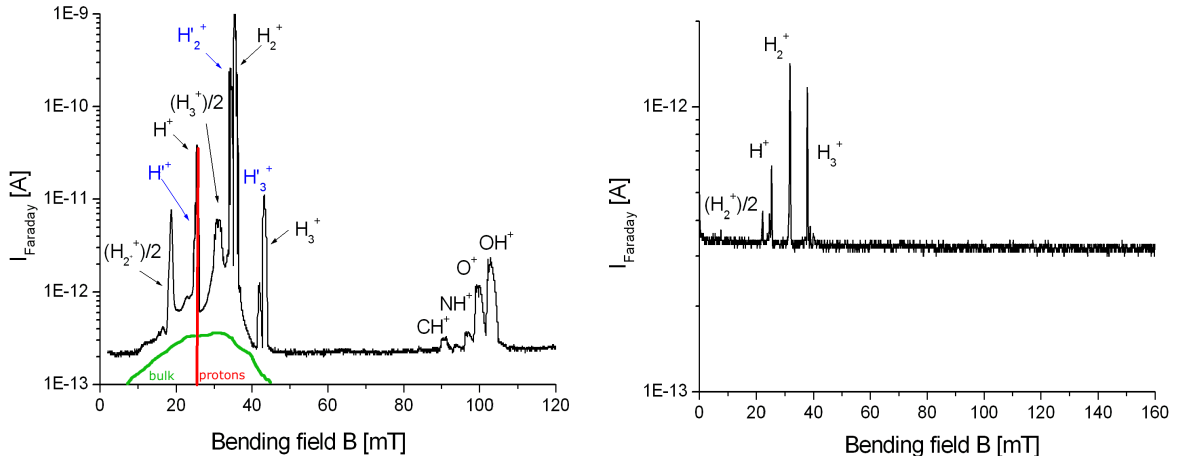


Figure 7.13: Mass spectrum of the ions extracted from the hydrogen plasma under normal operating conditions. Left: rest gas pressure of  $10^{-6} \text{ mbar}$  and normal operation  $H_2$  gas pressure added. The voltage setting was  $U_{\text{source}} = 2 \text{ kV}$ ,  $U_{\text{cage}} = 30 \text{ kV}$ . Right: low rest gas pressure of about  $< 10^{-7} \text{ mbar}$  and low  $H_2$  gas concentration. The voltage setting was  $U_{\text{source}} = 0.1 \text{ kV}$ ,  $U_{\text{cage}} = 30 \text{ kV}$  (right-hand side).

From the manufacturer specifications one would expect 1 – 3% ionisation probability for  $H^+$  and 99 – 97% for  $H_2^+$  and therefore only two peaks. At least 14 main peaks were observed and shown in fig. 7.13.

For ions with a fixed mass  $m_{\text{Ion}}$ , charge  $q$  and velocity  $v_{\text{Ion}}$  the B-field necessary to get the ions with the right bending radius  $r(30^\circ)$  into the beam tube behind the magnet can be easily calculated (eq. 7.4).

$$F_{\text{centrifugal}} = F_{\text{Lorentz}} \rightarrow \frac{m_{\text{Ion}} v_{\text{Ion}}^2}{r} = q \cdot v B_{\text{bending}} \sin \alpha \quad (7.2)$$

$$E_{\text{kin}} = U_{\text{acc}} \cdot d_{\text{cage}} = \frac{1}{2} m_{\text{Ion}} \cdot v_{\text{Ion}}^2, \quad (7.3)$$

$$r_{30^\circ} = \sqrt{\frac{2m_{\text{Ion}} U_{\text{acc}} d_{\text{cage}}}{q^2 B_{\text{bending}}^2}} \propto \sqrt{m_{\text{Ion}}}. \quad (7.4)$$

This leads to a first guess for the position of the proton peak. The relative peak height of the most pronounced  $\text{H}_2^+$  and  $\text{H}^+$  peaks with the intensity ratio of 99.97/1.3 corresponding to the ionization probability allows to identify these peak in the spectrum. Now the abscissa can be rescaled into mass units. The main peaks with masses of 2, 1 and 3 u fit perfectly. The following improvements finally lead to the clean signal shown on the right hand side.

- The source part was flushed  $10^{-7}$  mbar  $\longleftrightarrow$   $10^{-4}$  mbar many times with hydrogen gas before normal operation: Almost all peaks caused by ionization of rest-gas molecules inside the source 90 mT vanished<sup>3</sup>(visible at  $B > 60$ ) in fig. 7.13.
- The gas pressure of the hydrogen gas inside the source and the source part was reduced by three orders of magnitude: the bulk intensity indicated in green disappeared. Events could be identified as pick-up reactions ions in the beam from the neutral hydrogen gas, see [182]. Typical reactions are listed in table 7.5.
- The ratio of the acceleration potentials was changed from  $U_{\text{source}}/U_{\text{cage}} = 2 \text{ kV}/30 \text{ kV} \rightarrow 0.1 \text{ kV}/30 \text{ kV}$ : The double peak structure indicated with Ion  $I$  and Ion  $I'$  (in blue) almost disappeared. Ions from the source are created inside the plasma volume and accelerated by the sum of  $U_{\text{source}}$  and  $U_{\text{cage}}$ , others are created at the extraction hole by charge exchange between neutral rest gas atoms and beam ions. They get just the energy  $U_{\text{cage}}$ . The peaks become sharp as predicted by the simulations fig. 7.11 if the source voltage is reduced to a small value. This can also be seen by the pictures from the phosphor screen section 7.20.
- Pick-up reactions of  $\text{H}_2^+$  and  $\text{H}_2$  lead to the formation of quite stable  $\text{H}_3^+$  ions. The relative intensity between extracted  $\text{H}^+$ ,  $\text{H}_2^+$  and  $\text{H}_3^+$  depend strong on the geometry of the source and the extraction electrodes [190]
- Electrons released from the wall (between source and bending magnet) outside the isolator are accelerated into the positively charged ion beam and towards the source by the cage potential. At a certain velocity, determined by the ionization potential of hydrogen,  $\text{H}^+$  ions are created from the neutral hydrogen molecules. These ions are then accelerated by the potential difference between from the place where they were created and the isolator in the direction to the separation magnet. They form the  $\frac{1}{2}\text{H}^+$  peak. This peak does not show the double peak structure and scales as  $\text{H}^+$  and  $\text{H}_2^+$  intensities with the  $\text{H}_2$  gas pressure.
- The broad peak at  $B_{\text{bending}} \approx 30 \text{ mT}$  (corresponding to 1.5 proton masses) is generated by charge exchange between protons and  $\text{H}_2$  molecules. The peak at 1/3 proton mass has a similar origin.

The proton peak (drawn in red in the spectrum) is clearly identified and almost separated, as shown on the right-hand side of fig. 7.13. Once the origin of the other peaks is sufficiently well known, it is also possible to use these ions for experimental purposes.

## 7.3.2 Beam intensity variations

### Extraction current

Reducing the negative current  $I_{\text{plasma}}$  from the plasma at the source control unit is the easiest way to reduce the beam intensity  $I_{\text{extract}}$ . In fig. 7.14 the proton count rate of

---

<sup>3</sup>Rescaling the abscissa to a mass scale leads to identification of CH, NH and OH ions from air.

Process	Description	Reaction
1	rest gas ionization	$I^+ + X^0 \rightarrow I^+ + X^+ + e^-$
2	charge exchange beam $\leftarrow \rightarrow$ rest gas	$I^+ + X^0 \rightarrow I^0 + X^+$
3	higher ionization levels beam particle	$I^+ + X^0 \rightarrow I^{2+} + X^+ + 2e^-$
4	rest gas ionization through neutral particle	$I^0 + X^0 \rightarrow I^0 + X^+ + e^-$
5	heating of electrons through beam ions	$I^+ + e^- \rightarrow I^+ + e^-_{\text{fast}}$
6	beam ions scattering on rest gas	$I^+ + X^0 \rightarrow I^+ + X^+ + e^-$
7	electron capture from rest gas atoms	$I^+ + 2e^- \rightarrow I^0 + e^-$
8	electron capture by rest gas ions	$X^+ + 2e^- \rightarrow X^0 + e^-$
9	rest gas ionization by compensation electrons	$X^0 + e^- \rightarrow X^+ + 2e^-$

Table 7.5: Possible reactions of the ion beam atoms  $I$  with rest gas atoms  $X$  leading to the bulk intensity described in the text [182].

the MCP  $N_{\text{proton MCP}}$  with a 30-keV proton beam at a gas pressure of  $1.1 \cdot 10^{-5}$  mbar is plotted, together with two fit curves as a function of  $I_{\text{extract}}$ . The count rate was taken from the inner anode of the MCP detector with  $U_{\text{MCP}} = 1650$  V. Besides the linear behavior, the working area of the source, one can also see that below  $25 \mu\text{A}$  stable operation can no longer be guaranteed.

For later use we always kept  $I_{\text{plasma}} > 50 \mu\text{A}$ .

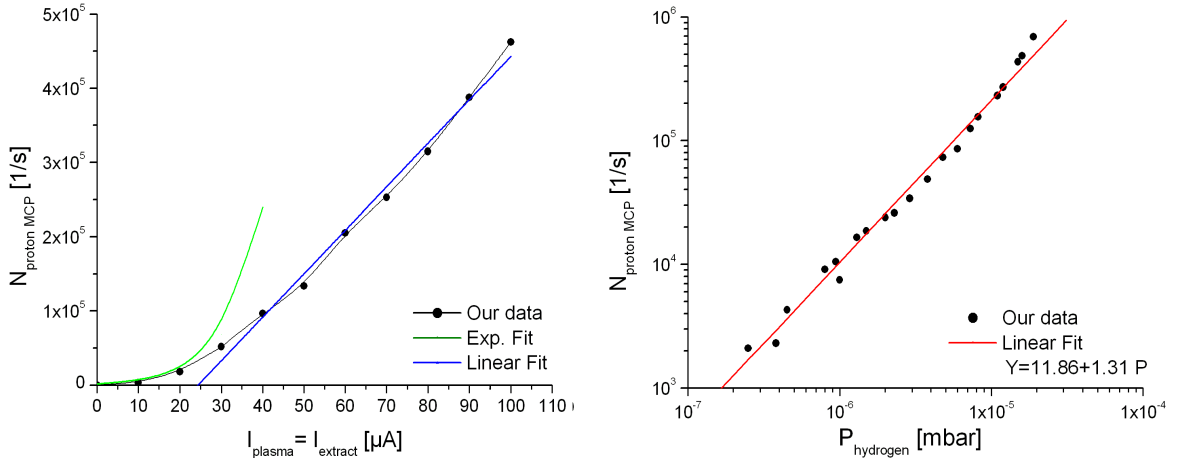


Figure 7.14: Left: proton count rate  $N_{\text{proton MCP}}$  at the MCP detector as a function of the extraction current  $I_{\text{extract}}$  as source control settings. Right: proton count rate as function of the hydrogen gas pressure inside the plasma source.

## Pressure

Changing the gas pressure is another way to control the plasma density and finally the beam intensity. In fig. 7.14, right-hand side, the MCP count rate for 30-keV protons is plotted as a function of hydrogen gas pressure  $p_{\text{hydrogen}}$  inside the chamber (the source). The source voltage was set to 100 V and the plasma current to 1000  $\mu\text{A}$ . As indicated

in the plot, the production follows a power law, which leads to the shown linear fit shown in red in the doubly logarithmic plot.

### Acceleration voltage

The applied acceleration potential has an influence on the beam intensity as well. The result of our investigation is presented in fig. 7.15. The count rate at the MCP detector  $N_{\text{proton\_MCP}}$  was measured for different kinetic energies  $E_{\text{kin}}$ . The source voltage  $U_{\text{source}}$  was kept constant at 1 kV and  $U_{\text{cage}}$  was changed. Of course the magnetic field was always adjusted to the new beam intensity maximum, as indicated in fig. 7.15 right-hand side which shows the bending field  $B_{\text{bending}}$  as a function of the kinetic energy of the protons.

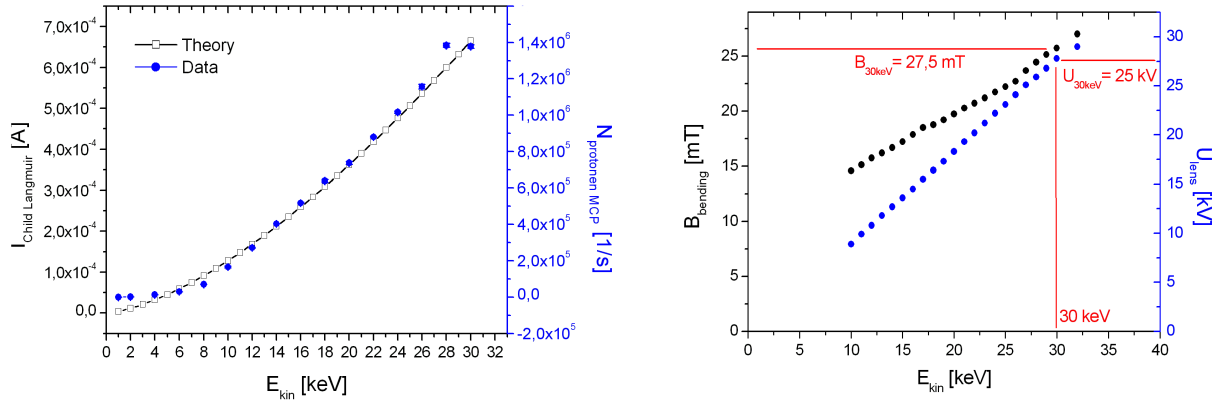


Figure 7.15: Left: measured ion count rate at the MCP as a function of the proton kinetic energy, compared with the  $I \propto U^{2/3}$  dependence predicted by the Child-Langmuir theory. Right: the settings of  $B_{\text{bending}}$  (black) necessary to get the maximum intensity of the proton beam with energy  $E_{\text{kin}}$  at the target. The voltage  $U_{\text{lens}}$  for a sharp focusing at the target position is shown in blue.

The Child-Langmuir theory developed for the description of diodes can also be used to calculate the extractable current  $I_{\text{Child-Langmuir}}$  with a pull-electrode potential  $U$  ( $U_{\text{cage}}$  in our case) from an infinite plasma area. In this case  $d$  is the distance between plasma and electrode and  $r_{\text{extract}}$  the beam extraction hole at the electrode. Further explanations can be found in [191] and [192] and the special application to plasma sources used here in [182]. The Child-Langmuir equation is:

$$j_{\text{Child Langmuir}} = j_{\text{C. L.}} = \frac{4}{9} \cdot e_0 \cdot \sqrt{\frac{2q}{m}} \cdot U^{\frac{2}{3}} d$$

$$I_{\text{extract C. L.}} = \pi \cdot r_{\text{hole}}^2 \cdot j_{\text{C. L.}}$$

$$I_{\text{extract C. L.}} \propto U^{\frac{3}{2}} \propto U_{\text{cage}}^{\frac{3}{2}} = M \cdot U_{\text{cage}}^{\frac{3}{2}}.$$

Differences to the model used in the theory, like an infinite extended plasma surface and the impact of the special source geometry has been included in the correction factor  $M$  (dielectric constant  $\epsilon_0$ , the mass  $m$  and charge  $q$  of the ions). The proportionality  $I_{\text{extract C. L.}} \propto U_{\text{cage}}^{2/3}$  to our cage voltage is shown with black points in fig. 7.15, left.

Theory and experimental data fit quite well.

## Beam defocusing

Most of the explained beam intensity variations are quite successful down to a count rate of  $10^4 \text{ s}^{-1}$ . In order to reach lower values, we used the Einzel lens for defocusing. The 30-keV proton spectra were taken with the CsI(Tl) scintillation counter. The result can be seen in fig. 7.16. A more detailed explanation of the data requires more information on the beam profile characterization and is given in section 7.3.6.

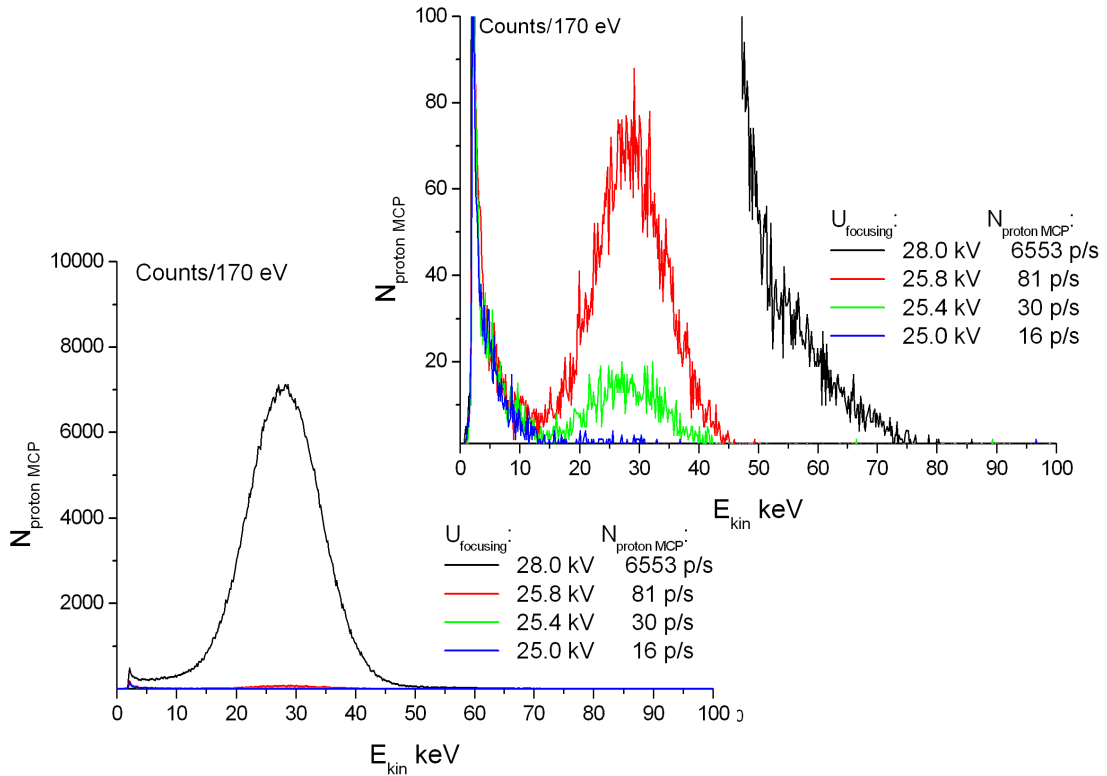


Figure 7.16: Beam intensity variation by changing the defocusing potential  $U_{\text{lens}}$  of the Einzel lens. The binning was 170 eV. The used lens voltage  $U_{\text{lens}}$  and the resulting intensity is listed next to the spectra.

Different 30 keV proton spectra are shown in fig. 7.16. The used lens voltage  $U_{\text{lens}}$  and the resulting intensity is listed next to the spectra. Signal pile-up set the upper limit for the black curve. The background count rate of  $\approx 15 \text{ s}^{-1}$  shown in blue sets the limit on the low intensity curve shown in green.

### 7.3.3 Beam energy

As mentioned in the last paragraph, changing the kinetic energy of the beam protons requires new settings of the separation magnetic field and if necessary, the lens potential to get again maximum proton intensity on the target position. Both free parameter

were measured as a function of the proton energy within the region of interest (10 to 32 keV). The result, together with the values for a 30 keV proton beam masked in red can be found in fig. 7.15.

Later it was possible to expand the usable area in both directions. Spectra have been measured at levels down to 1 keV and up to 45 keV without break-down problems.

### 7.3.4 Beam profile

The vertical,  $B_{\text{bending}} = B_x$  magnetic field from the ion separation magnet and the electron bending magnet (number 13 in fig. ??)  $B_{\text{electron}} B_y$  were used to measure the proton beam profile at the MCP monitor detector with an x-y scan ( $B_x, B_y$  variation). For this measurement a 30 keV proton beam was produced and the first peak indicated in fig. 7.13 with  $H_2^+/2$  were used<sup>4</sup>. The background was reduced as indicated in section 7.3.1 to get a spectrum similar to fig. 7.13 (left). In order to avoid beam splitting  $U_{\text{source}}$  was set to the lowest possible value of 50 V .

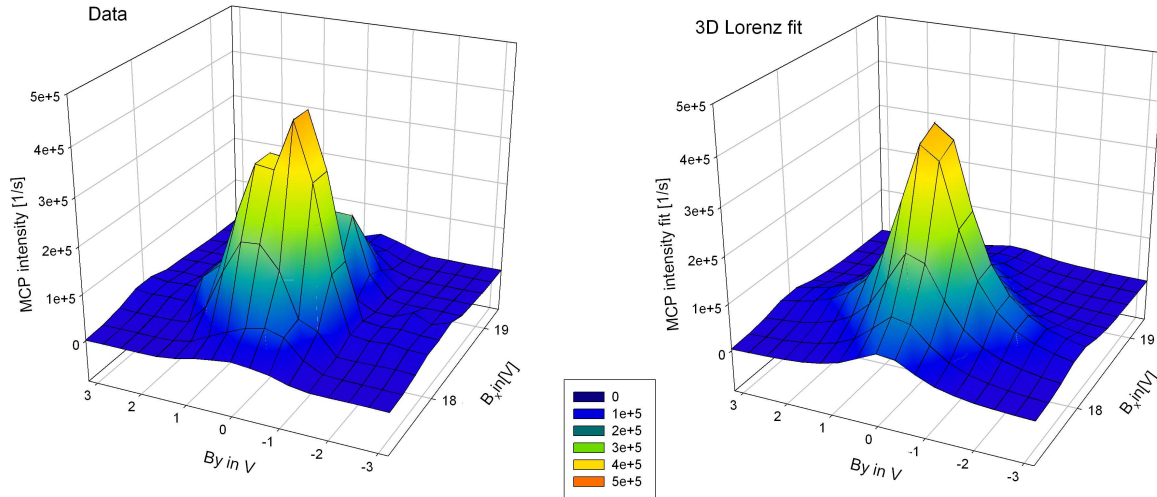


Figure 7.17: Left: beam profile measured with the two bending magnets and  $H_2^+/2$  ions of 30 keV energy. For further explanations see also section 7.3.1. Right: calculated profile with 2 Lorentz functions.

It was just possible to rescale the  $B_x$  magnetic field from the separation magnet because it was calibrated with a Hall probes (cf. section 7.3.1). The field from the  $e^-$  coils is much smaller and guided directly with an iron yoke to the steel beam tube. The correct  $B_y$  value can only be measured inside the beam tube itself. Therefore, the units are kept as the applied current through the coils.

A two-dimensional Lorentz fit of the measured intensity  $I_z$  showed a better consistence with the data than a 2D-fit of a Gaussian.

<sup>4</sup>The required magnetic field to bend the electrons is much lower than for the protons thus the  $B_y$  field is smaller. To still guarantee that the applied field is sufficient to cover the complete beam range in the  $x, y$  scan the hydrogen peak with the lowest kinetic energy was used.

$$I_z(\text{Lorentz}) = \frac{484651}{\left(1 + \left(\frac{B_x - 18,0}{0,288}\right)^2 \cdot 1 + \left(\frac{B_y + 0,140}{0,808}\right)^2\right)}$$

The beam profile is symmetric and shows the possibility to create background-free beams. The focusing effect of both separation magnets [?] can be used to even produce a point like intensity profile.

### 7.3.5 Beam monitoring system

As described in section 7.1.2 (Faraday cup) electrons ejected from the walls of the Faraday cup may lead to wrong beam-current readings. In order to avoid this, a suppression ring electrode was installed. Different suppression voltages  $U_{\text{sup}}$  were applied and the current was measured with the *paff* Faraday cup. This reference cup was 1200 mm long with a triple shielding on ground potential leading, together with a 5mm diameter beam collimation to a 100% detection efficiency. The result is shown in fig. 7.18. Above 200 V both cups show equal results, indicating that at this suppression voltage the losses of extracted electrons at our cup have already reached a negligible value. The measurements were made at a beam of the Maier-Leibnitz Laboratory (MLL) and afterwards cross-checked at our facility.

This maximum necessary suppression voltage to manipulate the unwanted electrons inside the beam was then also applied behind the irises for beam cleaning.

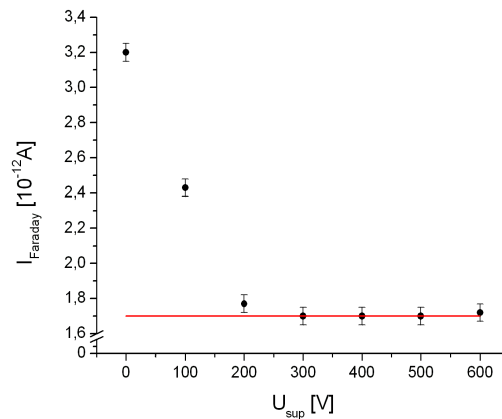


Figure 7.18: Faraday cup current as a function of the suppression voltage, (full circles black) compared with the count rate from the reference cup (red line).

The data set in fig. 7.19 shows the possibilities of the two monitor systems at the *paff* facility. Starting with medium intensity and the Faraday cup moved into the beam, the extraction current  $I_{\text{extract}}$  at the plasma source control unit was stepwise decreased and the particle count rate was calculated from the measured current at the electrometer. Below the sensitivity of the Faraday cup, the measurement was continued

with the MCP detector. Figure 7.19 shows a perfect transition between the two monitor detector regions. Hence, all beam intensities, from single events to the mA region, can be covered and frequently monitored.

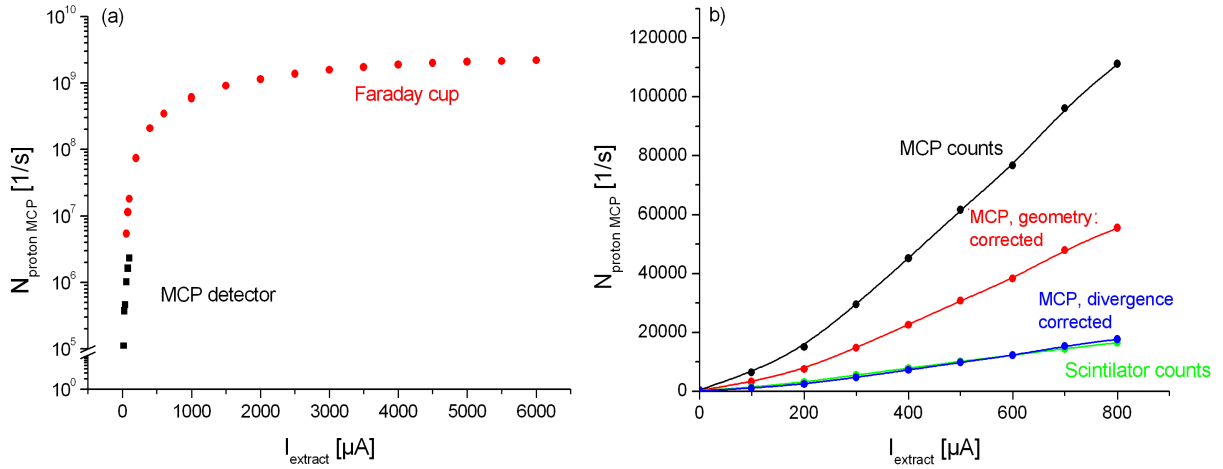


Figure 7.19: Left: the combination of the two monitor detector systems, MCP for low intensities and Faraday cup for high intensities. Right: the count rate at the MCP and the expected count rate from the scintillation counter. For further explanations see the text. The straight line between the data points are drawn to guide the eye.

On the right-hand side of this figure the MCP monitor count rate (black) is compared with the signal derived from a CsI(Tl) crystal ( $10 \cdot 10 \cdot 10 \text{ mm}^3$ ) on top of a Hamamatsu photomultiplier (cf. section 7.3) in green. Both are illuminated by 30 keV protons as function of the plasma extraction current  $I_{\text{extract}}$ . The red points indicate the MCP counts corrected for the beam divergence active areas of MCP inner anode ( $\varnothing 20 \text{ mm}$ ) and the scintillator size. The divergence correction factor (0.5) derived from the *Simion* simulations pushes the data down to the blue points. The expected and the measured count rate, shown in green agree very well and proof the reliability on the simulation and the monitor system .

### 7.3.6 Beam visualization

A phosphor screen [193] was used to visualize the shape of the beam and check the beam manipulating devices, collimator and Einzel lens. In a series of pictures, taken with a Philips web cam behind the screen and shown in fig. 7.20. The protons were accelerated with  $U_{\text{cage}} = 30 \text{ kV}$  and a variation in  $U_{\text{source}}$  between 200 V and 1000 V is shown.

The horizontal extension could be redrawn into a fine magnetic scale of the separation magnet. The pictures shown the origin of the peak splitting used as explanation in section 7.3.1 and shown in fig. 7.13. From the in situ analysis of the beam one also gets information that a pencil beam can be separated from its halo by a suitable choice of  $U_{\text{source}}/U_{\text{cage}}$ . The line structure which shows up instead of a beam spot can be explained by the absence of a focusing horizontal field component. The homogeneous field  $B_x$  acts like a cut through the circular beam profile leading to a line of ions

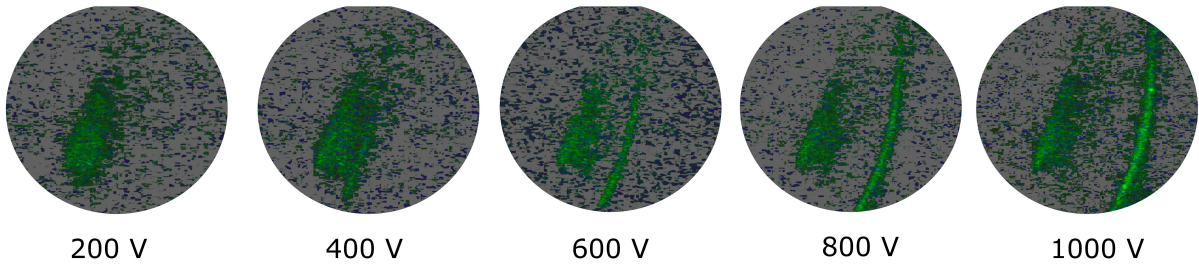


Figure 7.20: Shape of a 30-kV proton beam, as visualized with a phosphor screen for different source potentials  $U_{\text{source}}$ .

with the right mass-to-energy ratio. The beam curvature is caused by misalignment between source and magnet. This misalignment leads also to aberration effects in the electrostatic optical lens (cf. fig. 7.21).

The same beam was then studied as a function of the voltage applied to the Einzel lens and thus the refractive index of the lens. Instead of the expected continuous change of the beam intensity maximum with the focal point (cf. fig. 7.12) the curved beam entering the lens is deformed in the way shown in fig. 7.21. Besides the misalignment already mentioned, the Einzel lens cylinders are not perfectly parallel to the beam axis, which leads to such effects. The points mentioned above keep some potential for future improvements.

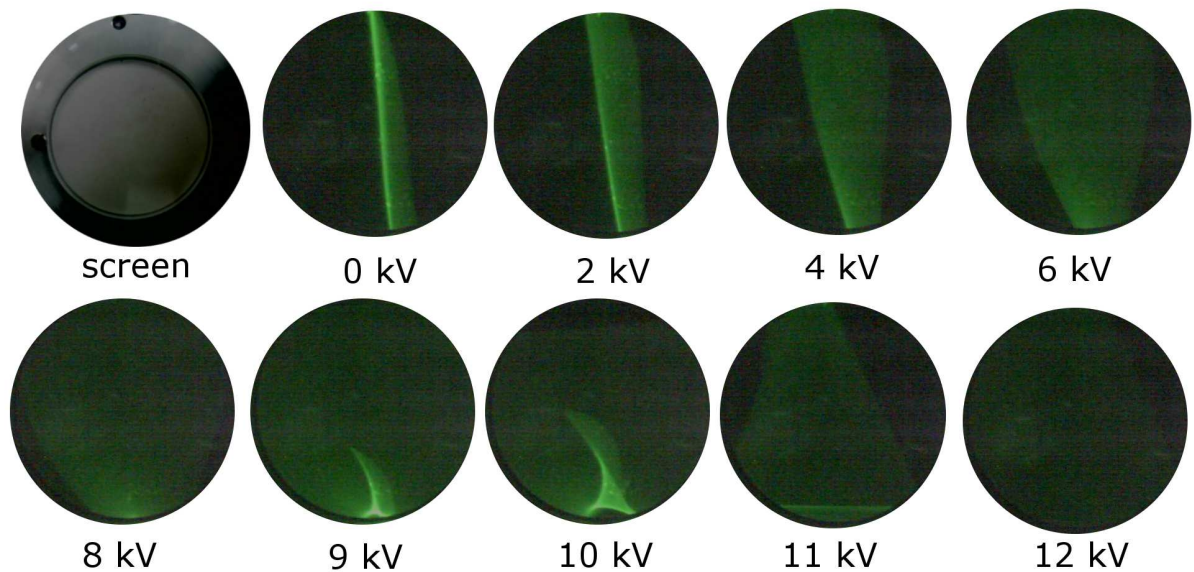


Figure 7.21: Astigmatism caused by the misalignment of the proton beam and the Einzel lens. The voltage at the different pictures are the  $U_{\text{lens}}$  values

Nevertheless for the task of reducing the beam intensity these misalignments are not harmful at all. To know about the beam behavior leads us even to the advantage, that the beam hits the target for three values settings of  $U_{\text{lens}}$ . Next to the expected parallel beam with 2-3 kV as well as the double reflected one at  $U_{\text{lens}} \approx 90\%$  beam energy the

lens failure produces an intermediate one. All maxima have different intensities and different intensity profiles, but drop to zero in between (not possible with an ideal concept). Hence, the count rate can be adjusted by choosing the distance to one of these maxima together with the collimator down to very small count rates.

### 7.3.7 Electron beam

A Faraday ring inside the  $e^-$  part of *paff* (number 11 and 12 in fig. 7.1) served to localize the  $e^-$  beam and measure the set beam intensity. By a systematic change of the currents through the two steering coil pairs, the  $B_x$  and  $B_y$  components in this region could be varied to scan over the whole cross section. The Faraday ring plus its support rod could be visualized from the measured current intensity shown in fig. 7.22  $I_{\text{Faraday ring}}(B_x, B_y)$ . The combination of (0.1 A, 1.0 A) let the  $e^-$  beam hit the ring and thus measure the beam intensity before the beam was shot with (0.9 A, 0.8 A) through the middle of the  $\approx \varnothing 15$  mm ring aperture. The mismatch to the perfect circle is due to the non-perpendicular alignment of the two steering coils.

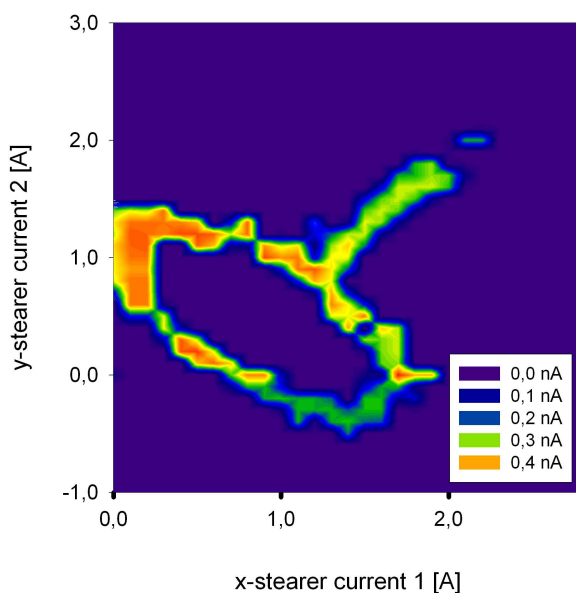


Figure 7.22:  $X, Y$  scan of the electron beam with the steering coils  $B_{x \text{ electron}}$  and  $B_{y \text{ electron}}$ . The intensity was measured at the Faraday ring, the monitor detector for the electron intensity.

With an electron-gun cathode current of  $0.4 \mu\text{A}$  we measured  $0.44 \text{ nA}$  at the Faraday ring. After bending into the proton beam tube, an intensity of a few pA was measured with the Faraday cup in front of the target position.

## 7.4 Experimental application of *pa ff*

### 7.4.1 *aSPECT*

The *pa ff* accelerator was used to check the performance of the silicon strip detector and the new silicon cylindrical drift detector for *aSPECT*. Besides investigating the detector response to protons, it was possible to fine tune the electronics for an improved signal to background ratio [194]. A  $\varnothing$  1 mm movable aperture in front of the detector was used to measure the spatial resolution of the Si strip detector with a 30-keV proton beam. The result is shown in fig. 7.23, left and published in ref. [195]. For the second generation of *aSPECT* detectors they switched to silicon drift detectors from PN-sensors[196]. Together with their front end electronics, it was possible at the *pa ff* accelerator to prove that their detectors can be used for low energy proton detection, even for energies in the range of 10 keV as shown in the fig. 7.23 right. From this point on it was possible to reduce the applied voltage by a factor of two and decrease the risk of high voltage break through significantly

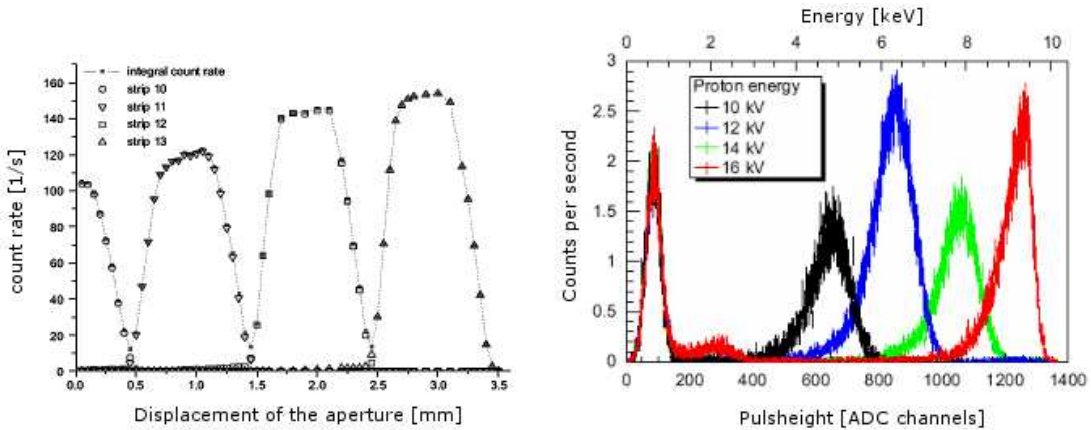


Figure 7.23: Count rates and proton spectra as measured with the silicon detectors of *aSPECT*. Left the silicon strip detector spatial resolution measured with a moved aperture  $1 \text{ mm}^2$  in front of the strips and on the right side the later used cylindrical drift detector with their improved signal to noise ratio to measure down to 10 keV protons.

### 7.4.2 *PENeLOPE*

The development of the large area proton scintillation counter for the neutron lifetime experiment *PENeLOPE* as described at sector 5 and the low temperature characterization of the LAAPD (section. 6) were performed at the *pa ff* facility.



# Chapter 8

## Summary

This thesis is divided into four parts, dealing with investigations of solid  $D_2$  as a converter material for UCN, tests of UCN guides, the development of low energy, large surface proton detector and studies of large area avalanche photodiodes at cryogenic temperatures.

- In the first part, a detailed investigation on the converter material for a UCN source via solid  $D_2$  was described. It was accomplished by optical and neutron inelastic scattering techniques. From the measured phonon density of states  $Z(\omega)$  it was possible to determine the most suitable cold source temperature to be  $T=40$  K as well as identify the excitations responsible for UCN production. Both have wide implications on the ongoing developments in this field. In addition we could show that the expected UCN production can be derived directly from the measured inelastic scattering data. This seems to be an ideal tool for future converter materials and converter treatments (temperature cycling) comparison for groups working in this field.

We performed the *cube* $D_2$  experiment a small test source at the cold neutron beam of the FRMII to produce UCN under different source parameters. It seems that an additional loss channel depending on the ortho  $D_2$  content has to be taken into account for deuterium based UCN converters.

A new concept for the mini $D_2$  UCN source inside the through going beam tube of the research reactor was developed and presented.

- A critical component for the performance of the experiment *PENeLOPE* is dealt with in the second part: efficient guiding of neutrons from the source towards the lifetime experiment. Two methods, the *two hole method* and the *storage method* for extracting the loss coefficient  $\mu$  (loss probability per wall collision) and  $f$  (diffuse scattering probability) for sample tubes were developed and could be experimentally compared. In the course of this thesis, the dependence of  $f$  and  $\mu$  on temperature and cleaning procedures could be determined. The results were compared to ray-tracing simulations.

- The third part deals with the development of a low energy proton detector for the lifetime experiment based on a thin layer of CsI scintillator. The temperature dependence of the light yield of pure and Tl doped CsI was measured down to 20 K with radioactive sources and low energy proton beams. Also the detection principle of a  $1.5 \mu\text{m}$  thin evaporated test detector was shown with 30 and 40 keV protons and an 18 keV electron beam.

- The fourth part describes a systematic study on the low temperature behavior of the two typical LAAPD realizations (*bevelledge* high voltage and *reachthrough* low voltage). A model based on the temperature dependent phonon scattering of the created electron hole pairs is used to explain the saturation of the gain at 60 K. However, it was confirmed, that both LAAPD may be used down to 20 K.
- The last chapter describes the *paff* accelerator, which was constructed for e and detector developments in conjunction with neutron decay. The accelerator facility provides a tunable proton beam of 1 keV-45 keV energy and intensities between  $10\text{ s}^{-1}$  and several  $10^{12}\text{ s}^{-1}$  (corresponding to energies and intensities from n-decay experiments). It is also possible to combine the proton beam with an electron beam of up to 18 keV to allow background studies. The target position of the accelerator is equipped with a cold-head, hence temperatures between 15 K and 350 K may be reached here.

# Chapter 9

## Outlook

Many of the developed experiments or parts of experiments will be used in the next future:

The  $\text{cubeD}_2$  setup will be set up again at the cold neutron beam MEPHISTO of the FRMII for ongoing systematic studies on converter materials like  $\text{CD}_4$  and solid  $\text{O}_2$ .

The introduced technique to extract the possible UCN production from inelastic neutron scattering data will be used on a short time perspective on He as converter material and later on solid oxygen and  $\text{CD}_4$ . However not only the materials will be addressed, also the different preparation conditions will be correlated with UCN important quantities.

The new concept of the  $\text{miniD}_2$  UCN source went through some evaluation discussions as well as optimization processes. A real scale model was sintered and at the moment first welding tests have been completed.

The UCN-valves have been used for the *Abex* experiment to study absorber materials for the *PENeLOPE* lifetime experiment. By the end of this year they will also be used for systematic tests of UCN guides from different manufacturers.

By the end of this year the *pafl* accelerator will be used again from the *aSPECT* collaboration for systematic improvement of their silicon drift detector.

On the other hand the *pafl* accelerator will be equipped with a second straight beam line to provide the *BOB* (bound beta decay of free neutrons into hydrogen molecules) collaboration with a neutral hydrogen beam as well as the proton beam for tests of their proton detector concept, development of a detector for neutral hydrogen and step by step test their laser manipulation and spin splitting systems on neutral hydrogen.



# Chapter 10

## Appendix

### 10.1 Oxisorb as converter material

The Oxisorb converter material used is strongly hygroscopic and usually used to clean gases from oxygen and water impurities. The different chromium and oxide compounds (mostly  $Cr_2O_3$ ) cover the surface of silica gel and form a black glass-like structure. Once the converter is contaminated with impurities, it can be reactivated by heating to temperatures above 400 °C. In our case, however, heating to this temperature was not possible because of the indium sealing. No decrease in performance was seen during one year of operation, in good agreement with the report from the PSI group [44]. Several experiments were performed to characterize the OXISORB material:

- The typical particle dimensions were measured using meshes with different DIN-ISO 3310/1 sizes. Their contribution listed at table 10.1 was determined from the weight of the grains
- The OXISORB density was measured for the two most abundant grain sizes with a pycnometer. Average densities of 2.2 g/cm<sup>3</sup> and 2.65 g/cm<sup>3</sup> were found for the grains with 1-2 mm and 0.5-1 mm diameter, respectively. The influence of the grain size on the average density may be explained by gas enclosures with the probability scaling with the grain size.
- In order to determine the specific surface available for catalysis the grains with diameters between 0.5 and 1 mm were dried in vacuo for two hours at 150 °C. Afterwards the specific surface was measured with the BET method using nitrogen gas in a Micrometrics Gemini 2375 surface analyzer. The result, an effective surface of 590 m<sup>2</sup>/g agrees with the value 800 m<sup>2</sup>/g given for pure silica-gel grains.
- The absorption of water from humid air as a function of time may give an idea about the amount of deuterium absorbed by the OXISORB during conversion (D<sub>2</sub> which can not easily be removed again). In order to determine its amount, the grains of size 1-2mm were dried in the vacuum stove again and afterwards stored at room temperature in air of 100% relative humidity, their mass increase  $\Delta m$ , was measured as a function of time.  $\Delta m$  normalized to 1 g of Oxisorb, is shown in ref. [57] together with the result of a fit function

$$\delta m = \Delta m \cdot (1 - e^{-t/\tau})$$

From the data shown in [57] we found a saturation value of  $\Delta m = 70.3 \pm 1 \text{ mgH}_2\text{O/g}$  Oxisorb and a time constant of  $\tau = 746 \text{ min}$ . From the density of water one may calculate the molecule density, the volume of one water molecule in a mono layer, naively assuming it to be a sphere and, finally, the area that is covered by one molecule. Dividing the measured effective surface of  $590 \text{ m}^2/\text{g}$  by this number and assuming a filling factor of 0.85 (for in two dimensional spheres closed packed) leads to the maximum amount of water that can be bound on the surface of 1g Oxisorb of  $4.40 \cdot 10^{21}$  molecules. The comparison of this number with the mass,  $0.0703 \text{ g} = 2.35 \cdot 10^{21}$  molecules, yields that only about one half of the OXISORB surface is covered by water molecules.

Mesh size	$\geq 2\text{mm}$	2-1mm	1-0.5 mm	0.5-0.25 mm	0.25-0.125 mm	$\leq 0.125 \text{ mm}$
Total weight	0.117	7.42	18.37	0.84	0.012	0.010
Percentage	0.44	27.7	68.6	3.1	$4.5 \cdot 10^{-2}$	$3.7 \cdot 10^{-2}$

Table 10.1: Size distribution of the Oxisorb particles ref. [57].

## 10.2 Inelastic neutron scattering

The introduction on inelastic neutron scattering was taken from [58, 31, 50]

The principle of neutron scattering is to measure the number of scattered neutrons depending on their momentum  $\hbar q$  and energy  $E$  exchanged with a sample. The number of counts in a detector  $I$  is proportional to the time averaged neutron flux at the sample  $\Phi$ , the number of atoms in the beam  $N$ , the detector solid angle  $\Delta\Omega$  and the detector efficiency  $f$ , and finally the width of an energy channel  $\Delta E$ . Hence

$$I = \Phi N \Delta\Omega f \Delta E \frac{d^2\Omega}{d\Omega dE}$$

In order to obtain a quantity that is completely independent of the details of the scattering experiment and hence being exclusively a property of the sample under investigation, the average scattering function  $S(q, \omega)$  is introduced:

$$\frac{d^2\Omega}{d\Omega dE} = \langle \bar{b}^2 \rangle \frac{k_f}{k_i} S(q, \omega)$$

With the already introduced averaged scattering length  $\langle \bar{b}^2 \rangle$  as the amplitude of the scattering wave. The averaged scattering function is given by

$$S(\vec{q}, \omega) = \frac{1}{2\pi\hbar N \langle \bar{b}^2 \rangle} \int_{-\infty}^{+\infty} \sum_{\mathbf{i}} J b_{\mathbf{i}} \bar{b}_J \langle e^{-i\vec{q}\vec{R}_{\mathbf{i}}(0)} e^{-i\vec{q}\vec{R}_J(t)} \rangle e^{i\omega t} dt$$

It contains a double index sum. The spins of the nuclei are generally not correlated, hence  $b_{\mathbf{i}} \bar{b}_J = \bar{b}_{\mathbf{i}} \bar{b}_J$  for  $\mathbf{i} \neq J$ . Therefore it becomes possible to separate the sum into two contributions that are called coherent and incoherent:

$$S_{coh}(\vec{q}, \omega) = \frac{1}{2\pi\hbar N \langle \bar{b}^2 \rangle} \int_{-\infty}^{+\infty} \sum_{\mathbf{i}} J \bar{b}_{\mathbf{i}} \bar{b}_J \langle e^{-i\vec{q}\vec{R}_{\mathbf{i}}(0)} e^{-i\vec{q}\vec{R}_J(t)} \rangle e^{i\omega t} dt$$

$$S_{inc}(\vec{q}, \omega) = \frac{1}{2\pi\hbar N \langle \bar{b}^2 \rangle} \int_{-\infty}^{+\infty} \sum_{\mathbf{i}} J(\bar{b}_i^2 - \bar{b}_J^2) \langle e^{-i\vec{q}\vec{R}_i(0)} e^{-i\vec{q}\vec{R}_J(t)} \rangle e^{i\omega t} dt$$

At ambient temperatures the atoms move around well defined equilibrium positions  $\vec{R}_i$ . If the corresponding wave vector is small compared to typical vibrational frequencies  $\omega_k$  ( $\omega_k > \hbar q^2/2M_i$ ), it is appropriate to expand the scattering function in terms of orders of phonon scattering:

$$S(\vec{q}, \omega) = \underbrace{S_{\text{elastic}}(\vec{q}, \omega)}_I + \underbrace{S_{1 \text{ phonon}}(\vec{q}, \omega)}_{II} + S_{2 \text{ phonon}}(\vec{q}, \omega) + \dots$$

In the harmonic approximation the first terms may be given in a closed form. In the following the various terms will be discussed regarding their physical information on the sample.

### zero order

The first term  $I$  contains information on the elastically scattered neutrons. Its coherent part reads

$$\begin{aligned} S_{\text{coh,elastic}}(\vec{q}, \omega) &= S_{\text{el}}\delta(\omega) \\ &= \delta(\omega) \frac{1}{N \langle \bar{b}^2 \rangle} \sum_{\mathbf{i}} J b_i \bar{b}_J \langle e^{-W_i + W_J} e^{i\vec{q}(\vec{R}_i - \vec{R}_J)} \rangle e^{i\omega t} dt \end{aligned}$$

$S_{\text{el}}(\vec{q})$  is the so called elastic structure factor. For an isotropy system the exponent terms are the Debye Waller factors with the time averaged mean displacement of atom  $I$  averaged over time  $\langle u_i^2 \rangle$

$$W_i(\vec{q}) = \frac{1}{6} q^2 \langle u_i^2 \rangle$$

the integration of  $S_{\text{coh}}(\vec{q}, \omega)$  over energy  $d\omega$  gives the static structure factor

$$S(q) = \frac{1}{N \langle \bar{b}^2 \rangle} \sum_{\mathbf{i}} J \bar{b}_i \bar{b}_J \langle e^{-i\vec{q}\vec{R}_i(0)} e^{-i\vec{q}\vec{R}_J(0)} \rangle \quad (10.1)$$

$S(q)$  depend on the actual relative positions of the particles whereas  $S_{\text{el}}(\vec{q})$  depends on the relative position of equilibrium sites.

### first order

For phonon orders higher then zero, the scattering is naturally inelastic and two possibility for a neutron arise: Scattering with energy gain and scattering with energy loss. according to these two possibility, the higher order terms have always two contributions. The first order can be written as follows:

$$S_{1 \text{ phonon}} = \frac{1}{2N \langle \bar{b}^2 \rangle} \sum_k \frac{|F_k(\vec{q})|^2}{\omega_k} \left[ \underbrace{\langle n_k + 1 \rangle \delta(\omega - \omega_k)}_{\text{energy loss}} + \underbrace{\langle n_k \rangle \delta(\omega + \omega_k)}_{\text{energy gain}} \right]$$

with the dynamic structure factor

$$|F_k(\vec{q})|^2 = \sum_{\mathbf{i}} J \frac{\bar{b}_i \bar{b}_J}{\sqrt{M_i M_J}} e^{-W_i(\vec{q}) - W_J(\vec{q})} \left( \vec{q} \vec{e}_i^* \right) \left( \vec{q} \vec{e}_J^* \right) e^{i\vec{q}(\vec{R}_i - \vec{R}_J)}$$

where  $\vec{e}_i^k$  is the displacement vector of the atom  $I$  belonging to the normal mode  $k$  with eigen frequency  $\omega_k$  and the population factor  $\langle n_k \rangle$ .

$$\langle n_k \rangle = \frac{1}{e^{\hbar\omega_k/k_B T} - 1}$$

A common approximation in order to further simplify the expression for the first order approximation is the so called incoherent approximation the main idea of this approximation is to average  $q$  over a certain range to cancel the interference effects of the phase contribution. It can be shown that this is the case if the scattering arose completely from the incoherent part. For the case of neutron energy loss (phonon creation +1) the incoherent part is given as

$$S_{\text{inc},+1}(\vec{q}, \omega) = \frac{1}{N \langle \bar{b}^2 \rangle} 3 \sum_i \bar{b}_i^2 e^{-2W_i} \frac{|\vec{q}\vec{e}_i|^2}{2M_i\omega} \langle n_k + 1 \rangle Z(\omega)$$

with the one phonon density of state  $Z(\omega) \frac{1}{3} N \sum_k^{3N} \delta(\omega - \omega_k)$ .

## second and higher order

The third term  $S_{2 \text{ phonon}}$  and higher order represent scattering processes to which two or more phonons contribute simultaneous. In the case of an isotropic system the n-phonon scattering function can be written in incoherent approximation as

$$S_{\text{inc}}(\vec{q}, \omega) = e^{\frac{\hbar\omega}{k_B T}} e^{-\gamma q^2} \sum_n = 1^\infty \left( \frac{\hbar^2 q^2}{2M} \right)^n \frac{T_n(\hbar\omega)}{n!}$$

The mean square displacement  $\gamma$  can be expressed as

$$\gamma = \bar{u}^2 = \frac{\hbar^2}{2M} \int_0^\infty \frac{g(\hbar\omega)}{\hbar\omega} \cosh\left(\frac{\hbar\omega}{2k_B T}\right) d(\hbar\omega)$$

the functions  $T_n(\hbar\omega)$  are recursively defined via the expression

$$T_n(\hbar\omega) = \int_{-\infty}^{+\infty} T_1(\hbar\omega - \hbar\tilde{\omega}) T_{n-1}(\hbar\tilde{\omega}) d(\hbar\tilde{\omega})$$

and the starting expression  $T_1$

$$T_1(\hbar\omega) = \frac{g(\hbar\omega)}{2\hbar\omega \sinh\left(\frac{\hbar\omega}{2k_B T}\right)}$$

In an iterative process it becomes then possible to determine the whole inelastic scattering. The first step is to calculate the density of state as if higher orders would not exist. The result is taken to calculate  $\gamma$  and  $T_1$ . The deviation of the measured scattering function and the iterated one is then used to refine the guess for the vibrational density of states  $g(\omega)$  This process is repeated until the  $g(\omega)$  converges in a self consistent way. The order of phonon terms is freely chosen under the limits of good and rapid convergence.

### 10.3 Two hole method

The *two hole method* (fig. 3.1 b)) has the big advantage that both values  $\mu$  and  $f$  can be extracted from the same measurement. It is commonly used for measuring the effective black absorbing UCN area of a sample which is contained between two diaphragms A and B (fixed openings a). The theory and the explanations are taken from [80].

Considering a net constant flow from the flux balance of UCN  $J_i$  through the tube one can describe the density distribution  $\rho(x)$  along the tube by the one dimensional stationary diffusion equation (eq. 10.2):

$$D \frac{d\rho^2}{dx^2} - \frac{\rho}{\tau} = 0. \quad (10.2)$$

The parameter  $D$  is the diffusion coefficient and  $\tau$  the mean UCN lifetime in the tube. The inverse of the diffusion length  $\gamma = L^{-1} = \sqrt{\tau D}^{-1}$  will be used later. Assuming a sample radius  $R$  and a length  $X$  we can write the flux balance:

$$\frac{J_{\text{in}}}{iR^2} = -D \left( \frac{d\rho}{dx} \right)_{x=0} \quad (10.3)$$

$$\frac{J_{\text{out}}}{iR^2} = -D \left( \frac{d\rho}{dx} \right)_{x=X}. \quad (10.4)$$

Together with the boundary conditions (eq. 10.3 and eq. 10.4) which are defined by the incoming  $J_{\text{in}}$  and outgoing  $J_{\text{out}}$  flux the solution of the differential equation can be written as

$$\rho(x) = -J_{\text{in}} \frac{1}{\pi R^2 D \gamma} \sinh \gamma x + J_{\text{in}} \frac{1}{\pi R^2 D \gamma} \frac{\cosh \gamma X}{\sinh \gamma X} \cosh \gamma x.$$

The coefficient  $\beta$  is the ratio between the two reduced fluxes by the aperture a)  $J_{\text{in}}/J_{\text{out}}$ . For a rough estimation it is sufficient to use the mono energetic assumption instead of the wide energy spectrum. Assuming full isotropy of the angular distribution, the flux density  $J_{\text{det}}^b$  through the aperture a and an average neutron velocity  $v$  is given in general as

$$\frac{J_{\text{in}}}{b_{\text{in}}} = \frac{1}{4} v \rho.$$

The concept of an effective black area allows to connect the net flux  $J_{\text{in}}$ ,  $J_{\text{out}}$  and the blackness of the inlet part  $b_{\text{in}}$  (flux balance on the source side) and outlet part (flux balance on the transmission detector side) with the corresponding aperture fluxes:

$$\frac{1}{4} v \rho(0) = \frac{J_{\text{in}}}{b_{\text{in}}} = J_{\text{in}} \frac{v}{4\pi R^2 D \gamma} \frac{\cosh \gamma X - \beta}{\sinh \gamma X} \quad (10.5)$$

$$\frac{1}{4} v \rho(X) = \frac{J_{\text{out}}}{b_{\text{out}}} = J_{\text{out}} \frac{v}{4\pi R^2 D \gamma} \frac{1 - \beta \cosh \gamma X}{\sinh \gamma X}. \quad (10.6)$$

Without a detailed scattering model in the tube we assume the mean free path  $\langle l \rangle$  between two wall collisions as the tube diameter  $2R$  (ideal diffusion). Mean life time  $\tau$  in the sample and mean free path  $\langle l \rangle$  are connected by the mean velocity weighted with the loss probability per wall collision  $\mu$

$$\tau = \frac{\langle l \rangle}{v \cdot \mu} \quad \rightarrow \quad \mu = \frac{2R}{v \cdot \tau}.$$

With the diffusion expression  $\gamma^2 = (\tau D)^{-1}$  the equations eq. 10.5 and eq. 10.6 can be written as

$$\mu = b_{in} \frac{\gamma}{2\pi R} \frac{\cosh \gamma X - \beta}{\sinh \gamma X} \quad (10.7)$$

$$\mu = b_{out} \frac{\gamma}{2\pi R} \frac{1 - \beta \cosh \gamma X}{\beta \sinh \gamma X}. \quad (10.8)$$

Thus, eq. 10.7 or eq. 10.8 defines  $\mu$  as function of the inverse diffusion length  $\gamma$ . Combining these two leads to an equation for  $\gamma$  from the experimental values (incoming, outgoing flux  $b_{in}$  and inlet outlet  $b_{out}$  losses).

$$\beta \frac{b_{in}}{b_{out}} = \frac{1 - \beta \cosh \gamma X}{\cosh \gamma X - \beta} \quad (10.9)$$

The real diffusion coefficient  $D$  and the ideal coefficient  $D_0$  (for a totally diffuse reflecting tube) can be calculated as

$$D = \frac{\mu v}{2R\gamma^2} \quad ; \quad D_0 = \frac{2}{3} Rv.$$

The probability for diffuse reflection inside our sample tube

$$f = \frac{2D_0}{D_0 - D}. \quad (10.10)$$

Two assumptions of the theory required special treatment on the setup. A stainless steel net structure was used as spectrum shaper to cut the UCN spectrum on the high energy side as well as provides us with an isotropic beam. Several configurations shown in fig. 10.1 have to be measured to get the total incoming flux  $J_0$  a), the isotropy of  $J_0$  by b) and c) and the blackness  $b_{in}$  and  $b_{out}$  of the T pieces with b) and d)<sup>1</sup>.

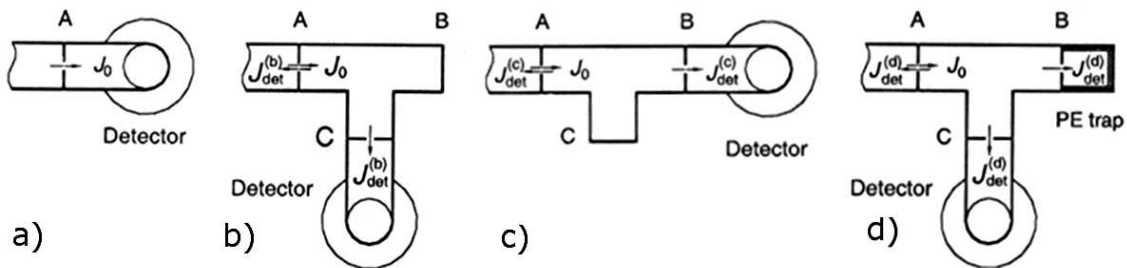


Figure 10.1: Scheme of the four necessary calibration measurements for estimation of the contribution from the different guiding parts to the later measurement.

<sup>1</sup>The detector count rate was corrected for the background counts, relative detector efficiency compared to the monitor detector and for the anisotropy coefficient.

## 10.4 electropolishing and discharge cleaning

### 10.4.1 Electropolishing

Effects to stainless steel due to electro polishing are listed and their possible influence on UCN transport outlined.

**Technique:** The most efficient and cost-efficient surface treatment is Electro Refinement (electro polishing). Typically, the metal work piece is immersed in a temperature controlled bath of electrolyte (often concentrated acids) and connected to the positive terminal (anode) of a DC power supply, the negative terminal being attached to an auxiliary electrode (cathode). An ionic current passes from the anode where metal is oxidized to the cathode where a reduction reaction, normally hydrogen evolution, takes place as can be seen in fig. 10.2 left.

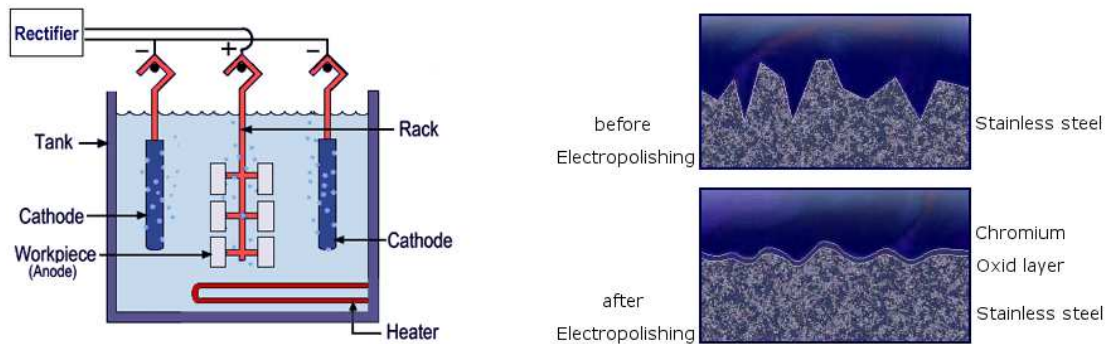


Figure 10.2: Left: principle of electropolishing. Right: the influence on the surface of the work piece right. Pictures are taken from [93].

**Surface Leveling:** According to the theory of Jacquet (viscous film theory), the dissolution products accumulate near the anode (electro polished surface) and form a viscous layer that increases the resistance of the system and limits the current. This viscous layer on top of peaks is much thinner than covering depressions. Consequently, the current density over peaks dissolves faster and the leveling effect smearing valleys is observed [87] (fig. 10.2 right). → The diffuse reflection probability of UCN may be reduced by this effect.

**Surface components:** Electro polishing changes the near surface chemistry of stainless steel. Figure 10.3 left shows Auger Electron Spectroscopy analyzes of electro polished stainless steel [88]. Electro polishing preferentially dissolves Iron from the material matrix and leaves the surface with a higher relative concentration of Chromium.

Upon exposure to oxygen, this improved surface will form a thicker and more uniform oxide layer with enhanced corrosion resistance properties. The oxide layer will be thicker than  $30 \text{ \AA}$  [88] (fig. 10.2 right).  $\rightarrow$  A possible layer of oxygen with a low UCN absorbing cross section<sup>2</sup> can improve the UCN guide quality.

**Hydrogen:** Electro polishing removes hydrogen from the surface and due to the passivation layer (oxygen) prevents hydrogen from re-entering [89].  $\rightarrow$  Reduction of UCN absorption during wall collisions.

**Cleanability:** the contact angle of water is reduced by 12% [87] due to surface smoothness and corrosion resistance components (layers) .  $\rightarrow$  Reduction and easier removing of surface water with its big absorption and upscattering cross section is a possible positive consequence.

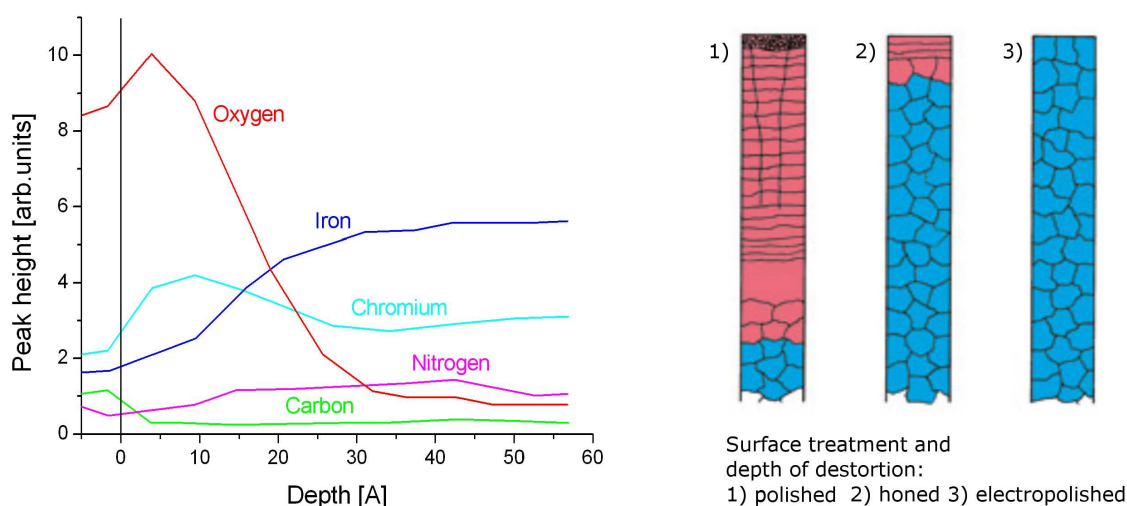


Figure 10.3: Left: shift of chemical composition on a stainless steel surface after electropolishing [88]. Right: the influence of mechanical treatments on the surface composition [90].

**Inclusion:** Stainless steel contains microscopic metallic and non metallic inclusions, which can not be avoided during manufacturing. Mechanical processing or polishing not only fails to remove inclusions, but also tends to push them further into the surface and even increases their quantity by further adding abrasive materials (fig. 10.3 right). Electro polishing restores the normal component composition again [93, 90].  $\rightarrow$  From the UCN point of view, impurities with lower Fermi potential may be avoided.

<sup>2</sup>The steel composition and the element distribution of stainless steel UCN neutron guides have been analyzed for example by ref. [77] . For the discussion of the possible shift of chemical composition to an oxide layer is interesting that they found 13 % Ti with its negative (attractive) Fermi potential for UCNs at untreated surfaces.

### 10.4.2 DC-discharge cleaning

A potential difference between the surface cathode and an anode as well as noble gases in between these two are the necessary ingredients for discharge cleaning. The current from the anode causes ionization of the gas whose ions are then accelerated onto the work piece surface. Impurities on the surface are then released by the ion bombardment and pumped away with the cleaning gas (fig. 10.4).

With the *two hole method* it was possible to measure the effect of in situ discharge cleaning before during and after UCN transmission. A potential difference between the tube and the anode wire, fixed in the center of the sample tube of  $U_{\text{discharge}} \approx 300 \text{ V}$  was applied. The setup is then filled with argon gas which has passed a nitrogen cold trap up to a pressure of  $1.5 \cdot 10^{-1} \text{ mbar}$ .  $U_{\text{discharge}}$  was increased until a stable plasma formation was reached at about  $I_{\text{discharge}} \approx 0.6 \text{ A}$ . Pictures taken through an eye hole of the burning plasma can be seen in fig. 10.4.

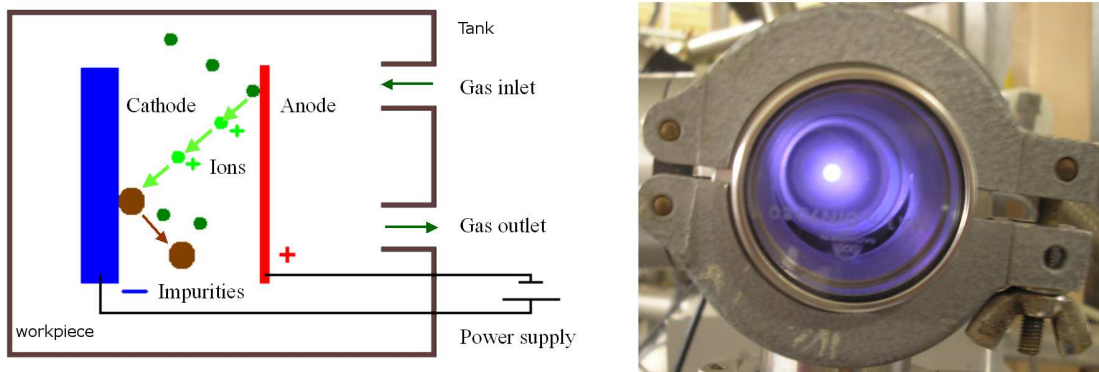


Figure 10.4: Left: principle of discharge cleaning. Right: Argon plasma to clean the sample tube for the *two hole method* setup.

One proof of the quality of the discharge cleaning effect is a gain in the possible applied  $U_{\text{discharge}}$  due to an increase of the break down voltage.

## 10.5 Mechanical and electropolishing

There are eight basic stainless steel mill plate finishes available. Finishes 3, 4, 6, 7 and 8 are produced mechanically by using abrasive compositions and buffing wheels. **Unpolished No. 1.** This is a very dull finish produced by hot-rolling the steel on hand sheet mills to specified thicknesses, followed by annealing and descaling. The surface is microscopically very porous and uneven, allowing a level of contamination pick-up that is many times its geometric surface area. Used in industrial applications where resistance to heat or corrosion, not a smooth finish, is desired.

**Unpolished No. 2D.** This is a dull finish produced on hand sheet mills or continuous mills by cold rolling the metal to the specified thickness, followed by annealing and descaling. The dull finish may result from the descaling operations or may be developed by a final light cold roll pass on dull rolls. This finish is favorable to the surface retention of lubricants in deep drawing operations, and it is generally used in

forming deep-drawn articles that may be polished after fabrication.

**Unpolished No. 2B.** This is a bright, cold-rolled finish produced similarly to the No. 2D finish, except the annealed and descaled sheet receives a final light cold roll pass on polished rolls. The metal grains are flattened, which facilitates removal of smearable contamination. However, the etched boundaries between the grains are only partially sealed, resulting in a network of sub-surface crevices. Contaminants lodging in these crevices are protected from contact with cleaning agents, leading to possible subsequent migration of trapped contaminants onto the cleaned surface (bleeding). No. 2B is a general purpose finish used for all but the most difficult deep-drawing applications, and it is more readily polished than No. 1 or No. 2D.

**Polished No. 3.** This is an intermediate polished finish for use where a semi-finished polished surface is required for subsequent finishing operations following fabrication, or as a final finish with a 50 or 80 grit abrasive compound. (In the case of metal sheets or articles that will not be subject to additional finishing and polishing, a No. 4 finish is ideal.)

**Polished No. 4.** This is a general purpose mechanically polished stainless steel finish that is widely used for architectural panels and trim as well as for restaurant, dairy and kitchen equipment. Initial grinding is followed by coarser abrasives, with sheets eventually finished out with 100-150 mesh abrasives. Although microscopically flat, the grain of Polished No. 4 stainless steel still contains deep grooves and other microscopic cavities that entrap and retain contaminants.

**Buffed No. 6.** A dull satin finish possessing low reflectivity, a Buffed No. 6 finish is produced with a greaseless compound and 200-grit abrasive, and is top-dressed with chrome rouge.

**Buffed No. 7.** This very reflective finish is produced by buffing a surface that first was refined with 220-grit abrasives to approximate a No. 6 finish. It is then buffed lightly with a white chrome rouge without removing the satin finish lines.

**Buffed No. 8.** This is the most reflective mechanical finish. It is obtained by polishing with progressively finer abrasives (320-grit and finer), followed by extensive buffing with very fine white chrome bar buffing compounds. To the unaided eye, the surface appears free of grit lines from previous grinding operations.

**Electropolished Surfaces.** Electropolished surfaces are extremely smooth, macroscopically flat, microscopically featureless, and exhibit high luster, reflectivity and brightness. Electropolishing process substantially reduces the surface area available for contamination pick-up and eliminates all micro-cracks and internal crevices. The text is taken from Delstar.com [93]

## 10.6 *FRED* versus an analytical calculation

The diploma thesis of Niederberger [117] addressed a read out problem similar to the one described in section 5.3. The Experimental results and an analytic model solution were used to compare the results with the same problem simulated with our *FRED* software. There is also an analytical model developed for the problem that a scintillator bar is irradiated by a radioactive point source at the long side of the bar. The photomultiplier detects the light from the small square perpendicular to the point source. The photon count rate expected by the analytical model is compared with experimental values in fig. 10.5. The agreement between their model and their

Mill No.	Grit No.	Before Electropolishing Surface Roughness, Ra		After Electropolishing* Surface Roughness, Ra	
		micrometer	microinches	micrometer	microinches
3	60	3.56 max	140 max	1.78-2.25	70-90
4	120	1.14 max	45 max	0.57-0.75	23-30
4	180	0.64 max	25 max	0.32-0.40	13-16
7	240	0.20-0.51	8-20	0.10-0.26	4-10
8	320	0.15-0.38	6-15	0.08-0.19	3-8
8	500	0.10-0.25	4-10	0.05-0.13	2-5

Table 10.2: Differences between Polished and Buffed Milled Finishes, Abrasive Grit Numbers and Surface Roughness (before and after Electropolishing)\*Values are approximate. Electropolishing generally reduces surface roughness readings of a non-electropolished surface by 50 percent. Data taken from Delstar.com [93]

experimental values is extremely accurate. In addition the simulations of the *FRED* calculations is shown in the same figure. Taking into account that it was not possible to find out which typical material values they used and that their scintillation bars were wrapped with an reflecting aluminum foil the agreement with our also wrapped simulation is quite good.

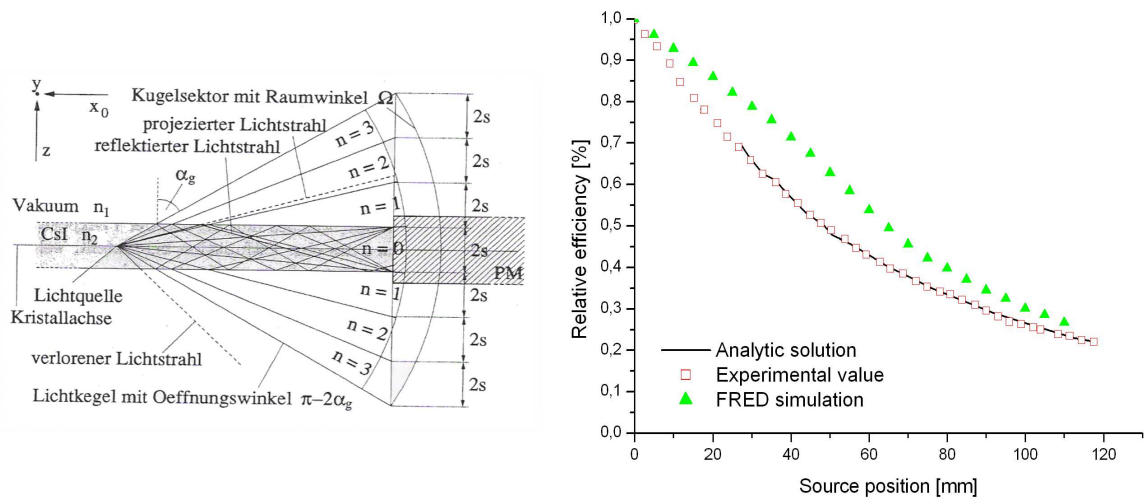


Figure 10.5: Analytical model for the read out of scintillation light through a surface perpendicular to the path of the incident particles. Comparison between the analytical model, experimental values and a similar problem calculated with *FRED*. Data taken from diploma thesis [111].

## 10.7 Pre preparation of Hamamatsu LAAPDs for cooling tests



Figure 10.6: LAAPD from Hamamatsu [159] with transparent glue as bought on stock. The glue was removed by bathing in acid. Shown are failures due to strong and to weak acids.

The Hamamatsu diodes are usually packed inside a ceramic housing with transparent glue. Due to the big difference of the thermal expansion coefficient of the different used materials the working temperature is limited to ( $T=330..240$  K) [159]. Careful cooling can be achieved down to 180 K before the LAAPD breaks and is destroyed for example fig. 10.6 on the right hand side. The following procedure to remove just the plastic cover was developed similar to the procedure used at the Athena [169] collaboration at PSI. Very helpful discussions with Dieter Renker [170] and David Taccu [171] are gracefully acknowledged. The LAAPD's were bathed in 95% acid for approximately 45 min. From time to time the first solved layer has been removed by washing them into pure ethanol and double distilled water before the acid procedure was repeated. Special care has to be taken on the acid concentration and the time. As indicated in fig. 10.6 left the result when the acid is too weak is shown. The last plastic pieces form bubbles on the surface. Longer bathing removes the unprotected metal guard ring and the gold bonding connections. The LAAPD is destroyed. The picture in the middle shows the worst case in the other direction. When the acid is too strong, the Si structure is degraded before the plastic from the bottom of the ceramic cup is removed. This LAAPD is still working in a sense of a diode but shows huge differences in signal to noise ratio (no separation between peak and noise) and a much higher noise level.

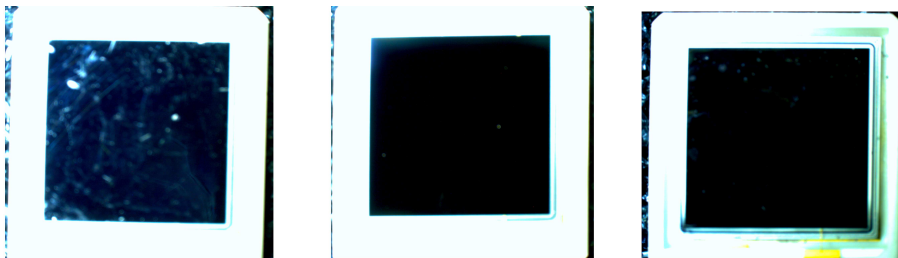


Figure 10.7: Same order of LAAPD viewed under an angle of 5 degree. On the left diode scratches on the protection transparent glass glue. On the etched diode some glue spots are still visible.

At fig. 10.7 one can see pictures from three HAM diodes taken with the light microscope from E18. The angle between the camera and the LAAPD s surface was approximately  $5^\circ$  thus the surfaces structure could be visualized. The first one with some scratches or impurities is the still covered LAAPD. The middle one is an LAAPD after an etching procedure and the left one for comparison is the one we were able to buy without any glue at all. The later two show both a perfect black surface.

From first characterization at low temperatures no significant difference between the self etched and the clean detector performance was found.

Because one can never exclude tiny damages to the surface form the acid the noise contribution at room temperature is slightly higher for the self cleaned one. But this noise level also vanishes at temperatures below 220 K.

## 10.8 Simulation results for the proton detector

Different detector shapes to cover the required ring have been simulated as function of detector size, shape and thickness. Two different materials as light guide have been addressed. The source was always a surface source of  $10^5$  photons emitted randomly from the CsI layer into the light guide. The tables show differnt possible geometries to cover the inner radius 10 cm and the outer radius of 30 cm. The thickness of the light guides is always given as  $t$  value.

number of pieces	4	6	8	12	16	18
Lucite $n_{\text{lucid}} = 1.45$	3495	4601	5363	6318	6725	6809
Quartz $n_{\text{quartz}} = 1.8$	5583	7462	10001	11487	11996	11781

Table 10.3: Trapeze coverage with a thickness of  $t=10\text{mm}$

number of segments	4	6	8	12	16	18
$n_{\text{lucid}} = 1.45$	3495	4601	5363	6318	6725	6809
$n_{\text{quartz}} = 1.8$	5583	7462	10001	11487	11996	11781

Table 10.4: Trapetze coverage with thickness  $t=3\text{mm}$

number of segments	4	6	8
$n_{\text{lucid}} = 1.45$	5515	6450	6816
$n_{\text{quartz}} = 1.8$	10444	11500	12605

Table 10.5: Coverage with circle segments thickness  $t=10\text{mm}$

number of segments	4	6	8
$n_{\text{lucid}} = 1.45$	3770	5146	6427
$n_{\text{quartz}} = 1.8$	5152	7581	8749

Table 10.6: Circle coverage with segments thickness  $t=3\text{mm}$ .

number of cuboid s	4	6	8	triangle	4	6	8
$n_{\text{lucid}} = 1.45$	3864	4004	3817		4906	6333	7137
$n_{\text{quartz}} = 1.8$	5003	5578	5132		8100	10196	12578

Table 10.7: coverage with triangle and cuboids thickness  $t=10\text{mm}$ .

number of cuboid s	4	8	triangle	4	8
$n_{\text{lucid}} = 1.45$	3780	4048		3804	3944
$n_{\text{quartz}} = 1.8$	4048	3944		5178	8618

Table 10.8: Coverage with triangle and cuboids thickness  $t=3\text{mm}$ .



# Bibliography

- [1] J. S. Nico and W. M. Snow, *Ann. Rev. Nucl. Part. Sci.* 55 (2005) 27.
- [2] H. Abele, *et al.*, *Eur. Phys. J. C*, 33 (2004) 01574.
- [3] J. M. Pendlebury *Ann. Rev. Nucl. Part. Sci.*, vol. 43 (1991) 173.
- [4] P. Herczeg *Prog. Part. Nucl. Phys.*, vol. 46 (2001) 413.
- [5] H. Leeb, J. Schmiedmayer *Phys. Rev. Lett.*, vol. 68 (1992) 1472.
- [6] Y. N. Pokotilovsky *Physics of Atomic Nuclei*, vol. 57 (1994) 390.
- [7] Y. Kamyshev, E. Kolbe *Phys. rev. D*, vol. 67 (2003) 076007.
- [8] R. Golub, D. Richardson, S. K. Lamoreaux, *Ultra-Cold Neutrons*, Adam Hilger Bristol (1991).
- [9] <http://www.nist.gov/srd/online.html>.
- [10] V. V. Nesvizhevsky and K. Protasov, *Class. Quantum Gravitation*, 21 (2004) 4557.
- [11] J. H. Gundlach, G. L. Smith, E. G. Adelberger, B. H. Heckel, H. E. Swanson, *Phys. Rev. Lett.* 78 (1996) 2523
- [12] V. K. Ignatovich, *The Physics of Ultracold Neutrons*, Clarendon Press, Oxford (1990).
- [13] J. Byrne, *Neutrons, Nuclei and Matter*, IOP publishing, Bristol (1997).
- [14] V. Ezhov, *Workshop: Fundamental physics with slow neutrons (2008)*, to be published, *Nucl. Instr. and Methods B* special edition.
- [15] B. M. Fisher *et al.*, *J. Res. Natl. Inst. Stand. Technol.* 110 (2005) 421.
- [16] Dollinger *et al.*, *Eur. Phys. J. A*30 (2006) 603.
- [17] N. Severijns, M. Beck, O. Navillat-Cuncic, *Rev. Mod. Phys.* 78 (2006) 991.
- [18] J. D. Jackson, S. B. Treiman, H. W. Wyld, *Phys. Rev.* 106 (1957) 517.
- [19] A. Serebrov *et al.*, *Phys. Lett. B*, 605 (2005) 72.
- [20] <http://www.ucn.web.psi.ch>.
- [21] <http://www.lanl.gov>.

- [22] <http://www.e18.physik.tu-muenchen.de>.
- [23] <http://www.pnpi.spb.ru>.
- [24] <http://www.kernchemie.uni-mainz.de>.
- [25] H. Yoshiki *et al.*, Phys. Rev. Lett. 68 (1992) 1323.
- [26] Y. Pokotilovsky, ESS Special Expert Meeting UCN Factory Workshop, Wien (2002), <http://www.ati.ac.at/neutrweb/ess/ess.html>
- [27] C. Y. Liu, A superthermal ultracold neutron source, PhD thesis Princeton University (2002).
- [28] C. Y. Liu, Physics of superthermal UCN production in sD<sub>2</sub> and other materials, Proceedings of the 3th UCN workshop, Pushkin, (2001).
- [29] Ch. Seidel, Entwicklung einer UCN Quelle für das Strahlrohr SR4 des FRMII, diploma thesis, Technische Universität München (1999).
- [30] V. F. Turchin, Slow Neutrons, Sivan Press, Jerusalem (1963).
- [31] H. Schober, J.Phys. IV France 103 (2003) 173.
- [32] S. N. Taraskin, S. R. Elliott, Phys. Rev. B, 55, (1997) 117.
- [33] J. P. Elliot, P. G. Dawber, Symmetry in Physics, Vol. 2, Oxford University Press, New York (1984).
- [34] C. Y. Liu *et al.*, Phys. Rev. B, 62 (2000) 3581.
- [35] Y. Xu, Characterization of solid deuterium ultracold neutron source production and UCN transport, PhD thesis North Carolina State University (2006).
- [36] M. Kasprzak, Thermal up-scattering of very cold and ultra cold neutrons in solid deuterium, Diploma thesis, Jagellonian University of Cracow nucl-ex/0407 (2004).
- [37] F. Atchison *et al.*, Phys. Rev. Lett. 99 (2007) 262502.
- [38] A. Dianoux and G. Lander, Neutron Data Booklet, Institut Laue-Langevin (2002).
- [39] <http://www.oerlikon.com/leyboldvacuum/de>.
- [40] <http://www.shicryogenics.com>.
- [41] <http://www.lakeshore.com>.
- [42] <http://www.swagelok.de>.
- [43] <http://www.messer.de>.
- [44] K. Bodek *et.al*, Nucl. Instr. Methods A 533 (2004) 491.
- [45] C. Y. Liu, S. K. Lamoreaux, A. Saunders, D. Smith, A. R. Young, Nucl. Instr. Methods A 508 (2003) 257.

- [46] I. F. Silvera, *Rev. Mod. Phys.* 52 (1980) 393.
- [47] T. Unruh, J. Neuhaus, W. Petry, *Nucl. Instr. Methods A* 580 (2007) 1414.
- [48] R. Mittal *et al.*, *Phys. Rev. B*, 78 (2008) 104514.
- [49] <http://www.ill.eu/in4>.
- [50] G. L. Squires, *Introduction to the theory of thermal neutron scattering*, Dover New York (1996).
- [51] M. Urban, *Untersuchung von festem Deuterium als Konvertermaterial zur Erzeugung von ultrakalten Neutronen*, Diploma thesis (2008) Technische Universität München.
- [52] F. Atchison *et al.*, *Investigation of Solid Deuterium for UCN Sources*, Proceedings of the 17th Meeting of the International Collaboration on Advanced Neutron Sources ICANS Santa Fe, New Mexico (2005).
- [53] R. H. Haefer, *Cryopumping: Theory and Practice*, Science Publications Oxford (1989).
- [54] W. Mascher, *Über die Kondensation der Gase bei tiefen Temperaturen und niedrigen Drücken*, PhD thesis, Technische Universität Berlin (1967).
- [55] W. Dallügge, *Die Wärmeleitfähigkeit fester Gaskondensate*, PhD thesis, Technische Universität Berlin (1973).
- [56] S. Gröger, *Untersuchungen zu festem Deuterium als Konvertermaterial für ultrakalte Neutronen*, Diploma thesis, Technische Universität München (2001).
- [57] A. Frei, *et al.*, submitted to *Nucl. Instr. and Methods A*.
- [58] M. Poehlmann, *Structure and dynamics of hydrous silica(tes) as seen by molecular dynamics computer simulations and neutron scattering*, PhD thesis, Technische Universität München (2004).
- [59] K. F. Mucker, P. M. Harris, D. White, R. A. Erikson, *J. Chem. Phys.* 49 (1968) 1922.
- [60] <http://www.ccp14.ac.uk/tutorial/powdcell>.
- [61] J. van Kranendonk, *Solid hydrogen theory of the properties of solid H<sub>2</sub>, HD, D<sub>2</sub>*, Plenum Press, New York and London (1983).
- [62] J. Dawidowski, F. J. Bermejo, J. R. Granada, *Phys. Rev. B*, 58 (1998) 706.
- [63] J. Dawidowski *et al.*, *Phys. Rev. E* 53, (1996) 5079.
- [64] C. Barrett, L. Meyer, J. Wasserman, *J. Chem. Phys.* 45, (1966) 834.
- [65] *Inelastic neutron scattering data analysis meeting at the ILL* (2008).
- [66] M. Nielsen and H. B. Möller, *Phys. Rev. B* (1971) 4383.

- [67] A. P. Serebrov, *et al.*, JETP Lett., 59, (1994) 757.
- [68] D. Tortorella, Characterization of a solid deuterium converter for ultra cold neutrons (UCN) in the framework of the Mini-D<sub>2</sub> project at the FRM-II reactor, PhD thesis, Technische Universität München (2007).
- [69] F. Atchison *et al.*, Phys. Rev. Lett. 94 (2005) 212502.
- [70] <http://encyclopedia.airliquide.com/Encyclopedia.asp?GasID=20>.
- [71] F. Atchinson *et al.*, Phys. Rev. C 71 (2005) 054601.
- [72] A. Serebrov *et al.*, Nucl. Instr. Methods A 440 (2000) 658.
- [73] A. Young and O. Zimmer private communication workshop, Fundamental physics with slow neutrons ILL (2008).
- [74] E. Gutmiedl *et al.*, in Fundamental physics with slow neutrons (2008) ILL to be published Nucl. Instr. and Methods B special edition.
- [75] V. V. Nesvizhevsky, Nucl. Instr. Methods A 557 (2006) 576.
- [76] C. Plonka, P. Geltenbort, T. Soldner, H. Häse, Nucl. Instr. Methods A 578 (2007) 450.
- [77] L. Bondarenko *et al.*, Physica B 234-236 (1997) 1189.
- [78] T. Brys *et al.*, Rel. Mat. 15 (2006) 928.
- [79] S. Heule *et al.*, Applied Surface Science 253 (2007) 8245.
- [80] I. Altarev *et al.*, Nucl. Instr. Methods A 570 (2007) 101.
- [81] V. Ignatovich, *et al.*, Experiments on UCN storage in bottles in the channel mode, P3-82-811, Joint Institute Nuclear Research, Dubna 1982.
- [82] <http://www.nocado.com/index>.
- [83] <http://www.poligrat.de>.
- [84] R. Picker, PENELOPE and Abex- on the Way Towards a New Precise Neutron Lifetime Measurement, PhD thesis Technische Universität München (2008) .
- [85] I. Altarev, internal report E18 Physics Department Technical University Munich.
- [86] I. Altarev, private communication.
- [87] <http://www.electrobright.com>.
- [88] <http://www.harrisonep.com>.
- [89] <http://www.electromax-inc.com>.
- [90] <http://www.ELPOCHEM.ch>.

- [91] S. Dagen *et al.*, Glow discharge cleaning for LDX, Submitted for the DPP02 Meeting of the Am- Phys. Society.
- [92] E. Korobkina *et al.*, Phys. Rev. B 70 (2004) 928.
- [93] Delstar Metal Finishing, Inc. <http://www.delstar.com/how>.
- [94] <http://www.laser2000.co.uk/software-products.php?no=2>.
- [95] Al. Yu. Muzychka and Yu. N. Pokotilovsky, Nucl. Instr. Methods A 373 (1996) 81.
- [96] F. Atchinson *et al.*, Nucl. Instr. Methods A 552 (2005) 513.
- [97] Yu. Yu. Kosovintsev *et al.*, Proc. All-Union Conf. on Neutron Physics, part 2 UCN storage in a stainless steel bottle with variable area of slit. Transmission of neutron guides and elbows as well as angular distribution modification with guide length are reported INIS At, (1976) 9:354011, 354012.
- [98] R. Henneck, Proceedings of the International Workshop on Extreme High-vacuum-Application and Technology (X-VAT), Bad Liebenzell (2003).
- [99] A. Serebrov *et al.*, Phys. Lett. B 605, (2005) 72.
- [100] S. Arzumanov *et al.*, Neutron lifetime values measured by storing ultra cold neutrons with detection of inelastically scattered neutrons, in H. Abele and D. Mund, editors, *Quark-Mixing, CKM-Unitarity*, pp. 81-85, Mattes Verlag, Heidelberg (2002).
- [101] A. Steyerl, Use of low temperature fomblin for a neutron lifetime experiment, 3rd UCN workshop, Pushkin, St. Petersburg, (2001).
- [102] V. V. Vladimirkii, Sov. Phys. JETP, 12 (1961) 740.
- [103] H. Shimizu and T. Oku, J. Phys. Society Japan, 20 (2001) 431.
- [104] Y. G. Abov *et al.*, Sov. J. Nucl. Phys. 38 (1983) 240.
- [105] V. Ezhov, Lifetime measurement with a permanent magnetic trap, in 5th UCN workshop, Pushkin, St. Petersburg, (2005).
- [106] P. R. Huffman *et al.*, Nature 403 (2000) 62.
- [107] P. R. Huffman *et al.*, Nucl. Instr. Methods A 440 (2000) 522.
- [108] R. Picker, A new superconducting magnetic trap for ultra cold neutrons, Diploma thesis, Technische Universität München (2004).
- [109] J. Bröcker, Quellen systematischer Fehler bei der Messung der Neutronenlebensdauer mit einer magnetischen Flasche, Diploma thesis, Technische Universität München (2004).
- [110] <http://www.srim.org>.

- [111] Beikur *et al.*, Comprehensive Organic Chemistry volIII, Pergamon Press Oxford (1973) 405.
- [112] E. Schyns, Nucl. Instr. Methods A 494 (2002) 441.
- [113] F. Cusanno *et al.*, Nucl. Instr. Methods A 502 (2003) 251.
- [114] V. V. Nagarkar *et al.*, Structured CsI(Tl) scintillators for X-ray imaging application Radiation Monitoring Devices, IEEE Trans. vol. 45 (1998) 492.
- [115] <http://www.solidCAM.de>.
- [116] T. Massam, GUIDE7: a general program for evaluating the properties of scintillation and Cerenkov counter optical systems, Cern(Series) 76-21 (1976).
- [117] P. Niederberger, Untersuchung von CsI-Szintillatoren bei tiefen Temperaturen, Diploma thesis, Universität Zürich (1999).
- [118] P. Barton, private communication.
- [119] P. Barton, C. Stapels, J. Christian, D. Wehe, IEEE Nuclear Sciences Symposium Conference Record N24-122 (2008).
- [120] Hand book of cosmos works, solidworks (2005-2006).
- [121] D. Renker *et al.*, Avalanche photodiodes now and possible developments, Vienna conference on instrumentation (2004).
- [122] <http://cosmoexpress.ongames.t-online.de/>.
- [123] <http://www.solidworks.de/pages/products/cosmos/cosmosworks>.
- [124] W. R. Leo, Techniques for Nuclear and Particle Physics Experiments, Springer, Berlin (1994).
- [125] <http://www.altuglasint.com>.
- [126] <http://www.heraeus.de>.
- [127] L. M. Fernandes *et al.*, Nucl. Instr. Methods A 498 (2003) 362.
- [128] <http://www.saint-gobain.de>.
- [129] <http://www.hamamatsu.com>.
- [130] G. Knoll, Radiation Detection and Measurement, 3rd edition, Wiley, New York (1999).
- [131] J. D. Valentine *et al.*, Nucl. Instr. Methods A 325 (1993) 147.
- [132] Properties of Scintillator Materials Data Compiled by RMD Inc.
- [133] <http://www.korth.de>.
- [134] G. Keil, Nucl. Instr. Methods 87 (1970) 111.

- [135] Saint-Gobain Bicron Crystals and Detectors.
- [136] R. Gwin and R. B. Murray, Phys. Rev. 131 (1963) 508.
- [137] C. Amsler *et al.*, Nucl. Instr. Methods A 480 (2002) 494.
- [138] A. Glauser, Nucl. Instr. Methods A 504 (2003) 347.
- [139] C. L. Woody *et al.*, IEEE Trans. Nucl. Sci. 37 (1990) 492.
- [140] <http://www.hilger-crystals.co.uk/properties.asp?material>.
- [141] J. Valentine, D. Wehe, G. Knoll, C. Moss, Temperature dependence of absolute CsI(Tl) scintillation yield, Conference Record of the IEEE Nuclear Science Symposium and Medical Imaging Conference, (1991) 176.
- [142] H. Nishimura *et al.*, Phys. Rev. B 51 (1995) 2167.
- [143] <http://www.eljentechnology.com>.
- [144] E. Lorenz, private communication.
- [145] P. Maier-Komor *et al.*, Nucl. Instr. Methods A 362 (1995) 183.
- [146] M. A. Nitti *et al.*, Nucl. Instr. Methods A 523 (2004) 323.
- [147] V. I. Razin *et al.*, Nucl. Instr. Methods A 419 (1998) 621.
- [148] A. Lebedinsky *et al.*, Growth and scintillation of CsI(Tl) layers, in Proc. of the Eighth International Conference on Inorganic Scintillators and their Use in Scientific and Industrial Applications (SCINT 2005), Alushtat Crimea Ukraine. International conference on inorganic scintillators and their use in scientific and industrial applications (2005).
- [149] M. Boucher *et al.*, Nucl. Instr. Methods A 505 (2003) 136.
- [150] J. E. Bateman, S. R. Burge, R. Stephenson, Technical design report RAL-TR-95-001, Rutherford laboratory, CLRC, (1995).
- [151] G. E. Stillman and C. M. Wolfe, "Avalanche Photodiodes", Semiconductor and Semimetals R. K. Willardson and A. C. Beer, Eds. New York Academic, vol. 12, Infrared Detectors II, (1977).
- [152] R. J. McIntyre, IEEE Trans. vol. 19 (1972) 703.
- [153] J. P. Pansart, Nucl. Instr. Methods A 387 (1997) 186.
- [154] P. P. Webb, R. J. McIntyre, J. Conradi, RCA Rev. 35 (1974) 234.
- [155] S. M. Sze, K. Ng. Kwok, Physics of Semiconductor Devices 3rd edition Wiley (2007).
- [156] A. Karar, Y. Musienko, J. Ch. Vanel, Nucl. Instr. Methods A 428 (1999) 413.

- [157] A. Baron, S. Kishimoto J. Morse, J. M. Rigal, J.Syn. Rad. 13 (2006) 131.
- [158] Radiation Monitoring Devices Watertown, Silicon Avalanche Photodiode operational manual and RMD APD data sheet.
- [159] Hamamatsu Si APD S8664 series short wavelength type APD data sheet and final inspection sheet.
- [160] M. Sato, private communication.
- [161] Application notes from Radiation Monitoring Devices.
- [162] L. Lubhova *et al.*, Nucl. Instr. Methods A 540 (2005) 169.
- [163] I. Tapan *et al.*, Nucl. Instr. Methods A 388 (1997)79.
- [164] D. Young *et al.*, Nucl. Instr. Methods A 508 (2003) 388.
- [165] A. Stoykov, R. Scheuermann, Silicon Avalanche Photodiodes, internal report Paul Scherer Institut Villigen Switzerland.
- [166] J. Ikagawa *et al.*, Nucl. Instr. Methods A 515 (2003) 671.
- [167] L. M. P. Fernandes, Characterization of large area avalanche photodiodes for detection of x-rays, vacuum ultraviolet and visible light, PhD thesis University of Coimbra (2005).
- [168] G. Schatz, A. Weidinger, *Nukleare Festkörperphysik* Teubner Stuttgart (1992).
- [169] <http://web.cern.ch/athena>.
- [170] D. Renker, private communication.
- [171] D. Taqqu, private communication.
- [172] R. Picker *et al.*, J. Res. Natl. Inst. stand. Technol., vol. 110 (2005) 357.
- [173] P. R. Huffman *et al.*, Nature, vol. 403 (2001) 62.
- [174] O. Zimmer *et al.*, Nucl. Instrum. Methods A 440 (2000) 543.
- [175] *et al.*, Nucl. Instrum. Methods A 545 (2005) 401.
- [176] D. R. Reich *et al.*, Nucl. Instrum. Methods A 481 (2002) 431.
- [177] A. R. Young *et al.*, in fundamental Physics with Pulsed Neutron Beams Singapore World Scientific, (2001).
- [178] <http://www.specs.de>.
- [179] R. Hoedl, Novel Proton Detectors, Ultra Cold Neutron Decay and Electron Backscatter, PhD thesis, Princeton University (2003).
- [180] F. Naab, L. O. Lamm, W. Zech, A. Garcia, P. Mumm, Nucl. Instr. Methods B 197 (2002) 278.

- [181] R. Wilhelm, Max Plank Institut für Plasmaphysik, lecture notes TUM,WS (2000/2001).
- [182] A. Lakatos, Extraktion und Transport von Strahlen aus negativen Wasserstoffionen; PhD thesis, Wolfgang Goethe-Universität Frankfurt am Main (2004).
- [183] Keithley Low Level Measurements Handbook, Precision DC current, Voltage, and Resistance Measurements 6th edition; <http://www.keithley.eu.com>.
- [184] E. Harting and T. H. Read, Electrostatic lenses, Elsevier Amsterdam (1976).
- [185] F. Hinterberger, private communication.
- [186] F. Großer, Einführung in die Teilchenoptik; Teubner Studienbücher Physik Stuttgart(1983).
- [187] J. Ulrich, private communication.
- [188] <http://www.simion.com>.
- [189] OPTIC-II a simulation software for accelerator parts from the Maier Leibnitz Laboratorium Garching.
- [190] O. Meusel, private communication.
- [191] C. D. Child, Phys. Rev. 32 (1911) 492.
- [192] I. Langmuir and K. T. Compton, Rev. Mod. Phys. 3 (1931) 191.
- [193] <http://www.proscan.de>.
- [194] G. Petzold, The Proton Spectrum in Neutron Beta Decay - First Results with the aSPECT Spectrometer, PhD thesis Technische Universität at München (2007).
- [195] M. Simson, First Measurements with the New Neutron Decay Spectrometer aSPECT at the Munich Research Reactor, Diploma thesis Technische Universität München (2006).
- [196] PNsensors GmbH, production of semiconductor detectors.

# Index

- $S(q,\omega)$ , 44
- cubeD<sub>2</sub>*, 35
- Absorption loss, 34
- Additional loss, 70, 79
- Advanced photonics, 143
- analytic light transport, 192
- Annealing, 52
- Annealing dynamic, 61
- Annealing structure, 60
- Annealing UCN, 77
- APD, 139
- aSPECT, 177
- Avalanche zone, 139
- Baffle U shape, 94
- Beveled edge, 143
- Boltzman occupation, 71
- Bragg equation, 43
- Bulk leakage current, 141
- Child Langmuir model, 170
- cleanability, 190
- Coherent production, 66
- Cold source temperature, 63
- Collimator, 162
- Convection, 47
- Conventional UCN production, 29
- Conversion rate, 54
- Conversion theory, 53
- Conversion zone, 139
- converter ortho/para, 39
- Converter UCN, 81
- Cooling system, 37
- Cross section production, 32
- CsI low temperature, 122
- CsI(Tl) low temperature, 122
- Debye Waller factor, 33
- Density of state production, 33
- Deuterium solidification, 48
- Diagnostics, 161
- Diffraction, 42
- Diffraction pattern, 43
- Direct condensation, 50
- Discharge cleaning, 191
- Drift region, 139
- dynamic structure factor UCN, 65
- Dynamic structure function, 42
- Edging, 194
- Einzel lens, 161
- Electro magnetic force, 25
- Electro polishing, 189, 191
- Electron background, 134
- Electron gun, 163
- Electron spectrum, 107
- energy neutron, 23
- Evaporated crystal, 129
- Excess noise factor, 142
- Extractor Ion source, 157
- Film, 128
- Foil shutter method, 46
- FRED light, 113
- FRED-UCN, 93
- Free neutron parabola, 66
- Freezing model, 48
- Front contact, 139
- Gain, 140
- Gas handling system, 38
- Geometry method, 46
- Gravitation, 25
- Guide, 85
- Hamamatsu, 144
- HCP, 57
- Hexagonla closed package, 57
- Homogeneity LAAPD, 118
- Hydrogen, 190
- Hygroscopy, 131

IN4, 41  
 Inclusions, 190  
 incoherent approximation, 186  
 Inelastic neutron scattering, 41  
 inelastic neutron scattering, 184  
 Ion source, 157  
  
 LAAPD, 137  
 LAAPD damage, 195  
 LAAPD edging, 194  
 Langmuir Child model, 170  
 Light guide, 127  
 Light transport efficiency, 115  
 Liquefaction, 48  
 Loss absorption, 34  
 Loss scattering, 34  
 Luminescence spectra, 124  
  
 Magnetic storage, 102  
 Mass spectrum, 167  
 McIntire model, 140  
 Micro channel plate, 160  
 Monitor detectors, 159  
 Multiphonon, 185  
 Multiphonon correction, 64  
 Multiphononen, 63  
 Muphacor formalism, 186  
  
 Nacke model, 48  
 Neon, 46  
 Neutron lifetime values, 27  
 Noise, 148  
  
 ortho/para converter, 39  
 Oxisorb, 183  
  
 Parallel noise, 141  
 PENELOPE, 101  
 Perkin Elmer Instruments, 144  
 Phonon density of states, 43  
 Phosphor screen, 174  
 Photomultiplier, 127  
 Photon counters, 115  
 Powdercell, 56  
 Production cross section, 69  
 Profil, 172  
 Proton detection, 121  
 Proton detector, 109, 134  
 Proton interaction, 111  
  
 Proton spectrum, 107  
  
 Quantum efficiency, 126  
  
 Ramalines, 41  
 Raman setup, 40  
 re-sublimation, 50  
 Reach through, 143  
 Rear contact, 139  
 Response Function, 42  
 Reverse reach through, 143  
 Richardson equation, 158  
 RMD, 143  
  
 $S(q)$ , 185  
 $S(q,\omega)$ , 42  
 Saha equation, 158  
 Scattering function, 42  
 scattering function UCN, 65  
 Scattering loss, 34  
 Scintillation efficiency, 127  
 Scintillator, 120  
 Simion, 164  
 Snow, 47  
 Spectral response, 150  
 Standard Model, 26  
 Storage method, 46  
 Storing method , 86  
 Stranski model, 48  
 Stress, 117  
 Strong interaction, 24  
 Structure, 43  
 Stucture freezing., 58  
 Superficial current, 141  
 Superthermal UCN production, 30  
 Surface components, 189  
 Surface current, 141  
 Surface leveling, 189  
 surface roughness, 193  
 $S_{q,\omega}$  UCN, 65  
  
 Targetcells, 35  
 Turbo, 51  
 Two hole method, 187  
  
 UCN, 24  
 UCN converter, 81  
 UCN test source, 44  
 UCN-VCN, 74

UCN-VCN-CN, 46  
Ultra cold neutrons, 24  
Under cooled, 52  
Unitarity, 27  
Unity gain, 148  
  
Volume leakage current, 141  
  
Wavelength shifter, 126  
Work function, 144  
Wrapping, 123

